

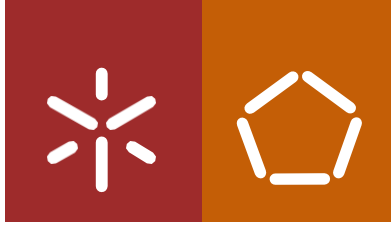


**Universidade do Minho**  
Escola de Engenharia

Marta Adriana Félix Forte

**Encapsulation of agrochemicals in  
polymeric microcapsules coated with  
photocatalytic nanomaterials**





**Universidade do Minho**  
Escola de Engenharia

Marta Adriana Félix Forte

**Encapsulation of agrochemicals in  
polymeric microcapsules coated with  
photocatalytic nanomaterials**

Tese de Doutoramento  
Programa Doutoral em Engenharia de Materiais e Processamento  
Avançados

Trabalho efetuado sob orientação do

**Professor Doutor Carlos José Macedo  
Tavares**

e do

**Professor Doutor Rui Ramos Ferreira e Silva**

## **DIREITOS DE AUTOR E CONDIÇÕES DE UTILIZAÇÃO DO TRABALHO POR TERCEIROS**

Este é um trabalho académico que pode ser utilizado por terceiros desde que respeitadas as regras e boas práticas internacionalmente aceites, no que concerne aos direitos de autor e direitos conexos.

Assim, o presente trabalho pode ser utilizado nos termos previstos na licença abaixo indicada.

Caso o utilizador necessite de permissão para poder fazer um uso do trabalho em condições não previstas no licenciamento indicado, deverá contactar o autor, através do RepositóriUM da Universidade do Minho.

### ***Licença concedida aos utilizadores deste trabalho***



**Atribuição-Compartilha Igual  
CC BY-SA**

<https://creativecommons.org/licenses/by-sa/4.0/>



## **Para a minha família**

É num abraço que me dou e me desfaço.  
Levo um pouco de ti e guardo com amor cada pedaço.

## **Acknowledgments**

My research would have been impossible without the aid and financial support of a Ph.D. grant in Advanced Materials and Processing - AdvaMTech - from Fundação para a Ciência e Tecnologia with reference: PD/BD/12849/2017. Also, I am grateful to ASCENZA®, specially to Engineer José Neves that accepted to be part of the project by suggesting the problem that originated the thesis, contributing with financial support, and supplying the agrochemicals. Basically, they were the electromotive source. A special thanks to Professor Ana Maria Pinto as representing and coordinating at the University of Minho this educational program that kindly provided me all the information and support during these years. Then, I would like to thank my supervisors, Professor Carlos Tavares and Professor Rui Silva, who agreed to do this project and embraced all the situations present during this adventure. I am grateful for the dedication, scientific guidance, and patience. Moreover, listening and understanding, resulting in space to be autonomous and imaginative to drive this project, creating my paths to success in the proposed tasks.

My sincere thanks to Juliana Marques that since day one guided, elucidated, supported, and taught me so much about science. Not only about the microencapsulation, photocatalysis, and controlled release that this thesis embraces but also about being a scientist in the way of thinking, organization, leadership, and confidence (yes, this is very important). It was an inspiration in so many conducts that shaped me as a worker in the field. Then, I want to say thanks to Ricardo Silva, who showed me what a material engineer really does and the perspective to solve the problems, as well as the path to find the answers. Also, teaching me about the atomic layer deposition technique (definitely) was a challenge.

This work was done at the University of Minho and the University of Aveiro. Thus, many people helped me in the administration part and technicians from SEMAT/UM at University of Minho and DEMaC/CICECO at the University of Aveiro. A notable standout to Dr. Edith Ariza and Professor Maria Sameiro for the patience and suggestions to do the SEM-EDX analysis and the NMR analysis plus the interpretation, respectively.

Last but not least, to all my laboratory friends that have met since 2016, I am so much thankful to be part of them. It was a pleasure to work with all the persons that passed by the laboratory through these years. Definitely, the working days were happy, fun and the scientific discussions were always an adventure. It was a beautiful journey because of them.

À minha família quero agradecer na minha língua, porque é em português que faz sentido

e onde encaixam os sentimentos. Obrigada do fundo do coração por me deixarem voar, por entenderem que a minha curiosidade científica é uma parte de mim, apesar de ser desafiante e darem-me constantemente força para ser melhor. Obrigada por todos os dias me ouvirem, apoiarem e darem as vossas opiniões. Acima de tudo, fico e ficarei agradecida por todo o amor, por me ajudarem, iluminarem os meus dias e a minha mente.

A cada momento as galáxias expandem-se, mas sei que nunca haverá espaço suficiente para o amor incondicional, nem para o aconchego de todos os abraços. Obrigada minha *ohana!*

## **FCT** Fundação para a Ciência e a Tecnologia

MINISTÉRIO DA CIÊNCIA, TECNOLOGIA E ENSINO SUPERIOR



UNIÃO EUROPEIA  
Fundo Europeu  
de Desenvolvimento Regional



## **STATEMENT OF INTEGRITY**

I hereby declare having conducted this academic work with integrity. I confirm that I have not used plagiarism or any form of undue use of information or falsification of results along the process leading to its elaboration.

I further declare that I have fully acknowledged the Code of Ethical Conduct of the University of Minho.

# Encapsulation of agrochemicals in polymeric microcapsules coated with photocatalytic nanomaterials

## Abstract

Excessive use of agricultural land using agrochemicals (AC) for human livelihood results in excessive pollution of soils and food chains. The nutritional deregulation of soils causes damage that takes years to restore. Therefore, it is urgent to reduce the amount and/or concentration of ACs and to create solutions for their gradual release.

Microencapsulation systems may help to reduce this problem as they protect the AC from external actions like water, light, and temperature. This work developed two controlled release systems. (1) Polymethyl methacrylate microcapsules (PMMA-MCs), using the solvent evaporation technique with double emulsion, followed by ZnO and TiO<sub>2</sub> coatings by atomic layer deposition (ALD) to degrade the PMMA-MCs and release the AC. Energy-dispersive X-ray spectrometry (EDX) proved the microcapsules configuration, as also the presence of the AC. (2) Gelatin microspheres (MSs) by gelification and crosslinking methods.

The ALD deposition depends on the substrate glass transition temperature (T<sub>g</sub>) and on the pre-treatment with ozone. The studied PMMA has a T<sub>g</sub> = 114 °C, resulting from a combination of tacticities determined by the three different proton and carbon peaks in 1D and 2D NMR, from each tactic structure. The syndiotactic PMMA is predominant because intense peaks were identified in UV-vis (212.8 nm) and FTIR (750, 915, and 1062 cm<sup>-1</sup>).

ALD permits to do ozonation as an *in situ* pre-treatment. The reactivity from the metallic precursor indicates the intensity of the pre-treatment. For titanium tetraisopropoxide it was necessary more 300 O<sub>3</sub> ALD cycles than for the diethylzinc. The X-ray diffractometer experiments revealed the amorphous structure of TiO<sub>2</sub> as the pattern shows the same diffractogram as for PMMA-MCs, coincident with the PDF card (00-064-1603). The ZnO coating resulted in a wurtzite structure coincident with the PDF card 04-022-5463. Moreover, ZnO can be used as a seed layer to further deposit TiO<sub>2</sub>. The TiO<sub>2</sub> coatings have a low photocatalytic activity. However, 400 ZnO ALD cycles degraded 95 % of the dye solution after 9 hours of UV irradiation.

A controlled release was lightly observed for ALD coated PMMA microcapsules after 24h, under Xe lamp irradiation, but it was not possible to quantify it. On the other side, the gelatin and polyvinyl alcohol microspheres allowed the AC release by swelling and diffusion, and the process took more than 8h to occurs entirely.

**Keywords:** Agrochemicals, ALD, Controlled release, Microcapsules, Photocatalysis

# Encapsulamento de agroquímicos em microcápsulas poliméricas revestidas com nanomateriais fotocatalíticos

## Resumo

O uso excessivo de agroquímicos (AQs) é vital para a obtenção de alimentos, todavia é uma fonte de poluição dos solos, cursos de água e cadeias alimentares. A desregulação nutricional dos solos causa danos que levam anos a serem reestabelecidos. Assim, é urgente reduzir a quantidade e/ou concentração de agroquímicos nos solos, promovendo a sua libertação gradual.

Os sistemas de microencapsulação conseguem solucionar esta falha, protegendo os AQ de ações externas como água, luz e temperatura. Neste trabalho foram desenvolvidos dois sistemas de libertação controlada. (1) Síntese de microcápsulas de polimetil metacrilato (MCs-PMMA), usando a evaporação do solvente associada à dupla emulsão, sendo seguidamente revestidas com ZnO e TiO<sub>2</sub> por deposição em camada atômica (DCA) para degradar as MCs-PMMA e posteriormente libertar o AQ. A espectrometria de raio-X por dispersão em energia provou a estrutura das MCs e a presença do AQ. (2) Formação de microesferas de gelatina por gelificação e *crosslinking*.

A DCA depende da temperatura de transição vítrea (T<sub>g</sub>) e do pré-tratamento com ozono. O PMMA estudado tem T<sub>g</sub> = 114°C, e é a combinação de taticidades que foram determinadas pelos respetivos picos de próton e carbono em 1D e 2D RMN. O PMMA é predominantemente sindiotático, com picos intensos em UV-vis (212.8 nm) e FTIR (750, 915 e 1062 cm<sup>-1</sup>).

A DCA permite fazer ozonação como um pré-tratamento *in situ*. A reatividade do precursor metálico dita a intensidade do pré-tratamento. Para o tetraisopropóxido de titânio foram precisos mais 300 ciclos de O<sub>3</sub> do que para o dietilzinc. Através da difração de raios-X determinou-se que o TiO<sub>2</sub> é amorfo uma vez que o difractograma é semelhante ao das MCs-PMMA, coincidente com a carta PDF 00-064-1603. O revestimento de ZnO tem a estrutura da wurtzite (carta PDF 04-022-5463). Adicionalmente, o ZnO pode ser usado como camada semente para crescer o TiO<sub>2</sub>. Os revestimentos de TiO<sub>2</sub> têm uma baixa atividade fotocatalítica. Todavia, 400 ciclos de ZnO degradaram 95% de solução de corante após irradiação com luz UV durante 9h.

A libertação controlada foi testada sob irradiação com uma lâmpada de Xe, verificando-se este efeito em 24h, porém com variações ligeiras e difíceis de quantificar. As microesferas de gelatina e álcool polivinílico foram criadas para libertar o AQ por inchamento e difusão, e o processo demora mais de 8h.

**Palavras chave:** Agroquímicos, ALD, Fotocatálise, Libertação controlada, Microcápsulas

# Index

<b>ACKNOWLEDGMENTS .....</b>	<b>VI</b>
<b>ABSTRACT .....</b>	<b>IX</b>
<b>RESUMO .....</b>	<b>X</b>
<b>INDEX.....</b>	<b>XI</b>
<b>LIST OF ABBREVIATIONS.....</b>	<b>XIV</b>
<b>LIST OF SYMBOLS AND GREEK LETTERS.....</b>	<b>XIX</b>
<b>LIST OF FIGURES.....</b>	<b>XX</b>
<b>LIST OF TABLES .....</b>	<b>XXVIII</b>
<b>LIST OF EQUATIONS .....</b>	<b>XXIX</b>
<b>INTRODUCTION AND MOTIVATION .....</b>	<b>1</b>
<b>THESIS STRUCTURE .....</b>	<b>2</b>
<b>CHAPTER 1 STATE OF THE ART .....</b>	<b>4</b>
1.1.    AGROCHEMICALS ENVIRONMENTAL IMPACT AND CONTROLLED RELEASE SYSTEMS .....	5
1.2.    MICROENCAPSULATION AS A TECHNIQUE FOR THE AGROCHEMICALS INDUSTRY .....	8
1.2.1.    MICROENCAPSULATION AS A CONTROLLED RELEASING SYSTEM .....	9
1.2.2.    MICROENCAPSULATION TECHNIQUES .....	12
1.2.2.1.    SOLVENT EVAPORATION TECHNIQUE.....	13
1.2.2.2.    SOLVENT EXTRACTION TECHNIQUE .....	14
1.2.2.3.    GELIFICATION WITH CROSS-LINKING AGENT TECHNIQUE.....	15
1.3.    PHOTOCATALYSIS .....	17
1.3.1.    PHOTOCATALYSIS MECHANISM .....	17
1.3.2.    TITANIUM DIOXIDE, TiO <sub>2</sub> .....	19
1.3.3.    ZINC OXIDE .....	21
1.3.4.    TiO <sub>2</sub> AND ZnO NANOMATERIALS APPLIED IN PHOTOCATALYSIS .....	22
1.4.    ATOMIC LAYER DEPOSITION .....	25
1.4.1.    BRIEF HISTORY OF ATOMIC LAYER DEPOSITION.....	25
1.4.2.    COATINGS ON PMMA BY THERMAL ATOMIC LAYER DEPOSITION.....	26
1.4.2.1.    PMMA CHALLENGES FOR ALD .....	26
1.4.2.2.    NUCLEATION AND GROWTH STUDIES .....	28
1.4.2.3.    ADHESION AND MECHANICAL PROPERTIES.....	30
1.4.2.4.    APPLICATIONS .....	32
1.4.2.4.1.    APPLICATIONS IN PHOTONICS, PHOTOLUMINESCENCE, AND PHOTOCATALYSIS.....	32
1.4.2.4.2.    APPLICATIONS IN DENTISTRY.....	35

1.4.3.	ALD COATINGS ON PMMA AIDED BY SEED LAYER .....	36
1.4.4.	COATINGS ON PMMA BY PLASMA ATOMIC LAYER DEPOSITION .....	40
1.4.5.	AREA SELECTIVE ALD ON PMMA .....	42
1.4.5.1.	PMMA AS MASKING LAYER .....	42
1.4.5.2.	ALD ON DI-BLOCK COPOLYMER MASKS .....	45
<b>CHAPTER 2 MATERIALS AND METHODS.....</b>		<b>53</b>
2.1.	MICROENCAPSULATION SYNTHESIS AND STRATEGIES .....	54
2.2.	PMMA BASED MCS .....	56
2.2.1.	PMMA-MCS SYNTHESIS.....	56
2.2.2.	PHOTOCATALYTIC LAYER BY ALD ONTO PMMA-MCS .....	58
2.2.2.1.	ALD ARCHITECTURE AND WORKING AS TOOL TO CREATE THE COATING .....	58
2.2.2.2.	ALD OF METAL-OXIDES .....	59
2.2.3.	PHOTOCATALYTIC PROCESSES ASSOCIATED WITH PMMA-MCS.....	61
2.3.	UNCOATED GELATIN BASED MSS.....	63
2.3.1.	GELATIN BASED MSS SYNTHESIS .....	63
2.3.2.	CONTROLLED RELEASE .....	63
2.4.	CHARACTERIZATION TECHNIQUES .....	64
2.4.1.	CHARACTERIZATION TECHNIQUES EMPLOYED IN THE MICROENCAPSULATION STRATEGIES AND THE ALD .....	64
2.4.2.	CHARACTERIZATION TECHNIQUES ASSOCIATED WITH THE CONTROLLED RELEASE AND OTHER PHOTOCATALYTIC TESTS	71
<b>CHAPTER 3 MICROCAPSULES RESULTS DISCUSSION .....</b>		<b>73</b>
3.1.	SOLVENTS, PMMA AND UF RELEVANT PROPERTIES FOR MICROENCAPSULATION .....	74
3.2.	PMMA-MCS FROM STRATEGY 3.....	75
3.2.1.	ATOMIC LAYER DEPOSITION ONTO PMMA-MCS .....	81
3.2.1.1.	ZNO COATING DEPOSITION ON PMMA-MCS .....	84
3.2.1.2.	ZNO SEED LAYER DEPOSITION ON PMMA-MCS .....	90
3.2.1.3.	TiO <sub>2</sub> COATING DEPOSITION ON PMMA-MCS.....	93
3.2.2.	ATOMIC LAYER DEPOSITION ON PMMA-MCS-UF.....	108
3.2.3.	PHOTOCATALYTIC PROCESSES ASSOCIATED WITH PMMA-MCS-UF AND PMMA-MCS.....	111
3.2.3.1.	COATED PMMA-MCS AS PHOTOCATALYTIC SUBSTRATES .....	111
3.2.3.2.	CONTROLLED RELEASE ONTO COATED PMMA-MCS-UF.....	114
<b>CHAPTER 4 MICROSPHERES RESULTS AND DISCUSSION.....</b>		<b>121</b>
4.1.	GELATIN-BASED MSS FROM STRATEGY 4 .....	122
4.2.	GELATIN-BASED MSS IN CONTROLLED RELEASE SYSTEMS .....	128
<b>CHAPTER 5 CONCLUSIONS AND FUTURE WORK .....</b>		<b>131</b>
5.1.	CONCLUSIONS AND OVERVIEW .....	132
5.2.	LIMITATIONS AND SUGGESTIONS FOR FUTURE WORK .....	134



<b>REFERENCES</b> .....	<b>136</b>
<b>APPENDIX 1</b> .....	<b>163</b>
PMMA-MCS FROM STRATEGY 1 .....	163
PMMA-MCS FROM STRATEGY 2 .....	171
<b>APPENDIX 2</b> .....	<b>175</b>
NMR SPECTRA .....	175
HBQC SPECTRA .....	176
HMBC SPECTRA AND SIGNAL TABLE .....	177

## List of abbreviations

### 1-10

3DMAS Tris(Dimethylamino)Silane,  $(\text{Me}_2\text{N})_3\text{SiH}$

### A

AA Active Agent

AC Agrochemical

AG Arabic gun

ALD Atomic Layer Deposition

ALE Atomic Layer Epitaxy

AS-ALD Area-Selective Atomic Layer Deposition

### B

BCP block copolymer

BET Brunauer-Emmett-Teller

BSE Backscattering electron

### C

CA Cellulose Acetate

$\text{Ce}(\text{thd})_4$  Tetrakis(2,2,6,6-Tetramethyl-3,5-Heptanedionato)Cerium,  $\text{Ce}(\text{C}_{11}\text{H}_{19}\text{O}_2)_4$

CF Chloroform

CL Crosslinker

CP Continuous Phase

c-PMMA-MCs Coated Poly(Methyl Methacrylate) Microcapsules

c-PMMA-MCs-UF Coated Poly(Methyl Methacrylate) Microcapsules with Agrochemical Encapsulated

CTEM Conventional Transmission Electron Microscopy

CVD Chemical Vapor Deposition

### D

DBC Diblock Copolymer

DCA Deposição Em Camadas Atômicas

DCM Dichloromethane/Methylene Chloride

DEPT 135 Distortionless Enhancement By Polarization Transfer

DEZ	Diethylzinc, $Zn(C_2H_5)_2$
DMSO	Dimethyl Sulfoxide
DSC	Differential Scanning Calorimetry
DTGA	Derivative Thermogravimetric Analysis
<b>E</b>	
EDDHA	Ethylenediamine-N,N'-Bis(2-Hydroxyphenyl)Acetic Acid
EDX or EDAX	Energy Dispersive X-Ray Spectroscopy
ES	Extractor Solvent
ETFE	Ethylene Tetrafluoroethylene
<b>F</b>	
FED	Fluorinated Ethylene Propylene
FEG	Field Emission Gun
FEG/SEM	Field Emission Gun Scanning Electron Microscopy
FIB-SEM	Focused Ion Beam Scanning Electron Microscopy
FTIR	Fourier Transform Infrared Spectroscopy
FTIR-ATR	Fourier Transformed Infrared – Attenuated Total Reflectance
FWHM	Full Width at Half-Maximum
<b>G</b>	
GC-MS	Gas Chromatography Acoplated To Mass Spectroscopy
GPC	Growth Per Cycle
<b>H</b>	
HMBC	Heteronuclear Multi Bond Correlation
HMQC	Heteronuclear Multiple Quantum Correlation
HPLC-MS	High Performance Liquid Chromatography Mass Spectroscopy
<b>I</b>	
Ir(acac) <sub>3</sub>	Iridium Acetylacetonate
<b>L</b>	
LED	Light Emission Diode
<b>M</b>	
MB	Methylene Blue

MCs	Microcapsules
MeCpPtMe <sub>3</sub>	Trimethyl(Methylcyclopentadienyl)Platinum (IV)
ML	Masking Layer
MSs	Microspheres
MSs-UF	Microspheres with Ultraferro
M <sub>w</sub>	Molecular Weight
<b>N</b>	
NIR	near-infrared
NPs	Nanoparticles
<b>O</b>	
O	Oil
OM	Optical microscopy
O/W	Oil-In-Water
O/W/O	Oil-In-Water-In-Oil
O <sub>1</sub> /O <sub>2</sub> /W	Oil-In-Oil-In-Water
O <sub>3</sub> -PMMA-MCs	Oxidized Poly(Methyl Methacrylate) Microcapsules
OTS	Octadecyl-Trichlorosilane
<b>P</b>	
PA-ALD	Plasma-Assisted Atomic Layer Deposition
PC	Polycarbonate
PE-ALD	Plasma-Enhanced Atomic Layer Deposition
PEEK	Polyether Ether Ketone
PEG	Polyethylene Glycol
PMMA	Poly (Methyl Methacrylate)
PMMA-MCs	Poly(Methyl Methacrylate) Microcapsules
PMMA-MCs-UF	Poly(Methyl Methacrylate) Microcapsules with Agrochemical Encapsulated
PP	Polypropylene
PS	Polystyrene
PS- <i>b</i> -PMMA	Polystyrene- <i>Block</i> -Poly(Methyl Methacrylate)
PS- <i>r</i> -PMMA	Polystyrene- <i>Random</i> -Poly(Methyl Methacrylate)
PTFE	Polytetrafluoroethylene

PVA	Polyviyl Alchool
PVC	Polyvinyl Chloride
<b>Q</b>	
QCM	Quartz Crystal Microbalance
<b>R</b>	
RE-ALD	Radical Enhanced Atomic Layer Deposition
rpm	Rotation Per Minute
<b>S</b>	
S	Surfactant
S/O/W	Solid-In-Oil-In-Water
SAM	Self-Assembled Monolayers
SDS	Sodium Dodcedyl Sulphate
SE	Secondary Electrons
SEM	Scanning Electron Microscopy
SEM-EDX	Scanning Electron Microscopy Energy Dispersive X-Ray Spectroscopy
SERS	Surface-Enhanced Raman Spectroscopy
STEM	Scanning Transmission Electron Microscopy
<b>T</b>	
T-ALD	Thermal Atomic Layer Deposition
TDMAH	Tetrakis(Dimethylamido)Hafnium, $[(CH_3)_2N]_4Hf$
TDMAT	(Tetrakis Dimethylamino)Titanium, $[(CH_3)_2N]_4Ti$
TDMAz	Tetrakis(Dimethylamido)Zirconium, $[(CH_3)_2N]_4Zr$
TEM	Transition Electrons Microscopy
TGA	Thermogravimetric Analysis
TiO <sub>2</sub> -O <sub>3</sub> -PMMA-MCs	Poly(Methyl Methacrylate) Microcapsules Oxidized And Coated with Titanium Dioxide
TiO <sub>2</sub> -O <sub>3</sub> -PMMA-MCs-UF	Poly(Methyl Methacrylate) Microcapsules with Encapsulated Agrochemical, Oxidized And Coated with Titanium Dioxide
TMA	Trimethylaluminum, $Al(CH_3)_3$
TTIP	Titanium Tetraisopropoxide, $Ti[OCH(CH_3)_2]_4$
TXRF	Total Reflection X-ray Fluorescence

**U**

UF	Ultraferro
UV	Ultraviolet
UV-VIS	Ultraviolet-Visible

**V**

Vis	Visible
-----	---------

**W**

$W_1/O/W_2$	Water-In-Oil-In-Water
WCA	Water Contact Angle
$WF_6$	Tungsten Hexafluoride
W	Water

**X**

XANES	X-Ray Absorption Near Edge Structure
XPS	X-Ray Photoelectron Spectroscopy
XRD	X-Ray Diffraction

**Z**

$ZnO-O_3$ -PMMA-MCs	Poly(Methyl Methacrylate) Microcapsules Oxidized And Coated with Zinc Oxide
$ZnO-O_3$ -PMMA-MCs-UF	Poly(Methyl Methacrylate) Microcapsules with Encapsulated Agrochemical, Oxidized And Coated with Zinc Oxide
$ZnO-O_3-SiO_2/Si$	Silicon Coated with Silicon Dioxide Oxidized And Coated with Zinc Oxide

## List of symbols and Greek letters

$\Delta E$	Energetic Transitions
$\beta\text{-NaYF}_4:25\%\text{Er}^{3+}$	Sodium Yttrium Fluoride Active Nanoparticles Doped with Trivalent Erbium Ions
$^{13}\text{C}$	Carbon-13
$^{13}\text{C-NMR}$	Carbon-13 Nuclear Magnetic Resonance
$^1\text{H}$	Proton
$^1\text{H-NMR}$	Proton Nuclear Magnetic Resonance
$a$	basal plan
$\beta$	Half-Height Width
$B_0$	Magnetic Field
$b$	bond length
$c$	basal direction
$C$	Concentration
$C_0$	Initial concentration
$d$	d-spacing
$e^-$	Electron
$h$	Planck Constant
$h^+$	Holes
$l$	Quantic spin number
$k$	Scherrer Constant
$P$	Crystallite Size
$r$	Interchain Distance
$t$	Time
$T_g$	Glass Transition Temperature
$\gamma$	Gyromagnetic Ratio Or Angular Momentum
$\delta$	Chemical Shift
$\theta$	Angle
$\lambda$	Wavelength
$\nu$	Frequency

## List of figures

<b>Figure 1.</b> Schematic illustration of the controlled release systems for the coated microcapsules and the microspheres.....	2
<b>Figure 2.</b> Agrochemical concentration obtained from two applications, for a conventional formulation (blue), and agrochemical concentration release when it is controlled by time, with one application (black) [46]. .....	8
<b>Figure 3.</b> Microcapsule morphologies: a) core-shell, b) heterogeneous, c) acorn, d) heteroaggregated and e) microspheres.....	9
<b>Figure 4. Solvent evaporation</b> steps: a) a solution made of polymer (P) and active agent (AA) is dispersed into a solution with a surfactant (S); b) emulsification; c) solvent evaporation and microcapsules wall formation.....	13
<b>Figure 5. Solvent extraction</b> steps: a) a solution made of polymer (P), active agent (AA) and extractor solvent (ES) is dispersed into a solution with a surfactant (S); b) emulsion formation; c) lixiviation and and microcapsules wall formation.....	14
<b>Figure 6. Gelification with cross-linking agent</b> steps: a) solution with polymer (P), active agent (AA) and cross-linker (CL) and a continuous phase (CP); b) polymer reticulation made by the cross-linking agent; c) microsphere gelification. ....	16
<b>Figure 7.</b> Band models applied to transition metals, $n$ and $p$ type intrinsic semiconductors and insulators. ....	18
<b>Figure 8.</b> Photoexcitation scheme (left side), recombination (above) and oxidation and reduction reactions (below) in the semiconductor correspondent to the photocatalysis process.....	19
<b>Figure 9.</b> Schematic representation of the ALD formation of the first $\text{Al}_2\text{O}_3$ monolayer from: (1) TMA pulsing; (2) TMA chemisorption in the surface (first half-reaction); (3) after purging of unreacted TMA and methane; (4) water pulsing; (5) water chemisorption on the by-product from the first half-reaction; and (6) after purging of unreacted water and methane. ....	27
<b>Figure 10.</b> Synthesis of PMMA by addition polymerization of MMA (adapted from [279]). .....	27
<b>Figure 11.</b> PMMA tacticities: isotactic, syndiotactic, and atactic and respective glass transition temperature. The tacticities values were collected from [281]. .....	28
<b>Figure 12.</b> Mass change measurements by QCM versus number cycles of $\text{Al}_2\text{O}_3$ ALD on PMMA at 85 °C for (a) 30 and (b) 5 cycles [275]. .....	29
<b>Figure 13.</b> In-situ FTIR analysis of uncoated PMMA spin-coated onto Si, first, and second ALD half-reactions. $\text{Al}_2\text{O}_3$ coating was made from TMA and $\text{H}_2\text{O}$ at 80 °C. A FTIR run followed each half-	



cycle, and between half-cycles, the reactor was purged for 10 s [290].	30
<b>Figure 14.</b> On-load and residual depth curves for Al <sub>2</sub> O <sub>3</sub> /PMMA and Al <sub>2</sub> O <sub>3</sub> /PC (polycarbonate) after the nanoscratch. The test was repeated five times per sample; each scratch had 500 μm of length, at a scanning velocity of 10 μm/s, and a ramped load varying from 0.1 mn to 60 mn [291].	31
<b>Figure 15.</b> Thermoplastic-epoxy resin with the double Al <sub>2</sub> O <sub>3</sub> coating; wettability test of a water droplet in coated and uncoated PMMA surface, and the interfacial toughness of PMMA and fluorinated ethylene propylene (FED) (wedge test) [292].	32
<b>Figure 16.</b> (a) Bragg stack (multilayered material comprised of TiO <sub>2</sub> layers/PMMA+NPs) for charge generation in a solar cell by a photonic upconverter. Scanning electron micrographs of the (b) Bragg stack and (c) of upconverter nanoparticles. (d) Scheme of core–shell upconverter NPs, converting near-infrared (NIR) to visible (VIS) photons in the core. (e) Energy levels in the upconverter Er <sup>3+</sup> and the upconversion process [295].	33
<b>Figure 17.</b> Photocatalytic efficiency of the amorphous TiO <sub>2</sub> . After 90 min, the methylene orange dye degraded 5% under UV-A illumination [297].	34
<b>Figure 18.</b> XRD pattern of ZnO/PMMA composite after the seven MB discoloration runs [300]. (a) Degradation of paracetamol drug as a function of irradiation time for paracetamol alone (squares), paracetamol with ZnO/PMMA (circles), and paracetamol with Ag/ZnO/PMMA (triangles) samples (b), under UV illumination [299].	35
<b>Figure 19.</b> XPS results of coated PMMA unbrushed (red) and brushed (blue), storage in water and brushed again after 5 months [285]. PMMA has great mechanical properties and low toxicity for the dental prosthesis fabrication.	36
<b>Figure 20.</b> Profilometry measurements of W ALD film thickness on different polymers vs. the number of W ALD cycles. Al <sub>2</sub> O <sub>3</sub> ALD was used as a seed layer (10 ALD cycles) [302].	36
<b>Figure 21.</b> Mass loss of uncoated and coated PMMA with Al <sub>2</sub> O <sub>3</sub> and Al <sub>2</sub> O <sub>3</sub> /TiO <sub>2</sub> when exposed to vacuum UV radiation over time [303].	37
<b>Figure 22.</b> XRD patterns of anatase TiO <sub>2</sub> films in substrates made of (a) Si at 200 °C, (b) PMMA at 250 °C, and (c) ETFE at 200 °C. Si substrate was used as a reference, for comparison purpose [304].	38
<b>Figure 23.</b> Water contact angles (θ) of UV-illuminated ZnO deposited on bulk PMMA (red), spin-coated PMMA (blue), and Si substrates as a function of ZnO ALD cycles (black). The two right-most points represent the contact angles of ZnO deposited on 100 cycles Al <sub>2</sub> O <sub>3</sub> intermediate layer (a). XRD patterns for 800 cycles of ZnO ALD onto: Si (black) and bulk PMMA substrates with (red) and	

without Al <sub>2</sub> O <sub>3</sub> seed layer (blue), and an XRD pattern of 1600 cycles ZnO film on bulk PMMA (grey). (b) [305].....	39
<b>Figure 24.</b> Schematic representation of one cycle of Al <sub>2</sub> O <sub>3</sub> by thermal ALD and plasma ALD techniques. In plasma ALD, the H <sub>2</sub> O co-reactant is replaced with a plasma exposure (e.g., O <sub>2</sub> plasma) to grow metal oxides.....	40
<b>Figure 25.</b> (a) Optical microscopic images after cross-hatch tests and (b) after climate test of antireflection coatings double-sided coated PMMA. Focused ion beam scanning electron microscopy (FIB-SEM) cross-sectional image of multilayered antireflection coatings on PMMA (c) focused on a crack (d) focused on a crack-free region [286]. ....	42
<b>Figure 26.</b> SEM micrographs of patterns produced on PMMA by AS-ALD tool for (a) Pt (b) Ir (c) Ru [319]; (d) TiO <sub>2</sub> [336]; (e) TiO <sub>2</sub> [329]; (f) HfO <sub>2</sub> [338] coatings in a silicon substrate. ....	44
<b>Figure 27.</b> SEM micrographs of patterns produced from a diblock copolymer with PMMA; (a1) cross-section top view (a2) of Si nanowire array with an Al <sub>2</sub> O <sub>3</sub> mask [318]. Top view, 40° tilt on top and cross-section of (b1) Al <sub>2</sub> O <sub>3</sub> hexagonally packed nanopillars array treated with plasma and (b2) nanowires made of Si with Al <sub>2</sub> O <sub>3</sub> mask on top [345]......	45
<b>Figure 28.</b> PMMA in an AS-ALD process, where the block copolymers are polystyrene- <i>random</i> -poly(methylmethacrylate) or polystyrene- <i>block</i> -poly(methylmethacrylate). ....	46
<b>Figure 29.</b> Microencapsulation approaches and the final product-controlled release.....	55
<b>Figure 30.</b> Schematic of the ALD reactor used in the experiments.....	58
<b>Figure 31.</b> SEM micrograph of PMMA-MCs displayed in the center. The sample was coated with Au before the SEM analysis. ALD approach for coating the PMMA-MCs: (1) titania direct deposition; (2 and 5) ozone as pre-treatment followed by the titania deposition; (3) zinc oxide deposition with ozone as pre-treatment; (4) ozone as pre-treatment and zinc oxide as a seed layer to promote the titania growth.....	59
<b>Figure 32.</b> Photocatalytic studies performed in the PMMA-MCs. ....	61
<b>Figure 33.</b> Schematic of the support made for the PMMA-MCs using carbon tape and glass slide introduced into a MB solution to monitor the photocatalytic activity when exposed to a UV-radiation. ....	62
<b>Figure 34.</b> Exemplification of a setup of photocatalysis experiments using a Xe lamp. ....	62
<b>Figure 35.</b> Electronic interactions in the SEM analysis [373]. ....	66
<b>Figure 36.</b> PMMA dried film, with UF. The polymer was previously dissolved in (a) acetone and (b) DCM. ....	75

<b>Figure 37.</b> (a) Theoretical and (b) experimental core-shell PMMA-MCs-UF structures. ....	75
<b>Figure 38.</b> SEM micrographs of products from PMMA synthesis using chloroform and methylene chloride as solvents. The double emulsion step took place at 5 °C or 40 °C. The samples were coated with Au before SEM analysis. ....	77
<b>Figure 40.</b> Optimized microencapsulation synthesis and PMMA-MCs diameter histograms from the SEM observations. The samples were coated with Au before SEM analysis.....	80
<b>Figure 41.</b> Images of pristine PMMA-MCs and PMMA-MCs after ozone pre-treatments organized by temperature and pulse time (G2-G6.2).....	82
<b>Figure 42.</b> PMMA-MCs DSC thermogram with heating and cooling ramps in a N <sub>2</sub> atmosphere. ....	83
<b>Figure 43.</b> UV-VIS spectrum of a PMMA film on a glass slide.....	84
<b>Figure 44.</b> (a) SEM micrographs and correspondent EDX maps of ZnO-O <sub>3</sub> -PMMA-MCs, where red represents the zinc content, green the carbon component, and blue the oxygen contribution. Cross-section SEM micrographs of ZnO-O <sub>3</sub> -SiO <sub>2</sub> -Si with (b1) 100 cycles and (b2) 400 cycles of ZnO deposited by ALD with an ozone pre-treatment of 100 cycles.....	85
<b>Figure 45.</b> (a) percentual TG and DTG (b) from PMMA, uncoated and coated PMMA-MCs, (c) and the respective reactants and product from the PMMA-MCs synthesis (d) amplification of (c) in lowers DTG values. ....	86
<b>Figure 46.</b> FTIR-ATR spectra of PMMA, PMMA-MCs and ZnO-O <sub>3</sub> -PMMA-MCs. ....	88
<b>Figure 47.</b> X-ray diffractograms from PMMA materials.....	90
<b>Figure 48.</b> SEM micrographs of TiO <sub>2</sub> -O <sub>3</sub> -ZnO-O <sub>3</sub> -PMMA-MCs at different TiO <sub>2</sub> deposition temperatures. The samples were coated with Au/Pd before the SEM analysis.....	91
<b>Figure 49.</b> Percentual TG (a) and DTG (b) from PMMA, uncoated and coated PMMA-MCs.....	92
<b>Figure 50.</b> SEM images of PMMA-MCs coated by ALD technique with TiO <sub>2</sub> previously pre-treated with (a) 100 cycles (magenta), (b) 200 cycles (pink), (c) 400 cycles (blue) and (d) 600 cycles (purple) of pre-treatment using O <sub>3</sub> . In the center the correspondent EDX signals are shown, in order to compare the increasing Ti content. The SEM images were taken after the EDX analysis to measure the coating thickness. All samples were coated with Au/Pd before SEM analysis. ....	94
<b>Figure 51.</b> Cross-section SEM micrographs of TiO <sub>2</sub> -O <sub>3</sub> -SiO <sub>2</sub> -Si with 400 cycles of TiO <sub>2</sub> deposited by ALD with an ozone pre-treatment of 400 cycles.....	95
<b>Figure 52.</b> X-ray diffractograms for PMMA, PMMA-MCs and TiO <sub>2</sub> -O <sub>3</sub> -PMMA-MCs with 100 cycles of pre-treatment and 400 cycles of TiO <sub>2</sub> deposition. ....	96

<b>Figure 53.</b> FTIR spectrums from the PMMA, PMMA-MCs, oxidized PMMA-MCs, and oxidized plus coated PMMA-MCs. ....	97
<b>Figure 54.</b> (a) FTIR spectrums of PMMA, PMMA-MCs, pre-treated microcapsules ( $O_3$ -PMMA-MCs) with 100, 200 and 400 cycles of ozone by ALD, and the respective coated microcapsules ( $TiO_2$ - $O_3$ -PMMA-MCs) with 400 cycles of $TiO_2$ deposited by ALD. The coated microcapsules have side by side the (a) FITR and (b) EDX spectra of the coated PMMA-MCs with $TiO_2$ to visualize the increment of Ti with the increasing pre-treatment cycles. ....	98
<b>Figure 55.</b> $^1H$ -NMR spectra for PMMA, PMMA-MCs, PMMA-MCs with DMSO, pre-treated microcapsules ( $O_3$ -PMMA-MCs) with 400 and 800 cycles of ozone by ALD treatment, and coated microcapsules ( $TiO_2$ - $O_3$ -PMMA-MCs) previously pre-treated with 400 cycles of ozone and further coated with 400 cycles of $TiO_2$ deposited by ALD. The crossed peak at $\delta = 1.58$ ppm is a water contamination. All the samples were dissolved into $CDCl_3$ . ....	100
<b>Figure 56.</b> Amplified $^1H$ -NMR spectra of PMMA-MCs, PMMA-MCs pre-treated microcapsules ( $O_3$ -PMMA-MCs) with 400 and 800 cycles of ozone by ALD treatment, and coated microcapsules ( $TiO_2$ - $O_3$ -PMMA-MCs) previously pre-treated with 400 cycles of ozone and further coated with 400 cycles of $TiO_2$ deposited by ALD. All samples were dissolved into $CDCl_3$ . ....	101
<b>Figure 57.</b> amplified $^{13}C$ -NMR spectra of PMMA-MCs and PMMA-MCs pre-treated microcapsules ( $O_3$ -PMMA-MCs) with 400 cycles of ozone by ALD, as well the respective DEPT 135 spectra overlaid in darker colors. All the samples were dissolved into $CDCl_3$ . ....	103
<b>Figure 58.</b> Amplified HMQC spectra of (a) PMMA-MCs and (b) $O_3$ -PMMA-MCs pre-treated with 400 cycles of ozone by ALD. ....	104
<b>Figure 59.</b> HMQC interactions that each carbon has with the protons in the PMMA-MCs before and after oxidation. ....	105
<b>Figure 60.</b> SEM micrographs of PMMA-MCs, $ZnO$ - $O_3$ -PMMA-MCs and $ZnO$ - $O_3$ -PMMA-MCs-UF, with different cycles, at $100^\circ C$ . All samples were coated with Au before SEM analysis. ....	108
<b>Figure 61.</b> X-ray diffractograms from PMMA, PMMA-MCs-UF, the respective pre-treatment ( $O_3$ -PMMA-MCs-UF (400 cycles)) as well as the coatings with varying oxidation cycles for constant the titania cycles, ( $TiO_2$ - $O_3$ -PMMA-MCs-UF (200 + 400 cycles) and $TiO_2$ - $O_3$ -PMMA-MCs-UF (400 + 400 cycles)), plus the core (UF). ....	109
<b>Figure 62.</b> SEM micrographs of PMMA-MCs-UF and $TiO_2$ - $O_3$ -PMMA-MCs-UF as well the EDX map from the oxygen (dark blue dots), iron (light blue dots), carbon (green dots) and titanium (red dots). The images on top were taken after the EDX analysis. The samples were coated with Au/Pd before	

the SEM-EDX analysis. ....	110
<b>Figure 63.</b> EDX spectra of PMMA-MCs-UF pre-treated with ozone and then coated with TiO <sub>2</sub> or ZnO by ALD technique. The samples were coated with Au/Pd before SEM-EDX analysis, the micrographs were acquired after the EDX acquisition. ....	111
<b>Figure 64.</b> Photocatalytic performance of PMMA-MCs and coated samples on degradation of a MB solution with 1x10 <sup>-5</sup> M. The samples were placed 3h in the dark (grey zone in the graph) followed by 6h of UV illumination 2 mW/cm <sup>2</sup> (white zone in the graph). The image demonstrates the ZnO–O <sub>3</sub> -PMMA-MCs photocatalytic performance showing the MB solution before (left) and after (right) test.....	112
<b>Figure 65.</b> TXRF spectra from TiO <sub>2</sub> -PMMA-MCs-UF in aqueous solution unirradiated and irradiated with Xenon lamp for 30h.....	116
<b>Figure 66.</b> (a) DTG of a 150 ppb UF solution, aliquots of TiO <sub>2</sub> -O <sub>3</sub> -PMMA-MCs-UF pre-treated with 400 ozone ALD cycles and coated with 400 ALD cycles of TiO <sub>2</sub> placed in the dark (unirradiated) and exposed to Xe lamp (irradiated). From the TiO <sub>2</sub> -O <sub>3</sub> -PMMA-MCs-UF aliquots was extracted the supernatant part and the precipitate containing the water and the TiO <sub>2</sub> -O <sub>3</sub> -PMMA-MCs-UF. (b) and (c) are the DTG amplified in the zones of interest to observe the presence of TiO <sub>2</sub> -O <sub>3</sub> -PMMA-MCs and the agrochemical. ....	117
<b>Figure 67.</b> Aqueous solutions of agrochemical, uncoated PMMA-MCs, and PMMA-MCs coated with TiO <sub>2</sub> or ZnO using an <i>in situ</i> pre-treatment with ozone. The images were taken in order to observe the controlled release from the variation in the agrochemical color.....	118
<b>Figure 68.</b> SEM micrographs and line EDX of cut PMMA-MCs-UF. The elements considered for the EDX line profile were oxygen, iron, carbon and chlorine. The samples were coated with Au/Pd before the SEM-EDX analysis. ....	119
<b>Figure 69.</b> Dehydration process in water:PVA 3% 10:90 MSs, with 1 g of gelatin and UF, during 8 days. ....	123
<b>Figure 70.</b> Chemical structures of the additives implemented in the gelatin:PVA MSs. ....	124
<b>Figure 71.</b> Microspherification synthesis parameters and the dried MSs with (top) and without UF (bottom). ....	125
<b>Figure 72.</b> Percentual TG (a) and DTG (b) from the different gels to produce MSs: gel 1 (water and gelatin), gel 2 (gelatin and a PVA 5% aqueous solution), gel 3 (gelatin, PVA 5% aqueous solution and urea) and gel 4 (gelatin, PVA 5% aqueous solution, urea and glycerin). Gel 4 corresponds to the MSs formulation. ....	126

<b>Figure 73.</b> DTG from gel 1 to 4 (color line in each graph) and the DTG of each compound added as purchase to form the gel (black thinner line). .....	127
<b>Figure 74.</b> spectra of (a) MEs and (b) MEs-UF in aqueous solution, in order to evaluate the cumulative controlled release. The gradient from lighter to darker correspond to the MSs (a) or MSs-UF (b) release overtime, meaning that the brown (a) and black (b) are the spectra at 495 min. Also, in (a) there is the same spectra amplified to visualize the band shape, and in (b) is present the absorbance intensity overtime, at 278 nm (grey curve) and at 480 nm (black curve). .....	130
<b>Figure i.1.</b> Experimental procedures for S/O/W and W <sub>1</sub> /O/W <sub>2</sub> double emulsions in the solvent (DCM) evaporation method, using a 4-blade helix as impeller. ....	163
<b>Figure i.2.</b> SEM micrographs of PMMA-MCs with UF, made from (a and c) S/O/W and (b and d) W <sub>1</sub> /O/W <sub>2</sub> , using 4% of PVA. The samples were coated with Au before SEM analysis.....	164
<b>Figure i.3.</b> Photographs of products from the double emulsions made by solvent evaporation technique with different solvents and maintaining the reaction temperature. ....	166
<b>Figure i.4.</b> Photographs of products from solvent evaporation, using Span®85 in the oily phase and PVA or Tween®20 aqueous solution as continuous phase. ....	167
<b>Figure i.5.</b> SEM micrographs of PMMA-MCs with UF from the S/O/W emulsion with varying PVA percentage. The samples were coated with Au before SEM analysis.....	168
<b>Figure i.6.</b> SEM micrographs of PMMA-MCs with UF from the following variables in the synthesis: surfactant and stirring time, impeller and stirring speed. The samples were coated with Au before SEM analysis. ....	170
<b>Figure i.7.</b> SEM micrographs of (a) cut MCs from the S/O/W solvent evaporation technique, (b) the same MCs with a rotation of 180°, (c) amplified MC with UF inside. The samples were coated with Au before SEM analysis. ....	171
<b>Figure i.8.</b> Products from the encapsulation W/O <sub>1</sub> /O <sub>2</sub> synthesis using different impellers (Ultra-Turrax®, 4-blade helix and magnetic stirring), where the W is a UF solution, O <sub>1</sub> is the PMMA solution and O <sub>2</sub> is sunflower oil.....	172
<b>Figure i.9.</b> (a) Amplified image of cellulose acetate capsules with UF as core (5%). (b) Photos of crushed cellulose acetate capsules with UF, synthesized with paraffin or sunflower oil as surfactants. The UF stained the filter and the capsules with sunflower oil also release the surfactant. ....	173
<b>Figure ii.1.</b> Amplified <sup>1</sup> H-NMR spectra of PMMA-MCs, PMMA-MCs pre-treated microcapsules (O <sub>3</sub> -PMMA-MCs) with 400 and 800 cycles of ozone by ALD treatment, and coated microcapsules (TiO <sub>2</sub> -	

O <sub>3</sub> -PMMA-MCs) previously pre-treated with 400 cycles of ozone and further coated with 400 cycles of TiO <sub>2</sub> deposited by ALD. All samples were dissolved into CDCl <sub>3</sub> .	175
<b>Figure ii.2.</b> HMQC spectrum of PMMA-MCs.	176
<b>Figure ii.3.</b> HMQC of O <sub>3</sub> -PMMA-MCs pre-treated with 400 cycles of ozone by ALD.	176
<b>Figure ii.4.</b> HMBC spectrum of PMMA-MCs.	177
<b>Figure ii.5.</b> HMBC of O <sub>3</sub> -PMMA-MCs pre-treated with 400 cycles of ozone by ALD.	177

## List of tables

<b>Table 1.</b> List of ACs with low environmental impact [38].	7
<b>Table 2.</b> General composition of a microcapsule suspension [94].	10
<b>Table 3.</b> Microencapsulation synthesis methods.	12
<b>Table 4.</b> TiO <sub>2</sub> crystallographic structures and respective properties (Ti are the white spheres and O are the red spheres) [201].	20
<b>Table 5.</b> ZnO crystallographic structures and respective properties (Zn are the yellow spheres and O are the purple spheres) [201].	22
<b>Table 6.</b> Techniques to synthesize TiO <sub>2</sub> and ZnO nanomaterials.	24
<b>Table 7.</b> Summary of literature data regarding ALD coatings on PMMA.	48
<b>Table 8.</b> ASCENZA® ACs characterization and respective properties.	54
<b>Table 9.</b> Deposition approaches and the respective experimental conditions for coating the PMMA-MCs with TiO <sub>2</sub> , ZnO or the combination of both metal-oxides associated to the ozone pre-treatment. Each approach corresponds to the deposition technique from <b>Figure 31</b> .	60
<b>Table 10.</b> Characterization techniques used in the MCs and MSs synthesis analysis, MCs coating by ALD, as well MCs and MSs UF controlled release monitoring.	64
<b>Table 11.</b> Physical and chemical properties from solvents employed in the microencapsulation to synthesize PMMA-MCs (adapted from [384]).	74
<b>Table 12.</b> FTIR-ATR maximum band values and the respective chemical bond and associated vibration.	88
<b>Table 13.</b> XRD results and calculated for PMMA materials.	90
<b>Table 14.</b> Growth per cycles ranges collected from the <b>Table 7</b> of TiO <sub>2</sub> thin films made by ALD when the Ti precursor is TDMAT, TiCl <sub>4</sub> or TTIP.	95
<b>Table 15.</b> Relative tacticities percentage from the protons in the -CH <sub>3</sub> obtained by <sup>1</sup> H-NMR.	99
<b>Table 16.</b> HMQC coordinates from chemical shifts associated with carbon and proton NMR, as well as signal identification for PMMA-MCs before and after the oxidation process.	107
<b>Table 17.</b> Percentual MB degradation rate after 3h with the LED off (dark), after 6h with the UV-LED on, and the total degradation during the photocatalysis tests.	113
<b>Table 18.</b> MSs synthesis parameters, products, and the respective stability overnight.	122
<b>Table i.1.</b> Surfactants and hydrophilic-lipophilic balance values.	166
<b>Table ii.1.</b> HMBC signals for the PMMA-MCs and the O <sub>3</sub> -PMMA-MCs and the respective chemical groups identification. The grey zones are unknown peaks.	178



## List of equations

Equation 1.....	24
Equation 2.....	24
Equation 3.....	24
Equation 4.....	24
Equation 5.....	62
Equation 6.....	69
Equation 7.....	69
Equation 8.....	69
Equation 9.....	70
Equation 10.....	70

## Introduction and motivation

Agriculture is one of the ordinary forms of supplying food to humans and livestock and it is in transformation due to the environmental impact [1]. Nowadays, the majority of the agrochemicals (ACs) are a concern because they are coated with polymers and/or are itself an extreme source of pollution to the fauna and flora.

ASCENZA® is an agrochemical manufacturer that is distributed mostly across Europe. One of the many ambitions is to reformulate the ACs synthesis and release methods, bringing new ways to encapsulate hydrophilic ACs to provide a controlled release.

This thesis focuses on solving the problematics that ASCENZA® experimented when creating an involucre where the compounds are retained in the interior, as a liquid or in solid-state. In this way, all the ACs characteristics are preserved given the conditions they must face during storage, transport, and subsequent lifetime when applied to agricultural land. Indeed, such microcapsules (MCs) have to be mechanically resistant, but able to dissociate when exposed to sunlight. Furthermore, they release the agrochemicals during the crop's development, minimizing the pollution. To attain this, it is imperative to functionalize the MCs wall through a photocatalytic and nanometric coating. As examples are titanium dioxide ( $\text{TiO}_2$ ) and zinc oxide (ZnO) [2,3].

The photocatalytic compound absorbs ultraviolet (UV) radiation and a fraction of visible (VIS) that triggers radical production. These will generate redox reactions, reducing itself and oxidizing the surrounding compounds. Since the MCs wall is adjacent to the coating, this one will be susceptible to oxidation and, over time, will be destructed. Thus, the release will be dependent on the MCs and coating properties.

The atomic layer deposition (ALD) is ideal for this purpose, since it produces conformal coatings, and the respective thickness is controlled at a nanometric scale. Moreover, by adjusting the ALD parameters, a second shell or cluster can be synthesized. The deposition temperature can induce crystallographic domains with photocatalytic performance, such as anatase from  $\text{TiO}_2$ . However, ALD on polymers is growing slowly due to structural limitations [4].

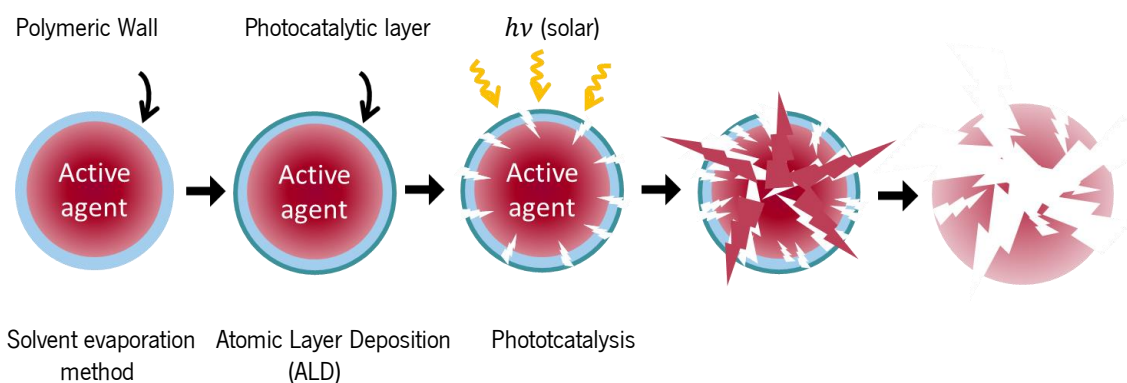
Besides the development of polymeric microcapsules coated by ALD with photocatalytic nanomaterials, another system was attempted for the microencapsulation of agrochemicals: microspheres (MSs). Here, the ACs controlled release is based on swelling and diffusion phenomena.

## Thesis structure

This work is mainly divided into three stages: (1) synthesis of the MCs and MSs with hydrophilic ACs, (2) ALD coating of them, and (3) study of the photocatalysis or swelling and diffusion mechanisms as controlled release processes (**Figure 1**). It is worth of note that each part has a novelty. Concerning the MCs systems where PMMA is used, there are a few encapsulated hydrophilic compounds reported so far. In the ALD section, the bibliography is rare, and the use of PMMA as support material is even scarce. The resultant review article, presented in the state of art, demonstrates that PMMA support substrate were 2D, so the presented MCs are a novelty in these ALD-coated polymers. Regarding the photocatalysis technology for releasing ACs, this approach is itself new.

### Controlled release systems

#### Microcapsules



#### Microspheres

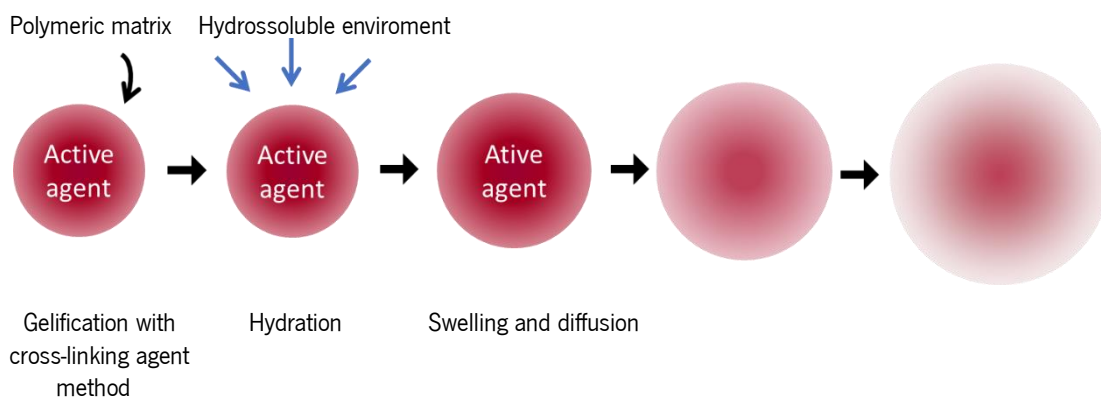


**Figure 1.** Schematic illustration of the controlled release systems for the coated microcapsules and the microspheres.

This thesis was separated into five chapters: i) state of the art; ii) materials and experimental methodologies; results and discussion for the MCs (iii) and MSs (iv). The last part (v) is comprised of conclusions, limitations, and future work.

Chapter 1 gives a perspective of AC types and the consequences of their use in crops. Then, it explains the ACs microencapsulation as a controlled release system on the way to preserve the soils, and its excellent performance when employed. Next, the various microcapsule types are described, as well as the experimental synthesis to produce them. This part explains the techniques that are relevant to this work, such as solvent evaporation, solvent extraction and gelification with cross-linking agent techniques.

Another part of this chapter is dedicated to the photocatalysis mechanism and provides information about the materials used for the photocatalytic layer (titanium dioxide and zinc oxide). Due to the heterostructured material complexity and the lack of scientific studies or reports, the ultimate part is an overview that explains the atomic layer deposition (ALD) technique. Here, there are experimental examples of PMMA either as support or as a substrate to create patterns.

Chapter 2 reports on materials and methods employed for the development of microcapsules with PMMA and/or cellulose acetate as a shell and for the gelatin-based microspheres. Initially, there is a plan to understand the process, and the steps put into practice, not just to make the polymeric microcapsules but also to create the coating. Following this, there is a brief explanation of the characterization techniques used and this importance of each one. In this section, the methods used to evaluate the controlled release and photocatalytic tests are described.

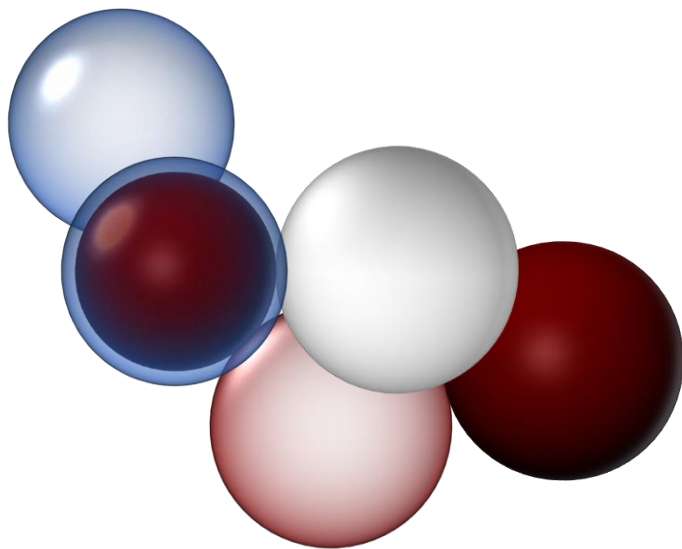
Chapter 3 presents the results and discussion about the microcapsules strategy. Failures are interpreted and the path to the successful MCs or coating via ALD is reached. There is also evidence obtained from different characterization techniques designed to create a solid foundation, giving robustness to the results and theories behind them.

Chapter 4 is a chapter similar to the previous one but dedicated to the microspheres development. This part describes the multiple ways to improve the MSs spherical shape and properties to carry the ACs. The ALD technique was not used because the MSs are hydrophilic, so the ACs will be released when in contact with environments that have a common solubility.

Finally, the Chapter 5 deals with the limitations from this work, some advice and adjustments that can be used to bring them closer to sustainable products. In the last topic, the most relevant conclusions are highlighted.

# **Chapter 1**

**State of the art**



## **1.1. Agrochemicals environmental impact and controlled release systems**

Agrochemicals (ACs) are chemical compounds, most of them synthetic [5–8], that are used for agricultural applications. They are categorized by their function: pesticides [6,9–11], fertilizers [6,9,11], plant growth agents [10,11] and pharmaceutical compounds for livestock [6,9].

The pesticides exterminate plagues that attack the crops, namely weeds (herbicides), insects (insecticides), fungus (fungicides), and others [1,6]. The fertilizers contain hydrophilic nutrients, that are uptake by the roots and finally provide nutrients. These fertilizers are rich in nitrogen, phosphorus and potassium [6,12,13]. The plant growth regulators have in their composition nutrients and hormones to stimulate the crops developing [14].

When ACs are applied, they are susceptible to photolysis [9], hydrolysis [15], microbial degradation, natural decay, and other dissipation routes [16]. Furthermore, the non-deteriorated part is vulnerable to evaporation [14,17], volatilization [18], leakage [17], lixiviation [14,17], root exudation [17] and root uptake [17,19]. Usually, it is necessary to apply a concentration higher than the necessary to ensure the resistance of the agrochemical, when exposed to the environmental conditions [14]. However, the agrochemical excess produces secondary effects [8,9,20,21].

The ecotoxicity affects the fauna and flora and may result in an overconcentration of the ACs in the human body, as well of the organisms after ingestion (bioaccumulation) [1,13,22–26]. Another side effect is the persistence when the chemical compounds are transferred to the ecosystem and do not degrade after a certain period (usually three months) [13]. Even if they are not persistent or bioaccumulative, it takes several years to be eliminated. Also, they are metabolized in contact with soils or plants [17]. So, distinct ACs can combine and develop a synergetic response, being a concern to the ecosystem [27,28].

Each toxicity type affects the soil in different ways. The ACs composition affects the N, P and K cycles and imbalances the soil's organic matter, triggering chemical reactions between the ACs and the soil composition [1,13,26]. In extreme concentrations, it changes the pH value to out of neutral pH, where the soil activity is not potentialized [13]. For longer expositions the soils are deforested [20,21,29,30], eroded [1,20,21,29,31] and there is also watercourse depletion [13,20,21,29,30].

To control and stop this environmental crisis, laws, norms, and guides were created by international organizations [6,12,13]. The Food and Agriculture Organization of the United Nations

is the most important and, in the past, established the maximum concentration allowed for ACs. In this domain, the European Union stipulated a maximum of 0.5 ppb of pesticides as total maximum concentration in potable water [32]. The implemented limits make it impossible to continue the traditional agricultural practices [10,33], and just reducing the amount applied to crops is not feasible. Consequently, it was essential to create excipients to insert the ACs [9,34] and a strategy to render uniform the distribution into the fields without losing the integrity and correspondent properties [33,35].

Due to the depletion of soils to produce enough to feed the humans and livestock, and the fact that the natural degradation of ACs is slow, the risk of their accumulation or persistence will increase [36]. The approach taken was to create systems to gradually release the ACs. By these mechanisms, the crops will always have a concentration that never reaches the toxicological effect. Once there is a barrier, the release will be gradual, so the accumulation is avoided. From the industrial point of view, these systems have advantages, such as the customization of release systems that combine ACs or even adjust their release time. The profit of a functional product of this type has prospects of being high, which is also very attractive for the industry.

The controlled or slower release systems for agriculture appeared at the end of the XX century [35]. Before 1980, different formulations such as grains with different sizes, aqueous solutions and oil-in-water emulsions (O/W), started to emerge [37]. Then, side by side, the technological developments presented innovations such as auxiliary formulations and inert compounds [10,11,38]. In this way, the quality, stability and biological activity of the ACs were enhanced [35,38,39]. Also, the solubility was controlled to act in the roots or leaves and decrease the impact in the ecosystem. These new products are advantageous since they are safe, during the production, storage and utilization steps. **Table 1** lists distinct ACs formulations, including microencapsulation [38].

The agrochemical industry invested in two release domains: the controlled and the slow release [40,41]. The EN 13266/2001 standard [42] defines slow release as the process that does not release more than 15% of the active agent (AA) in 24h and no more than 75% in 28 days. Another parameter to fulfill is to not release more than 75% of the AA during the established maximum time [7]. As examples, there are O/W emulsions, suspoemulsions, microemulsions, and multiple emulsions like water-in-oil-in-water ( $W_1/O/W_2$ ), oil-in-water-in-oil (O/W/O) [43] and solid-in-oil-in-water (S/O/W) [44].

In a general definition, controlled release is the one where the AA has a physical barrier.

This is influenced by a parameter that dictates the AA retention for a specific time period [11,36,53,45–52]. This mechanism differs from the slow release because the agrochemical properties are preserved; in other words, the physical barrier prevents the reaction from a physical or chemical process. This methodology ensures the ACs maximum efficacy [11,35,36].

**Table 1.** List of ACs with low environmental impact [38].

<b>Formulations types</b>
Granules
Wettable powders
Water dispersible granules
Suspensions
Concentrated solutions
Concentrated suspensions
Emulsifiable concentrated
Suspoemulsions
Microemulsions
O/W emulsions
Seed treatments
Microcapsules
Formulation employed in this study

In the first stage, the formulation introduced in the controlled release system is applied in the crops. So, the AC maintains the integrity and not an immediate action; over time, the release is gradual. The interaction between the formulation and the environment is minimized. Consequently, the AC concentration is effective for a more extended period without reaching the toxicological level. This approach takes more time than the conventional one. The last phase is the concentration decrease, until the agrochemical exhaustion (**Figure 2**) [35,46,54,55]. Overall, the number of applications per crop declines the ACs side effects and the bacterial transport from the ecosystem [35,56–63].

The agricultural industry has been enticed to synthesize new formulations. Despite the complexity and expense, the energetic cost is minor since the agrochemical quantities are less and the action time is longer [64]. Different formulations exist in the form of granules, matrix systems with physic entrapment [36,40,41,65], polymeric systems chemically bonded to the agrochemicals and formulations where the AC is covered by membranes, microcapsules, and coatings [36,41,65].

In conclusion, there are different controlled release systems; each one has a respective action mode that brings advantages compared with the AC in the simple formulation. Since there is a barrier, the release is slower, efficient and preserves the AC integrity. In all of them is verified



that the AC concentration does not reach toxic levels, keeping the ecosystem uncontaminated.

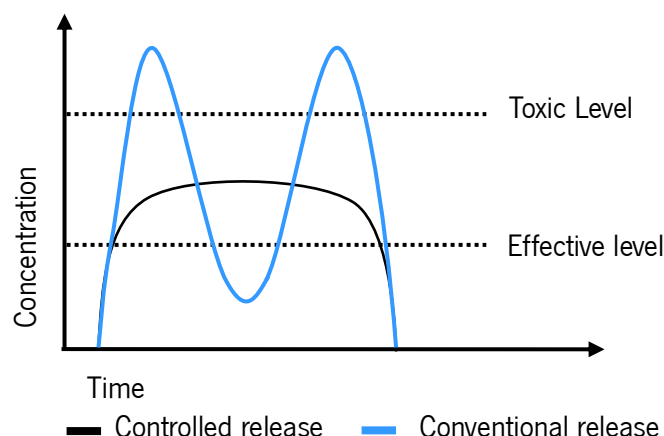


**Figure 2.** Agrochemical concentration obtained from two applications, for a conventional formulation (blue), and agrochemical concentration release when it is controlled by time, with one application (black) [46].

## 1.2. Microencapsulation as a technique for the agrochemicals industry

Microencapsulation is a technique wherein a compound creates a membrane and surrounds an AA, creating a microcapsule (MC) [11,35,36,46,56,66]. The diameter ranges from 1  $\mu\text{m}$  to 2 mm; if it is between 50 nm and 1  $\mu\text{m}$  it is considered a nanocapsule [67,68]. The MCs are constituted by a core and a shell. The AA is in the reservoir, where one or multiple AAs can be encapsulated in solid, liquid, or gaseous cores [36,56,68–73]. As an exception, the micelle type can only encapsulate one AA due to the chemical composition [27,66,74,75]. Complementary, the wall is the shell that preserves the core; there are several shells from natural, semisynthetic, and synthetic sources. The shell materials are based on polymeric compounds [76,77] and their selection depends on the encapsulation purpose [76,77].

Several approaches have been attempted to retain the core, creating different microcapsules (**Figure 3**) [46,56,77]. The AA physical state is crucial to produce the MCs and influences the MCs type [77]. It can be distributed as moncore, multicore, or matrices [71,78]. The perfect situation is when there is a central core and the shell protects it; this is the moncore case, also known as core-shell type because there is a reservoir formation [76,78–83]. It is easier to obtain core-shell MCs when the cores are aqueous or during the MCs synthesis by dispersion, followed by solidification [79–81,84–86].

The MCs with various cores have them dispersed in the structure in a heterogeneous way

[76,78]. The heterogeneous microcapsules have different configurations [81]. For example, the core can be introduced in globular structures out of the polymeric membrane, and these MCs are named heteroaggregated. The acorn MCs have a configuration characterized by the dislocated core, outside of the polymeric wall [81,87].

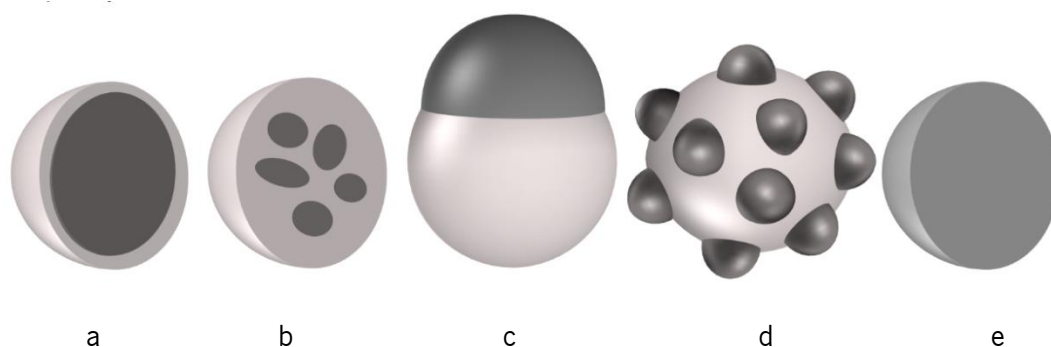


**Figure 3.** Microcapsule morphologies: a) core-shell, b) heterogeneous, c) acorn, d) heteroaggregated and e) microspheres.

A different microencapsulation system is the so-called microsphere (MS), **Figure 3 e**). The microspheres are similar to the MCs, with the difference that the AAs are integrated into the matrix as dispersion, suspension, or homogeneously dissolved [67,76,79,88]. Biopolymers, inorganic materials, compounds from natural or synthetic sources, and metal oxides, are some of the MSs compositions [89]. There is a deep controversy around the microsphere's classification because the definition of microcapsule consists of a phase with the AA and the other phase constitutes the matrix that will retain the encapsulated compound. Since the MSs are a unique phase, some authors introduce it in the MCs technology as they are considered as a system that retains AAs [67,68].

---

In this work, the MCs acronym refers to the core-shell configuration.

In analogy, the MSs acronym correspond to the microspheres.

---

### 1.2.1. Microencapsulation as a controlled releasing system

In 1962 Oertli and Lunt published a controlled release system with encapsulated mineral fertilizers [90]. After one year, Dhanke *et al.* created polyurethane MCs; the research goal was to encapsulate fertilizers and release them gradually [41]. In 1971, Allan and the co-workers made a

scientific publication where they encapsulated pesticides [91]. In the next decade, more precisely in 1984, Otey *et al.* developed a mixture of starch, natural rubber, and polyethylene-vinyl acetate as a MSs structure for fertilizer's controlled release [92]. The 90's were remarkable for agroindustry due to the introduction of polymeric hydrogels as compounds with the ability to preserve the ACs inside [11]. These studies were a springboard for the scientific community, since they aroused interest and appeared in numerous microencapsulation systems that ensure the ACs controlled release [41,45].

The industry took a while to follow this approach [11]. Nowadays, the number of MCs in this niche is very limited because of the complex chemical structures, being some of them unstable. This problem makes the ACs encapsulation a challenge, with a lack of standard methods, as well as expensive [11,64]. A considerable part of MCs formulations are suspensions in a media rich in surfactants and thickeners to ensure that the MCs do not precipitate on the recipient's bottom (**Table 2**) [43,93,94]. Following this context, there are other formulations in the form of granules and gels [93].

**Table 2.** General composition of a microcapsule suspension [94].

<b>Compound</b>	<b>% in weight</b>
Active agent	10-30
Emulsifier	1-5
Polymer	10-15
Solvent	5-15
Anti-sedimentary agents	1-3
Water	Remaining to 100

The main advantage of encapsulation is to preserve the ACs in a solid-state shell without compromising the physical state of the AC. In other words, liquid compounds can be coated by solid walls, resulting in a solid-state MC [11,56,66,69]. In this way, the ACs stay inert and masked; thus, olfactory detection will be greatly reduced [11,35,56,66,69]. There is a significant warranty of the stability and preservation when the AC is encapsulated during all the process steps (production, storage, transport, and utilization). Also, the plants metabolize and elevate the concentration of the ACs [11,56,66,69]. This technique is also attractive due to the possibility of combining incompatible compounds in the same formulation [66,69].

The MCs can release the AA by diffusion [14,35,36,56,65,66] or by destroying the shell [35,36,41,56,65,66]. The shell destruction can be triggered by physical processes, where a

mechanic external force is applied. Alternatively, some chemical processes are used to release the core, such as hydrolysis [35,41,56,65], biodegradation, and degradation by pH or temperature [35,41]. After this initiation, the membrane will release the contents very fast, which is not an advantage. In the case of porous microcapsules, a gradual release is promoted because the water penetrates the porous and then releases the compound [41].

The shell thickness [35,56] and porosity [35,56,95] are the main factors that command the controlled release. For example, thicker shells take more time to degrade, so the core will take more time to be released. In opposition, a porous structure has a faster release, as the core interacts almost immediately with the external environment. Another factor, and probably the foremost, contributes to the controlled release system: the core properties. The physical, chemical and biological core nature will be crucial for the process's selection and optimization [35,56,66].

The role of MCs in releasing the ACs can be an external imbalance induced from the inserted environment [35,69]. This effect can be obtained by a previous functionalization, changing the optical [35], thermal [35,69], physical and chemical [35,69], mechanical [35,69], magnetic [69], and/or biological properties [35,69]. So far, pH, temperature, as well as light irradiation and enzymatic reactions, are some of the most applied imbalances to trigger the controlled release in ACs [35].

In the MSs, the absence of an involucre limits the controlled release. The process is practically dependent on the sphere geometry, corresponding surface area, and the compounds that constitute the matrix [89,96]. In the MSs, it is possible to introduce hydrophilic or hydrophobic AAs. There are MSs with biodegradable and non-biodegradable matrices. In non-biodegradable MSs, AA diffusion is the predominant phenomenon associated with the release. For biodegradable matrices, the AA release depends on its degradation [96]. Since the major part of biopolymers used in biodegradable MSs, are water-soluble, the controlled release from spheres is dissolution, osmosis or swelling [89]. Furthermore, a significant percentage of MSs have an agent to drastically change the polymeric configuration by a chemical or physical cross-linking [97]. Once this compound is in the matrix, the controlled release is also dependent on the type and crosslinking degree [97–100]. The cross-linker enhances the MSs polymer properties: (1) increasing elasticity, (2) decreasing in the viscosity, (3) insolubility, (4) increasing transition temperature ( $T_g$ ), strength and toughness, (5) decreasing in melting point temperature, and (6) transformation of thermoplastics into thermosets [97]. The environment where the MSs are applied is also essential for the controlled release rate, because the process is hugely affected by the pH and presence of

hydrosoluble compounds [98].

### 1.2.2. Microencapsulation techniques

According to Shahidi, Han and Wilkins, the MCs can be grouped based on synthesis nature, whether chemical or physical [101,102]. Also, the physical process is divided into mechanical and physicochemical. **Table 3** shows some of the most used techniques to produce microcapsules. The interfacial polymerization, coacervation and evaporation/extraction of the solvent are widely selected for this practice [36,66].

**Table 3.** Microencapsulation synthesis methods.

		<b>Ref.</b>	
<b>Chemical methods</b>	Suspension	[56,65,69,76]	
	Dispersion	[56,65,69,76]	
	Emulsion	[56,65,69,76]	
	Interfacial polymerization	[27,56,66,69,76,95]	
	<b>Crosslinking</b>	[36,56]	
	Molecular inclusion	[27]	
<b>Physicochemical</b>	Coacervation	[27,35,56,65,66,69,76]	
	Layer-by-layer	[69]	
	Sol-gel encapsulation	[69]	
	Supercritical fluid	[69,76]	
	Electrostatic encapsulation	[69,76]	
	<b>Solvent evaporation</b>	[27,36,65,66,76]	
	Solvent extraction	[27,36,65,66,76]	
	Crystallization by emulsion/solidification	[27]	
	Emulsion by controlled diffusion	[27]	
	Liposome entrapment	[27]	
	<b>Physical methods</b>	Spray-drying	[27,56,69,76]
		Spray-congealing	[76]
Multiple nozzle Spraying		[69]	
Fluid-bed Coating		[27,56,69,76]	
Centrifugation		[69]	
Vacuum		[69]	
Electrostatic		[27]	
Extrusion		[27,76]	
Freeze drying		[27]	
Pan coating		[56]	
Atomization		[46]	
Spinning disk		[69]	
<b>Techniques employed in this study</b>			

The goal of the present research was to produce core-shell microcapsules through the solvent evaporation technique, using single and double emulsion methodologies. The experiments were conducted using polymers already synthesized in order to minimize the effect of by-products in the microencapsulation methods. However, it was necessary to create an efficient microencapsulation system to fulfill the industry requirements during the experimental part, and so, solvent extraction techniques were also employed. Also, the MSs strategy was used to fit the industrial purpose and MSs were produced by gelation with a cross-linking agent.

### 1.2.2.1. Solvent evaporation technique

Hickey was one of the pioneers of this microencapsulation method. The first microcapsules were produced in 1933 [103], however this process was only entirely understood and developed in the 80's [104]. The solvent evaporation technique consists of creating microcapsules from the polymer hardening procedure and has two approaches. In the first, the solvent evaporates from the polymeric solution; in the second approach, a co-solvent is added into the polymeric solution. Thus, all volume correspondent to the polymeric solution is dissolved, separating the constituents [105–109]. The experimental procedure is straightforward when compared with other microencapsulation methods; on the opposite, the window of opportunity is very narrow, so the process must be precise and accurate to successfully synthesize the MCs [110,111]. In the solvent evaporation technique, the MCs are made under continuous stirring [27,112–116].

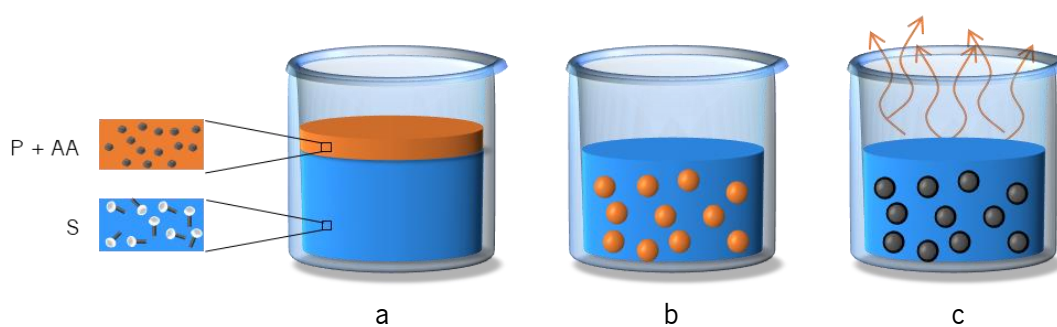


**Figure 4. Solvent evaporation** steps: a) a solution made of polymer (P) and active agent (AA) is dispersed into a solution with a surfactant (S); b) emulsification; c) solvent evaporation and microcapsules wall formation.

In this process, the polymer and the AA are dissolved in an appropriate solvent, named as dispersed phase or polymeric solution (**Figure 4**). Then, this phase is poured into a solution rich

in surfactant and/or stabilizers. When the two solutions are in contact, an emulsion is created, and simultaneously occurs the solvent evaporation process. This physic phenomenon promotes the polymer precipitation surrounding the AA. During the evaporation, the polymeric phase becomes tougher, forming the polymeric wall. The synthesis is concluded when the evaporation is completed [65,117–119].

The solvent from the polymeric solution does not need to be volatile at standard room conditions. The evaporation can be applied in a wide range of solvents. To encapsulate the AA is necessary to prepare the emulsification at a temperature near the boiling temperature. However, a huge part of ACs are unstable to thermal conditions, so the solvent and polymers list is inevitably more restrict [110]. Examples of volatile solvents are methylene chloride or dichloromethane [76,120,121], acetone [110], methanol [110], ethyl acetate [76,110], ethyl alcohol [110] and chloroform [76,110,122].

### 1.2.2.2. Solvent extraction technique

The microcapsules synthesis by solvent extraction adds a solvent into the disperse phase (**Figure 5**). This solvent has to be miscible in the disperse and continuous phases and must not dissolve the polymer [108,109]. The solvent extractor is added during the emulsification, which will then separate the polymer, the active agent, and the primary solvent of this phase [65,117,123,124]. The microcapsules are made by lixiviation that solidifies the polymer [124]. In this process, it is common to apply temperature or temperature ramps to promote the microcapsules formation [65,123]. As for the solvent evaporation technique, in solvent extraction the MCs are produced under continuous stirring.

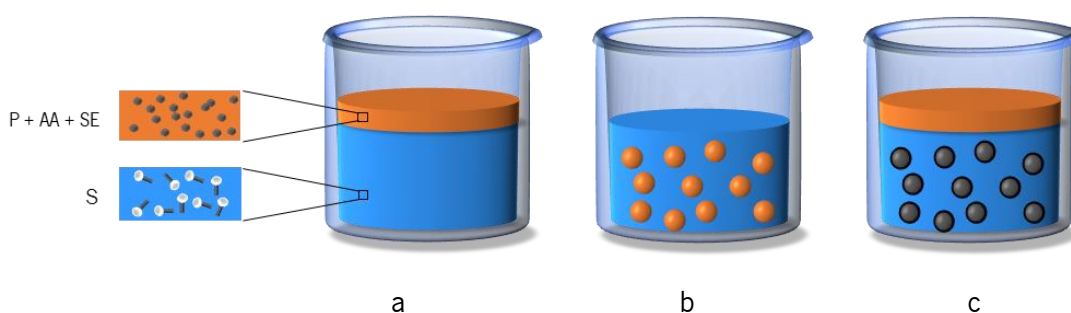


**Figure 5. Solvent extraction** steps: a) a solution made of polymer (P), active agent (AA) and extractor solvent (ES) is dispersed into a solution with a surfactant (S); b) emulsion formation; c) lixiviation and and microcapsules wall formation.

The microcapsules can be separated by the extractor solvent by filtration [65,125], centrifugation or ultracentrifugation [65,125,126]; then, they are washed [65,126,127] with deionized water [65,126], *n*-hexane [110,128], tampon solution [126], petroleum ether or cyclohexane [128]. The last phase is drying, the simplest way is at room conditions. In some situations it is necessary to decrease the drying temperature or pressure [127,128]; other cases refer to lyophilization as a drying technique [126,127].

Usually, the disperse phase is oily, and the continuous phase is aqueous [65,129]. Still, the AA solubility is different from the polymeric solution, which made mandatory that the continuous phase had to be compatible to promote the MCs formation. For example, for oily AA is imperative an oily continuous phase; they are poured into an aqueous phase, resulting in a single emulsion. The emulsion is oil (O) in water (W) and is widely use this abbreviation O/W [76,129]. The inverse is W/O, as a water phase introduced into an oily continuous phase. This are single emulsions, also in microencapsulation there are double or multiple emulsions. As the number of emulsion phases are increasing, the stability is more difficult to reach, but allows more encapsulation systems [76].

### **1.2.2.3. Gelification with cross-linking agent technique**

The gelification method is used to produce MCs and MSs. When the procedure is made by a single emulsion, the final product is a MS. The main requirement for this technique is to use a reactant that can form a gel. Most of them are biopolymers with hydrophilic character like polysaccharides (xanthan gum [64], alginate [56,130–133], agar [134], chitosan [130,135,136], starch [130,137], cellulose derivatives [130,137] and lignin [130,137,138]) and proteins (gelatin [61,139,140] and albumin [139,141]). Beyond these polymers exist synthetic hydrogels such as polyvinyl alcohol [142–144], glycerol [142,145], polyethylene glycol [97], polyacrylamide [146], polycaprolactone, poly (butyl-adipate-co-terephthalate) [147] and poly(butylene adipate-co-terephthalate) [148]. The hydrogels can be synthesized from a combination of several polymers and/or biopolymers [142–144,146]. From an experimental perspective, the hydrogel formation begins with the heating resulting from the agitation of the matrix components. The previously heated mixture is poured into a continuous phase, with a large volume, at lower temperatures. The thermal contrast creates the gel; in some polymers, the gelification process is favored when the continuous phase is set at negative temperatures (**Figure 6**). The last step is washing and drying of the resultant MCs or MSs.



Normally, the final gel does not contain the desired mechanical, chemical, or physical properties, so it is usual to enhance this property by using a cross-linking agent. The cross-linking increases the viscoelasticity [97,143,149], polymer insolubility [143,149], and toughness. Furthermore, polymeric transformations from thermoplastics into thermosets automatically change the melting and glass transition temperatures [97]. The cross-linking agent reticulates the polymer(s), rearranging the structure, so the final matrix will affect the controlled release. The release rate of the AA will be slower than for MCs or MSs without the cross-linking agent; in conclusion, the longevity will be longer [78,142]. Miao *et al.* and Fizur *et al.* also observed differences in cytotoxicity levels [143,149].

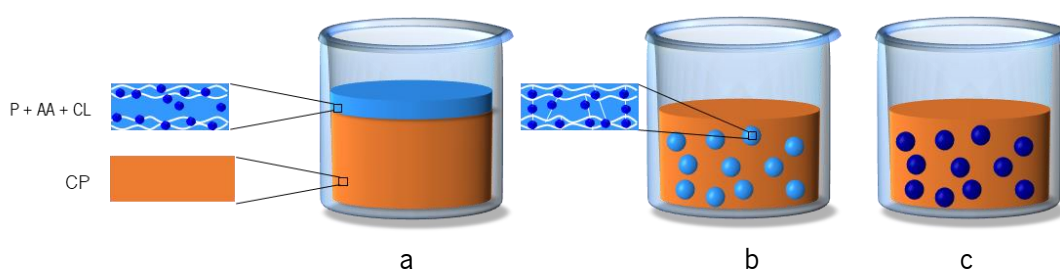


**Figure 6. Gelification with cross-linking agent** steps: a) solution with polymer (P), active agent (AA) and cross-linker (CL) and a continuous phase (CP); b) polymer reticulation made by the cross-linking agent; c) microsphere gelification.

The hydrogels used in this technique are grouped as chemical or physical cross-linking [150,151]. Physical cross-linking is referred when this compound and the polymer create stable bonds such as:

- ionic interaction,
- crystallization,
- stereocomplex formation,
- hydrophobized polysaccharides,
- protein interaction (ProLastins)
- hydrogen bond [152,153].

When the reticulation agent and the polymer make a covalent bond, chemical cross-linking takes place, being more efficient than the physical. Here, the polymerization reaction is triggered in the polymer. Addition, condensation and reactions that involve radiation (photocrosslinking) lead to crosslinking [154,155]. Glutaraldehyde is widely used as reticulation agent for gelatin

[142,144,156] and calcium chloride [133,145]; for sodium alginate there are studies with boric acid [145,157], zinc [158,159], borax [160], oxidated dextrans [161], oxidated alginate [158] and urea [149].

The gelification process (with or without reticulation agent) can be carried out with a simple syringe or associated with extrusion, atomization and electrostatic deposition methods [162].

These synthesis processes have demonstrated to be very promising to produce microcapsules with supplied ACs. The emulsion stability is undoubtedly crucial to be successful in the agrochemical's encapsulation, for liquid or solid-state, as well for water-soluble compounds or insoluble. The gelification is the most suitable method for the purpose, but the controlled release by diffusion could be difficult to achieve during all steps.

With the techniques shown previously in 1.2.2.1 and 1.2.2.2 the agrochemical will be preserved and protected. However, for microcapsules without controlled release it is necessary to associate a technology that activates the controlled release. One example is wall degradation when activated by UV radiation through photocatalysis.

### **1.3. Photocatalysis**

#### **1.3.1. Photocatalysis mechanism**

Photocatalysis is an area of study in materials that has been extensively studied and encompasses both homogenous and heterogeneous processes. The heterogeneous photocatalysis is a complex phenomenon that involves catalysis, photochemistry, surface science, spectroscopy techniques, with a special emphasis in the photocatalytic semiconductors materials [163].

The semiconductor's architecture is characterized by the energy gap between the valence and the conduction band. The valence band has valence electrons from all ions in the crystalline structure and it is more energetic than the conduction band, formed by unpaired electrons [164,165]. The energy range between both bands is named as band-gap (**Figure 7**, blue and red bands) [164–166]. In metals, photocatalysis does not occur because the bands are partially overlapped. On the contrary, the insulators do not have this property because the band-gap is greater than 4 eV, which means that the electrons do not have sufficient energy to go from the valence band to the conduction band (**Figure 7**, red band) [164,166]. The band-gap energy is associated with the photon wavenumber necessary to induce the transition, i.e., the incident photons need to have a wavenumber equal or higher than the band-gap energy to be subsequently

absorbed by the semiconductor [165,167,168].

Another property that influences the semiconductor photocatalysis is the Fermi energy. This property is defined as the energy where the probability of finding an electron is equal to  $\frac{1}{2}$ . It mostly corresponds to the electrochemical potential from the material in study. For intrinsic semiconductors, the Fermi energy is in the middle of the valence or conduction bands [164]. The  $n$ -type semiconductors have as principal characteristic a Fermi energy closer to the conduction band. The displacement is due to the presence of donor electrons (negatively charged). Contrarily, the  $p$ -type semiconductors accept electrons, so the Fermi energy is adjacent to the holes, with positive charges [164].

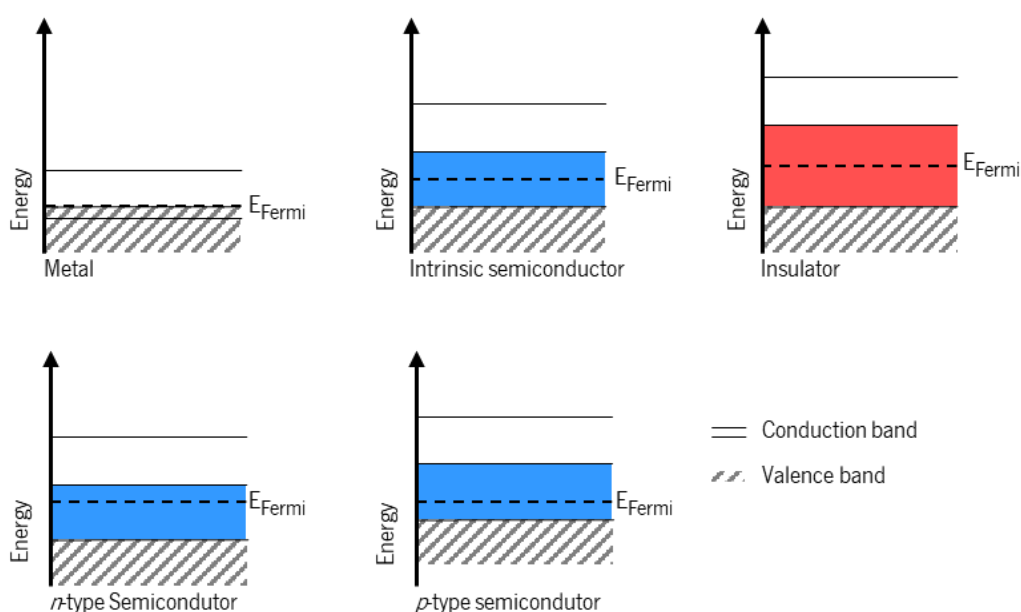


**Figure 7.** Band models applied to transition metals,  $n$ - and  $p$ -type intrinsic semiconductors and insulators.

The photocatalysis phenomenon starts when light is incident on the semiconductor. Then, the incident photons excite the electrons from the valence band; as a repercussion, the electrons move to an empty conduction band. This photoexcitation allows multiple mechanisms, such as forming holes, with a positive charge, in the valence band, and then generating an electron-hole pair. The electron participates in reduction reactions, and the hole in the oxidation reactions. For example, when water aids in this process, the electrons from the semiconductor reduce the oxygen and, at the same time, the hole oxidates the water molecules, triggering several degradation reactions at the semiconductor surface (**Figure 8**). The last step that occurs is the charge

recombination at the surface or inside of the semiconductor. Both contribute to the material degradation that is in contact with the photocatalytic semiconductor [168–174].

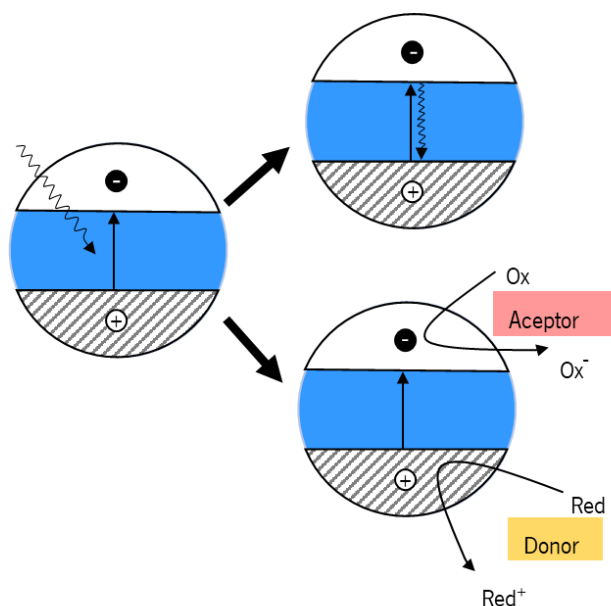


**Figure 8.** Photoexcitation scheme (left side), recombination (above) and oxidation and reduction reactions (below) in the semiconductor correspondent to the photocatalysis process.

### 1.3.2. Titanium dioxide, $\text{TiO}_2$

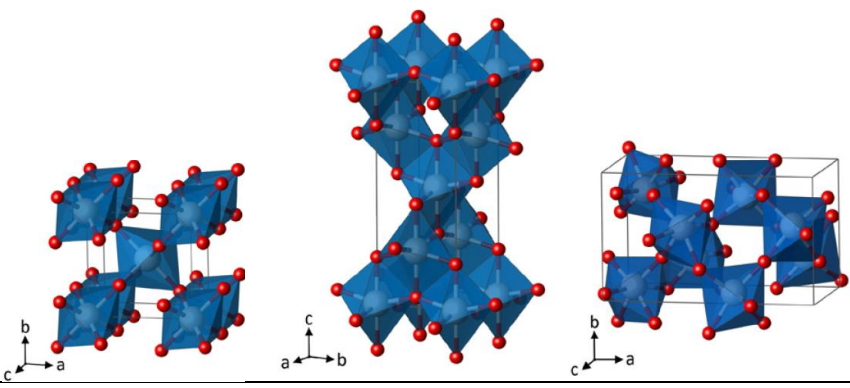
Titanium dioxide, or titania, is abundant, low-cost, easy to handle, very stable and shows resistance to chemical and photochemical erosion. Furthermore, it is a fascinating semiconductor because it presents several polymorphs. Rutile, anatase and brookite are the principal polymorphisms, each one has distinct properties and abundance (**Table 4**) [175–182]. Anatase and brookite are metastable, however when heated to 600 °C, they reorganize the crystallographic structure and transform into rutile [183–185]. Despite the rutile thermostability [164,178,179,186], the most predominant form is anatase, because it is the crystalline  $\text{TiO}_2$  with the lowest surface energy [178–180,184–188]. Another reason why anatase is so predominant is due to the variety of synthesis procedures and precursors employed [179]. In opposition, brookite is unstable and the synthesis is complex, which is why it is not so appellative for investigation [189].

Anatase has an tetragonal structure very distorted and rutile has a similar structure with less distortion in the octahedra [190]. This happens because anatase has 4 Ti atoms to 8 O atoms, counting as 4  $\text{TiO}_2$  molecules per unitary cell; however, rutile only had 2  $\text{TiO}_2$  molecules per unitary cell. In both polymorphisms, titanium is hexacoordinated and the oxygen is tricoordinated

[191,192]. Each octahedron from anatase is connected with 8 vicinal octahedra (4 sharing an edge of oxygen pairs and the other 4 sharing one oxygen in the vertices). In rutile, each octahedron shares with 10 vicinal octahedra (2 sharing an edge of oxygen pairs and 8 sharing one oxygen in the vertices) and 2 more at the edges. The Ti-Ti bonds are longer in anatase (3.79 Å and 3.04 Å) when compared with rutile (3.57 Å and 2.96 Å). Moreover the Ti-O bonds are smaller in anatase (anatase: 1.93 Å and 1.98 Å, rutile: 1.95 Å e 1.98 Å) [190,193]. This unitary cell configuration interferes directly in anatase, that is why anatase had inferior density [164,194,195]. Brookite had an octahedral orthorhombic structure [181], and the Ti is hexacoordinated [196].

From these three polymorphs, anatase is the one with the most attractive properties to reach superior results in photocatalytic activity. Anatase promotes better electron mobility, has a smaller dielectric constant and lower density. In addition, the correspondent conduction and valence bands are denser, providing intra-bands transitions after photon absorption with energy greater than the band-gap energy. Rutile scatters better the electromagnetic visible radiation, and anatase has a narrower absorption range, from the visible violet to the long wave ultraviolet radiation [170,197–200].

**Table 4.** TiO<sub>2</sub> crystallographic structures and respective properties (Ti are the white spheres and O are the red spheres) [201].



Phase	<b>Rutile</b>	<b>Anatase</b>	<b>Brookite</b>
Geometry	Tetragonal	Body-centered tetragonal	Orthorhombic
Density (g/cm <sup>3</sup> )	4.13	3.79	3.99
Band-gap (eV)	3.02	3.20	2.96

TiO<sub>2</sub> exists as pure titania and doped with metals or non-metals. Pure TiO<sub>2</sub> has low photocatalytic efficiency due to the low radiation absorption (3-5% of sunlight) [165,168], and an excess of defects such as charges, high number of holes or electrons, and interstitial gaps in the structure [164,202]. To take advantage of these defects, a doping strategy can be thought of. This

process is based on the substitution of some atoms or to introduce in the band-gap states from other atoms, such as niobium or chromium, then the photocatalytic effect is enhanced. The metallic and non-metallic atoms are from cationic and anionic doping, respectively [164,203–205]. Another possibility to enhance the photocatalytic activity is by decreasing the particle size to nanometric scale, to achieve a quantum effect.

### 1.3.3. Zinc oxide

Zinc oxide (ZnO) is a binary metal oxide, used to produce brass since the Romans. It is an abundant compound and relatively cheap, which is also appealing for industrial applications [206]. This semiconductor has three principal crystallographic structures named wurtzite, rocksalt and zinc blende (**Table 5**) [207–209]. At room temperature and low pressures, wurtzite is the most stable structure, and, at higher pressures (10 GPa), the most relevant morphism is the rocksalt [207,209]. ZnO is a *n*-type semiconductor. In the Zn orbital configuration, 10 electrons are in the 3d band and O has 4 electrons in the 2p band, so this semiconductor has a  $sp^3$  hybridization resulting in a tetrahedral geometry [209].

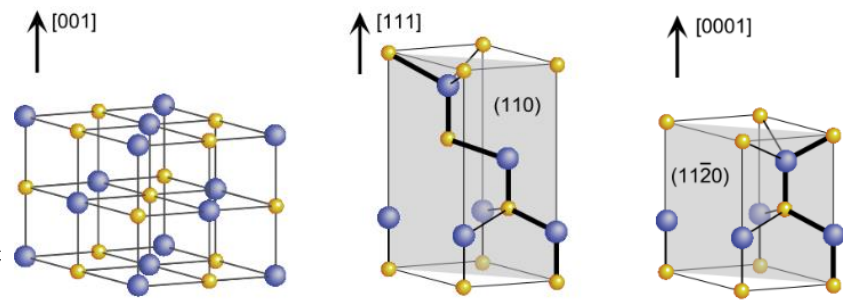
The unit cell for the wurtzite structure is hexagonal and it consists of 4 Zn atoms and 4 O atoms. Additionally, it has a basal-plane hexagon as lattice with lattice parameters  $a = b$  and  $c$ . The  $a$  corresponds to the basal plan,  $b$  is the bond length or the nearest-neighbour distance, and  $c$  the basal direction [207,208,210]. In an ideal wurtzite crystal, the  $c/a$  value is 1.633[207], and  $b/c$  or  $u$  parameter is 0.375 [208]. From experimental details, the lattice parameters  $a$  varies from 3.248 to 3.250 Å and  $c$  varies between 5.204 and 5.208 Å; automatically the  $c/a$  and  $u$  parameters are affected. The effect is possibly associated with the kinetics from compressive and tensile strain. When these values are lower, it is indicative that the wurtzite ionicity is also decreasing [211]. The asymmetric center enhances the electromechanical coupling effects. Hence, it is an interesting material for piezoelectric sensors and mechanical actuators [212].

Zinc blende or sphalerite is another ZnO crystallography form with an atomic displacement similar to wurtzite, but the tetrahedral structure has a  $60^\circ$  in-plane rotation, instead of  $0^\circ$ . Hence, the atoms are arranged in the close-packed (111) planes along the  $\langle 111 \rangle$  direction [210,211]. The unit cell is an oblique parallelepiped with one oxygen atom and one metal atom [213]. Also, it has two face-centered-cubic sublattices measuring  $\frac{1}{4}$  of diagonal axis [207]. This metastable form had a higher covalent character than the wurtzite [211,214]. The stronger in-plane bonds gives this crystal a higher electron density [211]. Zinc blende has a constant lattice parameter  $a$  with

ideal values from 4.18 [215] to 4.62 Å [216]. In reality, the values are lower because of the strain kinetics in the <001> direction. This material has interesting properties for electronic applications [213].

The rocksalt, Rochelle salt or Seignette salt, has a different organization where one Zn atom is hexacoordinated, so it has 6 neighbors [211]. Like zinc blend, rocksalt is also cubic [209] and only has one lattice parameter (*a*). The experimental data values determined for the lattice constant value are from 4.058 to 4.316 Å [217]. The dimensions are lower than zinc blend due to the interionic Coulomb interaction, that increases the crystal ionicity nature. This structure is also metastable over time in ambient conditions [209].

**Table 5.** ZnO crystallographic structures and respective properties (Zn are the yellow spheres and O are the purple spheres) [201].



Crystallographic structure	<b>Rocksalt</b> [207]	<b>Zinc blende</b> [207]	<b>Wurtzite</b> [207]
Phase	Octahedral [207]	Tetrahedral [207]	Hexagonal [207]
Unity cell	Octahedral [207] cubic [218]	Tetrahedral [207] cubic [218]	Hexagonal [207]
Sublattice parameter		Face centered cubic with sublattices shifted along the body diagonal [207]	Basal-plane [207] Hexagonal close packed [208]
Lattice constants*	4.058 - 4.316 nm [207]	ab = 4.50 nm [207] a = 4.18-4.62 [211]	a = b = 3.248-3.250 nm b = 5.2042-5.2075 nm [207,208]
Density (g/cm <sup>3</sup> )			5.67 [207,208]
Band-gap (eV)	2.7 [208]	2.7 [208] 0.87-3.59 [211] 3.59 [219]	3.4 [207,208]

\*average values collected from [207]

### 1.3.4. TiO<sub>2</sub> and ZnO nanomaterials applied in photocatalysis

There is a significant diversity of TiO<sub>2</sub> nanomaterials: particles, tubes, rods, wires, thin films and fibers [171,203,220–223]. All of them contribute for applications in pigments [203,224], cosmetics [224], solar cells [164,203,221,224], production and hydrogen storage [164,203,224],

sensing [164,203], batteries [203], electrocatalysis [164,203], self-cleaning and antibacterial materials [203,224], cancer treatment and prevention [203,224], pollutant degradation [203,223–226] and are also introduced in tactile screens [224].

Nanosized ZnO materials, such as films and particles were produced in varying morphologies like, rods [227,228], fibers [227], wires [227,229,230], tubes [227,231], needles [227], sheets [227], flowers [227], nanobelts that roll-up to and form nanohelices [232]. The ZnO nanoparticles are employed in electronics, optics [233], photovoltaics [234], data storage, gas sensors [235], photodetectors [236], photoluminescence [237], applications in agriculture [238], paints, tires and ceramics [239]. Additionally, they demonstrate antibacterial activity due to their low toxicity and great biocompatibility [240]. Nowadays, it is an essential component in diverse industries and processes, especially in the catalysis [239].

TiO<sub>2</sub> nanoparticles (under 50 nm in size), have distinct properties from the TiO<sub>2</sub> macroparticles [203,241]. The nanoparticles stand out from the very high specific surface area, exposing most of the atoms and ions to the photocatalytic process. The permeability [242,243], thermal and physical stability [203] are enhanced (specially in anatase [244–247]), and a have considerable advantage for the low-cost production [203,242].

The nanometric anatase has enhanced more crystallinity, as well as structural defects for electron-hole recombination [181,195,248]. Moreover, it possesses extra tolerance to distortion than anatase in other scales. By this way, doping is easier and consequently the photocatalytic effect is improved [242] The band-gap energy increases and shifts to higher redox potentials, from the creation of an intermediate band by the doping agent [181].

The electrons are photoexcited from an energetic source ( $h\nu$ ) (Equation 1 and Equation 2), below a specific wavelength (390 nm, for pure TiO<sub>2</sub>; for doped TiO<sub>2</sub> this value increases with the doping agent) [203,205]. Successively, it is formed an electron-hole pair, redox reactions and recombination [203,205].

Part of the electrons populate the conduction band, while other recombine to the valence band. The electrons in the conduction band reduce molecular oxygen (O<sub>2</sub>) generating superoxide radicals (O<sub>2</sub><sup>-</sup>) (Equation 3). In the valence band, the holes ( $h^+$ ) oxidate water molecules (H<sub>2</sub>O) and hydroxyl radicals are formed (HO·) (Equation 4). The radical's instability promotes reactions with the components that are in direct contact with the TiO<sub>2</sub>, degrading them. It was observed that this semiconductor degrades organic compounds, toxins, as well as compounds that are essential in the life cycles, such as water and carbon dioxide [203,249–251].





The ZnO band-gap is direct and for wurtzite at room temperature conditions is 3.37 eV [207,208,218]. As a direct band-gap semiconductor, the energetic momentum from both bands (conduction and valence) is equal, which will cause repercussions in the photocatalysis. When ZnO is exposed to radiation ( $h\nu$ ), the electrons are excited from the valence to the conduction band, forming an electron-hole pair (recombination, Equation 2). This photoexcitation occurs multiple times, as well as redox reactions. As described above, the electrons produce superoxide radicals and the holes oxidate water molecules (Equation 3 and Equation 4). These redox mechanisms initiate the degradation of several compounds. The main difference is that during the electronic transitions, a photon is emitted [209,210] (instead of a phonon, for  $\text{TiO}_2$  anatase [252]).

**Table 6** presents the most used techniques to produce  $\text{TiO}_2$  and ZnO nanomaterials. It is necessary to choose a technique compatible with the substrates and nanomaterial pretended. For coating as films or clusters, there are deposition techniques that have been very explored, such as physical vapor deposition and chemical vapor deposition, including the atomic layer deposition (ALD). The  $\text{TiO}_2$  and the ZnO are standard compounds to coating via ALD on PMMA.

**Table 6.** Techniques to synthesize  $\text{TiO}_2$  and ZnO nanomaterials.

<b>Synthesis technique</b>	<b>TiO<sub>2</sub></b>	<b>ZnO</b>
Catalyst-assisted vapor liquid solid	-	[237]
Direct oxidation	[253]	-
Electrodeposition	[203,253]	-
Emulsion and microemulsion	[203]	[237]
Free vapor-solid	-	[237]
Hydrothermal	[203,253]	[237]
Inverse micelle	[254]	-
MBE	-	
Mechanochemistry (ball milling)	-	[237]
Micelle	[254]	-
Microwave	-	[237]
Molecular beam epitaxy	-	[236][237]
Physical vapor deposition	[203,225,226,253]	[255–259]
Precipitation control (with or without surfactants)	-	[237]
Pulsed laser deposition	-	[236] [237]

Solution combustion	[203]	-
Sol,	[253]	-
Sol-gel	[203,253]	[237]
Solvothermal	[203,253],	[237]
Sonochemical	[203,253]	-
Spray method	-	[237]
Chemical vapor deposition	[203,253]	[237]

A variety of this technique, the Atomic Layer Deposition (ALD), is employed in this study

## 1.4. Atomic Layer Deposition

### 1.4.1. Brief History of Atomic Layer Deposition

Atomic layer deposition (ALD) discovery took place in Europe, in two different countries, separated by a few years. The first evidence of ALD was in the 1960s in USSR, by Aleskovskii and Koltsov (1965) [260], Shevjakov *et al.* (1967) [261] and Sveshnikova *et al.* (1969) [262], and they called it molecular layering. The works mentioned the deposition of metallic compounds on silicon surfaces. After a few years, not so far away, Tuomo Suntola developed the atomic layer epitaxy (ALE) process where ZnS, SnO<sub>2</sub>, and GaP were coated for electroluminescent flat panel displays. This work was patented and expanded not only in Finland but also in other countries [263,264]. The ALE experiments were very directed to halides in a gas–solid system, and in the 1970s started the depositions of other chemical elements [265]. In 1972, the first implementation of polymeric foils as a substrate was used by Suntola to create a miniaturized device able to measure the humidity in solid-state. This study resulted in a patent and nowadays these devices are very used regarding efficiency [266].

The 1980s were remarkable for this technology. The number of ALD publications was increasing, and alkyls and  $\beta$ -diketonates were used as reactants to generate new deposition processes for semiconductors [265]. Because of great interest in ALD research topic, the first conference about this expertise was organized in 1984. In parallel, ALD industrialization for electroluminescent displays took place with the name Lohja's [267]. ALE started to be applied in other fields, such as solar cells, catalysis, and microelectrochemistry industries. Regarding the application on polymer surfaces, in 1984 Molsenyat *et al.* prepared polyamide substrates coated with titanium oxide (TiO<sub>2</sub>) [268].

In 1990, Markku Leskelä suggested changing the name ALE to ALD, at the “International Symposium on Atomic Layer Epitaxy” [267,269]. As a result, there was an increment of inorganic reactants based in cyclopentadienyls, alkoxides, and alkylamides, to produce binary systems (e.g.,

metal oxides) [265], as well as the development of ternary systems [267]. Alumina ( $\text{Al}_2\text{O}_3$ ) was (and is) a well-established coating process, however, the growth is amorphous instead of epitaxial, so that was the driving force to change the name and amplify the variety of substrates [270,271].

Currently, ALD is mostly applied in microelectronics field, such as transistors, capacitors, energy storage, conversion, biomimetic membranes, and graphene for desalination supports, catalysts, and medical applications [272]. A very actual topic is the ALD modification of soft materials' surfaces, especially thermally fragile polymers, which are very challenging to processing due to the low deposition temperatures required or pre-functionalization treatments, as deeply presented in the following.

## **1.4.2. Coatings on PMMA by Thermal Atomic Layer Deposition**

### **1.4.2.1. PMMA Challenges for ALD**

PMMA surface engineering opens new opportunities to modify the polymer surface chemistry to attain improved properties with a second material. The ability to control the reaction between the ALD precursors and the PMMA surface paves the way for the ALD processing. From a practical point of view, the ALD coating is a product from sequential self-limiting surface reactions of two or more precursors, which make up an ALD cycle (**Figure 9**). In this context, inorganic compounds such as binary or ternary metal oxides can be produced depending on the number of precursors in the ALD process [273].

The mechanism of ALD on polymeric substrates, for binary reactions, is constituted by A and B precursors, that will react by chemisorption and create a solid AB coating (e.g., metal oxide) [274–276]. Precursor A is the metal source, and precursor B is the non-metal, such as  $\text{H}_2\text{O}$  or  $\text{O}_3$ . In the example illustrated in **Figure 9** the first precursor, trimethylaluminium, ( $\text{Al}(\text{CH}_3)_3/\text{TMA}$ ) is introduced in the chamber and reacts on the surface, followed by its diffusion; this step is named as half-cycle, and the final product is named ligand or by-product [275,276]. Then, the second precursor, water, is pulsed and reacts with the resulting previous ligands [275,276]. It is the complementary half cycle, together with the previous, that makes a cycle with the desirable  $\text{O-Al}_2(\text{OH})_3$  monolayer. With the repetition of these two half-cycles, the  $\text{Al}_2\text{O}_3$  growth takes place. It is worth to mention that between the two half-reactions there is a purging step assisted by the introduction of inert gas (e.g., Ar or  $\text{N}_2$ ). A homogeneous growth is promoted, preventing precursor–precursor, precursor–by-product, by-product–by-product reactions [276]. Consequently, the

formed coatings are very precise and controlled in a conformal configuration [277].

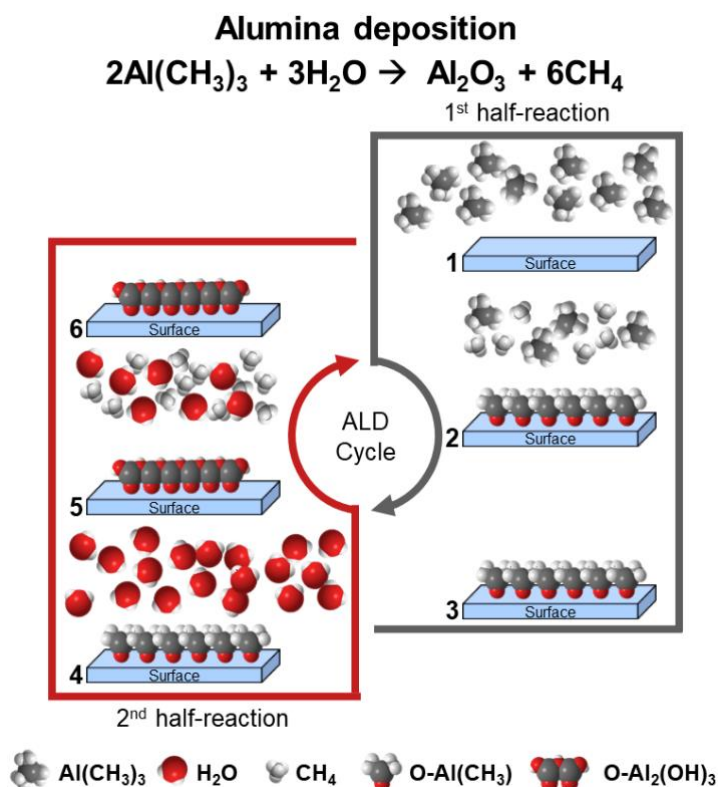


**Figure 9.** Schematic representation of the ALD formation of the first  $\text{Al}_2\text{O}_3$  monolayer from: (1) TMA pulsing; (2) TMA chemisorption in the surface (first half-reaction); (3) after purging of unreacted TMA and methane; (4) water pulsing; (5) water chemisorption on the by-product from the first half-reaction; and (6) after purging of unreacted water and methane.

The PMMA polymer is a very stable material; in other words, inert, consisting in strong chemical bonds, which hinder the modification of the chain [278]. The ester's presence,  $-\text{R-COOR}'$  in **Figure 10**, raises the polarity and limits the ALD coating because, generally, the precursors are nonpolar [275].

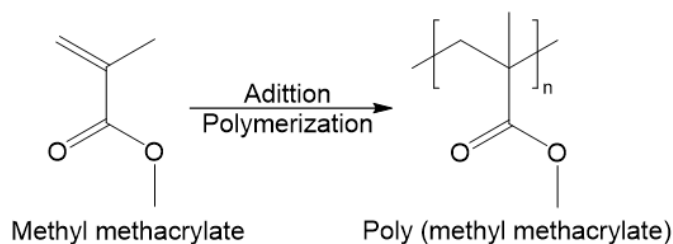


**Figure 10.** Synthesis of PMMA by addition polymerization of MMA (adapted from [279]).

A second challenge is the low transition temperature value ( $T_g$ ) of PMMA. This polymer

presents three main tacticities (isotactic, syndiotactic, and atactic), where pendant groups or hydrogens are laid in certain positions. In **Figure 11**, it is possible to observe these structures [280]. The chiral central's orientation will determine the transition temperature and crystallinity, thermal resistance, solubility, degree of biocompatibility, hydrolyzation, and other properties. For example, the  $T_g$  is the lowest (55 °C) for the isotactic structure when ester groups are disposed on one single side of the backbone structure, from a random or regular order, respectively. The chemical structure is more stable for the atactic and syndiotactic structures, so automatically increasing the  $T_g$  to 120 and 130 °C, respectively. The different percentages of tacticities result in an almost specific  $T_g$  for each PMMA substrate [281].

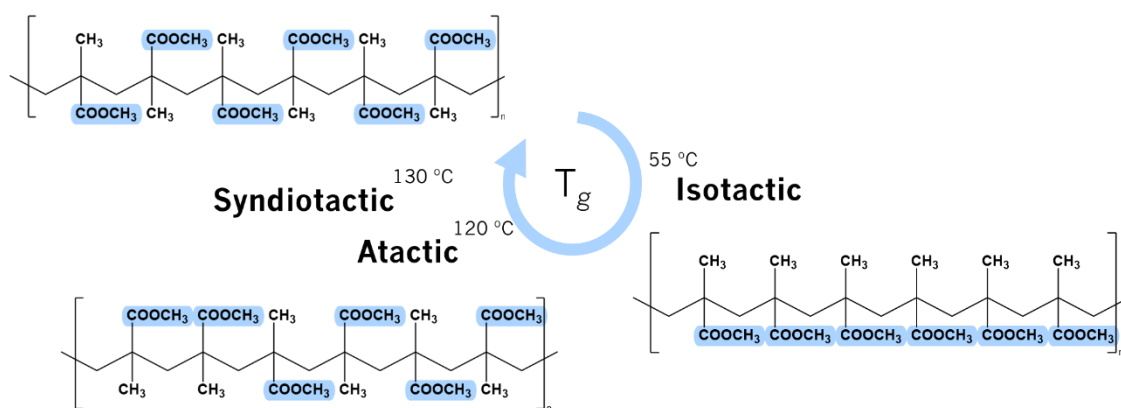


**Figure 11.** PMMA tacticities: isotactic, syndiotactic, and atactic and respective glass transition temperature. The tacticities values were collected from [281].

Depending on the ALD process, the deposition temperature ranges between room temperature ( $\approx 20$  °C) and 400 °C. In this context, the deposition temperature should be below the  $T_g$  of the PMMA to ensure that the polymer remains in the solid-state. For example, if the deposition temperature is too high, PMMA will start to decompose [275,282–288]. Considering that the majority of ALD processes occur for temperatures  $>100$  °C, the PMMA  $T_g$  value plays a key factor in the selection of the ALD process. One of the most investigated precursor combinations in ALD for  $\text{Al}_2\text{O}_3$  deposition is TMA with  $\text{H}_2\text{O}$  and the deposition temperature is typically  $\leq 300$  °C.  $\text{Al}_2\text{O}_3$  gives an example of a material that tends to grow in an amorphous form and it has been applied to thermally fragile substrates [289].

#### 1.4.2.2. Nucleation and Growth Studies

It can be found in the literature reports providing insights into ALD process and mechanism

of  $\text{Al}_2\text{O}_3$  growth on PMMA. For instance, Wilson *et al.* studied the nucleation and growth of  $\text{Al}_2\text{O}_3$  on spin-coated thin films of various polymeric compounds, including PMMA. To this end, the nucleation and growth process kinetics were monitored by the mass changes measured by a quartz crystal microbalance (QCM). In the first five cycles, TMA is adsorbed. Due to the insolubility of PMMA in the  $\text{Al}_2\text{O}_3$  precursor, 90% of TMA is desorbed when the water is pulsed. The remaining 10% are then hydrolyzed. With the increasing cycles, there are more functional groups from adsorbed TMA, and the desorption decreases. After 20 cycles, the desorption is almost negligible (**Figure 12**) [275].

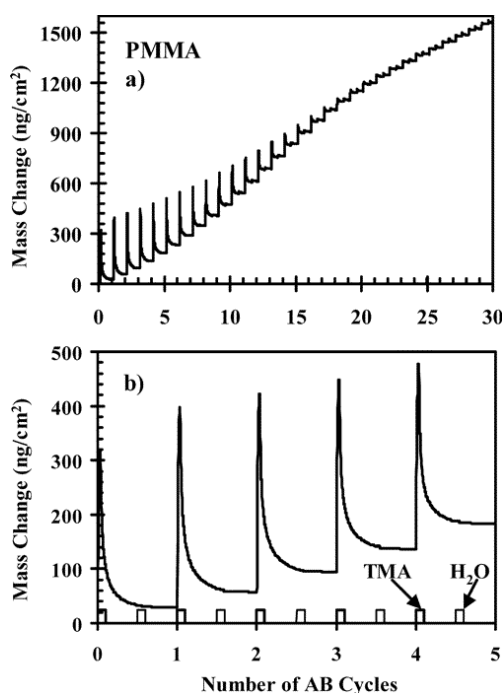


**Figure 12.** Mass change measurements by QCM versus number cycles of  $\text{Al}_2\text{O}_3$  ALD on PMMA at 85 °C for (a) 30 and (b) 5 cycles [275].

The  $\text{Al}_2\text{O}_3$  deposition mechanism on a ~200 nm thick PMMA film was also studied by in-situ Fourier transform infrared spectroscopy (FTIR). This study was carried out in an adapted ALD chamber to run the FTIR measurements, allowing the analysis of each ALD half-cycle to understand the correspondent reaction [290]. The FTIR results presented in **Figure 13** suggest that the aluminum attacks the ester, which decreases the amount of C=O and C-O FTIR bands; the product from the first half-reaction being aluminum carbonate. Then, as  $\text{H}_2\text{O}$  is pulsed into the chamber, FTIR reveals a decrease in  $-\text{CH}_3$  groups, which corresponds to the  $\text{Al}-\text{CH}_3$  and aluminum carbonate removing [290]. These studies demonstrate that a strong correlation exists in the PMMA surface

chemistry to initiate  $\text{Al}_2\text{O}_3$  by ALD. Moreover, the propensity for TMA or other ALD precursors to react on the surface or to diffuse in the sub-surface depends on the polymer [275,290].

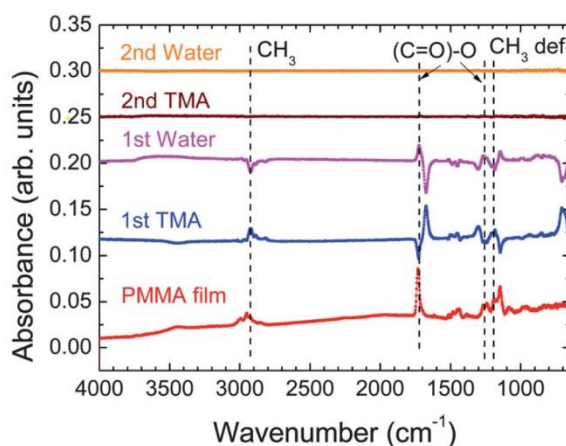


**Figure 13.** In-situ FTIR analysis of uncoated PMMA spin-coated onto Si, first, and second ALD half-reactions.  $\text{Al}_2\text{O}_3$  coating was made from TMA and  $\text{H}_2\text{O}$  at 80 °C. A FTIR run followed each half-cycle, and between half-cycles, the reactor was purged for 10 s [290].

#### 1.4.2.3. Adhesion and Mechanical Properties

The possibility of coating polymeric surfaces with a thin film of a metal oxide opened a wide range of potential applications. However, besides the  $T_g$  temperature and the surface polarity issues, the thermal and mechanical properties of the polymers may limit ALD coating. Here, the mechanical and tribological properties of  $\text{Al}_2\text{O}_3$  ALD thin films on PMMA plates were studied by nanoscratch testing, where the coating/substrate system is comprised by ‘hard’ coatings on ‘soft’ flexible PMMA substrates. Prior to the  $\text{Al}_2\text{O}_3$  deposition by ALD, the PMMA plates were pre-cleaned with a 5% sodium hydroxide solution for a short period of time and then in de-ionized water ultrasonic bath at room conditions to ensure an impurity-free substrate. An 85 nm thick  $\text{Al}_2\text{O}_3$  film on PMMA plate was submitted to nano-scratch tests through a diamond spherical indenter with 25  $\mu\text{m}$  of radius. The results suggest that there is a net elastic recuperation when the load is eliminated, and the  $\text{Al}_2\text{O}_3$ /PMMA resisted to plastic deformation up to 340  $\mu\text{m}$  of scratch length, presenting a residual depth ( $\sim 0.05 \mu\text{m}$ ) at the end of the test, as illustrated in **Figure 14**.

In parallel to  $\text{Al}_2\text{O}_3$ /PMMA, an  $\text{Al}_2\text{O}_3$ /PC (polycarbonate) system was also characterized under the same conditions (**Figure 14**) and the obtained results for both systems are directly related to the intrinsic properties of the polymeric substrates. In this way, the Young’s modulus and hardness of PMMA are higher than that of PC and will therefore give more support to the hard

film and a higher scratch resistance [291]. It is noteworthy that there was no coating delamination was observed in both systems.

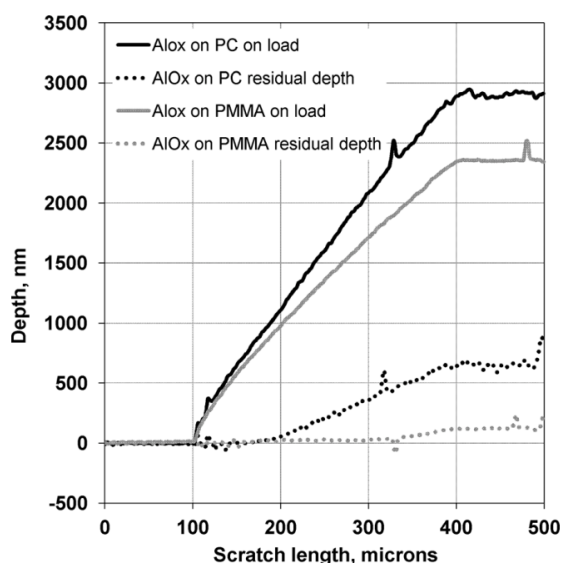


**Figure 14.** On-load and residual depth curves for  $\text{Al}_2\text{O}_3/\text{PMMA}$  and  $\text{Al}_2\text{O}_3/\text{PC}$  (polycarbonate) after the nanoscratch. The test was repeated five times per sample; each scratch had 500  $\mu\text{m}$  of length, at a scanning velocity of 10  $\mu\text{m}/\text{s}$ , and a ramped load varying from 0.1 mn to 60 mn [291].

Concerning the problematics of adhesion and mechanical resistance, Chen *et al.* reported on the enhancement of the PMMA and epoxy resin's interfacial toughness by depositing  $\text{Al}_2\text{O}_3$  thin films at 65  $^\circ\text{C}$  onto PMMA surface, to avoid fracture and delamination of polymer interfaces, as shown in **Figure 15** [292]. This interfacial improvement is particularly important in applications such as fiber reinforced composites, flexible electronics, and encapsulation layers for photovoltaics where the adhesion between two substrates is crucial. The role played by  $\text{Al}_2\text{O}_3$  ALD (130 nm thick) on PMMA surface was the wettability modification assessed by the decrease of the water contact angle (WCA) and consequently the increase of the polymer surface energy. It is of great importance to understanding this property in the adhesion phenomena which relates to physicochemical properties of the surface as well as with the mechanical properties. This work also emphasized the versatility of ALD in engineering the adhesive properties of chemically inert polymer surfaces.

Shahmohammadi *et al.* also studied the adhesion and mechanical properties. This group used tetrakisdimethylamino titanium,  $((\text{CH}_3)_2\text{N})_4\text{Ti}/\text{TDMAT}$  and ozone to deposit a  $\text{TiO}_2$  thin film onto PMMA with excellent properties without plasma assistance or seed layers. Taking into account the PMMA thermal stability (120  $^\circ\text{C}$ ), the ALD reactor temperature was established by



thermogravimetric analysis. The samples were coated from 50 to 500 cycles to understand the PMMA thickness, and the optimized growth per cycle was 1.39 Å/cycle. The presence of titanium was confirmed by X-ray photoelectron spectroscopy (XPS) and X-ray absorption near-edge structure (XANES). The coated PMMA reduced the water contact angle from 84° to almost 20°, which means a remarkable hydrophilicity improvement. The hardness of the sample with 30 nm TiO<sub>2</sub> was tested by Vickers' hardness method, applying a 300 g-force; the results were improved by almost 60% [293].

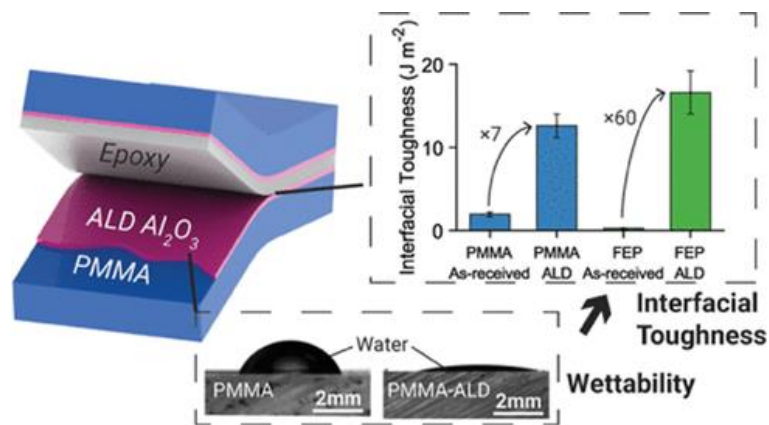


**Figure 15.** Thermoplastic-epoxy resin with the double Al<sub>2</sub>O<sub>3</sub> coating; wettability test of a water droplet in coated and uncoated PMMA surface, and the interfacial toughness of PMMA and fluorinated ethylene propylene (FEP) (wedge test) [292].

## 1.4.2.4. Applications

### 1.4.2.4.1. Applications in Photonics, Photoluminescence, and Photocatalysis

In another study, Hofmann et al. reported that thin layers of TiO<sub>2</sub> by ALD were used in the fabrication of an organic-inorganic hybrid Bragg stack and the photonic effects of the as-prepared Bragg stack were investigated on upconversion luminescence [294,295]. The architecture of the Bragg stack consists of TiO<sub>2</sub> ALD layers and PMMA with sodium yttrium fluoride active nanoparticles (NPs) doped with trivalent erbium ions ( $\beta$ -NaYF<sub>4</sub>:25%Er<sup>+3</sup>), mixed on borofloat 33 glass. The PMMA layers containing the active nanoparticles were produced by spin-coating. The number of stacked layers and their thickness plays a major role in the refractive indexes on upconversion luminescence performance and the low-temperature ALD process (100 °C) of TiO<sub>2</sub> from the reaction between titanium tetrachloride (TiCl<sub>4</sub>) and H<sub>2</sub>O revealed compatibility with the PMMA based

Bragg stack multilayer material (**Figure 16**).

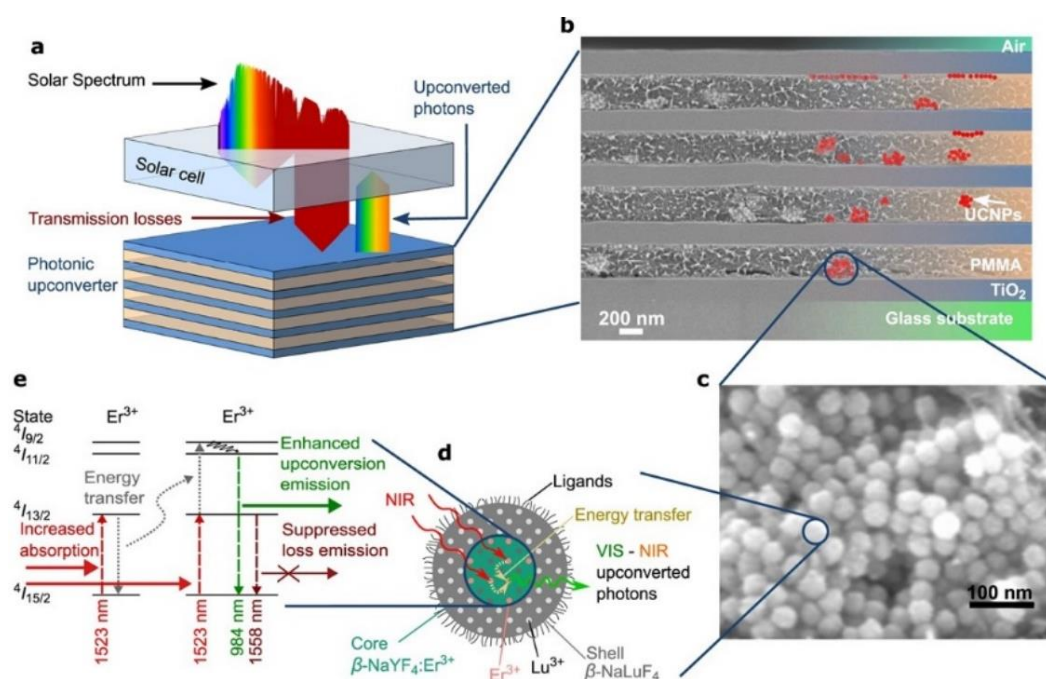


**Figure 16.** (a) Bragg stack (multilayered material comprised of  $\text{TiO}_2$  layers/PMMA+NPs) for charge generation in a solar cell by a photonic upconverter. Scanning electron micrographs of the (b) Bragg stack and (c) of upconverter nanoparticles. (d) Scheme of core-shell upconverter NPs, converting near-infrared (NIR) to visible (VIS) photons in the core. (e) Energy levels in the upconverter  $\text{Er}^{3+}$  and the upconversion process [295].

Apart from  $\text{Al}_2\text{O}_3$  and  $\text{TiO}_2$  ALD coatings, PMMA has been used as a support for crystalline zinc oxide (ZnO). Sing *et al.* reported on the coating of various thicknesses of PMMA thin films (5 nm, 32 nm, and 80 nm) spin-coated onto silicon (Si) substrates. The ZnO photoluminescence activity was evaluated as a function of the underneath PMMA film thickness, ZnO structure and morphology. The as-deposited wurtzite ZnO presented a strong orientation along the c-axis which is critical to the photoluminescence activity enhancement as well as reduction in thickness of PMMA templates. Interestingly, the ZnO deposition was carried out at near ambient temperature (ca. 35 °C) from diethylzinc,  $(\text{Zn}(\text{C}_2\text{H}_5)_2/\text{DEZ})$  and  $\text{H}_2\text{O}$  [296].

PMMA has also been coated by ALD to develop photocatalysts. One of the key materials in the degradation of organic pollutants is  $\text{TiO}_2$ , which presents photocatalytic activity. Kéri *et al.* investigated the photocatalyst activity of ALD grown  $\text{TiO}_2$  deposited at 80 °C onto PMMA NPs (50–100 nm) prepared by emulsion polymerization. As a result, amorphous  $\text{TiO}_2$  was obtained with detectable photocatalytic effect under UV-A illumination (**Figure 17**). This was relatively

unexpected for an amorphous phase, once it is well known that the crystalline anatase  $\text{TiO}_2$  polymorph presents the highest photocatalytic activity. The authors suggested that this effect may be related to the C incorporation during the ALD deposition. This statement was based on the increment of the C 1s signal from the XPS, when compared with the same film produced by sputtering [297].

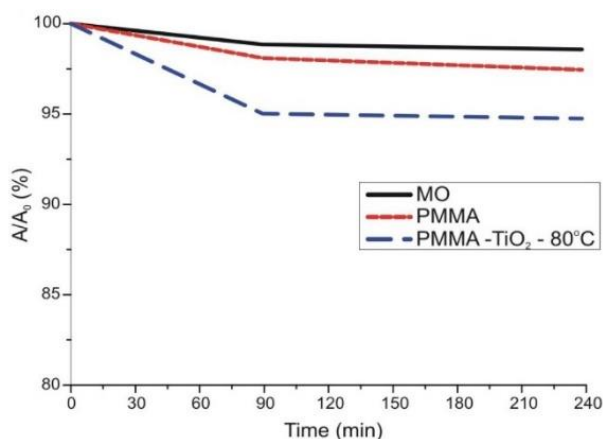


**Figure 17.** Photocatalytic efficiency of the amorphous  $\text{TiO}_2$ . After 90 min, the methylene orange dye degraded 5% under UV-A illumination [297].

ALD of ZnO was also studied on PMMA in the elaboration of photocatalysts for wastewater treatment. Di Mauro *et al.* explored ZnO/PMMA and Ag/ZnO/PMMA nanocomposites as photocatalyst materials for the degradation of pollutants and water reuse upon UV light illumination [298–300]. The authors used different forms of PMMA i.e., commercial PMMA powders (0.2–1 mm in diameter) and plates of PMMA (4 mm thick), and kept the deposition temperature at 80 °C, a temperature compatible with the thermal stability of the PMMA polymer which enabled the growth of polycrystalline ZnO wurtzite [298–300]. After the photocatalytic degradation tests, where an organic dye (methylene blue, MB) was used as a model pollutant, the ZnO on the PMMA nanocomposites demonstrated excellent photo-stability [300]. The addition of Ag to the ZnO/PMMA nanocomposites brought new features to the nanocomposite, in terms of improving the photocatalytic efficiency allowing degradation tests of other organic contaminants (e.g., paracetamol drug, sodium lauryl sulfate), besides MB [299]. **Figure 18** (a) shows the X-ray diffraction (XRD) patterns of the ZnO/PMMA composite after the degradation tests, where it is possible to observe that ZnO remained stable, maintaining the wurtzite crystallographic structure [300]. On the other hand, **Figure 18** (b) reveals the degradation of pharmaceuticals considered as emerging contaminants by the Ag/ZnO/PMMA nanocomposite, under UV illumination [299]. In

summary, these nanocomposites were stable and reusable in the degradation of organic pollutants and are easy to prepare and to recover after being tested.

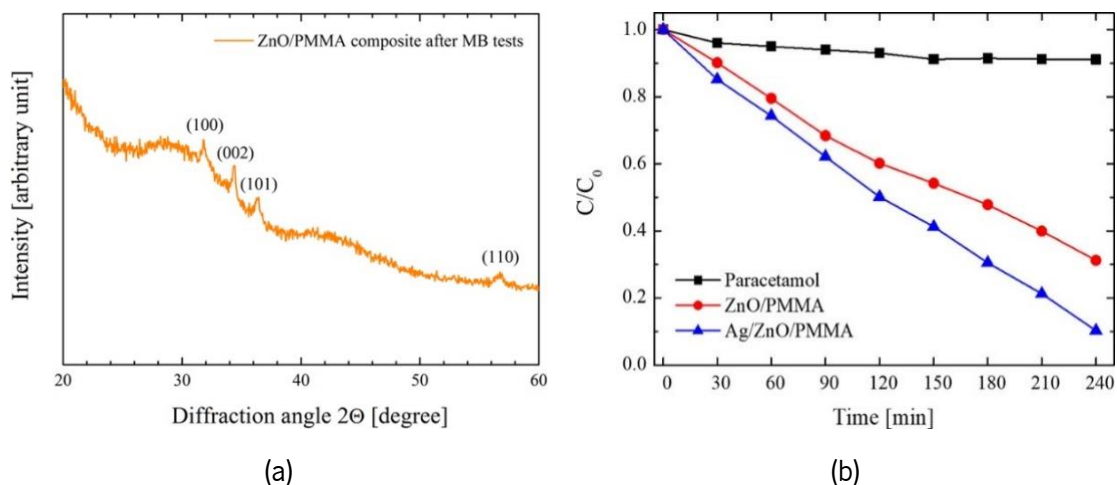


**Figure 18.** XRD pattern of ZnO/PMMA composite after the seven MB discoloration runs [300]. (a) Degradation of paracetamol drug as a function of irradiation time for paracetamol alone (squares), paracetamol with ZnO/PMMA (circles), and paracetamol with Ag/ZnO/PMMA (triangles) samples (b), under UV illumination [299].

#### 1.4.2.4.2. Applications in Dentistry

Another emergent field of application is dentistry. PMMA is a material of election for dental applications, mainly due to its biocompatibility and aesthetics. However, it is of great importance to increase the PMMA mechanical properties used in the dental material [301]. For instance, the wear resistance of dentures based on PMMA was increased after being coated with 30 nm  $TiO_2$  by ALD at 65 °C [285]. A mechanical tooth-brushing device was used to assess the denture sample wear resistance and, after a brushing test, it revealed that the coating remained intact **Figure 19** depicts the survey XPS spectra where the Ti peak is present in both brushed and unbrushed samples implying that the  $TiO_2$  thin film is stable and well adherent to the PMMA surface. Additionally, the surface microbial interactions were also studied by *Candida albicans* biofilm attachment and it was observed a reduction of microbial biofilm burden on the  $TiO_2$ -coated PMMA surface. This result arises from surface wettability modification of the  $TiO_2$ -coated PMMA. It is worth mentioning that, ALD technique represents a change in prosthesis fabrication method that would also include a final step of  $TiO_2$  coating after finishing and polishing [285].

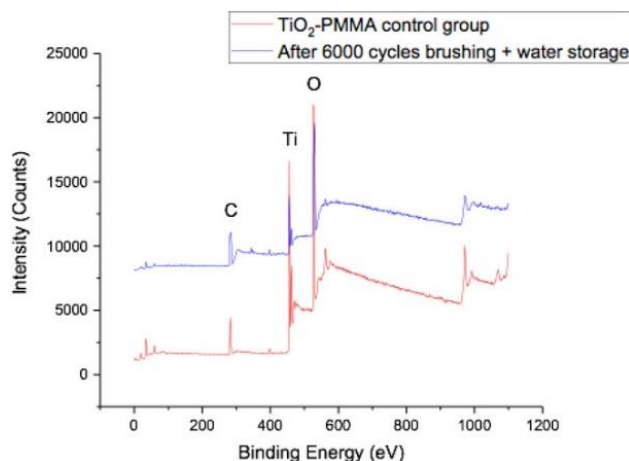


**Figure 19.** XPS results of coated PMMA unbrushed (red) and brushed (blue), storage in water and brushed again after 5 months [285]. PMMA has great mechanical properties and low toxicity for the dental prosthesis fabrication.

### 1.4.3. ALD Coatings on PMMA Aided by Seed Layer

The literature above presented demonstrated that PMMA is a viable polymer material for ALD coating process. However, the requirement of a low deposition temperature due to its low  $T_g$  raises another limitation: the known ALD precursors for thin film formation at low temperatures are very limited. A solution can be the use of seed layers.

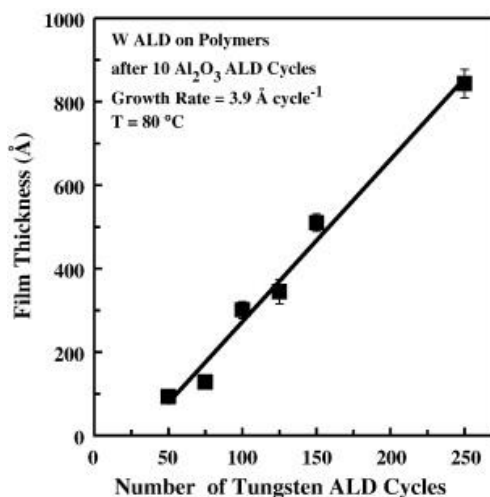


**Figure 20.** Profilometry measurements of W ALD film thickness on different polymers *vs.* the number of W ALD cycles. Al<sub>2</sub>O<sub>3</sub> ALD was used as a seed layer (10 ALD cycles) [302].

Wilson *et al.* reported on W deposition on polymers by ALD and their results showed that W nucleation was enhanced by a few previous cycles of Al<sub>2</sub>O<sub>3</sub> by ALD. In this case, Al<sub>2</sub>O<sub>3</sub> acts as a

seed layer of nucleation on a variety of spin-coated polymers such as PMMA, polyvinyl chloride (PVC), polystyrene (PS), polypropylene (PP), and polycarbonate (PC). A growth per cycle (GPC) of 3.9 Å for W ALD at 80 °C has been attained, as shown in **Figure 20** [302].

Minton *et al.* followed the same strategy in terms of using Al<sub>2</sub>O<sub>3</sub> ALD seed layer prior to TiO<sub>2</sub> ALD, because TiO<sub>2</sub> did not nucleate well on the PMMA surface. Their results showed that the uncoated PMMA lost a considerable part of its mass, when exposed in vacuum to UV radiation and the bilayers formed with 20 cycles of Al<sub>2</sub>O<sub>3</sub> and 100 or 200 cycles of TiO<sub>2</sub> were efficient in preserving PMMA (**Figure 21**) [303].

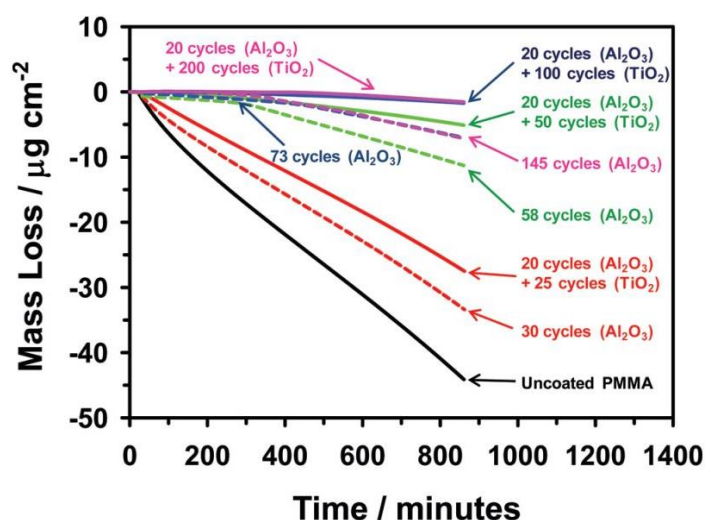


**Figure 21.** Mass loss of uncoated and coated PMMA with Al<sub>2</sub>O<sub>3</sub> and Al<sub>2</sub>O<sub>3</sub>/TiO<sub>2</sub> when exposed to vacuum UV radiation over time [303].

Kemell *et al.* also explored the ability of ALD coatings of Al<sub>2</sub>O<sub>3</sub> and TiO<sub>2</sub> on PMMA films, among other polymer films, like polyether ether ketone (PEEK), polytetrafluoroethylene (PTFE), and ethylene tetrafluoroethylene (ETFE) [304]. The deposition temperature range was from 80 to 250 °C, enabling the synthesis of amorphous and crystalline metal oxides. Firstly, amorphous Al<sub>2</sub>O<sub>3</sub> was deposited at 150–250 °C followed by TiO<sub>2</sub> deposited at 100 °C. For the case of TiO<sub>2</sub> deposition on Al<sub>2</sub>O<sub>3</sub>-coated PMMA at 250 °C, polycrystalline anatase TiO<sub>2</sub> films were obtained, as shown in **Figure 22**. These results highlight the importance of Al<sub>2</sub>O<sub>3</sub> seed layer, or interlayer, prior to TiO<sub>2</sub>. In fact, TiO<sub>2</sub> deposition on bare PMMA was attempted also at 250 °C, but virtually no growth was observed, revealing that TiO<sub>2</sub> does not nucleate well on PMMA. Interestingly, the authors did not point out any constraints of the polymer's thermal stability when deposition at 250 °C, in particular regarding PMMA stability.

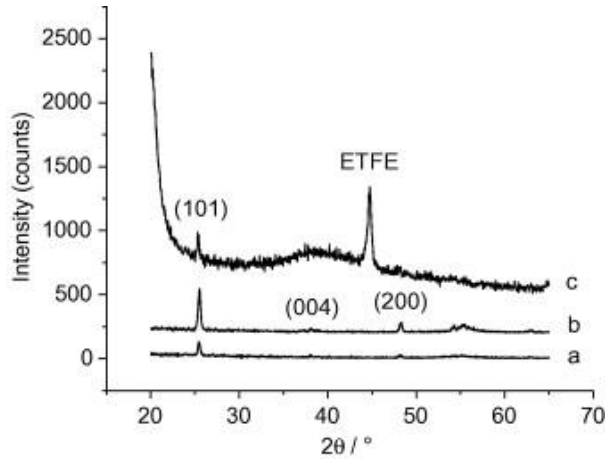
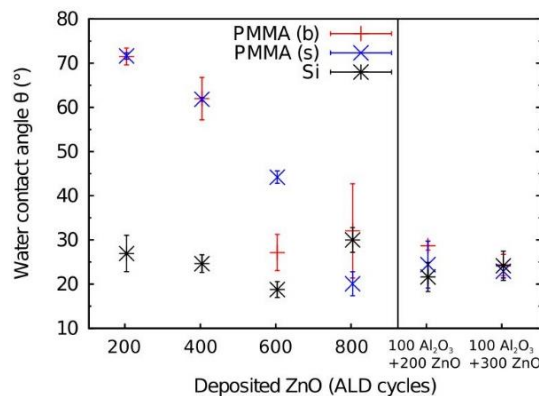


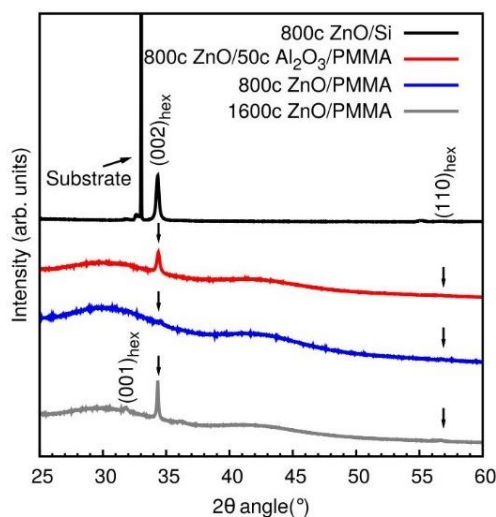
**Figure 22.** XRD patterns of anatase  $\text{TiO}_2$  films in substrates made of (a) Si at 200 °C, (b) PMMA at 250 °C, and (c) ETFE at 200 °C. Si substrate was used as a reference, for comparison purpose [304].

An identical approach was performed by Napari *et al.*. The authors reported on the influence of the deposition of an  $\text{Al}_2\text{O}_3$  seed layer to the ZnO film growth, morphology, and crystallinity, on PMMA commercial plates and spin-coated PMMA films on Si substrate. The  $\text{Al}_2\text{O}_3$  seed layer provides a pathway for blocking the DEZ precursor into the PMMA subsurface and improves the ZnO growth with some degree of hexagonal crystal orientation at low deposition temperature viz 35 °C (**Figure 23** (a)). The ZnO surface wetting properties were altered upon UV illumination (**Figure 23** (b)). As a consequence, this photoinduced changes on the wettability find applications in microfluidics, where thin functional coatings on patterned polymer platforms can be used to manipulate the fluid flows [305]. This work is a promising alternative for lab-on-a-chip technologies development and microfluidics platforms.



(a)





(b)

**Figure 23.** Water contact angles ( $\theta$ ) of UV-illuminated ZnO deposited on bulk PMMA (red), spin-coated PMMA (blue), and Si substrates as a function of ZnO ALD cycles (black). The two right-most points represent the contact angles of ZnO deposited on 100 cycles  $\text{Al}_2\text{O}_3$  intermediate layer (a). XRD patterns for 800 cycles of ZnO ALD onto: Si (black) and bulk PMMA substrates with (red) and without  $\text{Al}_2\text{O}_3$  seed layer (blue), and an XRD pattern of 1600 cycles ZnO film on bulk PMMA (grey). (b) [305].

In brief, the seed layer or interlayer approach on polymers can be seen as an in-situ two-step ALD process, consisting of the deposition of a few nanometer seed-like layer, at a lower temperature step, followed by a second process for the more refractory metal oxides. The choice of  $\text{Al}_2\text{O}_3$  ALD from TMA and  $\text{H}_2\text{O}$  precursors is a viable pathway to seeding layer on polymers because  $\text{Al}_2\text{O}_3$  ALD can be conducted at temperatures as low as 35 °C, conjugated with the TMA positive characteristics like its high volatility and reactivity towards different co-reactants at low temperatures. Based on the above studies, the majority of published work for ALD on polymers addresses  $\text{Al}_2\text{O}_3$  ALD from TMA and  $\text{H}_2\text{O}$  cycles, stressing out the versatility of this ALD process either as coating and/or seed layer, being also a method to study the influence of the polymer substrate properties on the nucleation and growth of metal oxides. Similar to  $\text{Al}_2\text{O}_3$ , ZnO ALD can also be performed on polymers by taking advantage of the DEZ high volatility and reactivity at low temperatures. It is clear that the modification of a polymer substrate that shows high reactivity towards a given ALD process is crucial to ensure high-density nucleation towards a homogeneous and uniform thin film.



#### 1.4.4. Coatings on PMMA by Plasma Atomic Layer Deposition

Plasma-enhanced ALD (PE-ALD) is an energy enhanced ALD method. In plasma-enhanced, also referred to as plasma-assisted ALD (PA-ALD), plasma ALD simply or, in some cases, radical enhanced ALD (RE-ALD), the substrate surface is exposed to the species generated by plasma during the reactant step [306]. For instance, the synthesis of metal oxides thin films by PE-ALD is schematically illustrated in **Figure 24**, in which an oxygen plasma is employed during a one-step of the cyclic deposition process.

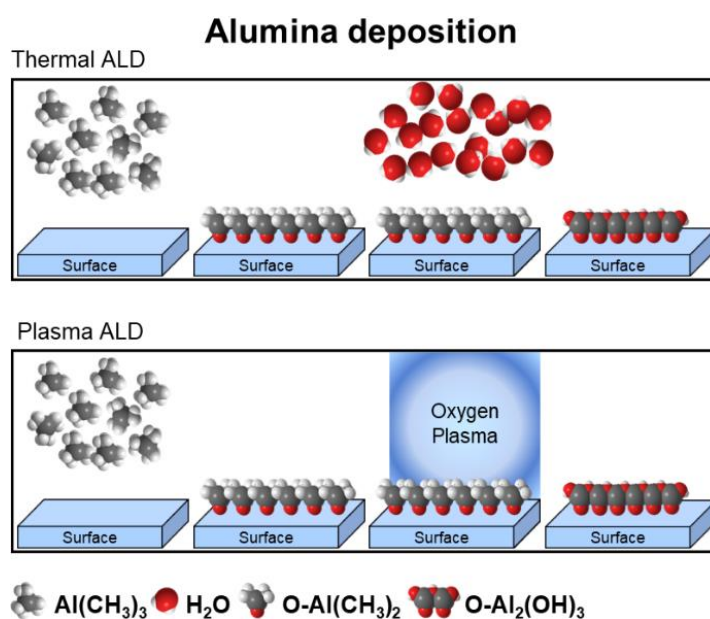


**Figure 24.** Schematic representation of one cycle of  $\text{Al}_2\text{O}_3$  by thermal ALD and plasma ALD techniques. In plasma ALD, the  $\text{H}_2\text{O}$  co-reactant is replaced with a plasma exposure (e.g.,  $\text{O}_2$  plasma) to grow metal oxides.

In this manner, the plasma is used to generate metastable species by gas dissociation increasing the reactivity delivered to the deposition surface. As a consequence, less thermal energy is necessary at the substrate surface to drive the ALD surface process allowing the thin film deposition at lower substrate temperatures comparing to thermal ALD [306,307]. Such high reactivity and low deposition temperatures extend the range of materials that can be used as (i) ALD precursors and (ii) thermally sensitive substrates. There are different types of plasma ALD reactor configurations: (i) in PA-ALD and PE-ALD (both meanings are the same) the substrate is exposed to the plasma discharge since it is located in the same space as the plasma source or very near the substrate; (ii) in radical enhanced ALD (RE-ALD), the plasma source is separated

from the substrate so that only radicals generated by the plasma are allowed to reach the substrate [306–308]. The plasma is ignited from an electrical discharge from radio-frequency or microwave energy when a continuous flow of  $O_2$ ,  $N_2$ ,  $H_2$ , or  $NH_3$  passes through the plasma sources [273,307]. Another aspect to take into consideration is the effect of the distance between the plasma and the sample, especially shorter distances where the substrate surface will be more exposed and more sensitive to the plasma [309,310]. The plasma ALD processes produce thin films with better characteristics, such as a lower level of impurities as a consequence of better stoichiometry, than a thin film produced by thermal ALD [289,306,311]. Nevertheless, it requires more complex equipment than that used for thermal ALD [306].

Kääriäinen *et al.* used non-functionalized PMMA commercial polymeric plates to deposit  $TiO_2$  from and plasma excited  $O_2$  precursors by PA-ALD. The authors investigated the relationship between the plasma power and the carrier gas (e.g., Ar and  $N_2$ ) to improve the film adhesion on the polymeric substrates. The best result in terms of  $TiO_2$  film adhesion was obtained for a relatively low plasma power (25 W) with Ar carrier gas. These experimental parameters also played a role in the variation of the  $TiO_2$  refractive index [308].

Surface-enhanced Raman spectroscopy (SERS) has been widely used in various types of ultrasensitive sensing applications in a wide variety of fields. This analytical tool is very powerful in biosensing and material science for the detection of analytes in very low concentrations. Huebner *et al.* developed a PMMA-based SERS substrate to simplify the fabrication process as well as improve the biosensing response. To this end, PMMA SERS-gratings were coated with  $Al_2O_3$  protective layer either by thermal-ALD (T-ALD) or by PA-ALD at low deposition temperatures (80–120 °C) for both processes and no influence on their physical properties has been mentioned. Afterwards, the  $Al_2O_3$ -enclosed PMMA-grating was coated with thermal evaporated Ag layer which serves as the structured plasmonic film for the enhancement of the light field [312]. It was found that a 10 nm  $Al_2O_3$  ALD layer is thick enough to suppress the PMMA Raman background signal safely. Moreover, this layer is also hard and dense enough to protect the polymer against organic solvents and allows the cleaning of the SERS substrate and, thereby, repeated use for SERS measurements [312].

Both T-ALD and PE-ALD processes were performed regarding optical components made of lightweight polymers, a good alternative to glass optics. Here, Paul *et al.* explored the antireflection properties of  $TiO_2$ ,  $Al_2O_3$ , and  $SiO_2$  ALD multilayered coatings on PMMA substrates. For all depositions, the temperature was kept at 60 °C which is well below the PMMA T<sub>g</sub>. After finding

the ideal conditions for ALD processes, the authors conclude that the best results were achieved when an  $\text{Al}_2\text{O}_3$  T-ALD layer is deposited on PMMA substrates to prevent surface cracking before the subsequent PE-ALD coatings. The plasma intensity played an important role in the film's adhesion and refractive index towards the antireflection coating property [286]. For instance, the  $\text{SiO}_2$  and  $\text{TiO}_2$  films deposited using the 'low' plasma (100 W) conditions on pre-coated PMMA substrates with 40 nm  $\text{Al}_2\text{O}_3$  T-ALD show no significant delamination of the film after the cross-hatch test. **Figure 25** illustrates the investigated multilayered coatings on PMMA, where it is possible to discern the well-defined  $\text{SiO}_2$ ,  $\text{TiO}_2$ , and  $\text{Al}_2\text{O}_3$  layers [286].

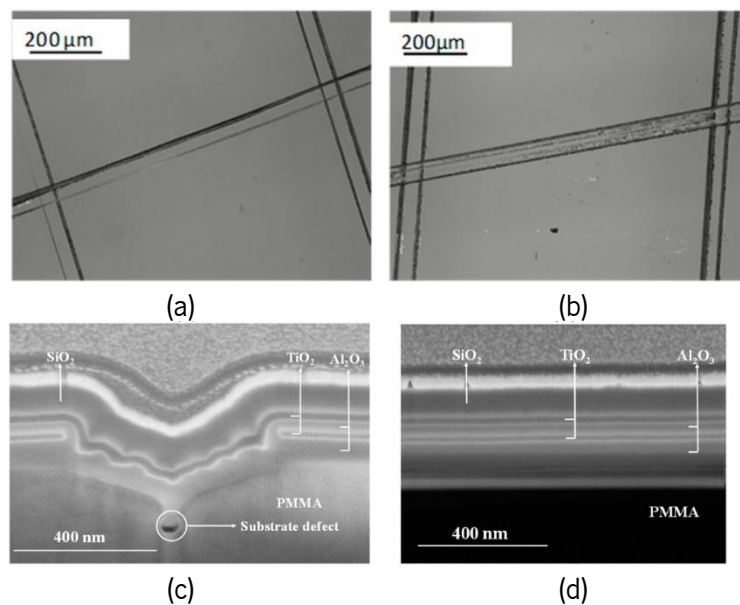


**Figure 25.** (a) Optical microscopic images after cross-hatch tests and (b) after climate test of antireflection coatings double-sided coated PMMA. Focused ion beam scanning electron microscopy (FIB-SEM) cross-sectional image of multilayered antireflection coatings on PMMA (c) focused on a crack (d) focused on a crack-free region [286].

## 1.4.5. Area Selective ALD on PMMA

### 1.4.5.1. PMMA as Masking Layer

An alternative approach for ALD on PMMA surfaces takes advantage of the low reactivity of PMMA. Several pre-treatments have been studied for PMMA surface modifications, aiming to enhance its surface hydrophilic properties. These include wet chemistry, plasma treatment and UV irradiation, where the treated PMMA either as a film or as plates are employed in biological samples immobilization and for improving component microchips [313–315]. However, the hydrophobic

nature of PMMA is advantageous for exploiting it as inhibiting mask layers (i.e., patterned areas of the sample) to prevent ALD growth, the so-called area-selective ALD (AS-ALD), where the film is deposited only on areas without the PMMA.

Self-assembled monolayers (SAM) of PMMA can passivate the active reactions sites on the growth surface and therefore hinder ALD nucleation [288,316–319]. Färm *et al.* produced a patterned masking layer from a PMMA SAM to passivate the Si surface against the ALD growth of Ir, Pt, Ru, and TiO<sub>2</sub> coatings. As a result, the coatings were selectively deposited on areas without the SAM [319]. TiO<sub>2</sub> ALD and PMMA masked area-selective ALD approach was also explored by the research groups of Sinha [317] and Haider [288]. Cho *et al.* created AS-ALD using PMMA in additive and subtractive printing [320]. Also Wei *et al.* created a passivation hybrid with PMMA and parylene and further coating with AlO<sub>x</sub> to create thin film transistors [321]. These results indicate that the PMMA films can work in area-selective ALD and the PMMA masking layer can be easily dissolved in acetone after the deposition process.

Shin *et al.* introduced an ALD/SAM multi-process to enhance the hydrophobic surface on PMMA, aiming at the development of antireflection coatings in self-cleaning applications. To this end, octadecyl-trichlorosilane (OTS) was chosen as SAM on PMMA, followed by Al<sub>2</sub>O<sub>3</sub> ALD. As a result, larger water contact angle values were obtained with this multi-process when compared to those without the ALD deposition process and the SAM layer did not affect the optical transmittance properties of the coated PMMA [282].

The PMMA removal step is an important feature in device fabrication and different strategies are ranging from wet to dry procedures. In this context, the PMMA layer can be eliminated by immersing in organic solvents (dichloromethane [322], acetone [323–327], isopropanol [325], or a mixture of acetone and isopropanol [325,327,328]), rinsing solvents like methanol [324,329] and finally washed with de-ionized water [322,329,330]. Sometimes, the PMMA residues are removed by annealing [324], Tan *et al.* and Cho *et al.* removed the layer with UV-ozone treatment [320,331]. **Figure 26** illustrates practical examples of the various PMMA patterns in AS-ALD. These patterns are based on the following geometrical shapes: circles [329,332,333], squares [317,329,332,334,335], crosses [336], line(s) [288,320,327], and shapes or draws with more complexity [311,337]. The masking layer, resultant from the PMMA with inhibited growth, can be constituted from TiO<sub>2</sub> [288,317,319,327,329,334], Al<sub>2</sub>O<sub>3</sub> [319,320,337,338], hafnium dioxide (HfO<sub>2</sub>), zirconium dioxide (ZrO<sub>2</sub>) [338], and ZnO [311,320,336], SnO<sub>2</sub> [320] Ir, Pt, and Ru [319].

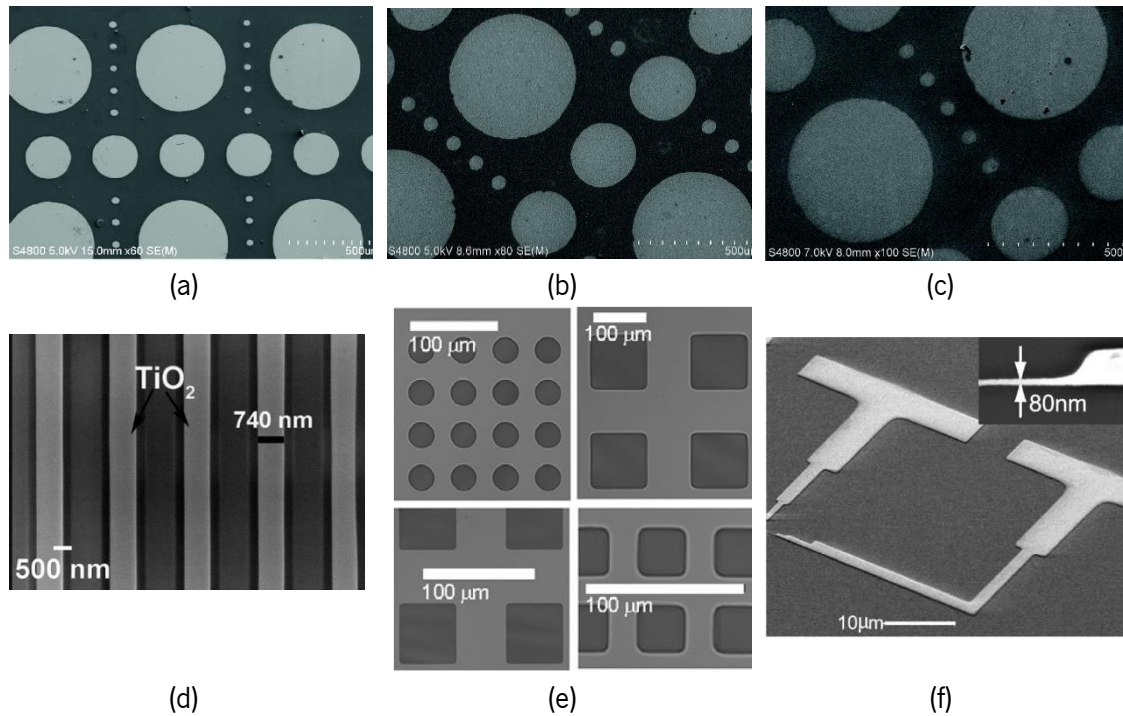


**Figure 26.** SEM micrographs of patterns produced on PMMA by AS-ALD tool for (a) Pt (b) Ir (c) Ru [319]; (d)  $\text{TiO}_2$  [336]; (e)  $\text{TiO}_2$  [329]; (f)  $\text{HfO}_2$  [338] coatings in a silicon substrate.

The PMMA mask can also be processed as a patterned layer, the first step consisting in spin-coating the polymer over the substrate [311,317,341,342,329,332,334–337,339,340] and, sometimes, heat treating at 180 °C [288,332,336,338] or soft heat treating [288,317,329,335] for a short time, followed by an etching process to reveal the desired pattern. The techniques employed to etch the PMMA substrate and create the pattern are: (1) lithography (optical lithography [335], photolithography [332,336], deep-UV lithography [317], electron beam lithography [288,323,327,340,341]); (2) heated cantilever probe tip (thermal writing) [334]; (3) chemical writing with isopropanol: methyl isobutyl ketone: methyl ethyl ketone in 75:24:1 ratios [338]; (4) nanoimprint and etching [337,342].

After the patterning, it is necessary to create a smooth surface and clean the excess of PMMA to regularize the template shapes; some authors suggest the  $\text{O}_2$  plasma descum etch [323,334,342] while others advise vacuum annealing [317,329]. Färm *et al.* and Sinha *et al.* used a similar approach exposing the resultant pattern to a solution of isopropyl alcohol/methyl isopropyl ketone [319] or isopropyl alcohol/methyl isobutyl ketone [317]. Both rinsed the material with isopropyl alcohol and water and pre-dried with a nitrogen stream; the last step consisted of drying it in an oven at 100 °C [317,319]. A similar method uses methylisobutylketon: isopropyl alcohol

solution and rinsing with the same alcohol [332]. Other authors simply did the ALD after the patterning [329,336,340]. Following this, the ALD takes place over the total material area—i.e., substrate and the PMMA pattern. Sharma *et al.* lift-off the PMMA with acetone [340]. Färm *et al.* and Sinha *et al.* used an ultrasonic bath with acetone, to ensure the PMMA removal. However, the total processes took about 1 h [317,319,329]. Tang *et al.* and Dhuey *et al.* hastened this process by substituting the acetone dipping for O<sub>2</sub> plasma [337,341].

### 1.4.5.2. ALD on Di-Block Copolymer Masks

Another approach for AS-ALD consists in using block copolymer (BCP) layer(s) to generate nm-sized features, e.g., nanotemplates [316,318,343] **Figure 27**). The strategy is to choose a polymer that delays the nucleation or does not promote any nucleation, such as polystyrene in PS-*b*-PMMA [316,318,343–345], polystyrene-*r*-poly(methyl methacrylate) (PS-*r*-PMMA) [316,345,346], and poly(styrene-co-methylmethacrylate-co-hydroxyethyl methacrylate) [318].

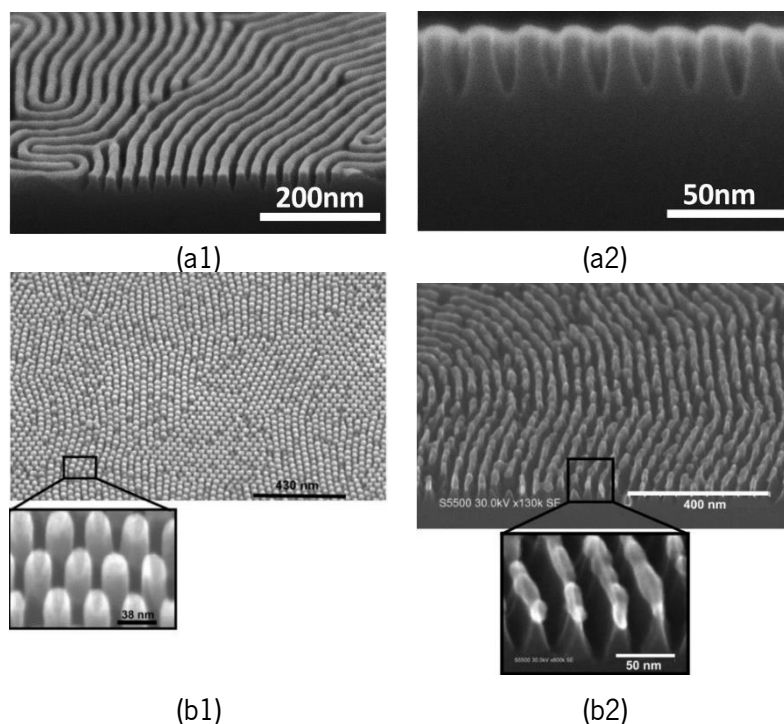


**Figure 27.** SEM micrographs of patterns produced from a diblock copolymer with PMMA; (a1) cross-section top view (a2) of Si nanowire array with an Al<sub>2</sub>O<sub>3</sub> mask [318]. Top view, 40° tilt on top and cross-section of (b1) Al<sub>2</sub>O<sub>3</sub> hexagonally packed nanopillars array treated with plasma and (b2) nanowires made of Si with Al<sub>2</sub>O<sub>3</sub> mask on top [345].

The route starts with the deposition of the BCP in substrates (silicon wafer [316,318,344,345] or magnesium oxide [343]) by spin-coating. Subsequently, BCP is annealed at a temperature above the glass transition temperature of both polymers [318] to neutralize and remove the excess solvent, followed by cleaning to eliminate the non-anchored chains [316,318,345]. Some authors add another BCP to create another layer, and the first one is named as brush layer; after the BCP deposition, the whole structure is annealed. Both layers have the same interfacial tension.

Hence, after annealing, the BCP film assembled into PMMA lamellae or cylinders. The transformation is spontaneous, resulting in a pattern with high aspect ratio and sharp edge [346]. Peng et al. experimented with just one BCP, where the ALD deposition happens over the pattern and, finally, the sample is treated with O<sub>2</sub> to remove the polymers and cleaned to ensure the total polymeric elimination [344]. For templates with a brush layer, there is no defined order for the subsequent steps. In fact, the desired effect depends on the order: (1) ALD deposition over the template; (2) exposition to UV light [316], piranha solution [318], plasma [344], acetic acid [316,345] or etching [343] to remove the PMMA and PS from the BCP and the brush layer; (3) cleaning to remove excess material from (2). According to the desired method, there is a possibility to remove the unexposed parts of the substrate by etching [318,345].

In resume, PMMA has proven to be a versatile polymer material, in a wide range of applications and is often chosen as a processing layer for AS-ALD of pure metals and metal oxides.

**Figure 28** illustrates the various PMMA material forms and processing stages in an AS-ALD.

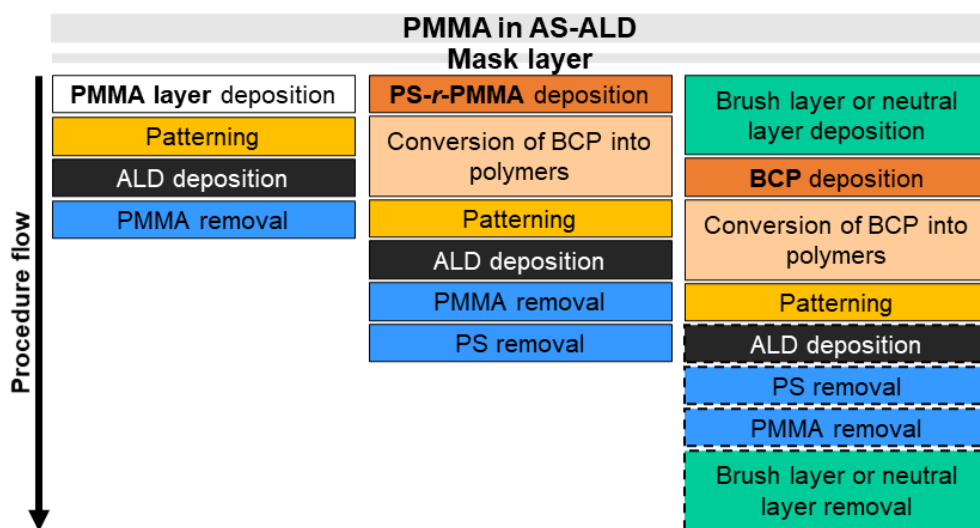


**Figure 28.** PMMA in an AS-ALD process, where the block copolymers are polystyrene-*random*-poly(methylmethacrylate) or polystyrene-*block*-poly(methylmethacrylate).

**Table 7** is a compilation of the main details of the supporting literature of this review devoted to the modification of PMMA surfaces by ALD technique. The table is organized by ALD types (thermal, plasma and area-selective) on different PMMA substrate geometries and describes the mainly ALD experimental details, such as deposition temperature, types of precursors and film thickness. Moreover, the table points out the different research topics of each paper, ranging from fundamental knowledge to practical applications.



**Table 7.** Summary of literature data regarding ALD coatings on PMMA.

<b>ALD type</b>	<b>PMMA substrate geometry</b>	<b>Precursors, time sequence (Pulse/purge/pulse/purge times)</b>	<b>Number of cycles (film thickness)</b>	<b>T<sub>Deposition</sub></b>	<b>Application or motivation</b>	<b>Ref</b>
<b>Thermal ALD</b>	Film (~70 nm) M <sub>w</sub> =350.000 spin-coated onto polished Si (100) <sup>a</sup>	<b>ZnO</b> DEZ/N <sub>2</sub> /H <sub>2</sub> O/N <sub>2</sub>	1000 (25 nm)	25 °C	Curved organic light emitting diodes	[347]
	1 mm sheet and film (2–2.5 μm) M <sub>w</sub> =950kDa spin-coated onto Si(111)	<b>ZnO</b> DEZ/N <sub>2</sub> / H <sub>2</sub> O/ N <sub>2</sub> 0.15-0.30/30/0.15-0.30/30 s <b>Al<sub>2</sub>O<sub>3</sub></b> TMA/N <sub>2</sub> / H <sub>2</sub> O/N <sub>2</sub> 0.30/30/0.3/30 s	100-800 (30 nm grains) 20-100 (10 nm) <b>Al<sub>2</sub>O<sub>3</sub> + ZnO</b> 20-50+200-800	35 °C	Microfluidics	[305]
	Film (5, 32 and 80 nm) M <sub>w</sub> =350.000 spin-coated onto Si(100) <sup>b</sup>	<b>ZnO</b> DEZ/N <sub>2</sub> / H <sub>2</sub> O/N <sub>2</sub> 1/120/1/120 s	150 (21.2, 18.6, 15.9 nm)	35 °C	Flexible electronics and nanoscale optoelectronic devices	[296]
	Plates 2 mm M <sub>w</sub> =150 000–160 000	<b>TiO<sub>2</sub></b> TDMAT, 40 °C/N <sub>2</sub> /O <sub>3</sub> /N <sub>2</sub> 0.5/10/4/10 s <b>Al<sub>2</sub>O<sub>3</sub></b> TMA, 20 °C/N <sub>2</sub> /O <sub>3</sub> /N <sub>2</sub> 0.25/6/4/6 s	1000 (60 nm) 1000 (85 nm)	60 to 65 °C	Nanoindentation and nanotribology studies	[291]
	Sheet extruded	<b>Al<sub>2</sub>O<sub>3</sub></b> TMA/residence/N <sub>2</sub> /H <sub>2</sub> O/residence/N <sub>2</sub> 0.10/10/45/0.2/10/45 s	750 (130 nm)	65 °C	To increase interfacial toughness	[292]
	Specimens (20 x 20 x 1 mm)	<b>TiO<sub>2</sub></b> TDMAT, 65 °C/Ar/O <sub>3</sub> /Ar 0.5/10/1/15 s	300 (30 nm)	65 °C	Dental implants	[285]
	PMMA NPs (50-100 nm)	<b>TiO<sub>2</sub></b> TTIP/purge/H <sub>2</sub> O/purge 0.5/15/0.5/15 s	250	80 °C	Photocatalysis	[297]
	Film (~200 nm) M <sub>w</sub> =350.000 spin-coated onto Si wafer <sup>c</sup>	<b>Al<sub>2</sub>O<sub>3</sub></b> TMA/Ar/H <sub>2</sub> O/Ar 60/30/60/30 s 5/60/5/60 s	(200 nm)	80 °C	Study of the ALD mechanisms	[290]
	Particles (~1–100 μm) and film M <sub>w</sub> =15.000 spin-coated onto silicon substrates	<b>W</b> WF <sub>6</sub> /N <sub>2</sub> /Si <sub>2</sub> H <sub>6</sub> /N <sub>2</sub> 1/60/5/60 s <b>Al<sub>2</sub>O<sub>3</sub></b> TMA/N <sub>2</sub> /H <sub>2</sub> O/N <sub>2</sub> 1/60/5/60 s	Film: <b>Al<sub>2</sub>O<sub>3</sub> + W</b> 10 + 50-250 (95-845 Å) Particles: <b>W</b> 25-200 <b>Al<sub>2</sub>O<sub>3</sub> + W</b> 5 + 25 (29 Å)	80 °C	Flexible optical mirrors, electromagnetic interference shielding, diffusion barriers	[302]

Thermal ALD (cont.)	Powder (0.2–1 mm) $M_w=120\text{kDa}$	<b>ZnO</b> DEZ, 22 °C/ $N_2$ / $H_2O$ / $N_2$ 0.3/3/0.1/5 s	400 (80 nm)	80 °C	Photocatalysis	[300]
	Plates (4 mm) and powder (0.2-1 mm) $M_w=120\text{kDa}$	<b>ZnO</b> DEZ, 22 °C/ $N_2$ / $H_2O$ / $N_2$ 0.3/3/0.1/5 s	Plates: 220-2200 (1-180nm) 1650 (100 nm) Powder: 1650 (80 nm)	80 °C	Photocatalysis	[298]
	Flat (2.5 x 2.5 cm) <sup>a</sup>	<b>ZnO</b> DEZ, 22 °C/ $N_2$ / $H_2O$ / $N_2$ 0.3/3/0.1/5 s	1650 (100 nm)	80 °C	Water reuse	[299]
	Film (4000 ± 1000 Å) $M_w=15.000$ spin-coated onto Si(100) wafer and QMC sensors	<b>Al<sub>2</sub>O<sub>3</sub></b> TMA/ $N_2$ / $H_2O$ / $N_2$ 1/29/1/29 s	30 cycles (1000-1500 Å)	85 °C	Organic light emitting diode	[275]
	Film ( $M_w=15.000$ ) spin-coated onto QCM Discs ~2 μm	<b>TiO<sub>2</sub></b> TiCl <sub>4</sub> / $N_2$ / $H_2O$ / $N_2$ <b>Al<sub>2</sub>O<sub>3</sub></b> TMA/ $N_2$ / $H_2O$ / $N_2$ 2/30/2/30 s	<b>Al<sub>2</sub>O<sub>3</sub></b> 30-45 (23.42-51.89Å) <b>Al<sub>2</sub>O<sub>3</sub> + TiO<sub>2</sub></b> 20 + 25-200 (26.09-146.84 Å)	90 °C	Aerospatial	[303]
	Film (305 nm) $M_w=120.000$ with β-NaYF <sub>4</sub> :Er <sup>3+</sup> NPs spin-coated onto borofloat 33 glass	<b>TiO<sub>2</sub></b> TiCl <sub>4</sub> /Ar/ $H_2O$ /Ar	(199 nm total)	100 °C	Upconversion luminescence	[294, 295]
	(1.5 x 1.5 cm)	<b>TiO<sub>2</sub></b> TDMAT, 70 °C / $N_2$ / $O_3$ / $N_2$ 1/15/1.8/15 s	50-500 (75-425 Å)	120 °C	Wettability and hardness improvement	[293]
	Flat (2 x 2 cm <sup>2</sup> ) <sup>a</sup> <i>pre-treated</i> with OTS and heptane solution (0.1:136), at 60°C (5-30 min)	<b>Al<sub>2</sub>O<sub>3</sub></b>	300-1200 (9-26 nm)	150 °C	Wettability improvement	[282]
	Film (0.1 μm) spin-coated onto (100) Y-stabilized ZrO <sub>2</sub> single crystal	<b>CeO<sub>2</sub></b> (Ce(thd) <sub>4</sub> and O <sub>3</sub> )	200 (3.5-5.5 nm)	200 °C	Memories technology	[287]
	Film (70-100 nm) $M_w=350.000$ spin-coated onto Si	<b>TiO<sub>2</sub></b> TiCl <sub>4</sub> / $N_2$ / $H_2O$ / $N_2$ 0.2 s/30 s/0.2 s/30 s <b>Al<sub>2</sub>O<sub>3</sub></b> TMA/ $N_2$ / $H_2O$ / $N_2$ 0.2 s/4 s/ 0.2 s/ 4 s AlCl <sub>3</sub> / $N_2$ / $H_2O$ / $N_2$ 0.5 s/2 s/1 s/2 s <b>Al<sub>2</sub>O<sub>3</sub> (TMA) + TiO<sub>2</sub></b> 0.2/4/0.2/4 s + 0.2/4/0.2/ 4 s	700 (20 nm) 3300 (350 nm) 1000 (100 nm) 200+1000 (43 nm)	100 °C 250 °C 250 °C 250 °C	Wettability improvement	[304]

Plasma ALD		O <sub>2</sub> Plasma 1 (300 W,50 sccm) O <sub>2</sub> Plasma 2 (100W, 90 sccm) <b>Al<sub>2</sub>O<sub>3</sub></b> TMA/purge/Plasma 2/purge 0.2/10/5/5 s <b>SiO<sub>2</sub></b> 3DMAS/residence/purge/Plasmas/purge 0.4/4/10/3/6 s <b>TiO<sub>2</sub></b> TTIP/purge/Plasmas/purge 1.5/7/6/5 s	(80 nm)  (40 nm)  (55 nm)	60 °C	Antireflection coatings	[286]
	PLEXIGLAS® XT Extruded acrylic sheets M <sub>w</sub> =150.000-160.000	Plasma (25-200W) <b>TiO<sub>2</sub></b> TDMAT/N <sub>2</sub> /plasma/N <sub>2</sub> 0.5/10/0.25-6/10 s	500	50 to 70 °C	Adhesion improvement	[308]
	Film (100 nm) on quartz	<b>Al<sub>2</sub>O<sub>3</sub></b> (TMA and O <sub>2</sub> plasma)	(10 nm)	80 to 120 °C	Substrates for SERS	[312]
Area selective ALD on PMMA	Lines (10-15 nm) by electron beam lithography	<b>Al<sub>2</sub>O<sub>3</sub></b> TMA/purge/O <sub>2</sub> plasma 30/60/210 ms	30 (6 nm)	25 °C	Fabrication of high-resolution imprint templates	[341]
	Squares by electron beam lithograph	<b>O<sub>2</sub> Plasma</b> (100 W) <b>MoO<sub>x</sub></b> [(N <sup>t</sup> Bu) <sub>2</sub> (NMe <sub>2</sub> ) <sub>2</sub> Mo]/Ar/Plasma/Ar 6/6/8/6 s	10-60 (1–4.5 nm)	50 °C	Nano and Optoelectronic applications	[340]
	Nanoporous film (75 000 g/mol) by electron beam lithography spin-coated onto SiO <sub>2</sub> /Si	<b>ZnO</b> DEZ/ N <sub>2</sub> /H <sub>2</sub> O/N <sub>2</sub> 0.3/2/0.3/2 s	25-225 (4-26 nm)	70 °C	Fabrication of charge-trap flash memories components	[342]
	Film ~350 nm (200 and 950k) spin-coated onto SiO <sub>2</sub> /Si	<b>Al<sub>2</sub>O<sub>3</sub></b> (TMA/N <sub>2</sub> /H <sub>2</sub> O/N <sub>2</sub> ) <b>HfO<sub>2</sub></b> (TDMAH/N <sub>2</sub> /H <sub>2</sub> O/N <sub>2</sub> ) <b>ZrO<sub>2</sub></b> (TDMAz /N <sub>2</sub> /H <sub>2</sub> O/N <sub>2</sub> )	(2.5–50 nm) (100–25 nm) (25–100 nm)	100 to 150 °C	Microelectronics and nanoelectronics	[338]
	Stripe (312 nm) M <sub>w</sub> =950.000 by etching spin-coated onto SiO <sub>2</sub> /Si	<b>ZnO</b> DEZ/Ar/H <sub>2</sub> O/Ar 0.05/45/0.1/45 s <b>Al<sub>2</sub>O<sub>3</sub></b> DMAI/Ar/ H <sub>2</sub> O/Ar 0.05/45/0.1/45 s <b>SnO<sub>2</sub></b> TDMASn/ Ar/ H <sub>2</sub> O/Ar 0.15/45/0.1/45 s	5-30 supercycles ratio 6:5 zinc/tin 1:1 zinc/tin 10:1 zinc/aluminum 15:1 zinc/aluminum	100 to 170 °C	Fabrication of bottom-gate, top-contact thin-films for transistors	[320]

Area selective ALD on PMMA (cont.)	Stripes 300 nm (950k) by electron beam lithography spin-coated onto SiO <sub>2</sub> /Si	<b>TiO<sub>2</sub></b> TiCl <sub>4</sub> /N <sub>2</sub> /H <sub>2</sub> O/N <sub>2</sub> 0.1/10/3/10 s	25-300 (0-14 nm)	120 °C	Photocatalysis	[327]
	Film ~350 nm (200 and 950k) spin-coated onto SiO <sub>2</sub> /Si	<b>Al<sub>2</sub>O<sub>3</sub></b> (TMA/N <sub>2</sub> /H <sub>2</sub> O/N <sub>2</sub> ) <b>HfO<sub>2</sub></b> (TDMAH/N <sub>2</sub> /H <sub>2</sub> O/N <sub>2</sub> ) <b>ZrO<sub>2</sub></b> (TDMAz /N <sub>2</sub> /H <sub>2</sub> O/N <sub>2</sub> )	(2.5-50 nm) (10–25 nm) (25–100 nm)	100 to 150 °C	Microelectronics and nanoelectronics	[338]
	Film (110 nm) M <sub>w</sub> =15.000 spin-coated onto silicon wafer	<b>TiO<sub>2</sub></b> TTIP/N <sub>2</sub> /H <sub>2</sub> O/N <sub>2</sub> 5/30/5/30 s	200 (2 nm)	140 °C	Heat cantilever probes	[334]
	Stripes from a ≈43 nm film M <sub>w</sub> =350.000 spin-coated onto Si(100) <i>pre-treated</i> with O <sub>2</sub> plasma(2 min)	<b>TiO<sub>2</sub></b> TDMAT/N <sub>2</sub> /H <sub>2</sub> O/N <sub>2</sub> 0.03/20/0.015/20 s	100-1200 (43-23.96 nm)	150 °C	Inhibition efficacy of TiO <sub>2</sub>	[288]
	Squares from a (32-420 nm) film M <sub>w</sub> =54.000 coated onto Si wafer*	<b>TiO<sub>2</sub></b> TTIP, 82 °C/N <sub>2</sub> /H <sub>2</sub> O/ N <sub>2</sub> 2/25/1/60 s TiCl <sub>4</sub> , 25 °C /N <sub>2</sub> /H <sub>2</sub> O/N <sub>2</sub> 2/25/2/30 s	150 (~10.5 nm) 500 (35 nm)	140 °C 160 °C	Amplified photoresist polymers	[329]
	Squares from a (32-420 nm) film M <sub>w</sub> =54.000 coated onto Si wafer*	<b>TiO<sub>2</sub></b> TiCl <sub>4</sub> /N <sub>2</sub> /H <sub>2</sub> O/N <sub>2</sub> 2/25/1/60 s	150	160 °C	Amplified photoresist polymers	[317]
	Squares from a 100 nm M <sub>w</sub> =54.000 film spin-coated onto p-type Si(100)*	<b>TiO<sub>2</sub></b> TiCl <sub>4</sub> , 23 °C/N <sub>2</sub> /H <sub>2</sub> O/N <sub>2</sub> TTIP, 85 °C/N <sub>2</sub> /H <sub>2</sub> O/N <sub>2</sub> 2/60/2/60 s	50-400 (3.5-28 nm) 50-500 (3.4-35 nm)	160 °C	Comparison of precursors	[348]
	Stripes from a (9-40 Å) film spin-coated onto Si wafer <i>pre-treated</i> with O <sub>2</sub> plasma	<b>ZnO</b> DEZ/63 ms/purge/H <sub>2</sub> O/63 ms/purge	600 (40 Å)	200 °C	Thin-film transistors	[336]
	Dots (50-500 nm of diameter) from a film (70-100 nm) M <sub>w</sub> =350.000 spin-coated onto Si (100)	<b>TiO<sub>2</sub></b> (Ti(OMe) <sub>4</sub> and H <sub>2</sub> O) <b>Ru</b> (RuCp <sub>2</sub> and air) <b>Pt</b> (MeCpPtMe <sub>3</sub> and O <sub>2</sub> ) <b>Ir</b> (Ir(acac) <sub>3</sub> and O <sub>2</sub> ) <b>Al<sub>2</sub>O<sub>3</sub></b> (AlCl <sub>3</sub> and H <sub>2</sub> O) <b>Al<sub>2</sub>O<sub>3</sub></b> (TMA and H <sub>2</sub> O)	500 500-100 2700 1000-500 500 (40 nm) 500	250 to 300 °C	Passivation effect studies	[339]
	Squares or circles from a film spin-coated onto Si (100) wafer	<b>Pt</b> (MeCpPtMe <sub>3</sub> e O <sub>2</sub> )	1000 (50.4 nm)	300 °C	Nanotechnology	[332]

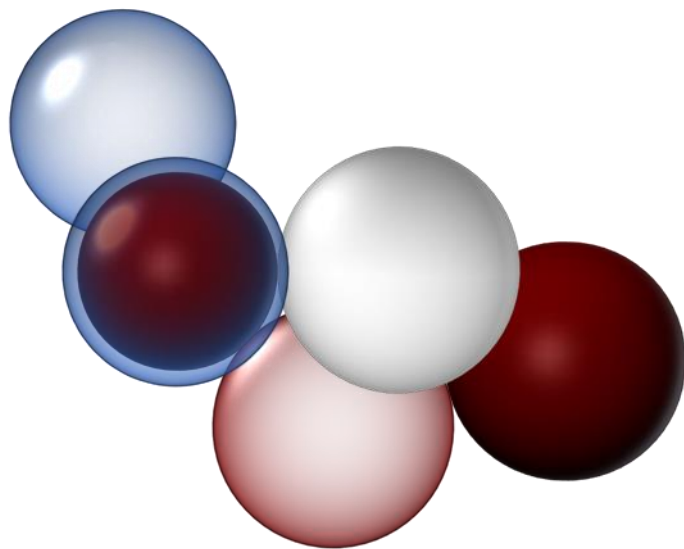
Area selective ALD on Di-block copolymers	PMMA cylinders (diameter $30 \pm 3$ nm) from treated PS- <i>b</i> -PMMA (60 nm), previously spin-coated onto SiO <sub>2</sub> /Si	<b>Al<sub>2</sub>O<sub>3</sub></b> , TMA, 25 °C/N <sub>2</sub> /H <sub>2</sub> O, 25 °C/N <sub>2</sub> 60/300/60/300 s 300/300/300/300 s	10 (8.48 nm) 10 (30.8 nm)	85 °C	Molecular sensing	[344]
	PMMA blocks from treated PS- <i>b</i> -PMMA (25 nm), previously spin-coated onto (8 nm) SiO <sub>2</sub> /Si	<b>Al<sub>2</sub>O<sub>3</sub></b> , TMA/purge/H <sub>2</sub> O/purge 30/60/30/60 s	10 (14.3 nm)	130 °C	Nanofabrication for complementary metal oxide semiconductor technology	[318]
	PMMA hexagonal nanopores from treated PS- <i>f</i> -PMMA and PS- <i>b</i> -PMMA, previously spin-coated onto SiO <sub>2</sub> /Si(100) wafers (50 nm)*	<b>Al<sub>2</sub>O<sub>3</sub></b> , TMA/N <sub>2</sub> /H <sub>2</sub> O/ N <sub>2</sub> 0.2 s/8 s/ 0.2 s/10 s	22 (2.2 ± 0.1 nm) 122 (10.7 ± 0.1 nm)	300 °C	Biomedical devices	[316]

**Cleaning methods:** <sup>a,b,d,g</sup>piranha solution; <sup>c</sup>JTP cleaning; <sup>e,f</sup>2M HNO<sub>3</sub> for 2 h

3DMAS, Tris(dimethylamino)silane ((Me<sub>2</sub>N)<sub>3</sub>SiH); AlCl<sub>3</sub>, Aluminum trichloride; Ce(thd)<sub>4</sub>, Tetrakis(2,2,6,6-tetramethyl-3,5-heptanedionato)cerium (Ce(C<sub>11</sub>H<sub>19</sub>O<sub>2</sub>)<sub>4</sub>); CeO<sub>2</sub>, Ceric dioxide; HfO<sub>2</sub>, Hafnium dioxide; Ir(acac)<sub>3</sub>, Iridium acetylacetonate; MeCpPtMe<sub>3</sub>, [(N-Bu)<sub>2</sub>(NMe)<sub>2</sub>Mo], bis(tertbutylimido)-bis(dimethylamido)molybdenum; Trimethyl(methylcyclopentadienyl)platinum(IV); OTS, trichloro(octadecyl)silane; RuCp<sub>2</sub>, Ruthenium dicyclopentadienyl; SERS, surface-enhanced Raman spectroscopy; Si<sub>2</sub>H<sub>6</sub>, Disilane; TDMAH, Tetrakis(dimethylamido)hafnium ([[(CH<sub>3</sub>)<sub>2</sub>N]<sub>4</sub>Hf]); TDMASn, Tetrakis(dimethylamido)tin ([[(CH<sub>3</sub>)<sub>2</sub>N]<sub>4</sub>Sn]); TDMAz, Tetrakis(dimethylamido)zirconium ([[(CH<sub>3</sub>)<sub>2</sub>N]<sub>4</sub>Zr]); Ti(OMe)<sub>4</sub>, Titanium tetramethoxide; TiCl<sub>4</sub>, Titanium tetrachloride; TTIP, Titanium tetraisopropoxide (Ti[OCH(CH<sub>3</sub>)<sub>2</sub>]<sub>4</sub>); WF<sub>6</sub>, Tungsten hexafluoride; ZrO<sub>2</sub>, Zirconium dioxide; β-NaYF<sub>4</sub>:25%Er<sup>3+</sup>, sodium yttrium fluoride doped with trivalent erbium ions.

# **Chapter 2**

## **Materials and methods**



## 2.1. Microencapsulation synthesis and strategies

One of the main objectives for this thesis is to create a microencapsulation system to retain hydrosoluble ACs. **Table 8** shows some agrochemical properties provided from each data sheet information. The plant-based ACs are liquids, and Ultraferro (UF) is a powder but can be converted into an aqueous solution by dissolution. Thus, all compounds share similar characteristics, such as solubility, so that the encapsulation approach will be similar.

Theoretically, when a microencapsulation system is designed, it should be efficient for a large spectrum of active agents, especially the compounds with the same solubility. This work was focused on the UF encapsulation due to the high solubility constant. Notwithstanding, the Fitoalgas Green and the Folivex had a higher viscosity and composition complexity, which could not guarantee the encapsulation or encapsulation efficacy.

**Table 8.** ASCENZA® ACs characterization and respective properties.

Agrochemical function	Sample	Physical state	Density (g/cm <sup>3</sup> )	pH	Solubility	Ref
Biostimulant	Fitoalgas Green	Liquid	1.10	4.5	water	[349]
Fertilizer	Ultraferro	Solid	0.55	8.5	water, 60 g/L	[350]
	Folivex Crescimento	Liquid	1.24	3.6	Non-defined	[351]

Considering (and combining) the industrial challenge and ACs solubilities, the polymeric wall must be hydrophobic to create a MC with two separated phases: the AC inside and the protective shell outside. There is already an emulsion at this stage. Since this emulsion (UF and polymer) have to be poured into the continuous phase, it results in a double emulsion. This was the main reason to produce the ACs encapsulation using the double emulsion system. The solvent evaporation method was selected because of the hydrophobicity of the solvent to dissolve the polymers, and the UF inertia to the solvents.

In this work, the MCs and MSs are both considered on microencapsulation synthesis. During the microencapsulation phase, PMMA and cellulose acetate (CA) were blended as polymeric shell to overcome the diffusion problems from the microspheres. The microencapsulation study was elaborated using four strategies, as shown in **Figure 29**. The predominant techniques were solvent evaporation (strategies 1 to 3) and gelification with a cross-linker (strategy 4).

A considerable part of reactants, polymers and solvents were applied in the different strategies and sometimes with different functions.

### Microencapsulation techniques, strategies and controlled release

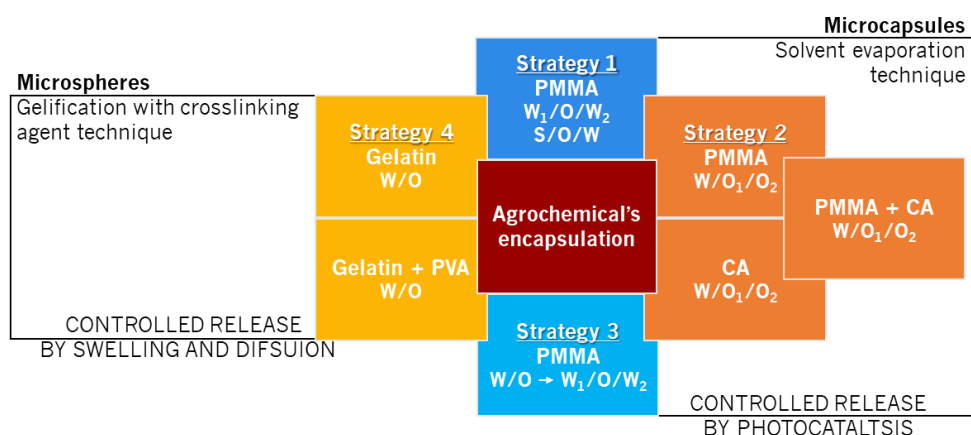


**Figure 29.** Microencapsulation approaches and the final product-controlled release.

The solvents were used as-received: acetone (99,5% Sigma Aldrich), chloroform (ACS grade, LABCHEM), methylene chloride (pa, Fisher Chemical), cyclohexane (ACS reagent, Sigma-Aldrich), 2-propanol (p.a., Honeywell), toluene (anhydrous, Carlos Erba Reagents), *n*-hexane (95%, Carlos Erba Reagents), chlorobenzene (Panreac), ethyl acetate (anhydrous, Sigma-Aldrich), ethanol (absolute, Pancreac), ethylene glycol (99%, Sigma-Aldrich), polyethylene glycol 200 (99.5%,  $M_w=190-210$ , Alfa Aesar), polyethylene glycol 300 (PEG, synthesis grade, Scharlau), glycerin (98%, Alfa Aesar), petroleum ether 40-60°C (pa, Fisher Chemical), methanol (99.8%, Acros Organics), Glacial acetic acid (p.a., Fischer Chemical), acetonitrile (HPLC gradient grade, Fischer Chemical).

The polymers applied in this study were poly(methyl methacrylate) (PMMA,  $M_w=400.000-500.000$ , Alfa Aesar), cellulose acetate (CA,  $M_w=50.000$ , Aldrich) and porcine skin gelatin (gel strength  $\sim 300$  g Bloom, Type A, Sigma-Aldrich). The hydrophilic cores utilized were water, agrochemicals (UF, Folivex and Fitoalgas Green), while the oily cores were citronella Java oil (Sigma-Aldrich), and a commercial perfume, *Eucalyptus Citriodora* (Plena Natura®).

The surfactants employed were: mineral oil (Alfa Aesar), Arabic gum (AG, CMD Chemicals), paraffin (CMD Chemicals), poly(vinyl alcohol) (PVA, 98-99% hydrolyzed, Alfa Aesar), sodium n-dodecyl sulphate sodium salt, (SDS, pure, Acros), Span®60 (TCI), Span®80 (Tokyo Chemical Industry), Span®85 (Sigma-Aldrich), Tween®20 (Alfa Aesar), Tween®40 (TCI), Tween®80 (Alfa Aesar), sunflower oil (pure, Carlos Erba), olive oil (supermarket), urea (assay, Panreac).



## 2.2. PMMA based MCs

### 2.2.1. PMMA-MCs synthesis

In three strategies with PMMA, this polymer was chosen mainly due to its incompatibility with the aqueous media and its commercialization at an accessible price. As a polymer previously synthesized, the purity level is high, and the by-products are in low concentrations; thus, there is less interference in the encapsulation. In other words, the variables from the raw material are minimized due to possible reactions with by-products. Another benefit is transparency, which helps to visualize the encapsulation and its homogeneity.

The thermal stability was a very attractive property for this industrial problem because the PMMA preserves the ACs from the moment they leave the factory until they are released in the crops or soil. During the transport, the temperatures that are reached are always higher than the ambient temperature. For example, on a typical summer day in Portugal, the outside temperatures can easily be higher than 30°C. Inside the transport, the temperatures are high, therefore, the MCs shell must not suffer changes that damage the agrochemical. This is important for both the producer and the consumer side.

#### Strategy 1

The first strategy implemented was the double emulsion of water in oil in water ( $W_1/O/W_2$ ). All PMMA articles are oriented to encapsulate oils [352–355]. Thus, the concept was to use the same approach for encapsulating aqueous cores. The  $W_1/O/W_2$  is characterized by two different aqueous phases, where in the  $W_1$  there was made a solution with UF. The other double emulsion (S/O/W) has the UF as it is, using it in the solid state (S). Both routes were focused on main aspects:

- $W_1/O$  or S/W emulsion (active agent and respective mass or concentration in solution, polymer mass, solvent and/co-solvent and respective volume(s), stirring type, stirring velocity and time)
- aqueous phase  $W_2$  (surfactant, surfactant concentration, and volume),
- double emulsion (temperature, stirring method, stirring velocity and time).

The emulsifications were performed by magnetic, vortex, and mechanic stirring by naval, helix or cowls impellers. The impeller used for the mechanical stirring is determinant because it promotes a specific flux. The ULTRA-TURRAX®, cowls, 3- and 4-blade are propellers that promote radial flux. Plus, the ULTRA-TURRAX® can homogenize and reduce the emulsion sizes due to the

fast speed associated with the stator/rotor working.

These parameters were changed in all the microencapsulation approaches. Each approach was accompanied by electron and optical microscopy to observe the MCs morphology, shape, size, heterogeneity and wall thickness. Energy Dispersive X-ray spectroscopy EDX enabled the identification of iron, which is present in the UF compound in the microcapsule core.

### Strategy 2

The emulsification process was changed in the second strategy to improve the encapsulation efficiency and the MCs morphology. This strategy involved the use of PMMA, cellulose acetate, or acetylcellulose and their combination. The double emulsion with two distinct oily phases ( $W/O_1/O_2$ ) was used to retain the agrochemicals in their own phase. When using this methodology, the encapsulation yields reach 100%. In this strategy, different variables were studied in comparison to strategy 1. Changing the polymeric wall to cellulose acetate (CA) and the combination of both polymers (CA and PMMA) was a way to discard if the PMMA was suitable for the purpose. Also, CA or a polymeric mixed wall could provide the MCs with unique properties.

The cellulose acetate is obtained from cellulose acetylation and is used in daily materials such as textiles, eyeglass frames and tool handles, packaging films, containers, retractable films, and others [356,357]. As a microencapsulation system, there is some information, mostly to encapsulate hydrophobic compounds. This biopolymer dissolves in organic solvents, which results into an oily emulsion phase. It shows properties non-existent in PMMA, for example, degradability and semi permeability [80,358–364]. Ideally, both could be effective for controlled release. If the photocatalysis was not activated, the cellulose acetate would start the chemical, biological, or photodegradation mechanism. Possibly it will trigger the photocatalysis to release the agrochemical.

### Strategy 3

Strategies 1 and 2 were a reproduction of PMMA articles in order to produce empty capsules, or capsules with UF or water. This strategy was a new approach starting from an oil encapsulation article [352,365]. With the collected knowledge from strategies 1 and 2, this last PMMA approach was established as a reproducible method to firstly create microcapsules with oily cores. Once these PMMA-MCs encapsulated oils, it was assumed that the encapsulation method could result for the UFs, although with a different yield depending on this AC.

## 2.2.2. Photocatalytic layer by ALD onto PMMA-MCs

### 2.2.2.1. ALD architecture and working as tool to create the coating

The thermal ALD depositions were carried out in a homemade tubular reactor equipped with rotary vacuum pump (**Figure 30**) working in exposed mode. Single side polished silicon wafer substrates from Siltronic ( $\text{SiO}_2/\text{Si}$  300 nm) were used as control to measure the coating thickness. The MCs were loaded in a stainless steel mesh crucible that was placed on a ceramic boat, as a sample holder. The ceramic boat was introduced into the furnace. Each precursor was kept separately in a stainless-steel canister, connected to a pneumatic ALD valve. This valve actuation allows the precursors dosing into the reaction chamber in a sequential manner. The diethyl zinc (DEZ) canister was kept at room temperature (RT) while the titanium tetraisopropoxide (TTIP) canister was heated at  $80^\circ\text{C}$  to ensure sufficient precursor vapor pressure. The delivery tubing lines were heated with a heating mantle to maintain a constant temperature of  $100^\circ\text{C}$  to prevent the precursor's condensation throughout the deposition process. The total flow rate of the pure Ar was 50 sccm, as both carrier and purging gas, and the pressure during each pulse was 0.24 kPa.

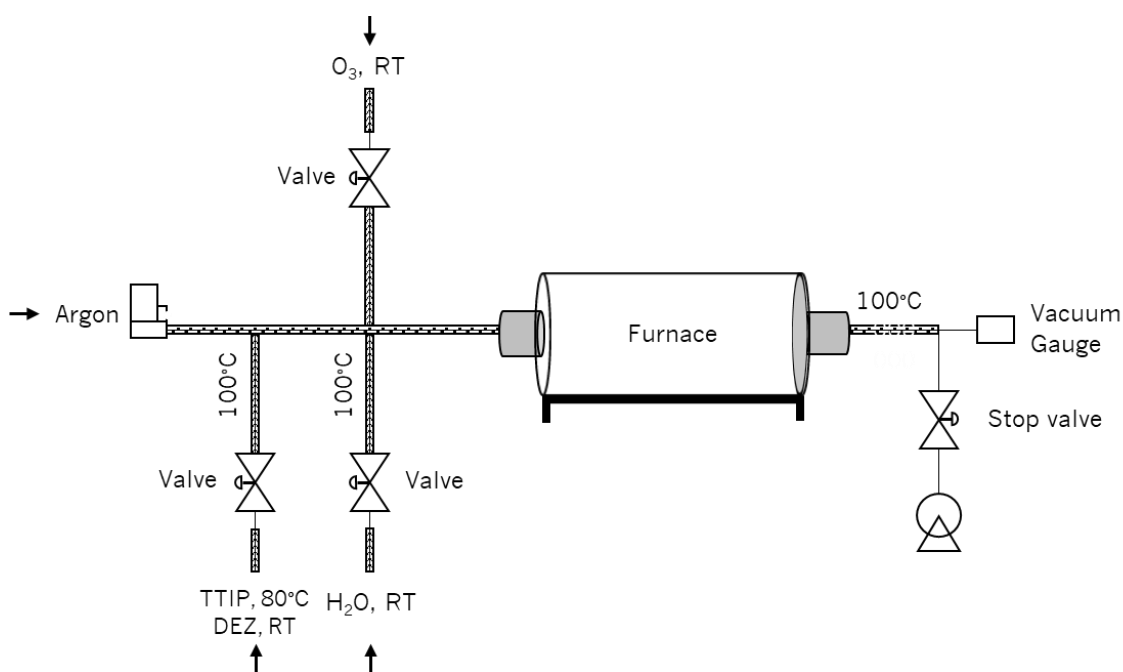


**Figure 30.** Schematic of the ALD reactor used in the experiments.

Typically, one ALD cycle is defined by a timing sequence as follows: (i) pulse precursor A, (ii) purge, (iii) pulse precursor B, (iv) purge. The precursor A (TTIP or DEZ) is pulsed into the reaction chamber, followed by a pressure increase (residence time, stop valve is closed). The unreacted

reactant A will be removed from the chamber assisted by a purging gas (e.g., Ar or N<sub>2</sub>) and, consequently, the pressure decreases to the minimum value (purge time, stop valve is open). The precursor B (H<sub>2</sub>O or O<sub>3</sub>) is pulsed into the reaction chamber to react with the precursor A adsorbed species, followed by the increase of the pressure (residence time, stop valve is closed). After, the excess is purged with a subsequent decrease in pressure decreasing value (purge time, stop valve is open). This cycle repeats until the desired coating thickness is reached.

### 2.2.2.2. ALD of metal-oxides

The schematic representation in **Figure 31** shows the different approaches for coating the MCs with metal-oxides by means of ALD technique. **Table 9** collects the most relevant information about the ozone pre-treatment parameters and the half-cycle description for the approaches mentioned in **Figure 31**.

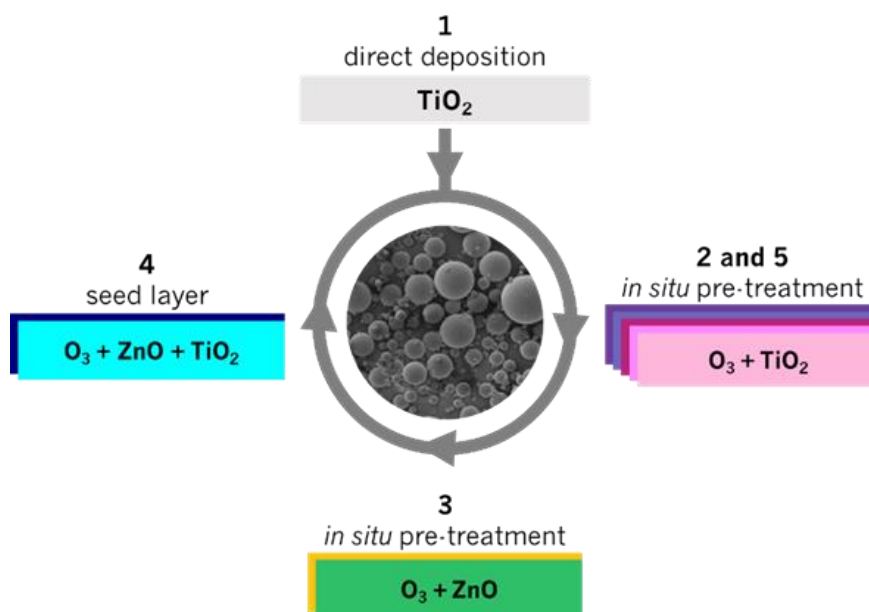


**Figure 31.** SEM micrograph of PMMA-MCs displayed in the center. The sample was coated with Au before the SEM analysis. ALD approach for coating the PMMA-MCs: (1) titania direct deposition; (2 and 5) ozone as pre-treatment followed by the titania deposition; (3) zinc oxide deposition with ozone as pre-treatment; (4) ozone as pre-treatment and zinc oxide as a seed layer to promote the titania growth.

As mentioned above, the ALD precursors as metal sources were TTIP (98% STREM Chemicals) and DEZ (95%, Sigma-Aldrich). Ultra-pure Milli-Q water (H<sub>2</sub>O, resistivity 18 MΩ.cm), and

ozone ( $O_3$ ) generated from the BMT803N ozone delivery system from pure oxygen, with a concentration ranging from 100 to 250  $g.Nm^{-3}$ , were used as oxygen sources.

**Table 9.** Deposition approaches and the respective experimental conditions for coating the PMMA-MCs with  $TiO_2$ , ZnO or the combination of both metal-oxides associated to the ozone pre-treatment. Each approach corresponds to the deposition technique from **Figure 31**.

Experimental conditions		Approach				
		1	2	3	4	5
<b>Pre-treatment</b>	<b>Precursor</b>	<b><math>O_3</math></b>				
	Cycles	-	-	100	-	100 to 600
	Pulse time	-	0.05 s	-	0.125 s	-
	Residence time	-	5 s	-	20 s	-
	Purge time	-	-	-	5 s	-
<b>Coating Deposition</b>	<b>Metallic precursor</b>	<b>TTIP</b>	<b>DEZ</b>	<b>DEZ + TTIP</b>	<b>TTIP</b>	
	Cycles	400	50 to 400	400	200	50 to 400
	Pulse time	-	-	0.5 s	-	-
	Residence time	20 s	30 s	-	-	20 s
	Purge time	-	-	10 s	-	-
	<b>Precursor</b>	<b><math>H_2O</math></b>				
	Pulse time	-	-	2 s	-	-
	Residence time	15 s	30 s	-	-	15 s
Purge time	-	-	10 s	-	-	

The first approach was  $TiO_2$  direct deposition, varying some parameters related with the cycle, such as precursor pulse time, purge time, residence time, oxygen sources ( $H_2O$  and  $O_3$ ), number of cycles, and deposition temperature. The  $TiO_2$  reactions were performed with TTIP and  $H_2O$  or  $O_3$ . The information collected from the published review served as a basis for innovating on the topic [366]. Once there are significant results in the literature about  $TiO_2$  direct deposition into PMMA, an emphasis is given in the present work to the use of TTIP and  $H_2O$  at low deposition temperatures.

A considerable amount of coatings were performed on the PMMA-MCs and on the  $SiO_2/Si$  substrates. In the latter, the Si has a  $SiO_2$  layer to increase the hydrophilicity and therefore facilitate the nucleation and growth of the coatings. In this line, the PMMA needed a similar surface chemistry. So, the PMMA-MCs were pre-treated with  $O_3$  for a period of time at low temperature (100 °C) before the  $TiO_2$  deposition.

In addition to the  $O_3$  pre-treatment, the deposition of ZnO as seed layer was also carried out allowing the production of bilayers composed of ZnO/ $TiO_2$ .

The uncoated and coated samples were submitted to a vast number of characterization techniques to identify the metal-oxide(s) presence and the alterations in the material properties. Additionally, the controlled release effect was evaluated using different oxidation cycles, while maintaining the TiO<sub>2</sub> parameters deposition.

### 2.2.3. Photocatalytic processes associated with PMMA-MCs

Before the controlled release studies, it is necessary to fully understand the **UF sensibility to UV-Vis radiation (Figure 32)**. A 30 ppm UF aqueous solution was exposed to: (1) UV radiation, (2) visible radiation in contact with atmosphere, (3) visible radiation in a closed recipient (to avoid certain reactions due to the present of an oxidative environment), and (4) the dark as control. The AC stability was associated to the UV-vis response. Aliquots of the UF solution in a quartz cell (12.5 mm × 12.5 mm × 40 mm) were taken hourly and the respective absorbance was measured in the spectrophotometer (Shimadzu UV-2501 PC) for a 200-900 nm range. The UV light source was a UV-A LED (Thorlabs, 700 mA) with irradiance of 2 mW/cm<sup>2</sup> centered at 365 nm, previously measure by a photo-radiometer (Delta Ohm HD2102.1). The UF band with maximum at  $\lambda \approx 480$  nm, associated with iron in the chelate was monitored at different times.

Photocatalysis		
Controlled release tests		Degradation test
Photolysis		
UF stability	UF release	MB degradation
UF (aq)	MCs-UF (aq)	MCs + MB (aq)
	Coated-MCs-UF (aq)	Coated-MCs + MB (aq)
Dark, Vis and UV-Vis radiation	UV-Vis radiation	

**Figure 32.** Photocatalytic studies performed in the PMMA-MCs.

One portion of MCs without AC was submitted to the same ALD conditions, to coating equally. Following this, 1 mg/mL of the coated MCs were placed into a MB solution with 1x10<sup>-6</sup>M concentration. A carbon tape with 1 cm x 1 cm of area was placed onto a glass slide, then 10 mg of MCs were fixed in the carbon tape. This support with the MCs was introduced into the cuvette/beaker with the MB solution and the MCs was exposed to the UV radiation using the

previous UV-LED lamp (**Figure 33**).

The **dye degradation** is related to the variation in the absorption peak intensity at 664 nm, which was analyzed using a spectrophotometer. The TiO<sub>2</sub> kinetics of the photocatalytic degradation of MB was calculated to verify if it is a pseudo-first-order reaction, when C<sub>0</sub> is the initial MB concentration, C the dye concentration at a t time and k is the reaction first-order constant (Equation 5) [367]. This study was also replicated for the uncoated MCs as a control sample and without MCs to evaluate the MB photolysis.

$$\ln\left(\frac{C}{C_0}\right) = -kt \quad \text{Equation 5}$$

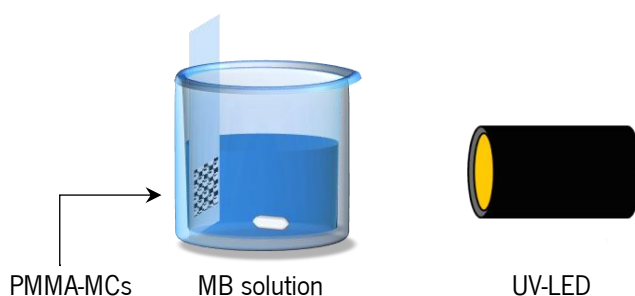


**Figure 33.** Schematic of the support made for the PMMA-MCs using carbon tape and glass slide introduced into a MB solution to monitor the photocatalytic activity when exposed to a UV-radiation.

After, the **controlled release effect** was compared between coated and uncoated MCs-UF. For irradiation using a visible light, an aqueous solution with 1.5 mg/mL of MCs-UF was exposed to a Xe lamp (Oriel Corporation 66002), with a power of 150 W and filtered to the 400-800 nm range and with an irradiance of 2 mW/cm<sup>2</sup>, previously measure by a photo-radiometer (Delta Ohm HD2102.1) (**Figure 34**). The MCs were placed as described in the previous figure and the UF absorbance peaks were monitored as described before. From this, the controlled release kinetics model was determined.

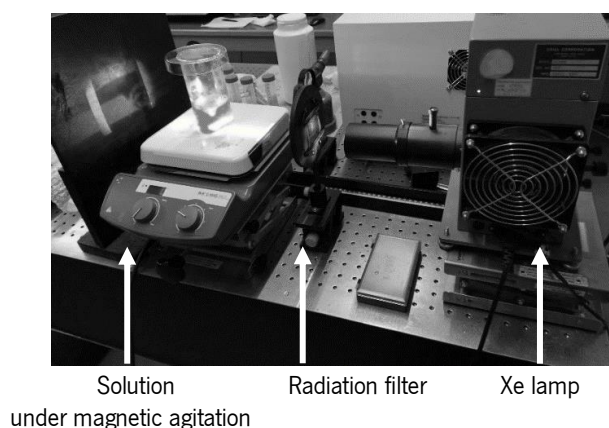


**Figure 34.** Exemplification of a setup of photocatalysis experiments using a Xe lamp.

## 2.3. Uncoated Gelatin based MSs

### 2.3.1. Gelatin based MSs Synthesis

#### Strategy 4

In this strategy, the resultant products are gelatin MSs or commonly called beads. Gelatin is an amphiphilic biopolymer rich in proteins from hydrolyzed animal collagen. Here, the protein constitution depends on the raw material. The raw material was soaked in either bath an acid or basic medium for the gelatin synthesis, followed by a thermal treatment, deionized, sterilized, and dried, resulting in a gelatin type A or gelatin type B, respectively [78,368]. Gelatin presents a viscous form for temperatures below 35°C, and between 35 °C to 60 °C is transformed into a gel-solid form. In these temperature ranges, this biopolymer can be cooled and heated several times without losing its integrity. However, above 60 °C, it starts to denature, and the process is not reversible. This material can be cross-linked or blended with other compounds to control properties like dissolution, hardness, thermal stability, among others [368].

Although this is a simple method, the gelatin thermal stability has to be enhanced using excipients to improve the MSs lifetime. After some research, PVA was selected because it is synthetic and hydrophilic and, when dissolved in water, it forms a gel [369,370]. As a hydrogel, PVA improves the water retention and swelling properties [369], plus it can be cross-linked [369] or used as cross-linker [143] and thus it can be integrated into controlled release and loading systems [369]. Here, the PVA was introduced into the gelatin matrix as a gelatin cross-linker to increase the plasticizer effect, thermal resistance, and consequently the MEs longevity [371].

### 2.3.2. Controlled release

Due to the matrix and agrochemical hydrophilicity, the release occurs when the MSs contact environments that have a similar solubility; also, they are extremely susceptible to thermal variations. For the presented reasons, the ALD coating is not necessary to liberate the UF, as for the MCs. The release process, named **diffusion and swelling**, was tested using the UV-VIS spectrophotometer over time, at room conditions. The agrochemical release was directly related to the absorbance increment in the UF band, at  $\lambda \approx 485$  nm.



## 2.4. Characterization Techniques

### 2.4.1. Characterization techniques employed in the microencapsulation strategies and the ALD

In this thesis, several characterization techniques were used to characterize the produced materials. **Table 10** lists these techniques, their purpose, and which samples were analyzed. There are four techniques that are necessary to draw attention because they were important, in their own way: i) SEM-EDX; ii) DSC; iii) NMR; iv) UV-VIS.

**Table 10.** Characterization techniques used in the MCs and MSs synthesis analysis, MCs coating by ALD, as well MCs and MSs UF controlled release monitoring.

<b>Microencapsulation</b>		
<b>Microcapsules (MCs) and Microspheres (MSs) Agrochemical: Ultraferro (UF)</b>		
<b>Microcapsules or microspheres with Ultraferro (MCs-UF, MSs-UF)</b>		
<p><b><u>SEM-EDX and OM</u></b> (UF, MCs, MSs, MCs-UF, MSs-UF)</p> <p>Presence of holes and pores Presence of polymeric residues UF encapsulation Homogeneity from the synthesis Size distribution Chemical identification</p>	<p><b><u>TGA</u></b> (UF, MCs, MSs, MCs-UF, MSs-UF, reactants)</p> <p>Thermal stability Material's degradation Reactant's encapsulation UF encapsulation or entrapment Cross-linking effect</p>	
<b>ALD coating</b>		
<b>Microcapsules (MCs) and Microcapsules with Ultraferro (MCs-UF) Pre-treated microcapsules (O<sub>3</sub>-MCs)</b>		
<b>Coated microcapsules and Coated microcapsules with Ultraferro (C-MCs, C- MCs-UF)</b>		
<p><b><u>SEM-EDX and OM</u></b> (MCs, MCs-UF, C-MCs, C- MCs-UF)</p> <p>Coating thickness Coating morphology Coating composition Pre-treatment effect</p>	<p><b><u>FTIR-ATR</u></b> (polymer, MCs, O<sub>3</sub>-MCs, C-O<sub>3</sub>-MCs, )</p> <p>Pre-treatment effect Coating – polymer bond Tacticities</p>	<p><b><u>DSC</u></b> (MCs)</p> <p>T<sub>g</sub> value Tacticity ALD conditions</p>
<p><b><u>XRD</u></b> (MCs, MCs-UF, C-MCs, C- MCs-UF)</p> <p>Crystallinity Crystalline phase Pre-treatment effect</p>	<p><b><u>TGA</u></b> (Reactants, MCs, O<sub>3</sub>-MCs, C-O<sub>3</sub>-MCs)</p> <p>Thermal stability Material's degradation</p>	<p><b><u>UV-vis</u></b> (polymer film)</p> <p>Tacticity Transparency</p>
	<p><b><u>NMR</u></b> (polymer, MCs, O<sub>3</sub>-MCs, C-MCs)</p> <p>Pre-treatment effect Tacticity</p>	<p><b><u>BET</u></b> (MCs, MCs-UF, O<sub>3</sub>-MCs)</p> <p>Surface area</p>

<b>Controlled release</b>	
<b>Microcapsules (MCs) and Microcapsules with Ultraferro (MCs-UF)</b>	
<b>Pre-treated microcapsules (O<sub>3</sub>-MCs)</b>	
<b>Coated microcapsules and Coated microcapsules with Ultraferro (C-MCs, C- MCs-UF)</b>	
<b>UV-vis</b> (C-MCs, C-MCs-AA, MSs-UF, MSs)	<b>XRF</b> (C-MCs, C-MCs-AA)
Controlled release UF stability MB degradation MB Photolysis	UF and coating detection
	<b>TGA</b> (C-MCs, C-MCs-AA)
	UF and Ti detection

Scanning electron microscopy associated with energy dispersive x-ray spectroscopy (**SEM-EDX**) was the most used technique for the visualization of the MCs wall morphology, size range, parts of polymeric waste, MCs coating by ALD, and agrochemicals controlled release. A NanoSEM - FEI Nova 200 (FEG/SEM) with EDAX - Pegasus X4M (EDS/EBSD) at SEMAT/UM and a SEM Hitachi SU-70 with Bruker Quantax 400 (B-U) EDS at CICECO/UA were used. In microencapsulation it is a tool to see the MC's size; their morphology and porosity, to measure the MCs wall thickness and analyze the surface area. The latter property was further determined by Brunauer-Emmett-Teller (**BET**, Micrometric Instruments Gemini V2.0 from CICECO at the University of Aveiro) for the pristine PMMA-MCs, O<sub>3</sub>-PMMA-MCs and PMMA-MCs-UF in order to determine if the agrochemical's encapsulation promoted changes in the surface. The MCs morphology and homogeneity from the synthesis, as well the presence of polymeric residues can be seen in an ordinary microscope. However, the UF encapsulation, size distribution and chemical identification, and the presence of pores in the PMMA-MCs can only be seen by SEM, since it provides a more significant magnification that allows seeing macroscopic, mesoscopic, and microscopic features [372].

The SEM-EDX technique is a powerful tool due to the presence of an energetic focused electron beam (1 to 50 keV). Electrons are produced from a thermionic (W, LaB<sub>6</sub>), field-emission (W), or Schottky-emission (ZrO<sub>2</sub>/W) guns, and travel through electromagnetic condensed and objective lens, where the respective apertures straighten and focus the electron beam [372]. These electrons interact with the sample where they penetrate it and produce elastic or inelastic scattering. The image can be made with secondary electrons (SE) detection from inelastic scattering or with backscattered electrons (BSE) from the inverse scattering. Since they penetrate the sample surface, the correspondent energy is shallow (**Figure 35**). There are other electrons and interactions that need to stand out. The sample absorbs some electrons. The Auger electrons

are the lowest energetic electrons and only penetrate 0.4 to 5 nm below the surface. The BSEs are obtained from the elastic scattering, and the resolution is intermediate, because the interaction volume and subsequently the energy associated is larger.

The X-ray emission from excited electrons is the most energetic, as consequence they can penetrate in the sample deeper, providing a more effective resolution. These electrons are responsible for the EDX analysis and can reach 5  $\mu\text{m}$  of surface depth, widely used to assess the sample composition. The last electronic interaction is the transmitted electrons, which are detected for the conventional or scanning transmission electron microscopy (CTEM and STEM, respectively) [372–374].

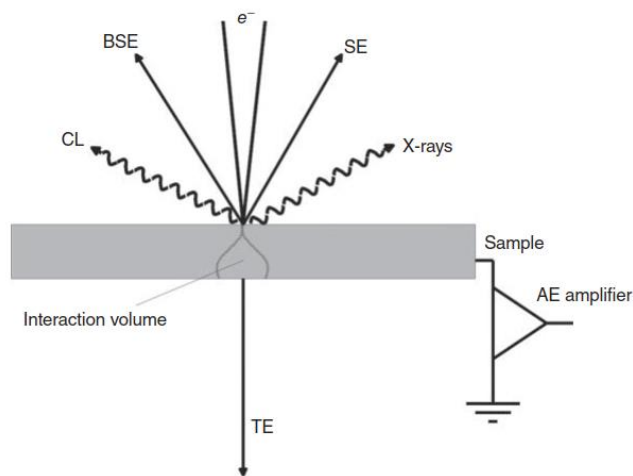


**Figure 35.** Electronic interactions in the SEM analysis [373].

The polymeric materials are susceptible to electronic interactions with their skeleton structure (C, H, O) that are very light and non-conductive. The BSE yield is lower, causing low contrast in the micrography [374]. It is necessary to control the exposition in order to not trigger the ionization, further reticulation, and consequently the chemical bond rupture. There are several approaches to work this out. The sample is manipulated by adding a nanometric coating. The usual coatings are carbon, gold-palladium alloy, and gold. Gold is the heaviest, which provides an excellent protection for the sample due to the electron conduction and production of high electron secondary electron yield, enhancing image resolution [375]. Certain polymers, like PMMA, are very sensitive to SEM-EDX analysis, so there are some parameters that can be adjusted in order to preserve the samples during the characterization [372]. As examples, the electron beam energy and the acceleration voltage can be lower ( $\sim 5$  keV) [372,374], the working distance can be increased, and selecting electronic detection with low interaction volume type it is also

advantageous. Some SEM types of equipment can work in low vacuum, such as environmental SEM, which is dedicated to biological samples and soft materials, like polymers. The environmental SEM can produce images without a coating because the image acquisition is with gaseous SE [373].

The pre-treated O<sub>2</sub>-PMMA-MCs were analyzed by SEM, and the surface area was determined by a **BET** to understand possible texture properties changes from the oxidation. After coating the MCs by ALD, the layer can bestow more resistance to the SEM conditions. Nevertheless, only **SEM-EDX** detects the Ti or Zn presence in the MCs and measure the film or nanoparticles thicknesses. Moreover SEM-EDX will be used as a qualitative perspective of know the agrochemical encapsulation. Due to the massive interaction volume from the X-rays, the sample will be more susceptible to decomposition but can be preciously coated with fewer conductor materials, like carbon, Au/Pd and Au. SEM will be crucial to see the coating thickness (for a film) or morphology and grain typology. For more detailed coating information, TEM is a powerful technique.

The differential scanning calorimetry (**DSC**, Hitachi DSC7000X from CICECO at the University of Aveiro) analysis in polymers is a useful thermo-analytical technique to know intrinsic temperatures or thermal events. The DSC thermogram curves indicate the endothermic processes for negative contributions; the positive curves correspond to exothermic transitions. Melting [374,376], loss of water and/or volatile by-products, decomposition, desorption, reduction [374] and protein denaturation [376] are some of the endothermic processes. The exothermic transitions are associated with crystallization, polymerization, cross-linking (cure), oxidation or oxidative degradation, adsorption, etc [374]. The thermogram also provides information about second-order transitions, which are oscillations in the baseline such as glass transition temperature (T<sub>g</sub>) [374,376].

The mass loss degradation from thermogravimetric analysis (**TGA**, Hitachi STA7200 from both universities) in polymers gives information about the processes involved when exposed to a temperature gradient. For instance, there are main-chain scission, side group scission, elimination, depolymerization, cyclization, and cross-linking. The mass gain is associated with other processes such as oxidation or adsorption. TGA also detects the presence of polymeric fillers, excipients, and volatile compounds. This thermal technique distinguishes the adsorbed from the absorbed water since the temperatures are higher when it is absorbed [376]. It is crucial to underline that TGA provides information for the mass changes and does not identify the degradation mechanism [377]. There are some factors that affect the degradation like:

- The synthesis reaction to produce the sample [377]. For example, the radically polymerized PMMA has three steps in TGA, and the anionically polymerized PMMA has one step [378].

- The degree of polymerization will result in a specific degradation rate, and this can be a tool to identify the thermal degradation mechanism [377].

- Samples with an large  $M_w$  have less free volume, needing more temperature to heat [374]. Moreover, they can develop more TGA steps due to the formation of unstable linkages in the polymerization. PMMA with  $M_w = 320\ 000$  has a peak at  $200\ ^\circ\text{C}$ , which does not appear in the PMMA samples with lower  $M_w$  [377].

- Excessive sample weight dislocates the thermogravimetric peaks. In the exothermic reactions, the heat released by the sample is superior to the programmed temperature. As a consequence, some mass losses can merge into a step. Contrarily, the endothermic reactions accumulate heat, and the steps take more time to appear [374,377].

- The sample size was influenced in the same way as the weight. So, particles dislocate the steps to lower temperatures, and grains do the opposite [374].

- The atmospheric exposition is determinant. Yet in polymers with depolymerization capacity, the results are slightly affected by the gaseous environment [374,377]. In fact, an atmosphere like air or pure  $\text{O}_2$  is very reactive. Hence, it will speed up the degradation and the mass losses will appear at lower temperatures [376]; the atmosphere acts as a catalyst.

However, the unclear information about the commercial agrochemical makes them unexplorable to describe the decomposition mechanism. So, the idea was to analyze the PMMA-MCs and PMMA-MC-UF and attribute the differences in the signal to the agrochemical's presence. Also, the TGA was employed in the MSs to analyze the crosslinking effect by analyzing the first peak from the differential. For both MCs configurations, the TGA was performed using an  $\text{N}_2$  atmosphere (200 mL/ min) with a  $10^\circ\text{C}/\text{min}$  heat ramp, and the samples were placed into a platinum crucible.

X-ray diffraction (**XRD**) provides information on the materials crystallinity. XRD experiments were performed for PMMA, PMMA-MCs, UF,  $\text{O}_3$ -PMMA-MCs, c-PMMA-MCs, PMMA-MCs-UF,  $\text{O}_3$ -PMMA-MCs-UF, c-PMMA-MCs-UF, in order to analyze their crystalline structure. The most intense diffraction peaks will determine the dominant crystalline phase and provides the Miller indices of the respective atomic phases. From this analysis, the interplanar spacings ( $d$ ) are derived from the Bragg equation (Equation 6), and the crystallite size ( $P$ ) is determined from the Scherrer equation

(Equation 7) [379][373]. A PANalytical X'Pert Pro diffractometer from CICECO at University of Aveiro was performed using Cu-K $\alpha$  radiation ( $\lambda = 1.54060 \text{ \AA}$ ) and a step size of  $0.02^\circ$ .

The polymers in this study, PMMA, PVA, and gelatin are not crystalline. However, they are made from units that constantly repeat, providing an organization pattern which results in a diffractogram with diffraction bands instead of peaks. Thus, for polymers it is possible to calculate the interchain distance ( $r$ ) from Equation 8. The other components from the equations are wavelength ( $\lambda$ ),  $k$  is the Scherrer constant for spherical particles (0.89) and,  $\beta$  is the full width at half-maximum (FWHM) [379][373].

$$n\lambda = 2d\sin\theta \quad \text{Equation 6}$$

$$P = \frac{K\lambda}{\beta\cos\theta} \quad \text{Equation 7}$$

$$r = \frac{5\lambda}{8\sin\theta} \quad \text{Equation 8}$$

Fourier transformed infrared – attenuated total reflectance (**FTIR-ATR**) spectroscopy is an effective technique in determining the chemical composition of organic, inorganic, and polymeric materials, identifying the molecular vibrations. The samples are placed into a crystal, and subsequently exposed to radiation and go through total internal reflection. During the process, the sample absorbs part of the infrared, and the spectrum is built up based on the absorbance for the different wavenumbers. The acquired spectra will provide information concerning the vibrations in the sample molecules; assembling all of them will result in the chemical structure. This spectroscopy was employed to compare and understand if the PMMA structure change during the encapsulation and identify the chemical bond that PMMA provides to bond with the metal oxides. Is expected to have different bands from each tacticities in polymers. For this study, the equipment used was a GALAXY SERIES FT-IR 7000 with a deuterium triglycine sulfate and CsI detector and an ATR golden gate (CICECO, University of Aveiro).

Nuclear magnetic resonance (**NMR**) studies were performed to analyze the ALD effect in the MCs. PMMA is an aliphatic polymer, so the  $^1\text{H}$  and  $^{13}\text{C}$  are the nucleus used to produce the spectra. Both present two spin quantum numbers,  $l$ , ( $1/2$  and  $-1/2$ ) consisting in a nuclear angular moment. When the spins are exposed to a magnetic field, they will generate each magnetic field and transit between the two spins, resulting in energetic transitions ( $\Delta E$ ) measuring the resonance frequency ( $\nu$ ). Equation 9 present the energy formula, where  $h$  is Planck's constant.

$$\Delta E = h\nu$$

Equation 9

The  $^1\text{H}$  and  $^{13}\text{C}$  nucleus have a property named as a gyromagnetic ratio or angular momentum,  $\gamma$ . So, the frequency is dependent on the magnetic properties, such as magnetic field  $B_0$ ,  $\gamma$ , and the chemical shift,  $\delta$ . The last property is associated with the differences between the magnetic field created by the nucleus and the magnetic field felt by itself (shield effect) and the equipment frequency.

$$\delta = \frac{\nu_{\text{sample}} - \nu_{\text{reference (CDCl}_3)}}{\nu_{\text{equipment}}} \times 10^6$$

Equation 10

NMR can be used to investigate solid and liquid samples. The NMR studies in the present work were carried out in NMR equipments for liquid samples (300 MHz Varian Unity Plus and 400 MHz Bruker Avance II) from Chemistry Department at University of Minho, so it was necessary dissolve them in an appropriated solvent as a reference, such as deuterated chloroform ( $\text{CDCl}_3$ ) (Equation 10). PMMA, PMMA-MCs, and c-PMMA-MCs were analyzed for  $^1\text{H}$ -NMR,  $^{13}\text{C}$ -NMR, distortionless enhancement by polarization transfer (DEPT 135), heteronuclear Multi Bond Correlation (HMBC), and heteronuclear multiple quantum correlation (HMQC).

The proton NMR distinguishes the different hydrogens from the compounds, and the signal shape says how many protons are in the same chemical environment as neighbors. The  $^{13}\text{C}$ -NMR distinguish the carbons and for the PMMA all signals are from singlets. DEPT 135 evidence that the  $-\text{CH}_2$  groups yield a negative signal, giving a confirmation of the methylene group, which was not evident in the  $^{13}\text{C}$ -NMR. In the HMBC there is a correlation between carbons and protons separated by two, three, and, sometimes, in conjugated systems. In a certain way, HMQC is complementary because it shows the proton-carbon single bond correlations.

If the protons and carbons feel different chemical environments, the tacticities express unique signals, where a relative analysis can be executed for identifying the respective portion. The bibliographic research shows strong proof that the PMMA needs a pre-treatment to ensure the deposition of the photocatalytic active material [313]. If necessary, the pre-treated samples can be analyzed by NMR (and FTIR-ATR) to see the ozone treatment effect in the substrates. Furthermore, is expected that the metal-oxide coating will dislocate more significantly the chemical shifts due to the influence of the high electronegativity [374,375,380].

This technique has limitations linked to signal complexity from the tacticities and the

possible lack of differences in the NMR after the pre-treatment at atomic or nanometric level. Also, the presence of iron in the UF as well the metallic coatings suggests that the samples cannot be analyzed because these elements (Fe and Ti) had associated not only a spin but also a magnetic moment, certainly making incompatible samples for the proton and carbon NMR analysis.

#### **2.4.2. Characterization techniques associated with the controlled release and other photocatalytic tests**

One concern from this thesis was to understand the photocatalytic performance. In other words, if the nanometric photocatalytic coating is capable to destruct the MCs and release the ACs, or if it degrades the environment to where it is exposed. Therefore, the coating photocatalytic activity was evaluated by measuring the AC concentration and by degrading a MB solution, used as a control.

Ideally, in the TiO<sub>2</sub>-PMMA-MCs-UF, the UF's controlled-release efficiency is evaluated by analyzing the aqueous solution. The goal was to expose the coated and uncoated PMMA-MCs-UF to radiation (UV radiation or Xenon lamp). The PMMA is degraded due to the coating photocatalysis triggered by the light sources. During the process, the UF is released, and the solution will have an increment in UF concentration. To determine the controlled release, two approaches were employed: (1) monitoring the process by measuring the absorbance from the aqueous solution via UV-VIS spectrophotometry over time; (2) qualitatively comparing the aqueous solution at the beginning and end of light exposure.

The iron present in the AC gives a reddish color, resulting in absorbance-specific bands from the groups present in the UF. This AC is essentially a chelate with ethylenediamine-N,N'-bis(2-hydroxyphenyl)acetic acid (EDDHA), and iron. The literature shows three absorbance bands with maxima at 200 nm, 281 nm, and 482 nm corresponding to a benzene ring, ortho substitution in the ring, and iron-phenolate bonds, respectively [381].

The total reflection X-ray fluorescence (**TXRF**, Picofox S2 Bruker Nano from CICECO, University of Aveiro) is a detection technique where an x-ray radiation source interacts directly with the atoms present in the sample. The X-rays destabilizes the inner electronic levels. To reach the equilibrium the electrons from the lowest energetic levels are excited to the orbitals of the ejected electron. During this process occurs fluorescence that is specific for each material. So, each atom will provide an identity peak from specific orbital transitions. This technique can be used as qualitative or quantitative; in this work TXRF was implemented only as a qualitative technique to



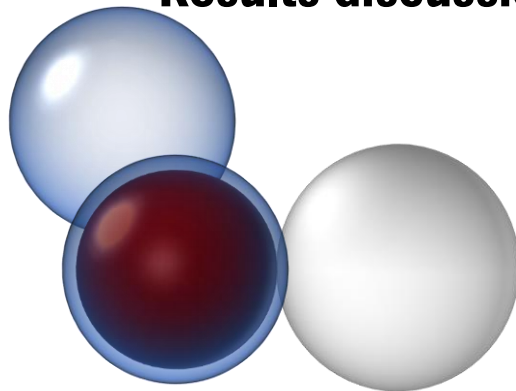
detect iron from the UF, Ti, and Zn from the coatings that can be in aqueous media presented in point (2) above [382].

Also, from the photocatalytic process, some coated PMMA-MCs were studied in an aqueous MB solution to evaluate the PMMA photocatalytic efficiency. The main idea was to interpret if the heterostructured material can degrade the environment as a photocatalyst. Since the MCs have a micrometric shell and the coatings are nanometric, there is a strong probability that degradation cannot occur, allowing the possibility to work as a 3D photocatalyst. The MB solution was chosen because it is a cationic dye, pollutant, and a well-known compound in photocatalysis.

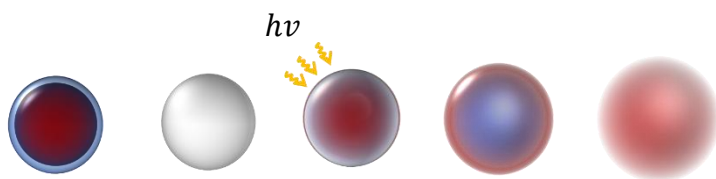
# Chapter 3

## Microcapsules

### Results discussion



### Controlled release



### 3.1. Solvents, PMMA and UF relevant properties for microencapsulation

First of all, PMMA and UF were dissolved in several solvents to understand the solvent's range without losing its properties. **Table 11** presents some solvent properties as well as the correspondent interactions with PMMA and UF. The AC (UF) dissolved very well in water and had a partial dissolution in isopropanol, but it was insoluble in the other solvents. However, a particular interaction was detected when in contact with acetone: the solution changed its color from red to brownish, indicating that the iron oxidation number was modified (**Figure 36**). Due to the low toxicity, isopropanol is an attractive solvent for this application. However, besides the UF low solubility in isopropanol, the PMMA did not dissolve in this solvent, so this green solvent was also excluded from the procedures. From the bibliography, the PMMA dissolves in a lot of organic solvents, such as alcohols, chlorides, and aromatic compounds (**Table 11**) [383]. The solvents were chosen based on the volatility or potential to be applied in the solvent extraction technique. Initially, one of the objectives of this work was to build a procedure based on green chemistry. Due to these limitations, the solvent methylene chloride, or dichloromethane (DCM), was chosen because it has a high vapor pressure, enabling a high volatility. In other words, a solvent that evaporates faster is a requisite for the microencapsulation technique.

**Table 11.** Physical and chemical properties from solvents employed in the microencapsulation to synthesize PMMA-MCs (adapted from [384]).

Solvent	Cyclohexane	Toluene	Chlorobenzene	Ethyl acetate	Chloroform	N-hexane	DCM	Acetone	Isopropanol	Water
Chemical formula	C <sub>6</sub> H <sub>12</sub>	C <sub>7</sub> H <sub>8</sub>	C <sub>6</sub> H <sub>5</sub> Cl	C <sub>4</sub> H <sub>8</sub> O <sub>2</sub>	CHCl <sub>3</sub>	C <sub>6</sub> H <sub>14</sub>	CH <sub>2</sub> Cl <sub>2</sub>	C <sub>3</sub> H <sub>6</sub> O	C <sub>3</sub> H <sub>8</sub> O	H <sub>2</sub> O
Density (g/mL)	0.779	0.867	1.106	0.894	1.498	0.655	1.326	0.786	0.785	0.998
Boiling point (°C)	80.7	110.6	132	77	61.2	69	39.8	56.2	82.4	100
H <sub>2</sub> O solubility	0.005	0.05	0.05	8.7	0.8	0.0014	1.32	M	M	M
Vapor pressure <sup>a</sup> (hPa)	104	29	12	97	210	160	475	240	44	17.5
Viscosity (10 <sup>-3</sup> Pa.s)	0.89	0.55	0.75	0.43	0.54	0.29	0.42	0.3	2.07	0.89
PMMA dissolution*	✓	✓	✓	✓	✓	✓	✓	✓	✓	✗
UF dissolution*	✗	✗	✗	✗	✗	✗	✗	✗	PD	✓

<sup>a</sup>values at 20°C, \*conclusions obtained experimentally. M – miscible, PD – partially dissolved.

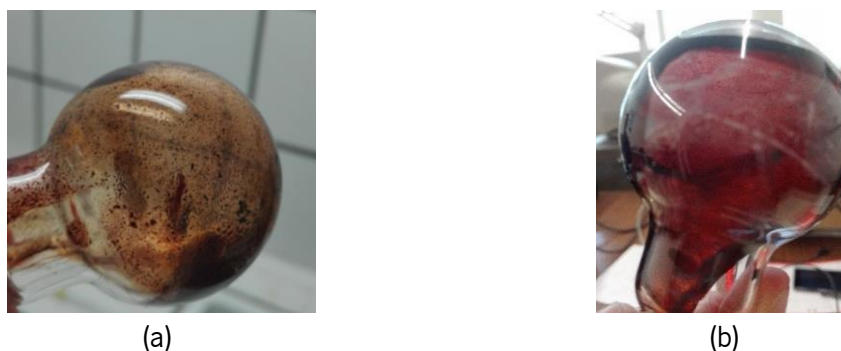


**Figure 36.** PMMA dried film, with UF. The polymer was previously dissolved in (a) acetone and (b) DCM.

In general, from the dissolution experiments it became clear that the ideal core-shell structure was not created. The emulsion made of PMMA, UF and solvent is colored. Hence, this visual information suggests that the UF is mixed with the PMMA. There were strong probabilities that the PMMA-MCs-UF would most likely have an empty or partially empty core, which adds a water absorption of 0.2-4% [385], **Figure 37**.

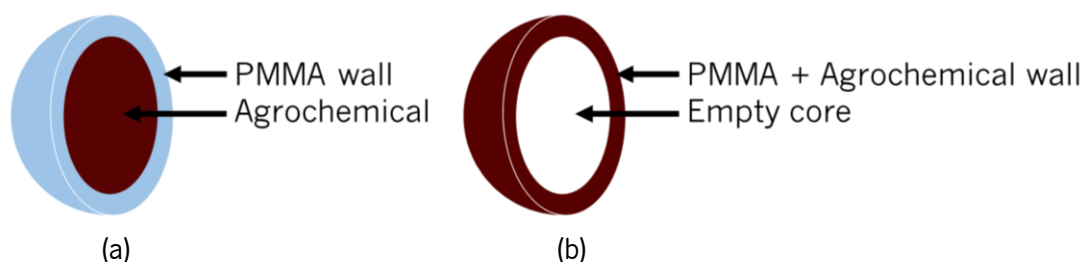


**Figure 37.** (a) Theoretical and (b) experimental core-shell PMMA-MCs-UF structures.

The microcapsules from strategies 1 and 2 were valuable to understand the synthesis route upon studying and changing, however they did not provide reliable and interesting PMMA-MCs to further proceed with the coating deposition by ALD and do the photocatalytic tests. So, the detailed approach, experimental conditions and results discussion of first and second strategies are presented in Appendix 1.

### 3.2. PMMA-MCs from strategy 3

As explained before, the strategy was to create a procedure encapsulating oils and further encapsulate the UF for later coating by ALD. This decision was made since the encapsulation yields in double emulsions are very low. By this way, at least, there is the certainty that the MCs are

efficient and could be universal.

The oil encapsulation started from the S/O/W protocol and the core was substituted by a commercial perfume or a *Eucalyptus citriodora* essential oil (O<sub>1</sub>/O<sub>2</sub>/W). The main variable was the solvent. MCs were crushed in a paper filter to visualize the perfume stain and detect the encapsulation by the smell. After the vacuum filtration, it was noticed that the MCs with failed encapsulation had oil on top of the filtrated part. The perfume is an oil (insoluble in W phase), it is denser than the continuous phase and the washing water. Therefore, after filtrating and washing the MCs, the non-encapsulated oil is a supernatant on water. For these reasons, the filtrated samples were always visualized and smelled to see if the perfume was encapsulated or not.

As usual, the Sharma [365] and Teeka [352] protocols for encapsulating the perfume were tried. The Sharma *et al.* experimental conditions were the most accurate once the PMMA-MCs were very similar, but the fragrance was not encapsulated. The ideal PMMA percentage from the Teeka *et al.* procedure led to a viscous solution that it was impracticable to pour the oily phase into the PVA solution. The PMMA percentage in the O<sub>1</sub> phase was thus decreased from 34% to 15% and in both procedures resulted in the formation of PMMA-MCs. However, upon changing stirring and the bath temperature, the products were not MCs. With this result and the information taken from strategy 1, only two solvents were applied in the following experiments: DCM and chloroform.

DCM and chloroform have demonstrated to be excellent solvents because they produced spherical and smooth PMMA-MCs with low polymeric residues (**Figure 38**). The PMMA-MCs with DCM and chloroform demonstrated the perfume encapsulation. However, the best procedure from DCM was not reproducible. One hypothesis is based on the temperature difference between the ice bath and room temperature. Besides this result, the subsequent experiences with DCM and CF were all made at higher temperatures (40 °C).

After filtrating and washing, the PMMA-MCs were analyzed by SEM. The DCM creates MCs and polymeric residues. Changing the solvent and the polymeric mass, the polymer waste decreases. Also, the solvent combined with a 3-blade naval impeller originated a PMMA-MCs smooth surface. Despite this, the perfume was not encapsulated.

From here, the parameters that were varied in order to encapsulate the perfume were:

- PVA percentage
- PMMA percentage
- Introduction of sodium dodecyl sulfate (SDS) and respective percentage
- Agitation speed

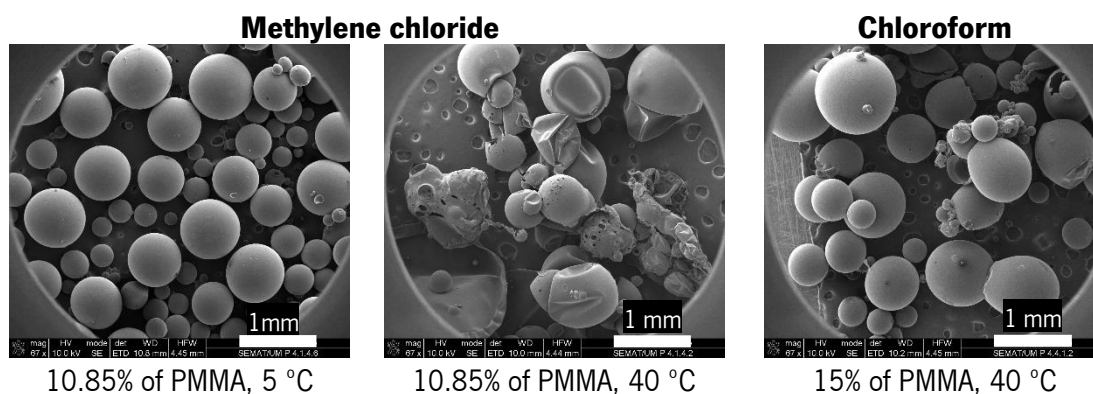
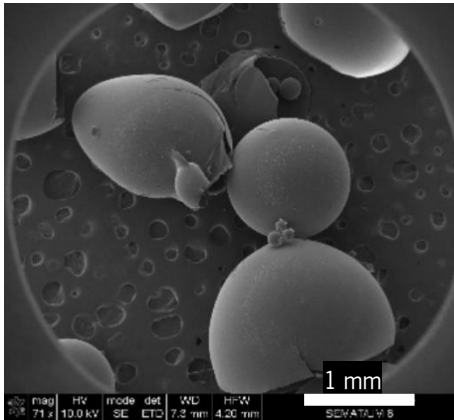


**Figure 38.** SEM micrographs of products from PMMA synthesis using chloroform and methylene chloride as solvents. The double emulsion step took place at 5 °C or 40 °C. The samples were coated with Au before SEM analysis.

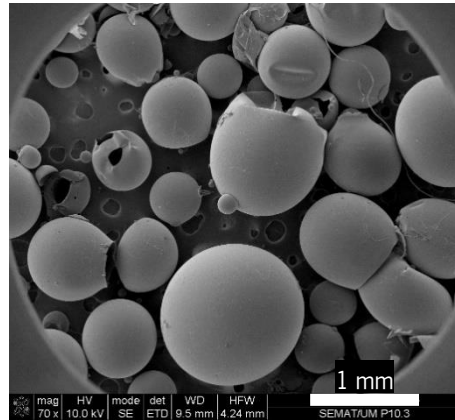
Some combinations resulted in odorless PMMA-MCs and the absence of perfume in the filtrated liquids during the tests. For these reasons, they were analyzed by SEM to see the morphology, wall features and dimensions. **Figure 39** presents the different conditions and the respective images. After observing the SEM images, it is concluded that the absence of perfume and the lack of fragrance is more associated with evaporation than encapsulation. Most of the products have a pellicular geometry that does not correspond to spherical MCs.

The MCs synthesis using PVA 3% and 20% of PMMA did not produce PMMA-MCs. The increment of PMMA content results in considerable increase of PMMA-MCs size, independently of the agitation speed. The size is not an essential factor, so the PMMA mass was decreased and stirred at different speeds with a 3-blade naval or 4-blade helix. However, both results were not satisfactory due to the presence of polymer waste. The PMMA-MCs synthesis using 15% of PMMA, and SDS dissolved in the PVA with the same ratio as the *Sharma et al*/study, decreases the MCs diameters. Also, the helix utilization promotes homogeneous MC sizes, for procedures using 15 or 20% of PMMA, and a continuous phase made of PVA 3% [365].

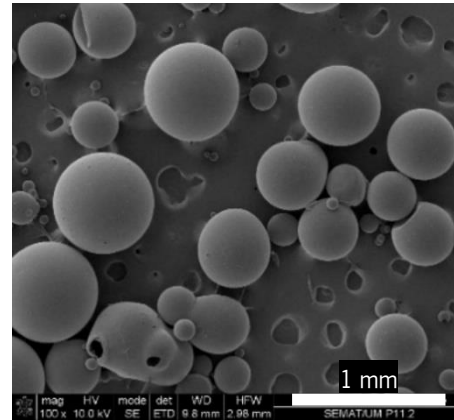
The SDS addition only did the intended purpose, i.e. to decrease the MCs dimensions, using low concentrations of PMMA and a higher viscosity of PVA. By using 20% PMMA and 1% PVA, with the optimized SDS concentration, it results in PMMA-MCs with a diameter of more than 300  $\mu\text{m}$ . So, SDS demonstrate to be the key to the encapsulation and to obtain small PMMA-MCs, when dissolved in high concentrations of PVA. Curiously, the PMMA mass had less influence in the process than the PVA concentration. But the excess of SDS creates more wires (possibly made of PMMA) than PMMA-MCs and, for this purpose, it is not practical.



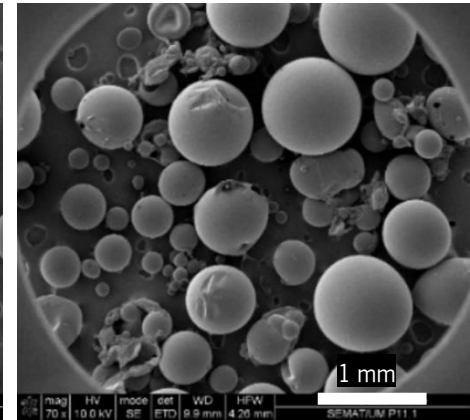
Perfume  
20% PMMA, 3% PVA  
**500 rpm**, Naval



*Eucalyptus Citroedora*  
20% PMMA, 3% PVA  
**1000 rpm**, Naval

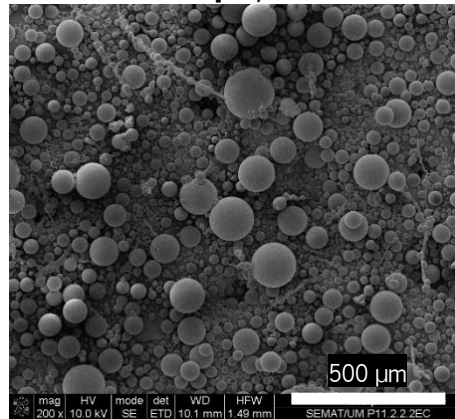


*Eucalyptus Citroedora*  
15% PMMA, 3% PVA  
**1000 rpm**, Helix

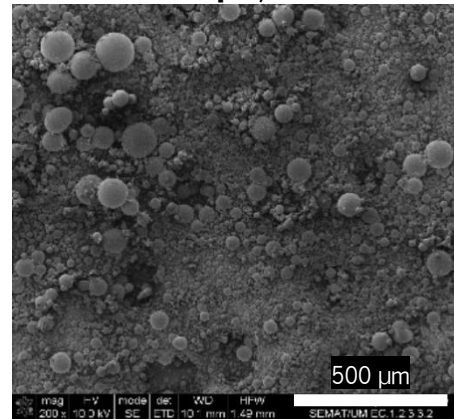


*Eucalyptus Citroedora*  
15% PMMA, 3% PVA  
**700 rpm**, Helix

↑  
**Speed**

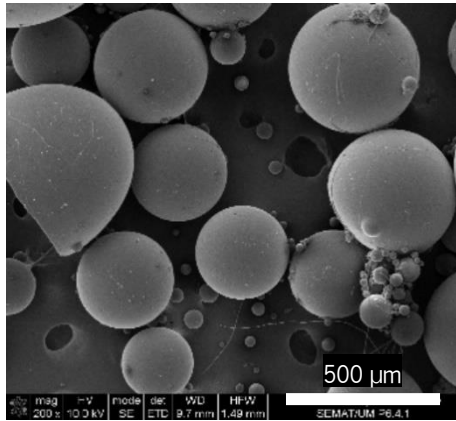


*Eucalyptus Citroedora*  
15% PMMA  
**3% PVA + 6 g SDS**  
**1000 rpm**, Naval



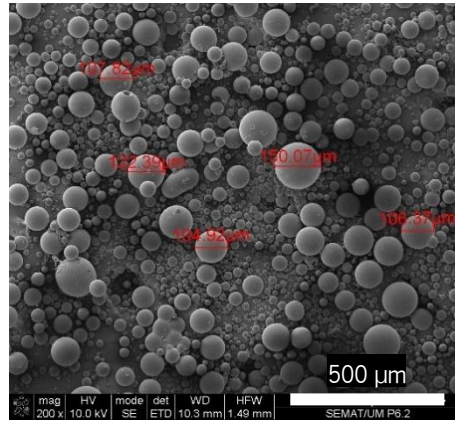
*Eucalyptus Citroedora*  
15% PMMA  
**3% PVA + 6 g SDS**  
**1000 rpm**, Helix

←  
**Speed and impeller**



Perfume

**20% PMMA, 1% PVA + 2.5 g SDS**  
700 rpms, Naval



Perfume

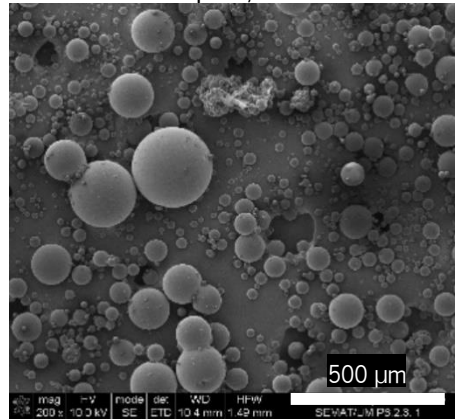
**10% PMMA, 5% PVA + 2.5 g SDS**  
700 rpms, Naval



**PMMA and PVA percentages**

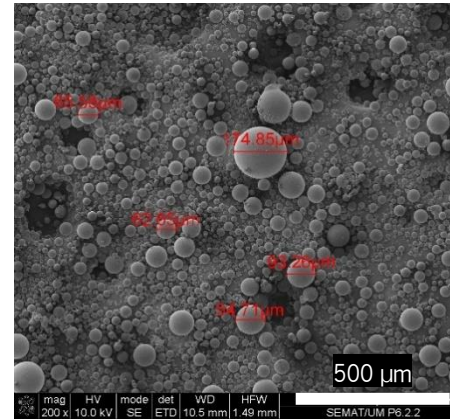


**SDS mass**



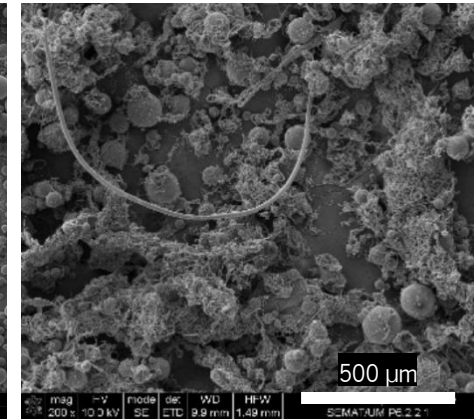
Perfume

**20% PMMA, 5% PVA + 1.25 g SDS**  
500 rpm, Naval



Perfume

**20% PMMA, 5% PVA + 2.5 g SDS**  
500 rpm, Naval



Perfume

**20% PMMA, 5% PVA + 7.5 g SDS**  
500 rpm, Naval

**Figure 39.** SEM micrographs of products from  $O_1/O_2/W$  synthesis to encapsulate a perfume or *Eucalyptus Citrodora*, using several experimental conditions.



The optimized procedures in the MCs are illustrated in **Figure 40**. From the micrographs it was possible to make a histogram with the MCs diameter size distribution by direct measurement of the PMMA-MCs diameter using ImageJ software. The standard deviation is more significant in both situations than the PMMA-MCs mean diameter associated with the process. In this thesis, the solvent evaporation technique was performed at room conditions. So, once the pouring step starts, the solution increases the viscosity because the solvents start to evaporate. Since there is no control of the pressure, the concentration from the beginning is not the same as at the end, resulting in a more viscous oily phase, which will increase the PMMA-MCs size due to the constant shear. Visually it is very difficult to control the process. Also, pipetting or introducing the solution into the continuous phase using a syringe was unsuitable because the solvent is more exposed to the room conditions and evaporates faster. Also, the pipettes and syringes clog very frequently. A suggestion to control the size is to add a pumping system, with a needle, in a controlled environment to avoid unstoppable evaporation in the pouring phase.

Since the PMMA-MCs with 20% of PMMA have a more homogenous size and smaller diameters, they were chosen to be coated with photocatalytic compounds. Most of the studies were made with blank PMMA-MCs, i.e., the PMMA-MCs without UF inside.

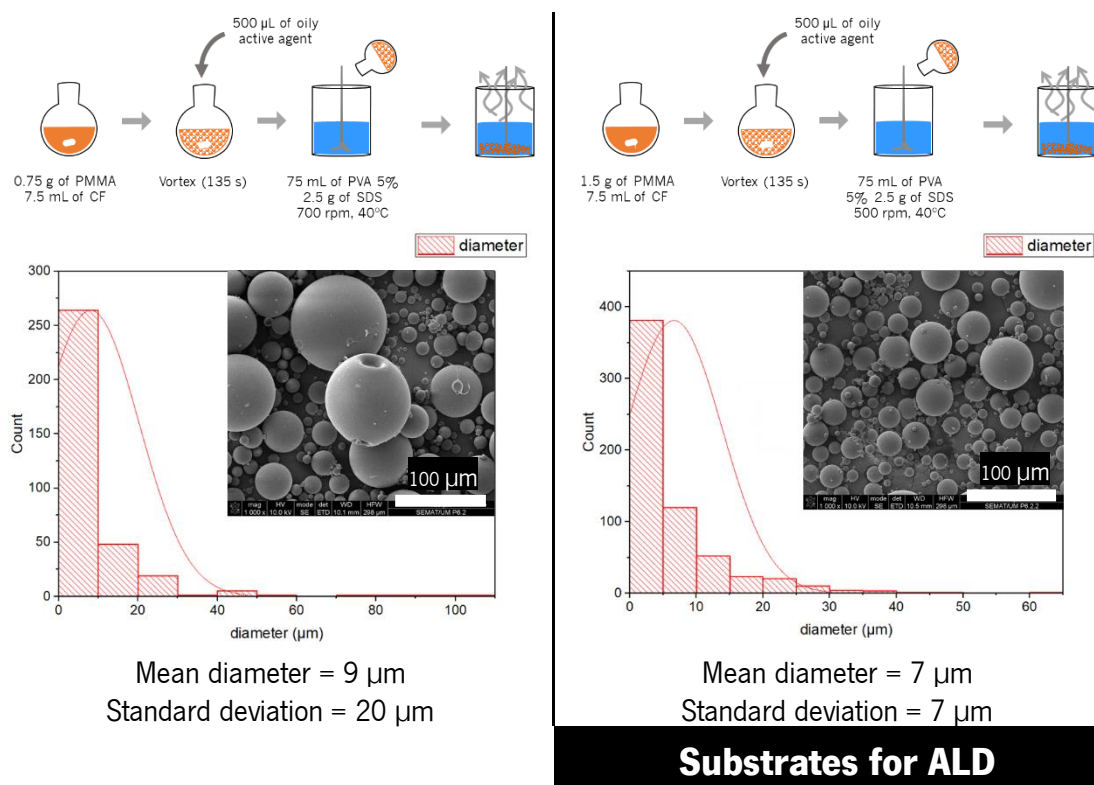


**Figure 40.** Optimized microencapsulation synthesis and PMMA-MCs diameter histograms from the SEM observations. The samples were coated with Au before SEM analysis.

### 3.2.1. Atomic layer deposition onto PMMA-MCs

The purpose of this part was to coat the PMMA-MCs with clusters or islands made from a photocatalytic metal oxide, such as anatase. As previously mentioned, ALD in polymers is a niche in this technological universe. This thesis is focused on ZnO and TiO<sub>2</sub> deposition on PMMA-MCs. The novelty of this work is the use of TTIP as a metallic precursor, because it is less harmful than TiCl<sub>4</sub>, more stable, and the price is notably less. In opposition, the reactivity is lower than in other precursors. This work is also pioneering in a way since the substrates are MCs, substrates with 3D geometry. A significant part of the study was made with the control samples (PMMA-MCs without UF) to understand the ALD process and discard potential UF effects in the deposition.

In PMMA, the main challenge is the low surface reactivity. From the experimental point of view, the polymer surface composition does not have the functional groups that act as nucleation sites to promote growth of the coatings. To this end, it is necessary to introduce a functionalization step on the PMMA surface, prior to the ALD process. There are different approaches for the PMMA functionalization such as atmospheric pressure plasma jet [386,387], plasma [388–392], dipping into a sol of silica nanoparticles [393], NaOH [394], H<sub>2</sub>SO<sub>4</sub>, ethylenediamine [392], LiAlH<sub>4</sub> [395] or HNO<sub>3</sub> solution [396], grafting with di-amino-PEG [397] and oxidation with UV and/or ozone [396,398].

In this line, before the ALD deposition, the PMMA-MCs were exposed to ozone during a period of time (pre-treatment step) in order to provide surface functionalization and to ensure the formation of surface groups from the reaction of ozone with the polymeric substrate.

The ozone pre-treatment step was studied for different furnace temperatures (100 to 175 °C) and the ozone pulse time from 0.125 to 0.5 s. One cycle corresponds to ozone pulse time, residence time and argon purge time (0.125/20/5 s). Then, the samples were collected and observed by a monocular lens. It is visible that for the most extended pulse times at 175 °C, the polymeric MCs melt and agglomerate substantially; some melted parts turn yellowish. Probably, this color is from extreme oxidation or an extreme effect like pyrolysis. As long as the pulse time is getting quicker, the MCs still create agglomerates, but the polymer color is more uniform and similar. When decreasing the furnace temperature, the MCs become less affected by the oxidation parameters. Hence, the O<sub>3</sub>-PMMA-MCs were chosen as the ones that were exposed to 0.125 s of ozone pulse time, at 100 °C, for 100 cycles (**Figure 41**).

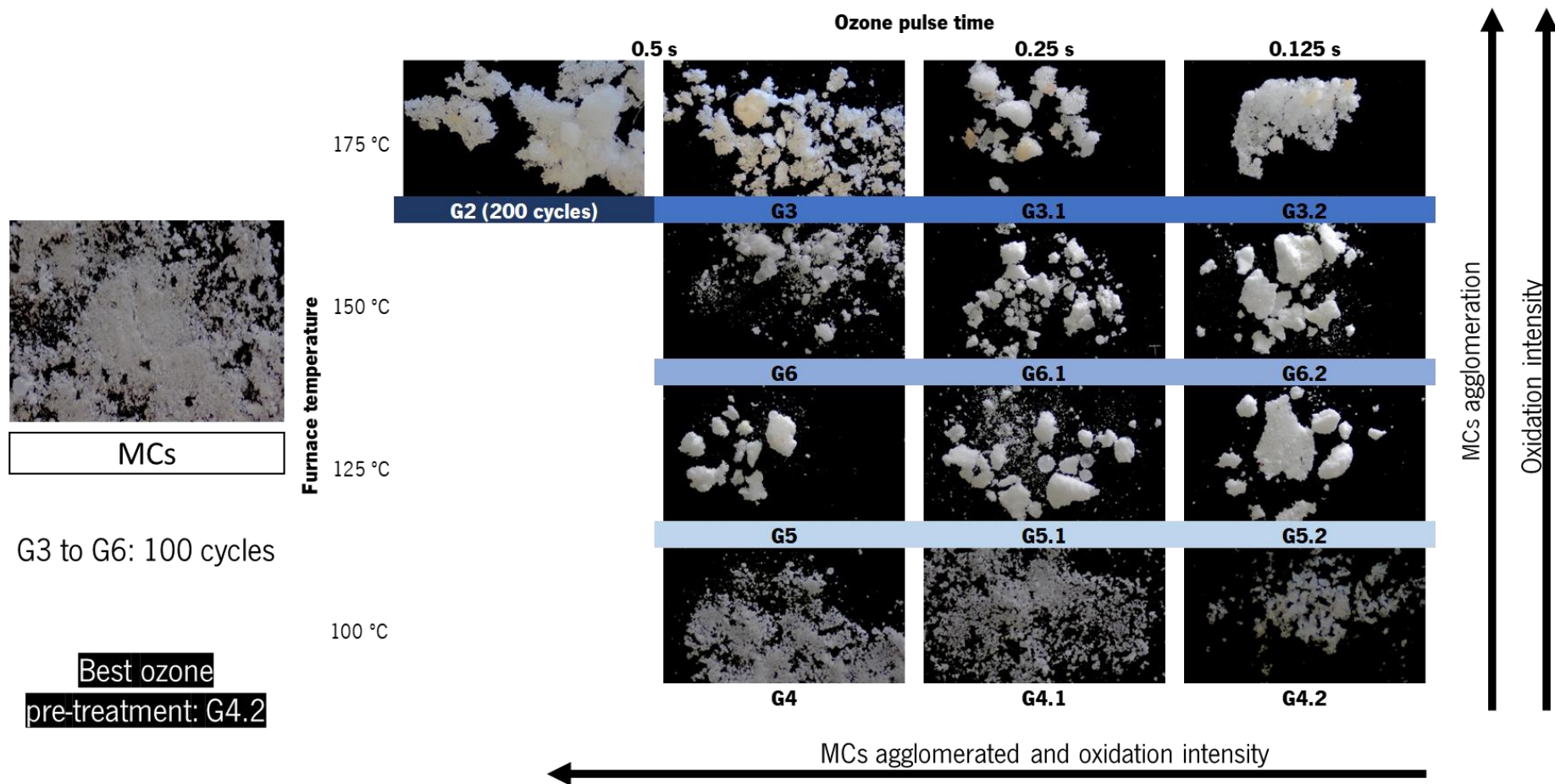


**Figure 41.** Images of pristine PMMA-MCs and PMMA-MCs after ozone pre-treatments organized by temperature and pulse time (G2-G6.2).

Overall, the ozone study asks questions about the PMMA thermal stability. After being established the pre-treatment experimental conditions, the PMMA-MCs were characterized by DSC analysis allowing the determination of the  $T_g$  value. In the first analysis, the PMMA-MCs were heated from 20 to 190 °C, giving a  $T_g$  value of 131 °C. In a second analysis, the sample was heated and cooled by three times (**Figure 42**), giving  $T_g$  values between 105 and 140 °C. The calculated,  $T_g$  average value is thus 114 °C. This confirms that the MCs are not atactic once  $T_{g,MCs} > T_{g,atactic}$ , but the variation in  $T_g$  did not confirm if they are isotactic or syndiotactic. The DSC results allowed the determination of the  $T_g$  value and the understanding of the thermal stability of PMMA-MCs, facilitating the establishment of the ALD deposition temperature without conditioning the thermal integrity of the substrate. In this way the deposition temperature was fixed at 100°C.

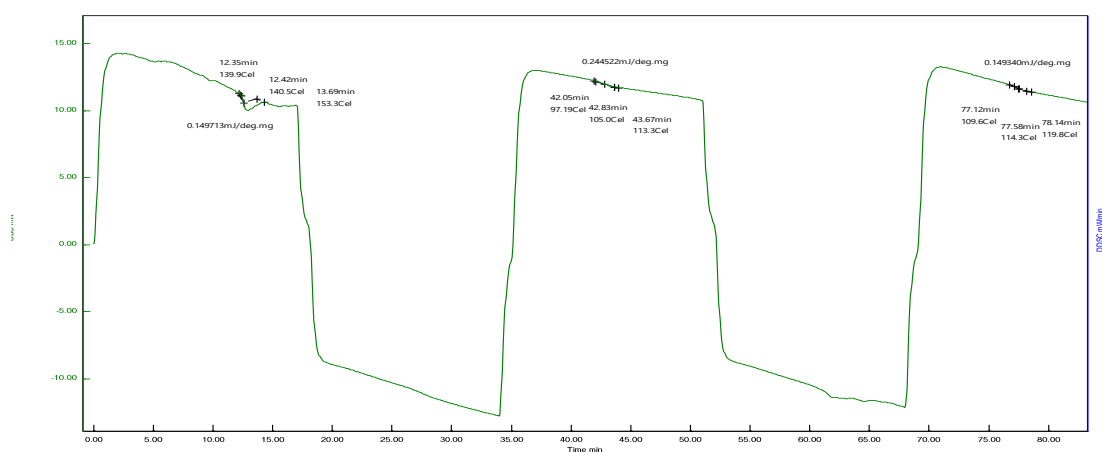


**Figure 42.** PMMA-MCs DSC thermogram with heating and cooling ramps in a  $N_2$  atmosphere.

To confirm the tacticity, a film of PMMA was made by dip coating a glass slide into the polymeric solution. The coated glass was dried in the vertical position into the *hotte* until the solvent evaporated completely. Since the PMMA poorly adhered to the glass substrate, it was possible to remove the PMMA as a free-standing film to be further analyzed by UV-VIS spectroscopy. The absence of absorption peaks in the visible range, attests the PMMA's transparency. In the wavelength range from 200 to 220 nm, the number of peaks is dense, indicating more than one tacticity. The syndiotactic characteristic is confirmed by the presence of a band at 212.8 nm and the isotactic tacticity presents a peak with a maximum at 207.0 nm with shoulders at 211.0 nm and 216.5 nm [385]. It can be concluded that the polymer is predominantly syndiotactic supported by the DSC and UV-Vis results; additionally, the number of peaks in UV-vis spectrum indicates a mixture of different tacticities (**Figure 43**).

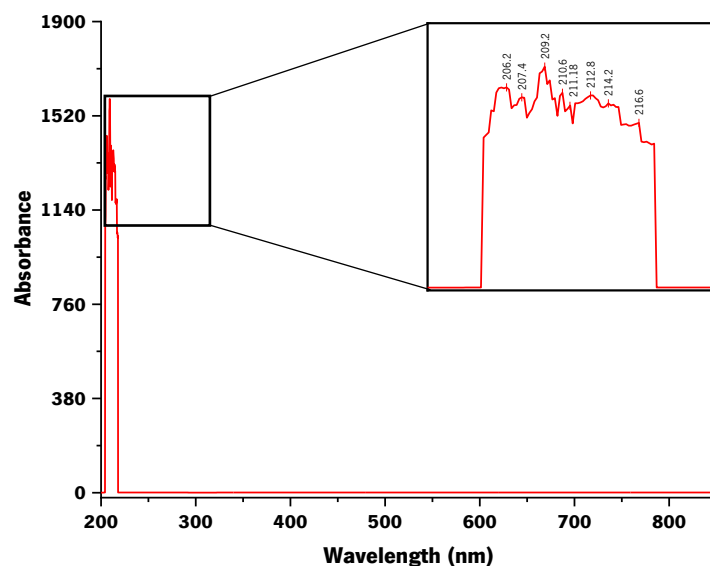


**Figure 43.** UV-VIS spectrum of a PMMA film on a glass slide.

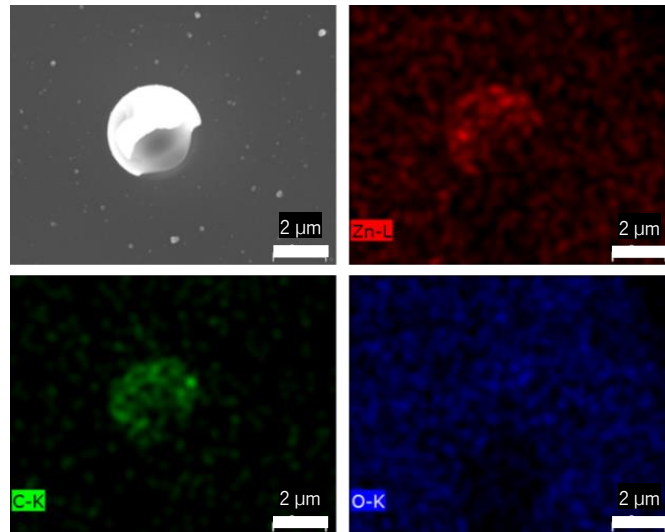
### 3.2.1.1. ZnO coating deposition on PMMA-MCs

Since ZnO ALD is a well-established process even at lower deposition temperatures, the PMMA-MCs were firstly coated with this metal oxide from the reaction of diethyl zinc (DEZ) and water (H<sub>2</sub>O). Usually, the as-prepared ZnO ALD is crystalline (wurtzite) known for its photocatalytic activity [299,300,399]. The PMMA-MCs were pre-treated with 100 cycles of ozone; as previously described, and the ZnO coating was formed by the DEZ and ozone reaction for 400 cycles. Each cycle had a pulse time, residence time, argon purge time for DEZ (0.5/60/15 s) and O<sub>3</sub> (0.04/10/5 s), at 175°C.

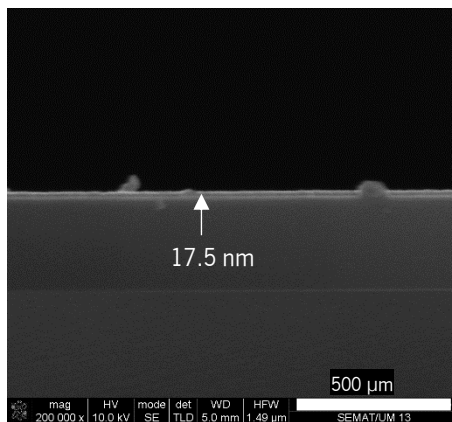
Alternatively, the same procedure was repeated substituting the -OH source (ozone) for water. As water is less reactive than ozone, the mass loss decreased. The cycle was adjusted to (0.5/30/10 s) and (2/30/10 s); the depositions occurred at 100 °C for 400 and 100 cycles. In order to achieve higher resolution EDX spectrums, the PMMA-MCs were suspended into ethanol and pipetted onto a SiO<sub>2</sub>/Si substrate, that was placed into a ceramic boat to be coated by ALD and then analyzed by SEM-EDX (**Figure 44**).

The ZnO coating can be seen as from the brighter contrast on the surface of the PMMA-MCs in the SEM micrographs (**Figure 44** (a)). The EDX map shows the Zn presence confirming that the ALD process can be conformal for PMMA-MCs creating a second shell. **Figure 44** (b1 and 2) also presents the ZnO layer in the silicon wafer. The ratio between the films thickness is 3.99, corresponding to the increment of 100 to 400 ALD cycles. Additionally, the film is granular

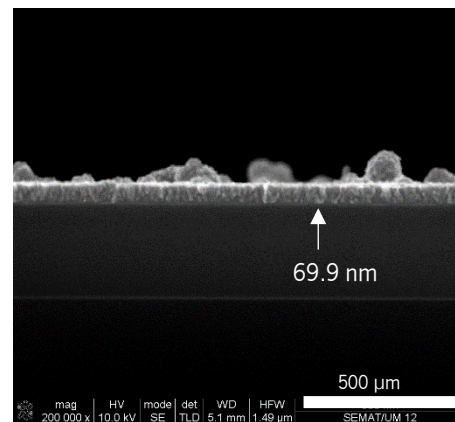
and conformal in both samples, totally covering the silicon wafer surface. Also, the GPC is approximately 0.175 nm/cy without counting the islands present in the structures. This value is coherent with the previous results from the laboratory workgroup [400] and the information collected from **Table 7**. The GPC range is from 0.2 down to 0.0045 nm/cy, for ZnO coatings made from DEZ, placing the results in the top of the table.



(a)



(b1)



(b2)

**Figure 44.** (a) SEM micrographs and correspondent EDX maps of ZnO-O<sub>3</sub>-PMMA-MCs, where red represents the zinc content, green the carbon component, and blue the oxygen contribution. Cross-section SEM micrographs of ZnO-O<sub>3</sub>-SiO<sub>2</sub>-Si with (b1) 100 cycles and (b2) 400 cycles of ZnO deposited by ALD with an ozone pre-treatment of 100 cycles.

The coated samples were placed on a platinum crucible and analyzed by TGA. The analysis was made in a N<sub>2</sub> atmosphere (200 mL/min) with a 10 °C/min heating ramp. This technique

confirmed the ZnO presence observed in SEM-EDX analysis, giving more robustness to the results. In addition, the polymer and the coated PMMA-MCs have similar stability, increasing the resistance compared with the substrate (PMMA-MCs). However, the ZnO-O<sub>3</sub>-PMMA-MCs, never reach the polymer thermal stability.

In **Figure 45**, from the derivative TGA (DTGA) analysis, the bare PMMA-MCs have a mass loss between 100 and 150 °C, which does not happen in the compounds for the synthesis (PMMA, H<sub>2</sub>O, PVA and SDS) and the coated PMMA-MCs. Upon adding a metallic coating there is evidence of a degradation band that appears in the 200-250 °C range.

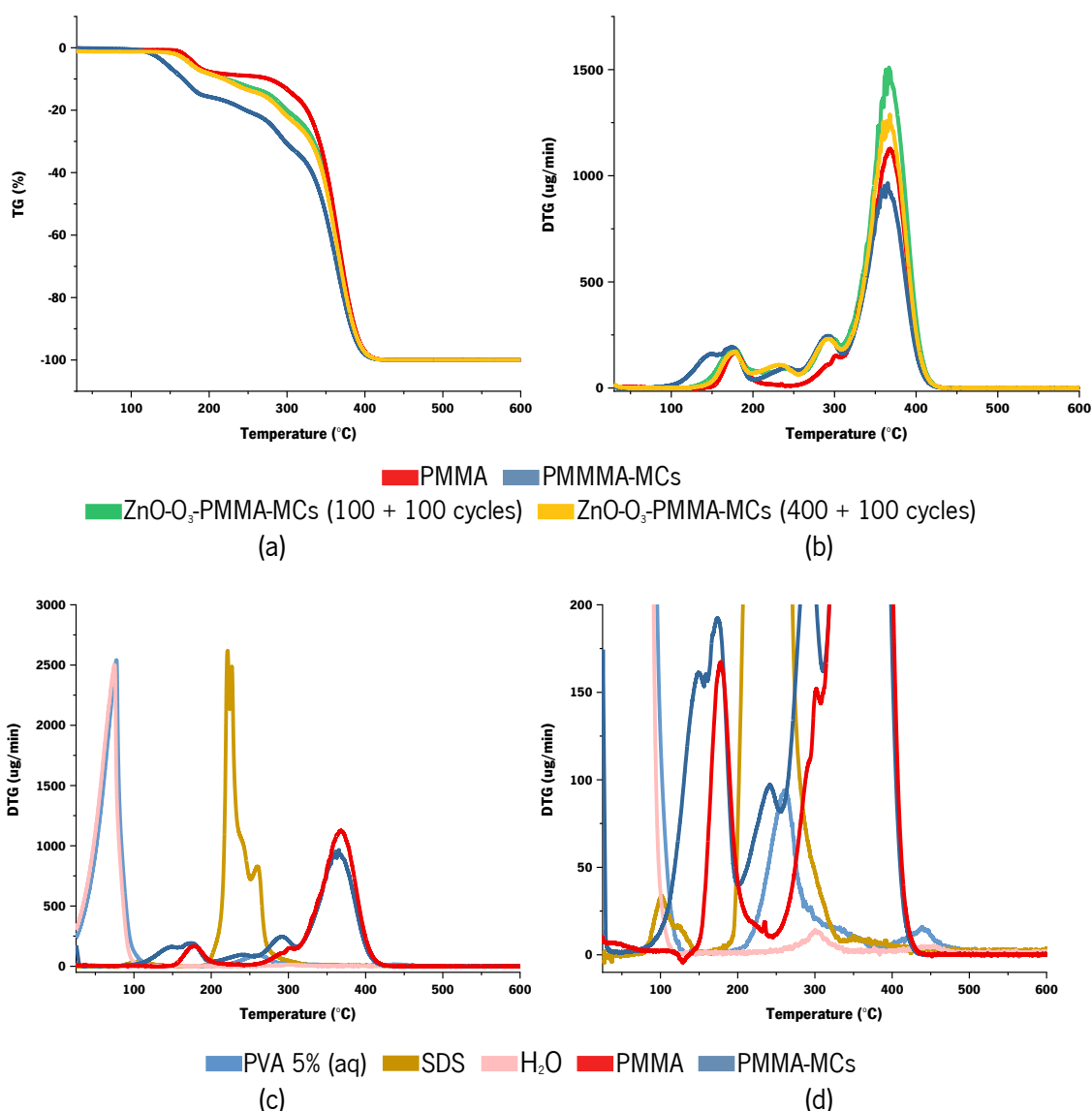


**Figure 45.** (a) percentual TG and DTG (b) from PMMA, uncoated and coated PMMA-MCs, (c) and the respective reactants and product from the PMMA-MCs synthesis (d) amplification of (c) in lowers DTG values.

From Kashiwagi *et al.* [378] and Manring [401] works, they were able to establish the relationship between the number of curves, the polymerization type and the obtained number of peaks in DTGA or steps in TGA that can be associated to the characteristic radical polymerization of the PMMA. The distinct band visualized in **Figure 45** for the PMMA-MCs is associated with the SDS. Once this compound is dissolved in a PVA 5% aqueous solution, the peaks must belong to the continuous outer phase, suggesting an inefficient washing or encapsulation.

The PMMA degradation starts at 178 °C with the breaking of hydrogen bonds from the head-to-head linkages in the oligomers (homolytic scission of methoxycarbonyl side groups). In other words, the depolymerization is initiated. Due to the PMMA molecular weight (400,000 to 500,000) and the continuous phase presence, the peak at 234 °C could be linked to unstable bonds generated in the polymerization and the degradation of PVA and SDS possibly present in the PMMA-MCs. The increment of temperature promotes the breaking of unsaturated vinylidene ends that finishes the depolymerization phase at 300 °C. The final peak is overlapped with the last one and terminates at 400 °C, which is the maximum degradation of the PMMA. This corresponds to the polymer backbone scission, resulting in the PMMA combustion. Formaldehyde, methane, and methanol are the products of the last reaction that posteriorly form CO, CO<sub>2</sub>, H<sub>2</sub>O, and release energy (**Figure 45**).

The coating presence was also observed by the FTIR-ATR technique (**Figure 46**), qualitatively, with a strong band in the fingerprint region, at 500-600 cm<sup>-1</sup>. It can be related to the ZnO coating because it is the only new band, plus the position in the fingerprint region anticipates a change in the material properties. The PMMA and PMMA-MCs spectra are very similar, and the microencapsulation process does not significantly alter the MCs. The extra peak presented in the PMMA-MCs spectrum can be associated with the first peak in the DTGA results. The explanation is that the solvent or PVA is encapsulated or present in the PMMA-MCs wall. This statement is based on such FTIR peak at ≈ 666 cm<sup>-1</sup>, plus the increment of the band maximum intensities, in the range from ≈ 750 cm<sup>-1</sup> to ≈ 1730 cm<sup>-1</sup>. Some of these bands coincide with the chloroform spectrum in the Wiley database [402].

It is worth to note that the solvent has a maximum intensity band at 750 cm<sup>-1</sup>, also linked to the syndiotactic PMMA, but in the ZnO-O<sub>3</sub>-PMMA-MCs this band is smaller. This does not happen with the other bands, indicating that the signal is from the solvent and the polymer. The solvent presence can also justify the first degradation in the PMMA-MCs DTGA analysis. Table 12 identifies the maximum intensities of the bands and suggests the functional groups with the corresponding



interaction when exposed to the radiation.

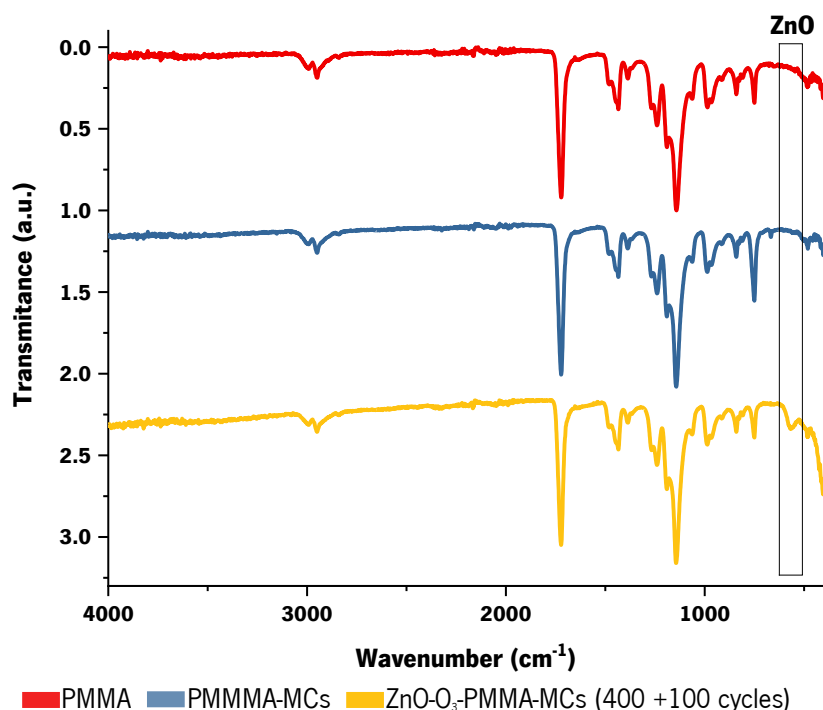


**Figure 46.** FTIR-ATR spectra of PMMA, PMMA-MCs and ZnO-O<sub>3</sub>-PMMA-MCs.

**Table 12.** FTIR-ATR maximum band values and the respective chemical bond and associated vibration.

PMMA	PMMA- MCs	ZnO-O <sub>3</sub> - PMMA- MCs	Vibrations
483		484	C-O-C Bending [403]
		569	Zn-O-Zn stretching frequencies and bending frequency [404,405]
	<b>667</b>		
<b>750</b>	<b>750</b>	<b>750</b>	C-H (-CH <sub>3</sub> ) rocking and skeletal stretching from PMMA syndiotactic [403]
840	840	840	C-O-C stretching [403]
915	915	915	PMMA syndiotactic [406]
966	965	966	C-CH <sub>3</sub> bending [407] α-CH <sub>3</sub> rocking [403]
985	986	987	C-O-C symmetric stretching coupled with CH <sub>3</sub> -O rocking [403]
1062	1062	1062	Intramolecular interactions from PMMA syndiotactic [403,406]
1141	1142	1143	Skeletal stretching coupled with internal C-H deformation vibration [403]
1189	1189	1189	
1240	1239	1240	C-C-O asymmetric stretching coupled with C-O stretching from PMMA
1268	1268	1267	syndiotactic [407-409]
1386	1387	1385	α-CH <sub>3</sub> symmetrical bending [406-408,410]

1434	1434	1433	CH <sub>3</sub> -O symmetrical bending from syndiotactic PMMA [403]
1445	1446	1445	CH <sub>2</sub> bending and symmetrical bending CH <sub>3</sub> -O from isotactic PMMA [403]
1479	1479	1479	α-CH <sub>3</sub> asymmetrical bending [403]
1722	1722	1722	C=O stretching [403,406–408,410–412]
2839	2839	2839	stretching vibration of the C-H [406]
2948	2949	2949	CH <sub>3</sub> -O, α-CH <sub>3</sub> and CH <sub>2</sub> symmetrical stretching [408,409,411,412] and α-CH <sub>3</sub> symmetrical stretching [403]
2991	2992	2992	CH <sub>3</sub> -O and CH <sub>2</sub> asymmetrical stretching [407,409]

The same samples were analyzed by XRD using Cu radiation with  $\lambda = 1.541 \text{ \AA}$ , in a step size of  $0.02^\circ$  (**Figure 47**). The PMMA amorphous character is similar for the PMMA and the PMMA-MCs, proving by a distinct technique that the process does not affect the polymer properties, including the chain orientation. When the PMMA-MCs are coated, the double-shell creates a combined effect from the polymer amorphous state with the ZnO crystalline phase (hexagonal wurtzite). It is necessary to note that the first diffraction peak is suppressed. Some authors identify the amorphous nature at  $2\theta = 9.16^\circ$  and  $42^\circ$  [410] or in the  $10\text{-}30^\circ$  interval [413]. The PMMA PDF card 00-064-1603, for Cu K $_{\alpha}$  radiation, presents diffraction peaks at  $14.215^\circ$ ,  $30.449^\circ$ , and  $42.105^\circ$ ; the diffractograms from PMMA and PMMA-MCs are slightly different in the band intensity but not in their shape.

The d-spacing was calculated from the Bragg's law (Equation 6) for the most intense peak. The values are similar to the d-spacing for the PDF card. Also, from the ChemDraw<sup>®</sup> program, the monomer distance was estimated ( $6.9 \text{ \AA}$ ), matching the previous values. The monomer is equivalent to the unitary crystal cell and makes sense since both are replicated in the structure. From the Scherrer equation (Equation 7), the interchain distance ( $r$ ) and crystallite size ( $P$ ) were calculated. Considering that PMMA does not have crystalline domains, it does not seem logical to have crystallites; the correspondent form is the chain width. The  $r$  and  $P$  values are slightly higher for PMMA than for the PMMA-MCs. Christofferson *et al.* determined the same parameters for different PMMA tacticities [414]. Considering the previous DSC and UV-VIS results and the Christofferson *et al.* work, it is possible to conclude that the studied PMMA has all tacticities as well as a helix shape (**Table 13**).

The ZnO coating provided a different diffractogram in the polymeric part/component. The main diffraction peak ( $\sim 14^\circ$ ) is shifted to lower Bragg angles and presents the lowest  $P$  value. The PMMA-MCs have the highest crystallite size value, possibly from a process that occurred during the synthesis. After the ZnO coating by ALD, the crystallite size value decreases from  $16.7$  to  $6.7 \text{ \AA}$ ; this could be indicative of an efficient pre-treatment that causes polymeric structural

modifications because the interchain value increases slightly due to the presence of the coating.

**Table 13.** XRD results and calculated for PMMA materials.

Sample	[°2 $\theta$ ]	Intensity[cts]	FWHM [°2 $\theta$ ]	d-spacing [Å]	P [Å]	r [Å]
PMMA PDF card	14.22			6.23		
PMMA	13.08	1182.93	4.48	6.77	9.7	8.5
PMMA-MCs	14.15	549.44	4.80	6.25	16.7	7.8
ZnO-O <sub>3</sub> -PMMA-MCs	12.94	976.37	5.37	6.83	6.7	8.5
	36.16	480.01	0.80	2.48		
ZnO PDF card	36.19			2.48		

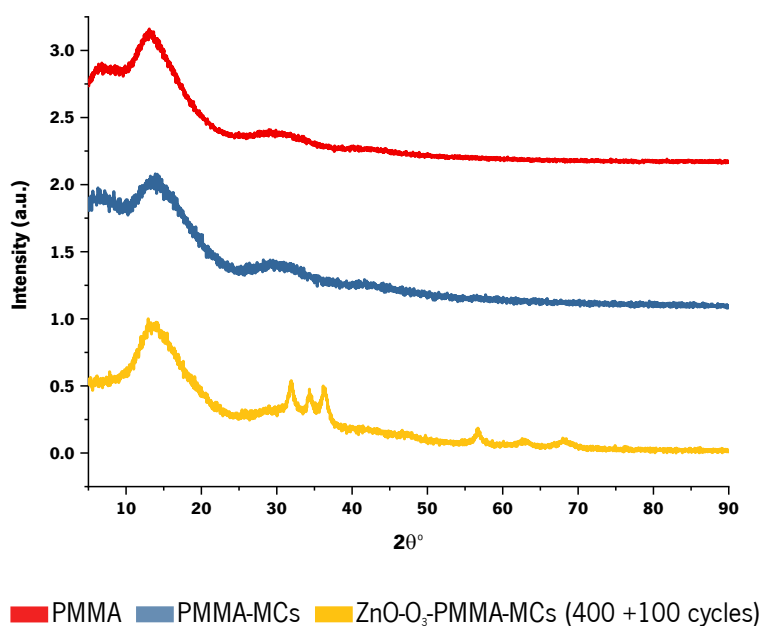


**Figure 47.** X-ray diffractograms from PMMA materials.

### 3.2.1.2. ZnO seed layer deposition on PMMA-MCs

Upon optimizing the growth conditions of ZnO by ALD, this semiconductor worked as a seed layer to promote the TiO<sub>2</sub> growth. Many parameters were tested, such as an increased number of cycles, the TTIP and water pulse, residence and purge times. From all parameters adjusted, emerged a metal-oxide deposition with 400 cycles made of TTIP pulse time, residence time, argon purge time (0.5/20/10 s), and water pulse time, residence time, argon purge time (2/15/10 s), at 100°C. This procedure will be called standard deposition, and throughout the text, the changed variables will be identified.

The 400 ALD cycles of ZnO were used as the seed layer for 200 ALD cycles of TiO<sub>2</sub> (**Figure 48**). Several samples at different deposition temperatures were prepared. SEM micrographs

enabled the measurements of the second and third shells made of ZnO and TiO<sub>2</sub>, respectively. The ZnO seed layer favors the titania growth forming the third shell. The cross-sections present a ZnO granulated film texture, and in opposition, TiO<sub>2</sub> has a smooth film. The thicknesses are almost the same for half of the cycles, which was expected since the DEZ is more reactive than TTIP. Also, the ZnO depositions result in a very similar thickness for each aliquot, meaning that the GPC is almost the same. In TiO<sub>2</sub> deposition, the temperature does significantly affect the GPC value. However, from these three depositions it is necessary to point out that the ZnO protects the PMMA-MCs from the thermal ALD conditions, totally preserving the polymeric material.

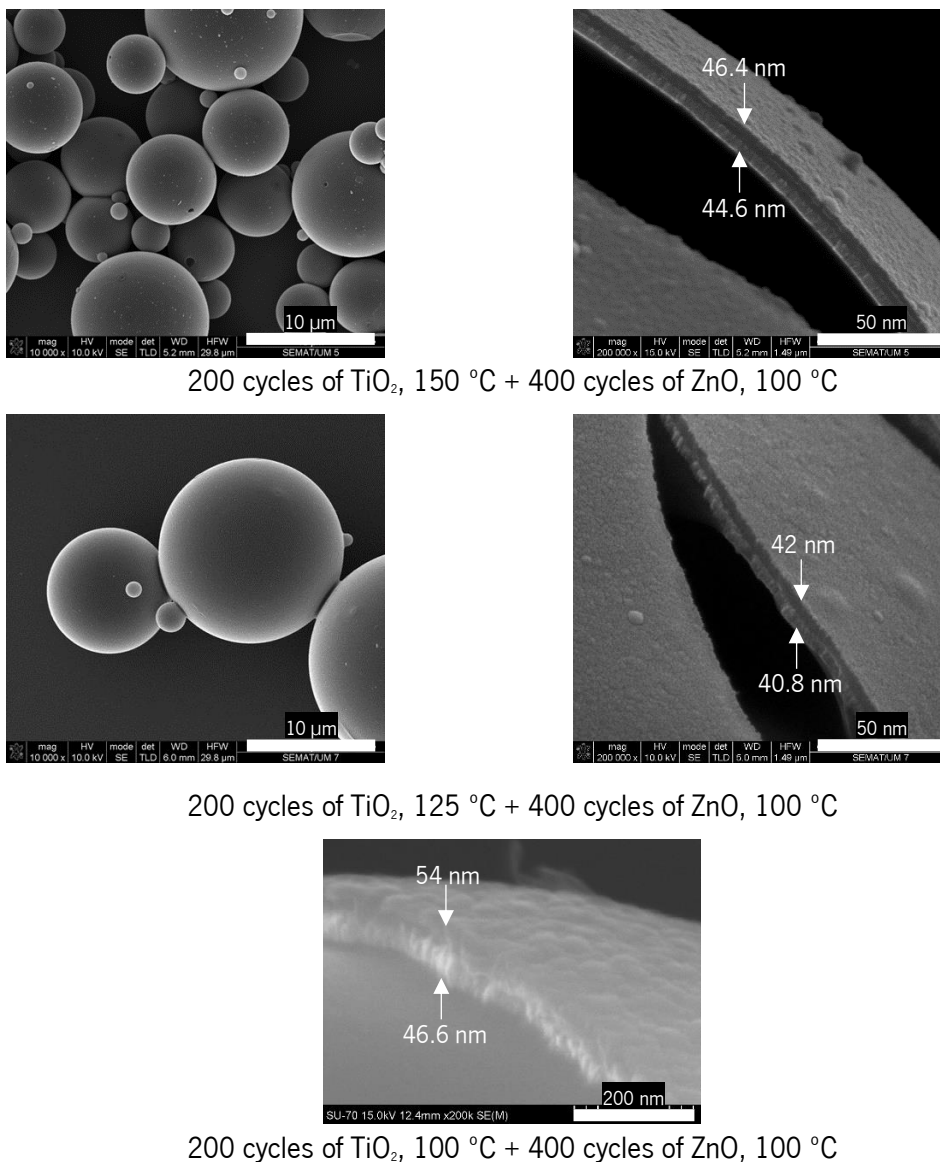


**Figure 48.** SEM micrographs of TiO<sub>2</sub>-O<sub>3</sub>-ZnO-O<sub>3</sub>-PMMA-MCs at different TiO<sub>2</sub> deposition temperatures. The samples were coated with Au/Pd before the SEM analysis.

However, the production of this heterostructured material is very time consuming for several reasons. Firstly, the reactor configuration is for two canisters: one for the metal precursor and the other for water. To produce two metal-oxide coatings it is necessary to do a vast number of batches. After achieving a satisfactory mass weight, it is crucial to remove, clean, and fill the canister with another metal precursor to deposit the second metal-oxide layer. As the precursors are extremely reactive, it is necessary to do it in a controlled atmosphere. The precursor is filled into the canister inside a glovebox. Subsequently, the canister is connected to the reactor, and the coated substrates are again deposited with the second shell. Secondly, since the reactor is tubular, it is not the most suitable for MCs, conditioning the mass utilized per deposition and taking much time to obtain mass for characterization and controlled release analysis. Creating two ALD layers will result in a double mass loss from the first and second deposition.

The seed layer effect was observed in TGA and DTGA analysis (**Figure 49**). For this analysis, the  $\text{TiO}_2$  deposition performed at  $100^\circ\text{C}$  was compared in terms of thermal stability, with and without seed layer. The  $\text{ZnO-O}_3\text{-PMMA-MCs}$  with a thicker ZnO layer are more stable than the PMMA because the degradation is delayed. Having or not a thinner ZnO seed layer gives the same stability, as they almost overlap in the thermogram. However, PMMA has less thermal sensibility than the coated MCs and the PMMA-MCs. The DTGA shows that the degradation from  $\text{TiO}_2$  is in the same temperature window of ZnO. These thermal results are the first evidence that the PMMA-MCs were properly coated with the pre-treatment and subsequently coating with  $\text{TiO}_2$ .

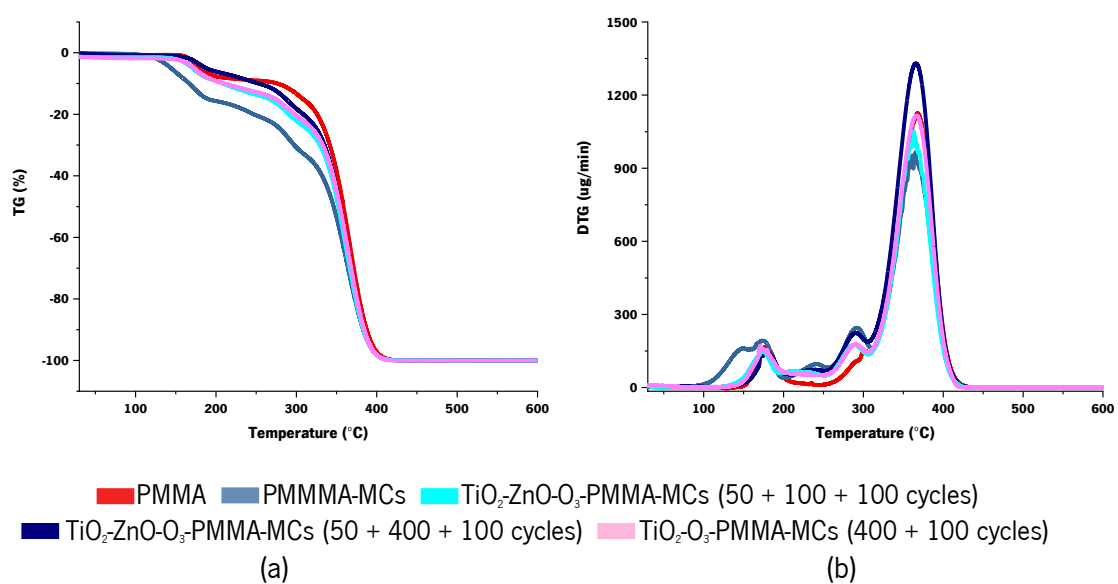


**Figure 49.** Percentual TG (a) and DTG (b) from PMMA, uncoated and coated PMMA-MCs.

### 3.2.1.3. TiO<sub>2</sub> coating deposition on PMMA-MCs

Considering the ALD table review (**Table 7**), the TTIP deposition by low temperature ALD was not explored by others with pre-treatment or using a seed layer. So, the present study continued with the creation of a photocatalytic coating without the ZnO layer. The methodology kept the TiO<sub>2</sub> standard deposition with 400 cycles and increased the ozone exposure time (100 to 200, 400, and 600 O<sub>3</sub> cycles). All samples were analyzed by SEM-EDX to visualize the film thickness and the Ti content. The resulting microcapsules did not have enough stability to enable the measurement of the photocatalytic layer thickness due to the beam energy effect from the SEM-EDX equipment.

**Figure 50** presents the EDX results from the abovementioned samples. Increasing ozone cycles proves to be effective for depositing a semiconductor coating. The TiO<sub>2</sub> layer thickness is emphasized in **Figure 50** (d). The use of 400 TiO<sub>2</sub> cycles + 600 O<sub>3</sub> cycles in the process results in a GPC of 0.23 nm/cy. If 400 TiO<sub>2</sub> ALD cycles were only considered, the GPC is 0.35 nm/cy. However, this value (0.35 nm/cy) is questionable because the variable is the ozonation reaction and not TiO<sub>2</sub>. In conclusion, the GPC is difficult to evaluate.

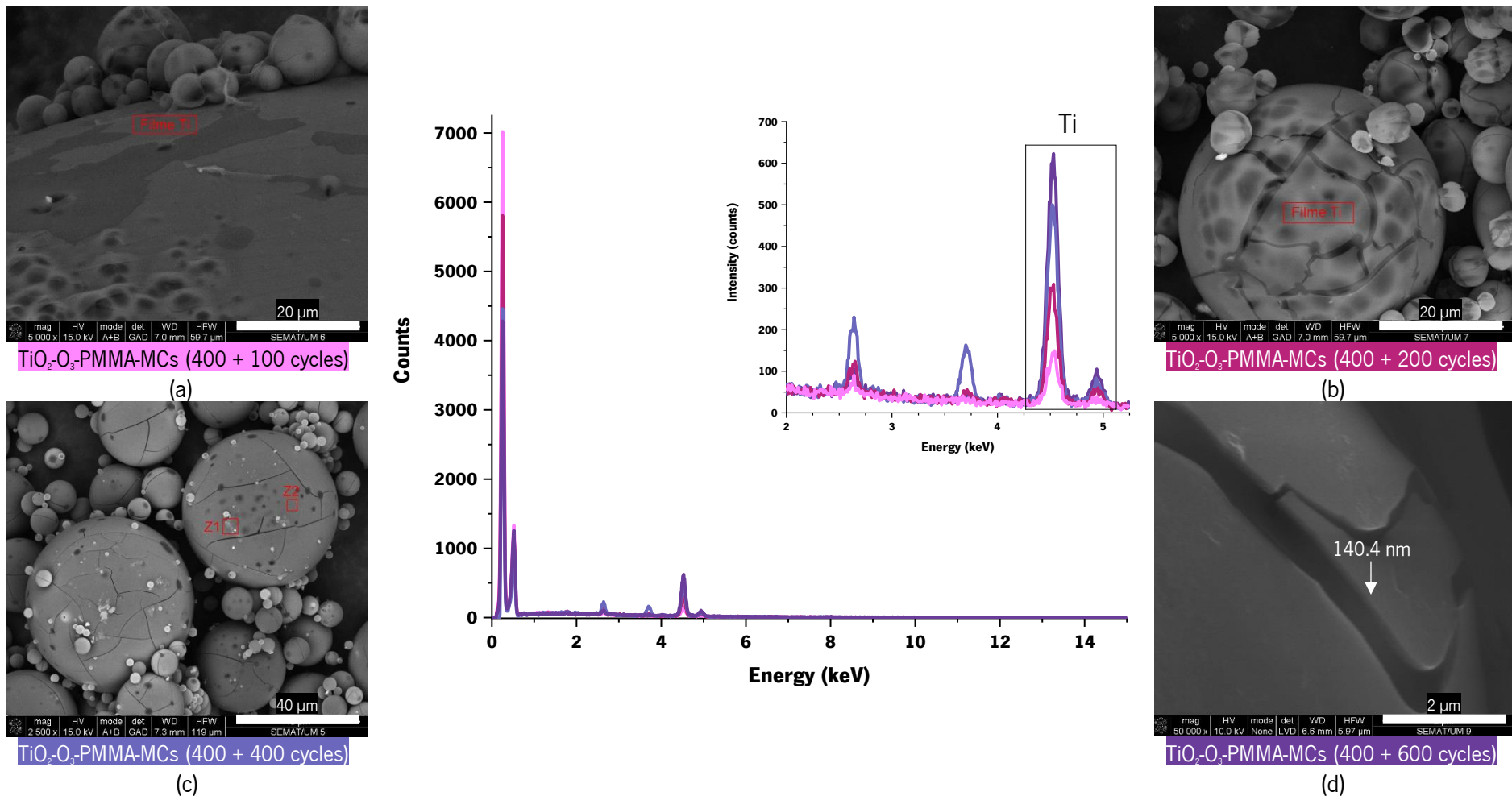


**Figure 50.** SEM images of PMMA-MCs coated by ALD technique with  $\text{TiO}_2$  previously pre-treated with (a) 100 cycles (magenta), (b) 200 cycles (pink), (c) 400 cycles (blue) and (d) 600 cycles (purple) of pre-treatment using  $\text{O}_3$ . In the center the correspondent EDX signals are shown, in order to compare the increasing Ti content. The SEM images were taken after the EDX analysis to measure the coating thickness. All samples were coated with Au/Pd before SEM analysis.

Due to the long time required to produce the sample  $\text{TiO}_2\text{-O}_3\text{-PMMA-MCs}$  (400 + 600 cycles), the oxidation was reduced to 400 cycles. This configuration was selected as the standard  $\text{TiO}_2$  ALD procedure because it can be made in one day. The coated MCs were characterized by techniques like FTIR, XRD, and NMR ( $^1\text{H-NMR}$ ,  $^{13}\text{C-NMR}$ , DEPT 135, HMDB, and HMQB). The resulting film does not have islands and has a smooth texture. The  $\text{TiO}_2$  deposition onto a silicon wafer, resulted in a GPC of 0.20 nm/cy for 400 cycles of oxidation (**Figure 51**). From the information collected in **Table 7**, this GPC is more similar to the  $\text{TiO}_2$  growth when TDMAT or  $\text{TiCl}_4$  are used, instead of TTIP (**Table 14**).

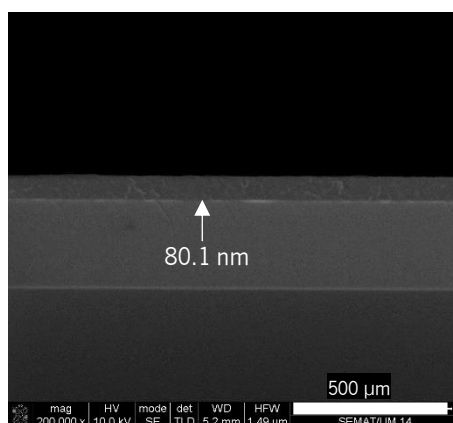


**Figure 51.** Cross-section SEM micrographs of  $\text{TiO}_2\text{-O}_3\text{-SiO}_2\text{-Si}$  with 400 cycles of  $\text{TiO}_2$  deposited by ALD with an ozone pre-treatment of 400 cycles.

**Table 14.** Growth per cycles ranges collected from the **Table 7** of  $\text{TiO}_2$  thin films made by ALD when the Ti precursor is TDMAT,  $\text{TiCl}_4$  or TTIP.

<b>Titanium precursor</b>	<b>GPC interval (nm/cycle)</b>
TDMAT	0.240 to 0.0358
$\text{TiCl}_4$	2.66 to 0.0286
TTIP	0.0100 to 0.0700

The XRD results for PMMA-MCs coated with 100 cycles of ozone pre-treatment do not present a  $\text{TiO}_2$  crystalline structure, which was expected for the ALD employed conditions [297]. For small  $2\theta$  positions, like in ZnO diffractogram, the typical PMMA band is absent, suggesting structural changes in the PMMA-MCs (**Figure 52**). The EDX map and spectrum revealed a peak from Ti contribution. Hence, the pre-treatment showed that it could be an excellent ZnO seed layer substitute in order to deposit the  $\text{TiO}_2$  coating onto PMMA-MCs, using TTIP as precursor.



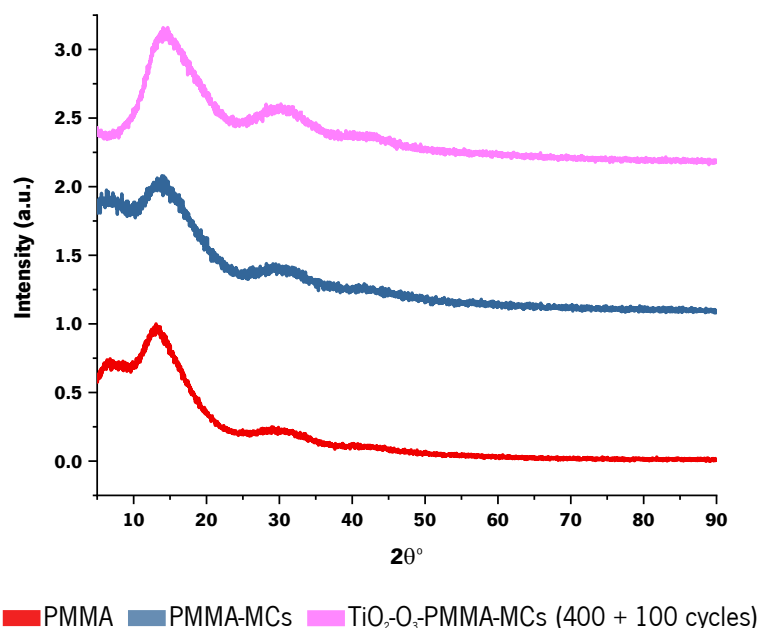


**Figure 52.** X-ray diffractograms for PMMA, PMMA-MCs and TiO<sub>2</sub>-O<sub>3</sub>-PMMA-MCs with 100 cycles of pre-treatment and 400 cycles of TiO<sub>2</sub> deposition.

The metal oxide deposition was compared with the PMMA and their microcapsules by FTIR-ATR analysis. As seen in **Figure 53** and **Figure 54** for the fingerprint region ( $< 550 \text{ cm}^{-1}$ ), the increment of oxidation cycles promotes an increase in the normalized transmittance, possibly from amorphous TiO<sub>2</sub> [415]. The samples with 200 and 400 O<sub>3</sub> cycles + 400 TiO<sub>2</sub> have irregular baselines, like ZnO FTIR-ATR. However, the only pre-treated samples with 100 and 200 O<sub>3</sub> cycles have the same baseline. Moreover, the peak ascribed to the solvent vanishes, and the MCs with longer pre-treatments have a band with a maximum at  $3590 \text{ cm}^{-1}$ , which is frequently associated with the stretching from -OH groups [415], suggesting a more significant effect. Besides, the FTIR-ATR had equal TiO<sub>2</sub> spectra with a band from  $3000$  to  $3600 \text{ cm}^{-1}$  (**Figure 53** and **Figure 54** (a)). **Figure 54** (b)) presents SEM-EDX demonstrating an increase in signal intensity at  $4.5 \text{ keV}$  associated with increased ALD ozone cycles, as a pre-treatment.

The TTIP low reactivity is indirectly perceptible by FTIR-ATR analysis, confirming that, to ensure a coating with TiO<sub>2</sub>, the substrates need to be more exposed to the pre-treatment, at least for 200 O<sub>3</sub> cycles. Nevertheless, with 400 O<sub>3</sub> cycles, the -OH presence is visible at high wavenumbers, suggesting that the oxidation process consists of promoting -OH groups in the polymeric chain. However, it does not precisely identifies where the oxidation occurs. In order to find the specific oxidation reaction between the PMMA and the ozone for the TiO<sub>2</sub> coating, PMMA, PMMA-MCs, oxidized and coated PMMA-MCs were analyzed by NMR.

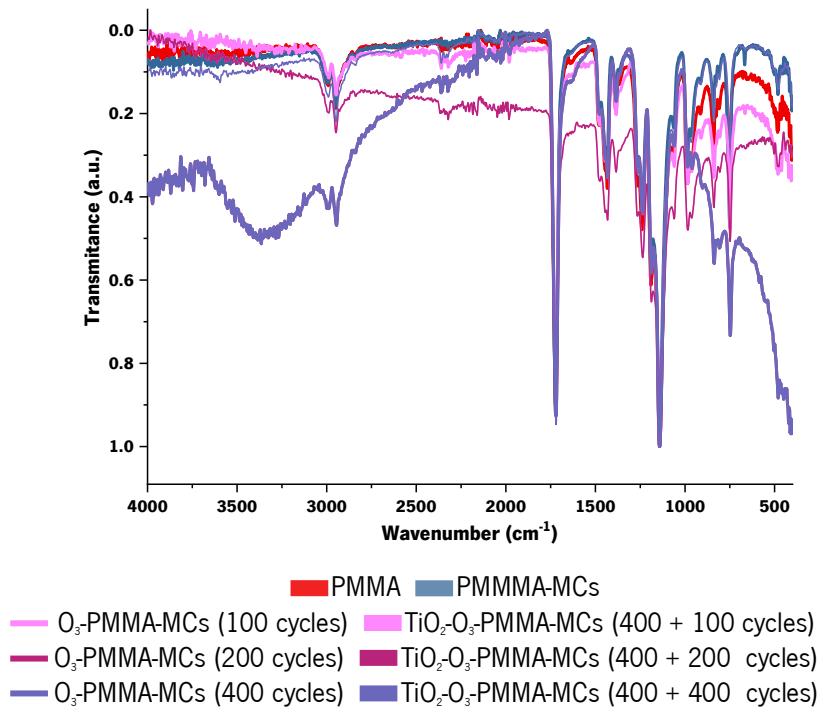


**Figure 53.** FTIR spectrums from the PMMA, PMMA-MCs, oxidized PMMA-MCs, and oxidized plus coated PMMA-MCs.

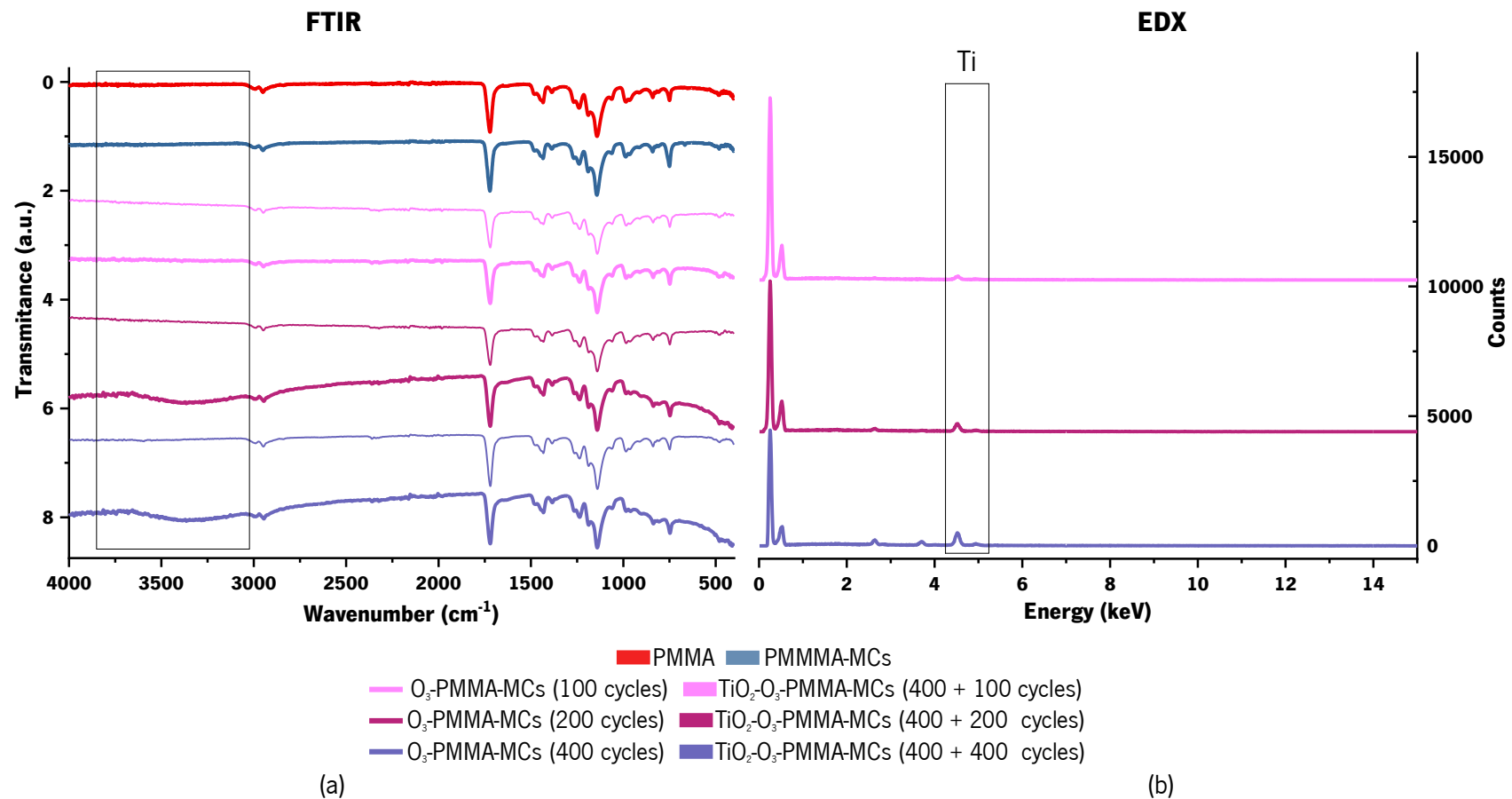


**Figure 54.** (a) FTIR spectrums of PMMA, PMMA-MCs, pre-treated microcapsules (O<sub>3</sub>-PMMA-MCs) with 100, 200 and 400 cycles of ozone by ALD, and the respective coated microcapsules (TiO<sub>2</sub>-O<sub>3</sub>-PMMA-MCs) with 400 cycles of TiO<sub>2</sub> deposited by ALD. The coated microcapsules have side by side the (a) FITR and (b) EDX spectra of the coated PMMA-MCs with TiO<sub>2</sub> to visualize the increment of Ti with the increasing pre-treatment cycles.

The  $^1\text{H-NMR}$  spectra were acquired from a solution containing the samples dissolved into  $\text{CDCl}_3$ . For the bidimensional spectrums (HMBC and HMQC), the samples were more concentrated to obtain better resolution. Unfortunately, the  $\text{TiO}_2\text{-O}_3\text{-PMMA-MCs}$  are partially soluble in the deuterated solvent. Hence, the nanometric  $\text{TiO}_2$  coating created a heterogeneous solution, rendering it impossible to perform NMR. From NMR it was expected to observe a decrease or vanishing of a peak associated to the  $-\text{OH}$  detected in FTIR ( $3000$  to  $3600\text{ cm}^{-1}$ ), in order to confirm the oxidation process and identifying the affected bond.

In **Figure 55**, the signal at  $\delta = 7.3$  ppm is from the solvent  $\text{CDCl}_3$  that was used to dissolve the samples. The PMMA and PMMA-MCs spectra are very similar, and the oxidation is minimal. This result was expected because it relates to surface oxidation, so, the changes are not significant. The signals are the same and are divided into three groups:  $-\text{CH}_3$ ,  $-\text{CH}_2$ , and  $-\text{OCH}_3$ . Since the polymer is a mixture of tacticities, the  $^1\text{H-NMR}$  provides a relative tacticity percentage. All samples have the syndiotactic, atactic, and isotactic forms (**Table 15**). PMMA is predominantly syndiotactic. During the encapsulation, a part of the  $-\text{CH}_3$  in syndiotactic and isotactic form is transformed into atactic PMMA. The pre-treatment promotes more “disorganization” in the chemical structure, resulting in an increment of the atactic form. The same effect is observed in all the oxidized samples, however, the differences between 600 and 800  $\text{O}_3$  cycles are very minor suggesting a saturation point. In the three samples it is plausible to say that there is an oxidation effect. The DMSO was tested as the solvent; in most samples, the spectra detected water was at  $\delta = 1.58$  ppm (**Figure 55** and **Figure 56**).

**Table 15.** Relative tacticities percentage from the protons in the  $-\text{CH}_3$  obtained by  $^1\text{H-NMR}$ .

	<b>Syndiotactic</b>	<b>Atactic</b>	<b>Isotactic</b>
PMMA	59.09	34.02	6.89
PMMA-MCs	56.41	37.33	6.26
$\text{O}_3\text{-PMMA-MCs}$ (400 cycles)	56.38	37.58	6.04
$\text{O}_3\text{-PMMA-MCs}$ (600 cycles)	57.31	38.06	4.64
$\text{O}_3\text{-PMMA-MCs}$ (800 cycles)	57.31	38.28	4.41
$\text{TiO}_2\text{-O}_3\text{-PMMA-MCs}$ (400 + 400 cycles)	55.73	37.23	7.04
<b>Subtraction</b>			
PMMA – PMMA-MCs	2.67	-3.30	0.63
PMMA-MCs – $\text{O}_3\text{-PMMA-MCs}$ (400 cycles)	0.04	-0.26	0.22
PMMA-MCs – $\text{O}_3\text{-PMMA-MCs}$ (600 cycles)	-0.89	-0.73	1.62
PMMA-MCs – $\text{O}_3\text{-PMMA-MCs}$ (800 cycles)	-0.90	-0.95	1.85
PMMA-MCs – $\text{TiO}_2\text{-O}_3\text{-PMMA-MCs}$ (400 + 400 cycles)	0.69	0.10	-0.78
PMMA – $\text{TiO}_2\text{-O}_3\text{-PMMA-MCs}$ (400 + 400 cycles)	3.36	-3.21	-0.15

Signal's identification [375]:

- 0.75-0.90 ppm, 3H, d,  $-\underline{\text{C}}\text{H}_3$  (syndiotactic)
- 1.028 ppm, 3H, s,  $-\underline{\text{C}}\text{H}_3$  (atactic)
- 1.20-1.27 ppm, 3H, m,  $-\underline{\text{C}}\text{H}_3$  (isotactic)
- 1.35-1.49 ppm, 2H, m,  $-\underline{\text{C}}\text{H}_2$ , rmr
- 1.597 ppm, 2H, s,  $\text{H}_2\text{O}$
- 1.82 ppm, 2H, s,  $-\underline{\text{C}}\text{H}_2$ , rrr, (syndiotactic)
- 1.85-1.91 ppm, 2H, m,  $-\underline{\text{C}}\text{H}_2$ , mrr
- 1.91-1.99 ppm, 2H, m,  $-\underline{\text{C}}\text{H}_2$ , rmr
- 2.00-2.10 ppm, 2H, m,  $-\underline{\text{C}}\text{H}_2$ , mmr
- 3.61 ppm, 3H, s,  $-\text{O}\underline{\text{C}}\text{H}_3$

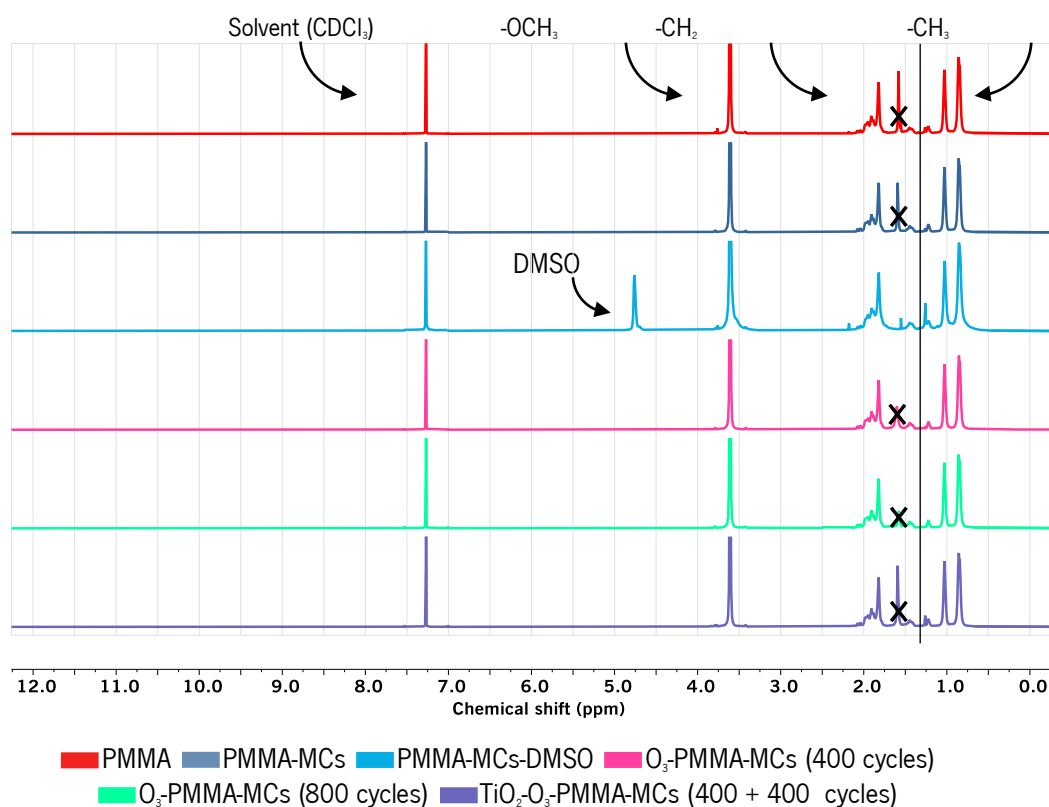


**Figure 55.**  $^1\text{H}$ -NMR spectra for PMMA, PMMA-MCs, PMMA-MCs with DMSO, pre-treated microcapsules (O<sub>3</sub>-PMMA-MCs) with 400 and 800 cycles of ozone by ALD treatment, and coated microcapsules (TiO<sub>2</sub>-O<sub>3</sub>-PMMA-MCs) previously pre-treated with 400 cycles of ozone and further coated with 400 cycles of TiO<sub>2</sub> deposited by ALD. The crossed peak at  $\delta = 1.58$  ppm is a water contamination. All the samples were dissolved into CDCl<sub>3</sub>.

The oxidation effect it is very subtle (**Figure 56**). From  $\delta = 1.20$  to  $1.27$  ppm, the  $-\text{CH}_3$  from the isotactic component has a peak that decreases with the increment of  $\text{O}_3$  ALD cycles. This indicates that this methyl group is affected by the pre-treatment. After the  $\text{TiO}_2$  coating, the same peak drastically increases, being higher than in the pure PMMA. Since it is the only significant and direct detectable change, there is a high probability that these protons are not oxidized to further create a bond with the metal oxide.

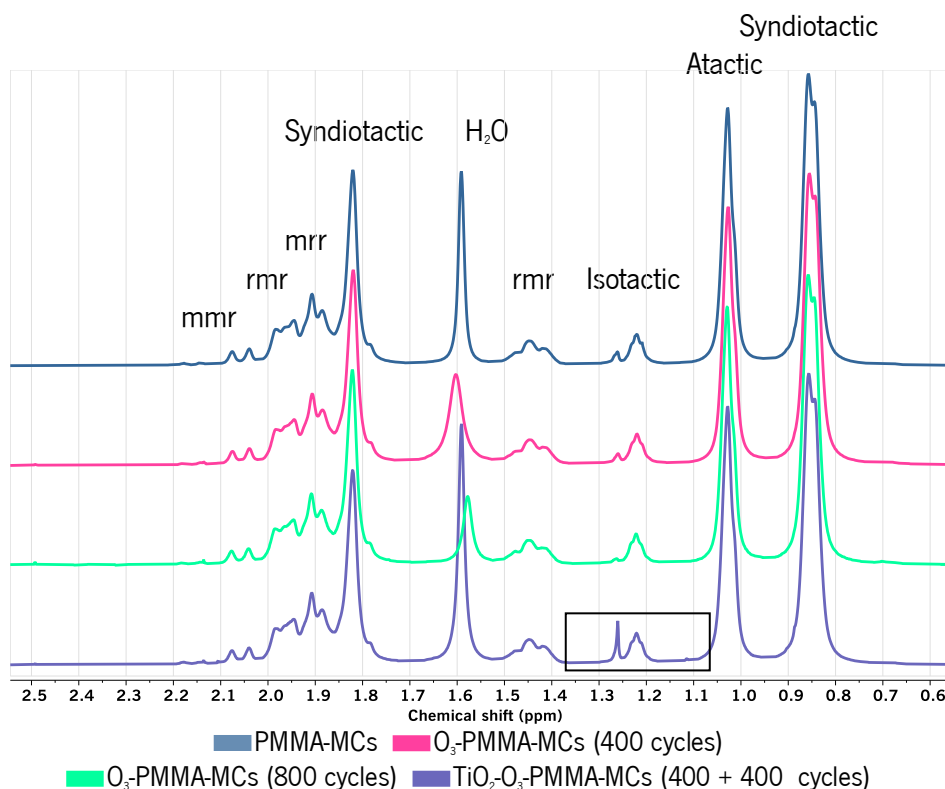


**Figure 56.** Amplified  $^1\text{H-NMR}$  spectra of PMMA-MCs, PMMA-MCs pre-treated microcapsules ( $\text{O}_3$ -PMMA-MCs) with 400 and 800 cycles of ozone by ALD treatment, and coated microcapsules ( $\text{TiO}_2$ - $\text{O}_3$ -PMMA-MCs) previously pre-treated with 400 cycles of ozone and further coated with 400 cycles of  $\text{TiO}_2$  deposited by ALD. All samples were dissolved into  $\text{CDCl}_3$ .

Upon magnifying part of the spectra, new peaks are discerned in the oxidized and coated samples (**Figure ii.1** from Appendix 2). The first one, present after the  $-\text{CH}_2$  peaks ( $\delta = 2.43$  ppm), the zone of  $-\text{OCH}_3$  is also affected by the oxidation, for higher chemical shifts. In this region, the signal was previously classified as a singlet. However, upon close inspection, it is a symmetrical triplet with two smaller peaks at  $2.39$  ppm and  $3.76$  ppm. During the ALD, the triplet is transformed into a multiple, with a narrow and sharp signal at  $\delta = 3.73$  ppm. Also, there are two singlets at  $3.82$

and 3.85 ppm. At  $\delta = 5.73$  ppm, a new peak appears and increases with the pre-treatments and maintained after the coating deposition. There are exceptions that only are present in the  $\text{TiO}_2\text{-O}_3\text{-PMMA-MCs}$  spectra. The peak at 1.08 ppm seems to incorporate the  $-\text{CH}_3$  atactic signal and there is a peak at 5.53 ppm from the coated sample.

Most of the peaks are certainly from the same functional groups ( $-\text{CH}_2$ ,  $-\text{CH}_3$  and  $-\text{OCH}_3$ ) and the slight chemical shifts could be from the presence of the coating. The chemical shifts from the peaks at 5.53 and 5.73 have a strong probability to be from the  $\text{TiO}_2$  thin film. Comparing with the FTIR results, the coating presents  $-\text{OH}$  groups, so these two peaks could be from the film surface (Ti-O-H). However, it is not clear why the signal in FTIR is so pronounced and in the  $^1\text{H-NMR}$  has such a low intensity. Some articles analyze the  $^1\text{H}$  linked to the titanium (Ti-OH) using the magnetic angle spinning mode, which can explain the low intensity [416–418]. Soria *et al.* studied nanocrystalline anatase and found the peaks at 1.1 ppm and 5.5 ppm. At  $\delta = 5.5$  ppm the signal is from strongly adsorbed water that interacts with acid hydroxyls from the coating. Another hypothesis is that region is could be from other  $-\text{OH}$  groups from the polymer that were changed during the ALD process.

In the  $^{13}\text{C-NMR}$  and DEPT 135, the signal at  $\delta = 77$  ppm is from the  $\text{CDCl}_3$  used to dissolve the samples. The spectra are coincident with the references, and new three tacticities are also identified with the same relative amount. The proportion of isotactic form is so low that the correspondent  $-\text{CH}_3$  and  $-\text{C}=\text{O}$  signals do not appear. The  $-\text{OCH}_3$  represents the total carbons, and it is the highest signal in  $^{13}\text{C}$ ,  $^1\text{H}$ , and DEPT 135. Also, the  $\text{PMMA-MCs}$  spectrum is coincident with the  $\text{O}_3$ -oxidized  $\text{PMMA-MCs}$  with 400  $\text{O}_3$  cycles; the only exception is a new signal at  $\delta = 52.995$  ppm and at  $\delta = 178.376$  ppm. Kawamura *et al.* identified by COSY that the first signal is from another mmr triad ( $-\text{CH}_2$ ). The signal from the  $\text{sp}^3$  hybridization is from mrrm pentad ( $-\text{C}=\text{O}$ ). The oxidation seems to only disturb these groups [419].

The DEPT 135 validates those signals from  $\delta = 52\text{-}55$  ppm are from  $-\text{CH}_2$  because they are negative (**Figure 57**). The absence of signals at  $\delta = 176\text{-}178$  ppm proves that it belongs to the carbonyl carbon. The signals from  $\text{PMMA-MCs}$  and  $\text{O}_3$ -oxidized  $\text{PMMA-MCs}$  with 400  $\text{O}_3$  cycles are very similar; the only exception is an unidentified signal that appears at  $\delta = 22.5$  ppm. Possibly, this signal is from the mm  $-\text{CH}_3$  (isotactic). So, the oxidation increases the isotactic form but this is not enough to quantify the signal.

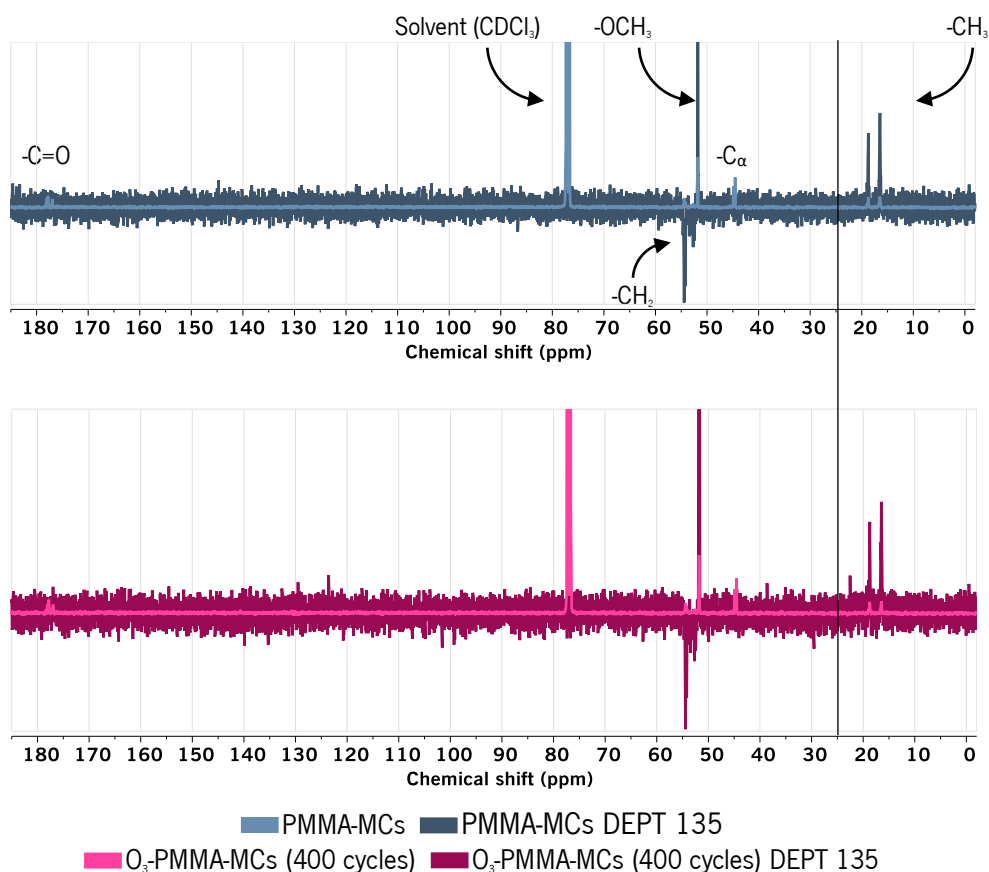


**Figure 57.** amplified  $^{13}\text{C}$ -NMR spectra of PMMA-MCs and PMMA-MCs pre-treated microcapsules ( $\text{O}_3$ -PMMA-MCs) with 400 cycles of ozone by ALD, as well the respective DEPT 135 spectra overlaid in darker colors. All the samples were dissolved into  $\text{CDCl}_3$ .

Signal's identification [419,420]:

- 16.49 ppm, 1C, s,  $\underline{\text{C}}\text{H}_3$ , rr (syndiotactic)
- 18.50-19.00 ppm, 2C, long distance doublet,  $\underline{\text{C}}\text{H}_3$ , rmrr+mmrr and mrmr+rmmr (atactic)
- 44.55 ppm, 1C, s,  $-\underline{\alpha}\text{C}$ , rr (syndiotactic)
- 44.89 ppm, 1C, s,  $-\underline{\alpha}\text{C}$ , mr+rm (atactic)
- 45.5-45.6 ppm, 1C, long distance doublet/m,  $\underline{\alpha}\text{-C}$ , mm (isotactic)
- 51.81 ppm, 1C, s,  $-\underline{\text{O}}\text{CH}_3$
- 52.40-52.8 ppm, 2C, long-distance duplet/m,  $-\underline{\text{C}}\text{H}_2$ , mrr and mmm (isotactic)
- 53.45 ppm, 1C, s,  $-\underline{\text{C}}\text{H}_2$ , mmr (**PMMA-MCs**)/52.9-53.5 ppm, 2C, long distance duplet/m,  $-\underline{\text{C}}\text{H}_2$ , mmr (**O<sub>3</sub>-PMMA-MCs (400 cycles)**)
- 54.10-54.5 ppm, 1C, m,  $-\underline{\text{C}}\text{H}_2$ , rrr (syndiotactic) and rmr
- 176.97 ppm, 1C, s,  $-\underline{\text{C}}=\text{O}$ , mmrr and rmrr



- 177.13 ppm, 1C, s,  $\underline{\text{C}}=\text{O}$ , mrrm and rrrm
- 177.79 ppm, 1C, s,  $\underline{\text{C}}=\text{O}$ , rrr (syndiotactic)
- 178.08 ppm, 1C, s,  $\underline{\text{C}}=\text{O}$ , mrrr and rrrm
- 178,38 ppm, 1C, s,  $\underline{\text{C}}=\text{O}$ , mrrm (**O<sub>3</sub>-PMMA-MCs (400 cycles)**)

HMQC confirms that the protons from each group are correlated with the respective carbons (**Figure 58**). The solvent connects with itself and at higher chemical shifts, while <sup>13</sup>C does not associate with the protons, so it validates that at  $\delta = 170$  ppm the carbon corresponds to the carbonyl group (**Figure ii.2** and **Figure ii.3** from Appendix 2). The opposite effect was observed for the water signal at  $\delta = 1.58$  ppm that correlates with the <sup>13</sup>Cs. The -OCH<sub>3</sub> protons have an intense HMQC signal with the correspondent carbon (-OCH<sub>3</sub>) and the signal seems to interact with almost the other PMMA carbons ( $\underline{\alpha\text{C}}$  and  $\underline{\text{C}}\text{H}_2$ ). Comparing the PMMA-MCs with the O<sub>3</sub>-PMMA-MCs, the results are very similar, and after the oxidation all signals decrease. The group most affected by the pre-treatment are the -CH<sub>2</sub> groups, which it is not quite clear because this group is part of the main chain.

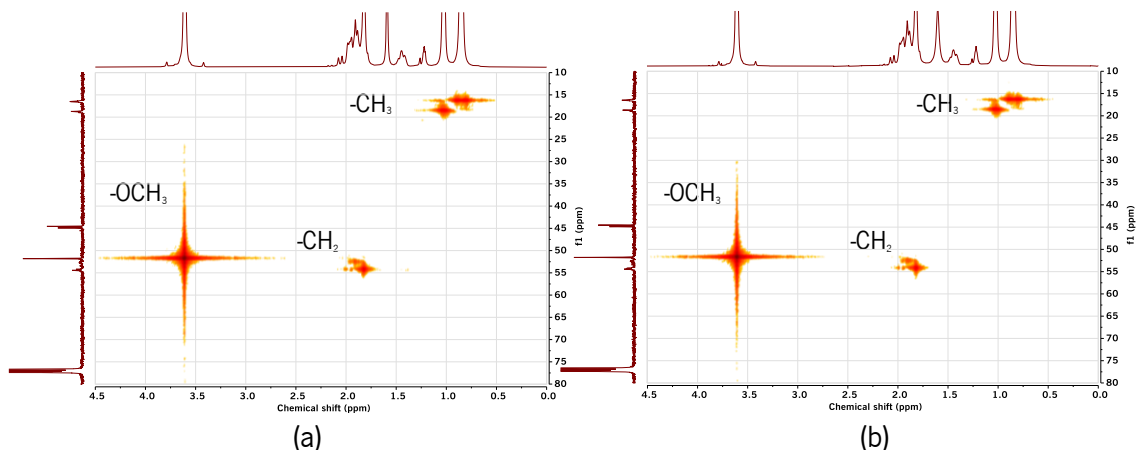


**Figure 58.** Amplified HMQC spectra of (a) PMMA-MCs and (b) O<sub>3</sub>-PMMA-MCs pre-treated with 400 cycles of ozone by ALD.

As a reminder, HMBC identifies longer-range couplings, from 2 to 4 bond coupling. **Table 16** present each <sup>13</sup>C-<sup>1</sup>H correlation in the PMMA-MCs and O<sub>3</sub>-PMMA-MCs, and **Figure 59** identify it using colors in the polymer chemical structure. **Figure ii.4** and **Figure ii.5** from Appendix 2 shows the amplified spectra for both samples and **Table ii.1** presents all the detailed signals obtained from the previous HMBC spectra and the correspondent identification for <sup>13</sup>C and <sup>1</sup>H.

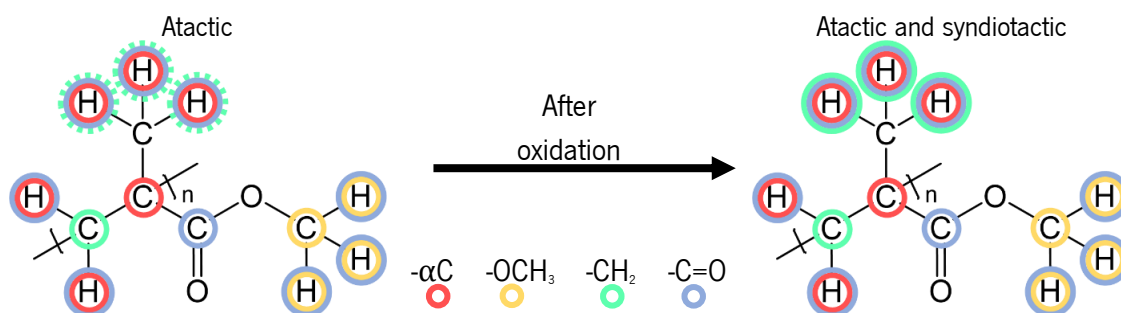


**Figure 59.** HMQC interactions that each carbon has with the protons in the PMMA-MCs before and after oxidation.

In  $^{13}\text{C}$ , the  $-\text{CH}_3$  is only present in the syndiotactic and atactic form. In HMBC, both interact with the methyl and methylene protons from the same tacticities. The pre-treatment does not promote relevant changes in this group. The signal from the quaternary carbon was the most affected by the ALD pre-treatment. This carbon is linked to other groups with protons, so the number of signals is the highest. The isotactic  $^{13}\text{C}$  is correlated with the isotactic and atactic from  $-\text{CH}_2$  and  $-\text{CH}_3$  configurations. The same occurs for the syndiotactic and atactic. The pre-treatment almost vanished the signal. The predominant form is the atactic and there are vestigial signals from the syndiotactic signal; as well, the isotactic  $^{13}\text{C}$  is only related with isotactic protons from the methyl group.

The methylene group from the  $^{13}\text{C}$  signal has a correlation with the syndiotactic and atactic methyl, the signal  $-\text{CH}_2$  is it the only that is correlated with the isotactic methylene. After the ozone ALD cycles, the interaction between  $^{13}\text{C}-^1\text{H}$  is very affected and the methylene carbons only reacts with the protons from atactic and syndiotactic methyl and the syndiotactic methylene. The methoxy carbon only correlates with the methoxy protons because the other are too distant. This signal does not suffer drastic changes after the oxidation. In the PMMA-MCs the carbon from the carbonyl groups correlates with methyl and methoxy groups in an aleatory way. After the oxidation, the  $^{13}\text{C}$  from atactic  $-\text{C}=\text{O}$  correlates with the protons from the atactic methyl, atactic methylene and methoxy groups. In analogy, the  $-\text{C}=\text{O}$  syndiotactic and  $mrrr + rrrm$  signals are correlated with the protons from the syndiotactic groups, as well the methoxy termination (since the singlet does not have tacticity).

Summarizing, the pre-treatment affected all the groups present in the polymeric structure. As seen in Table 15, with the oxidation, the syndiotactic form increases and the others decrease but

there is not a specific group that can be identified. The oxidized MCs have new signals dispersed in the  $sp^2$  region. The isotactic  $-CH_3$ , the  $rmr$ , and  $mrr$   $-CH_2$  have more signals from the correlation with  $C=O$ ; also, it disappears one correlation from protons  $rmr$  in the  $-CH_2$ . The syndiotactic PMMA decreases the correlation with  $-CH_2$ . Comparing these results with the  $TiO_2-O_3$ -PMMA-MCs spectrum, the most affected peak is the  $-CH_2$  from the  $mrr$  triad; consequently,  $-CH_3$  is also influenced.

**Table 16.** HMQC coordinates from chemical shifts associated with carbon and proton NMR, as well as signal identification for PMMA-MCs before and after the oxidation process.

PMMA-MCs				O <sub>3</sub> -PMMA-MCs			
<sup>13</sup> C-NMR	<sup>1</sup> H-NMR	<sup>13</sup> C	<sup>1</sup> H	<sup>13</sup> C-NMR	<sup>1</sup> H-NMR	<sup>13</sup> C	<sup>1</sup> H
δ (ppm)		Signal identification		δ (ppm)		Signal identification	
44.57	0.85	-αC, rr (syndiotactic)	-CH <sub>3</sub> (syndiotactic)	44.57	0.84	-αC, rr (syndiotactic)	-CH <sub>3</sub> (syndiotactic)
44.57	1.82	-αC, rr (syndiotactic)	-CH <sub>2</sub> , rrr (syndiotactic)	44.57	1.81	-αC, rr (syndiotactic)	-CH <sub>2</sub> , rrr (syndiotactic)
44.89	1.03	-αC, mr+rm (atactic)	-CH <sub>3</sub> (atactic)	44.89	1.02	-αC, mr+rm (atactic)	-CH <sub>3</sub> (atactic)
51.83	3.78	-OCH <sub>3</sub>	-OCH <sub>3</sub>	51.83	3.77	-OCH <sub>3</sub>	-OCH <sub>3</sub>
51.83	3.42	-OCH <sub>3</sub>	-OCH <sub>3</sub>	51.83	3.41	-OCH <sub>3</sub>	-OCH <sub>3</sub>
54.43	1.02	-CH <sub>2</sub> , rrr (syndiotactic) and rmr	-CH <sub>3</sub> (atactic)	54.21	0.85	-CH <sub>2</sub> , rrr (syndiotactic) and rmr	-CH <sub>3</sub> (syndiotactic)
54.43	1.02	-CH <sub>2</sub> , rrr (syndiotactic) and rmr	-CH <sub>3</sub> (atactic)	54.43	1.02	-CH <sub>2</sub> , rrr (syndiotactic) and rmr	-CH <sub>3</sub> (atactic)
176.95	1.02	-C=O, mmrr and rmrr	-CH <sub>3</sub> (atactic)	176.95	1.02	-C=O, mmrr and rmrr	-CH <sub>3</sub> (atactic)
177.05	3.60	-C=O, mmrm and rrmr	-OCH <sub>3</sub>	177.05	3.60	-C=O, mmrm and rrmr	-OCH <sub>3</sub>
177.81	3.59	-C=O, rrr (syndiotactic)	-OCH <sub>3</sub>	177.81	3.60	-C=O, rrr (syndiotactic)	-OCH <sub>3</sub>
177.81	1.81	-C=O, rrr (syndiotactic)	-CH <sub>2</sub> , rrr (syndiotactic)	177.81	1.82	-C=O, rrr (syndiotactic)	-CH <sub>2</sub> , rrr (syndiotactic)
177.94	0.85	-C=O, mrrr and rrrm	-CH <sub>3</sub> (syndiotactic)	177.81	0.85	-C=O, mrrr and rrrm	-CH <sub>3</sub> (syndiotactic)
178.14	0.83	C=O, mrrr and rrrm	-CH <sub>3</sub> (syndiotactic)	178.14	0.83	C=O, mrrr and rrrm	-CH <sub>3</sub> (syndiotactic)

### 3.2.2. Atomic layer deposition on PMMA-MCs-UF

In analogy, the PMMA-MCs-UF were coated with ZnO and TiO<sub>2</sub>, and then characterized to understand the effects of adding a coating on the microcapsules with the encapsulated Ultraferro. Since, at visual perception, the PMMA-MCs-UF have a mixture of agrochemical and PMMA in the shell, there was a concern that the ozone could damage the MCs intensely. These substrates were exposed to 100 cycles of ozone followed by 100 or 400 cycles of ZnO ALD deposition and analyzed by scanning electron microscopy. The SEM images confirmed that the ZnO-PMMA-MCs-UF can be coated as well as the control samples. This technique showed that the MCs maintain the spherical configuration and there is evidence of some surface morphological features, possibly from the coating as for 400 cycles the amount is higher and independent of the UF presence (**Figure 60**).

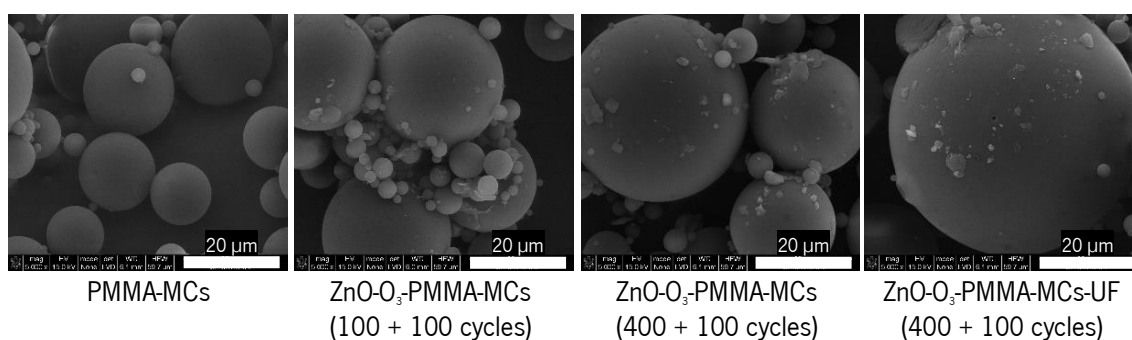


**Figure 60.** SEM micrographs of PMMA-MCs, ZnO-O<sub>3</sub>-PMMA-MCs and ZnO-O<sub>3</sub>-PMMA-MCs-UF, with different cycles, at 100°C. All samples were coated with Au before SEM analysis.

BET analysis was performed to determine the specific surface area and the results are coherent with SEM micrographs because the differences are very imperceptible. The PMMA-MCs have a surface area of 0.734 m<sup>2</sup>/g. After oxidation, this value slightly increases to 0.739 m<sup>2</sup>/g and assures that the oxidation process is at the surface without damaging to the PMMA-MCs structure.

Following this, the PMMA-MCs-UF were coated with TiO<sub>2</sub> by ALD. Due to the low TTIP reactivity, the number of cycles is higher than for the process used for the ZnO deposition. XRD was the characterization technique selected to monitor structural changes in the substrate caused by oxidation in-situ. Some aliquots of PMMA-MCs-UF were exposed to 400 cycles of ozonation, 400 cycles of oxidation followed by 200 cycles of TiO<sub>2</sub> ALD deposition, and 400 cycles of oxidation followed by 400 cycles of TiO<sub>2</sub>. The agrochemical, as supplied, and the PMMA-MCs-UF were also examined by XRD. The diffractogram pattern from the agrochemical is absent after encapsulation.

The UF diffraction pattern is more evident for 200 TiO<sub>2</sub> cycles than for 400 TiO<sub>2</sub> cycles, demonstrating the amorphous character of metal-oxide and burying the UF diffraction signal (**Figure 61**).

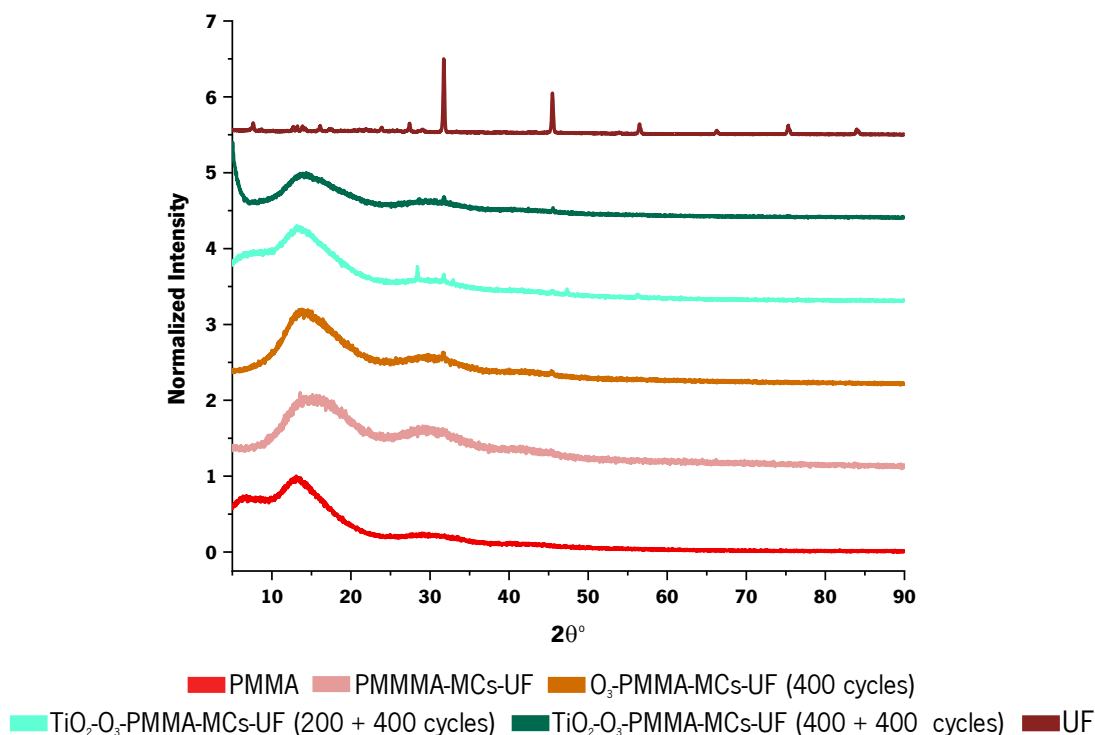


**Figure 61.** X-ray diffractograms from PMMA, PMMA-MCs-UF, the respective pre-treatment (O<sub>3</sub>-PMMA-MCs-UF (400 cycles)) as well as the coatings with varying oxidation cycles for constant the titania cycles, (TiO<sub>2</sub>-O<sub>3</sub>-PMMA-MCs-UF (200 + 400 cycles) and TiO<sub>2</sub>-O<sub>3</sub>-PMMA-MCs-UF (400 + 400 cycles)), plus the core (UF).

From the XRD patterns it is possible to conclude that there is no evidence that the PMMA microcapsules are affected by the ozonation treatment step in the ALD process. So, both samples with 400 cycles of photocatalyst (ZnO-O<sub>3</sub>-PMMA-MCs-UF and TiO<sub>2</sub>-O<sub>3</sub>-PMMA-MCs-UF) were submitted to a SEM-EDX analysis. Additionally, the TiO<sub>2</sub> layer was mapped by EDX to visualize the Fe and Ti content (**Figure 62**) in the PMMA-MCs-UF. EDX maps reveal that the Zn and Ti contribution is significant. At  $\approx 6$  keV there is a signal from the agrochemical in both samples. The TiO<sub>2</sub> EDX maps evidence that the iron and carbon contents are maintained. This procedure was chosen to do the UF controlled release experiments, so a substantial weight of PMMA-MCs and PMM-MCs-UF batches were coated to obtain enough mass for the characterization techniques.



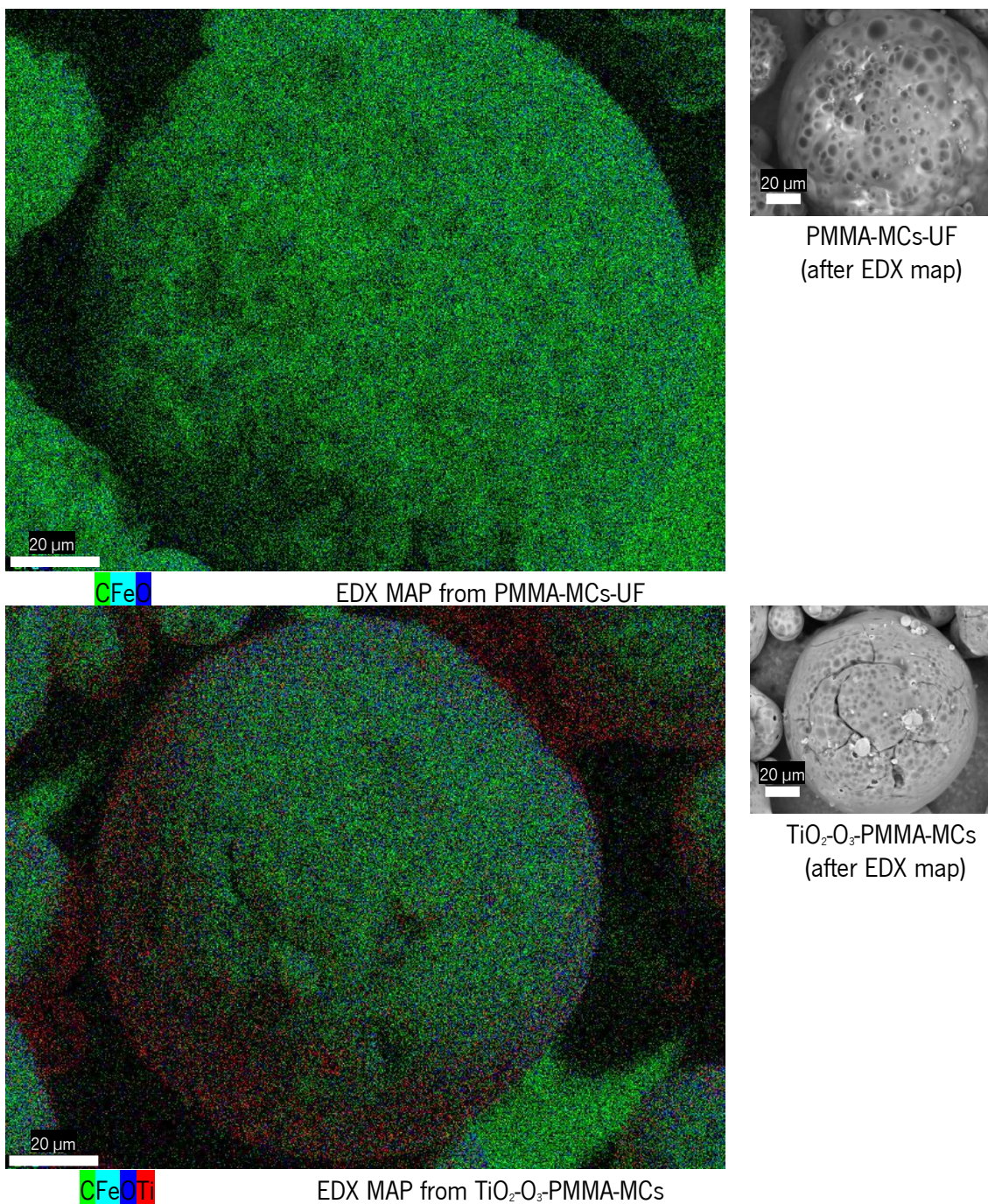


**Figure 62.** SEM micrographs of PMMA-MCs-UF and  $\text{TiO}_2\text{-O}_3\text{-PMMA-MCs-UF}$  as well the EDX map from the oxygen (dark blue dots), iron (light blue dots), carbon (green dots) and titanium (red dots). The images on top were taken after the EDX analysis. The samples were coated with Au/Pd before the SEM-EDX analysis.

Due to the ALD coating on the PMMA-MCs presence, the thermal stability during the SEM analysis was improved. However, for prolonged SEM or EDX acquisition, the coated MCs degrade,

developing pores on their surface (**Figure 62** and **Figure 63**). From the detailed SEM acquisition, the coating starts to crack, and the PMMA-MCs breaks apart. By manipulating the SEM operating conditions, it was possible to open the ZnO-O<sub>3</sub>-PMMA-MCs and posteriorly determine the film thickness on the PMMA-MCs surface. When ZnO was used as seed layer was easy to reproduce the method to measure the film thickness. However, for the TiO<sub>2</sub>, it was very difficult to measure the film thickness.

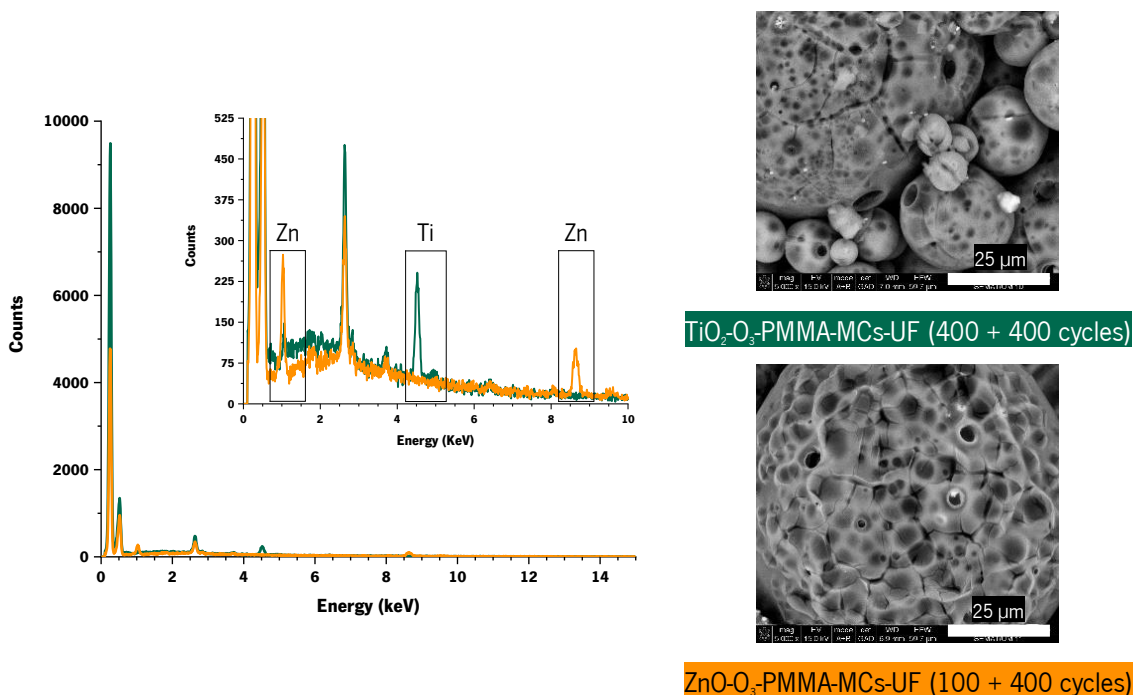


**Figure 63.** EDX spectra of PMMA-MCs-UF pre-treated with ozone and then coated with TiO<sub>2</sub> or ZnO by ALD technique. The samples were coated with Au/Pd before SEM-EDX analysis, the micrographs were acquired after the EDX acquisition.

### 3.2.3. Photocatalytic processes associated with PMMA-MCs-UF and PMMA-MCs

#### 3.2.3.1. Coated PMMA-MCs as photocatalytic substrates

Since PMMA-MCs have a second layer, it would be interesting to investigate whether they function as a support for photocatalysis. Furthermore, there is a standardized method to investigate this type of photocatalysis, based on the study of the degradation rate. The hypothesis is if the metal-oxide coating can react with the environment where it is inserted, degrading it firstly. Thus, ideally, the photocatalyst should degrade the MC shell to liberate the core agent. The samples were



introduced into a  $1 \times 10^{-5}$  M dye solution in the dark for 3h. Subsequently this solution was placed for 6h under UV light to quantify the degradation kinetics. The 3h stay in the dark was the interval time necessary to establish adsorption equilibrium. The control sample was the uncoated PMMA-MCs, placed into the same dye solution. The degradation result was compared with the coated samples. The photocatalytic effect was tested for ZnO-O<sub>3</sub>-PMMA-MCs made from 100 and 400 ZnO ALD cycles; ZnO as seed layer with 400 cycles and the TiO<sub>2</sub> layer synthesized by 50 ALD cycles (TiO<sub>2</sub>-ZnO-O<sub>3</sub>-PMMA-MCs). Finally, the MB degradation was studied with TiO<sub>2</sub> directly deposited in the PMMA shell with the same number of TiO<sub>2</sub> cycles (400) and altering the pre-treatment cycles, from 100 to 600 O<sub>3</sub> cycles, TiO<sub>2</sub>-O<sub>3</sub>-PMMA-MCs (**Figure 64** and **Table 17**).

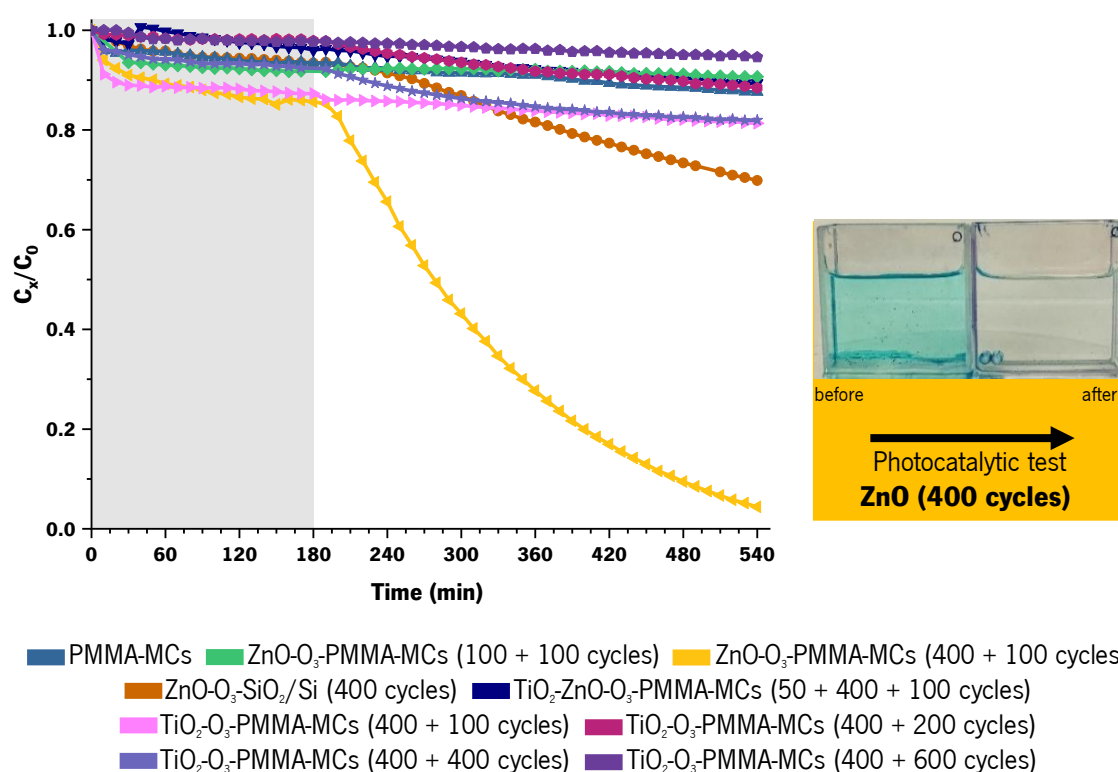


**Figure 64.** Photocatalytic performance of PMMA-MCs and coated samples on degradation of a MB solution with  $1 \times 10^{-5}$  M. The samples were placed 3h in the dark (grey zone in the graph) followed by 6h of UV illumination  $2 \text{ mW/cm}^2$  (white zone in the graph). The image demonstrates the ZnO-O<sub>3</sub>-PMMA-MCs photocatalytic performance showing the MB solution before (left) and after (right) test.

Overall, the main absorption peak is associated with the dye at  $\approx 666 \text{ nm}$  in the dark and decreases substantially when exposed to UV light. As an exception, the PMMA-MCs degrade more

in the dark, indicating that the adsorption mechanisms are more predominant than the degradation. The same effect was noted in the ZnO-O<sub>3</sub>-PMMA-MCs (100 cycles) and TiO<sub>2</sub>-O<sub>3</sub>-PMMA-MCs pre-treated with 100 cycles. From the results presented before, these two samples have low metal oxide content, so the adsorption can occur because the coating is not conformal with the PMMA-MCs sell, which absorbs the dye.

The thicker ZnO coating is the most promising as a photocatalyst for pollutant degradation. After 9h the MB degraded more than 95%, and a considerable part occurred when the UV-LED was ON. A silicon wafer sample with 1x1 cm<sup>2</sup> was coated using the same conditions as the ZnO-O<sub>3</sub>-PMMA-MCs and ZnO-O<sub>3</sub>-SiO<sub>2</sub>/Si. Hereafter, they were tested in the same conditions, and the total MB dye degradation amounted to 30%, which is very promising because the 3D coated substrates gave an excellent result.

**Table 17.** Percentual MB degradation rate after 3h with the LED off (dark), after 6h with the UV-LED on, and the total degradation during the photocatalysis tests.

Sample	Degradation (UV-LED off)	Degradation (UV-LED on)	Total degradation
PMMA-MCs	6,53%	5,83%	12,37%
ZnO-O <sub>3</sub> -PMMA-MCs (100 cycles)	8,16%	1,16%	9,32%
ZnO-O <sub>3</sub> -PMMA-MCs (400 cycles)	14,34%	81,26%	95,60%
ZnO-O <sub>3</sub> -SiO <sub>2</sub> /Si (400 cycles)	6,56%	23,56%	30,12%
TiO <sub>2</sub> -ZnO-O <sub>3</sub> -PMMA-MCs (50 + 400 + 100 cycles)	3,94%	6,66%	10,61%
TiO <sub>2</sub> -O <sub>3</sub> -PMMA-MCs (400 + 100 cycles)	12,70%	5,97%	18,67%
TiO <sub>2</sub> -O <sub>3</sub> -PMMA-MCs (400 + 400 cycles)	2,11%	9,43%	11,54%
<b>TiO<sub>2</sub>-O<sub>3</sub>-PMMA-MCs (400 + 400 cycles)</b>	7,00%	11,04%	18,04%
TiO <sub>2</sub> -O <sub>3</sub> -PMMA-MCs (400 + 600 cycles)	2,32%	3,08%	5,41%

Standard method to coat the PMMA-MCs-UF and characterize by TXRF and TGA before and do the photocatalytic studies

The sample with the two metal-oxides was synthesized to create a combined effect in photocatalysis, hermetically closed for improving the results. The equal thickness of ZnO was used as a seed layer, then 50 TiO<sub>2</sub> ALD cycles were the second coating. Since the number of TiO<sub>2</sub> cycles was short, there were more possibilities to create TiO<sub>2</sub> islands, instead of a uniform conformal coating. However, the results did not improve in both phases, meaning that the ALD TiO<sub>2</sub> amorphous nature negatively contributes to photocatalysis. A similar effect was observed in the titania direct deposition. The total MB dye degradation range is comprised between 5 to 19%, after 9h of UV illumination. Curiously, the sample with an intense pre-treatment is the one with the worst

degradation efficiency, and there is no linear behavior that can be correlated with the oxidation increase. It is necessary to highlight that the samples with 200 and 600 oxidation ALD cycles have a better performance when compared to the control sample.

In conclusion, the photocatalytic assays suggest that no matter the film dimensions, the crystallographic nature is more dominant to contribute to photocatalysis activity. That is why the wurtzite ZnO demonstrates a high photocatalytic activity when compared to the samples coated with amorphous TiO<sub>2</sub>. In order to improve the TiO<sub>2</sub> ALD deposition to enhance the film crystallinity, a higher temperature is required. However, this would inevitably lead to PMMA-MCs degradation. Due to the agrochemical application, the UF release must be slow. Besides the great result from the ZnO-O<sub>3</sub>-PMMA-MCs with 400 ZnO ALD cycles, the sample selected to do the controlled release tests was the TiO<sub>2</sub>-O<sub>3</sub>-PMMA-MCs with 400 pre-treatment cycles and 400 TiO<sub>2</sub> ALD cycles. This one was chosen because it demonstrates the capacity to degrade the MB in the dark and when irradiated. From the practical perspective, it can indicate that the controlled release could happen when the coated PMMA-MCs-UF are not directly exposed to the UV light or sunlight, which can often occur due to the weather conditions.

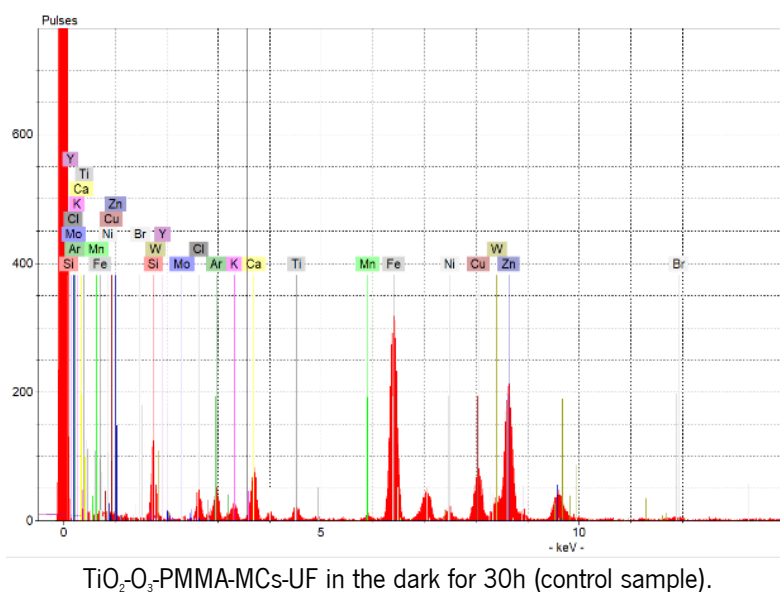
### **3.2.3.2. Controlled release onto coated PMMA-MCs-UF**

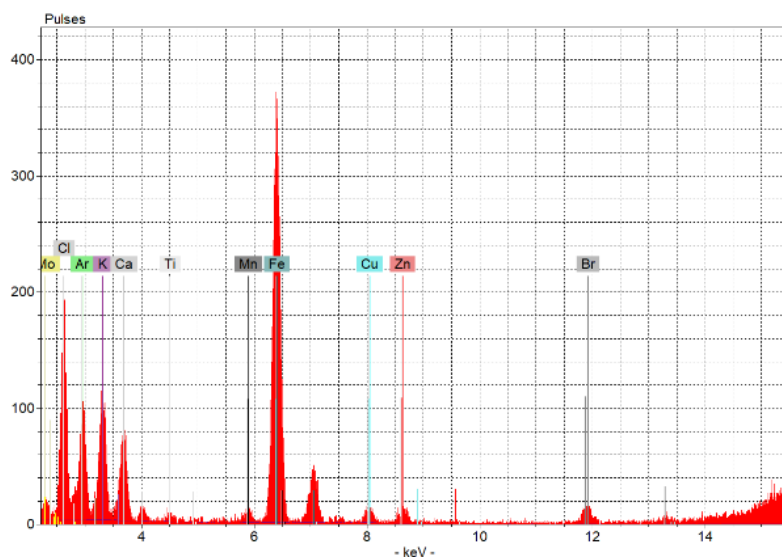
Before initiating the controlled release experiments, the UF stability was confirmed in the dark, ambient conditions covered and uncovered, and exposed to UV radiation. The UF have two absorption bands coincident with the bibliography at 280 and 480 nm in all environments. As long as it is exposed to UV radiation and to the Xenon lamp (UV + visible radiation), the UV-VIS spectrum displays a third band at a lower wavelength (250 nm), and the principal band decreases the absorbance intensity. The UV-VIS modification is related to the UF susceptibility to the deferration process, reducing the Fe<sup>+3</sup> to Fe<sup>+2</sup> [381]. After realizing the UF behavior in the experimental conditions, a controlled release study was endured using the PMMA-MCs-UF, the TiO<sub>2</sub>-O<sub>3</sub>-PMMA-MCs-UF (400 + 400 cycles) with and without the Xenon lamp.

The results are difficult to understand because the UF signal appears in all absorption measurements. Since the signal is not constant, it is impossible to exclude the MCs contribution (as background) from the measurements. Likewise, the PMMA is transparent, so it does not mask the encapsulated UF. Also, by doing a different aliquot for each irradiation step time and filtrate the samples, it was not representative for two reasons: (1) doing a different aliquot requires that the PMMA-MCs-UF used are always different. So, the UF concentration changes randomly in each

sample, meaning that it is difficult to see linearity in the process because the error is higher than the respective UF concentration. (2) Usually, heterogeneous solutions constituted by an aqueous phase and a solid phase are separated employing methods like filtration, centrifugation, decantation, or sedimentation. Filtration is not possible because the paper filter retains the UF. Centrifugation can collapse the PMMA-MCs-UF and the UF in the wall can be released, so the UF concentration is not fully associated with controlled release. Also, the decantation is difficult to ensure when the PMMA-MCs-UF are micrometric and heterogeneous. Finally, the sedimentation cannot be implemented because the process needs agitation in order to homogeneously aerate the solution and further trigger the photocatalysis.

In general, the UF is always released, whether or not a Xenon lamp is used. The first idea was to associate the signal to the  $\text{TiO}_2\text{-O}_3\text{-PMMA-MCs-UF}$  present in the removed volume. Excluding this, it was decided to carry out a TXRF and TGA analysis to verify if the UF is in an aqueous solution (or not), for the irradiated samples and the unexposed to ultraviolet light for 30 hours. These methods were selected because a small volume is required and therefore the probability of collecting  $\text{TiO}_2\text{-O}_3\text{-PMMA-MCs-UF}$  is lower. In TXRF, UF was detected above the detection limit in both samples (irradiated and non-irradiated). Thus, it seems that the  $\text{TiO}_2$  obtained under these conditions as a controlled release system by photocatalysis is limited by its very nature (amorphous), restricting this action. In this case, the photocatalytic activity is decreased. **(Figure 65).**

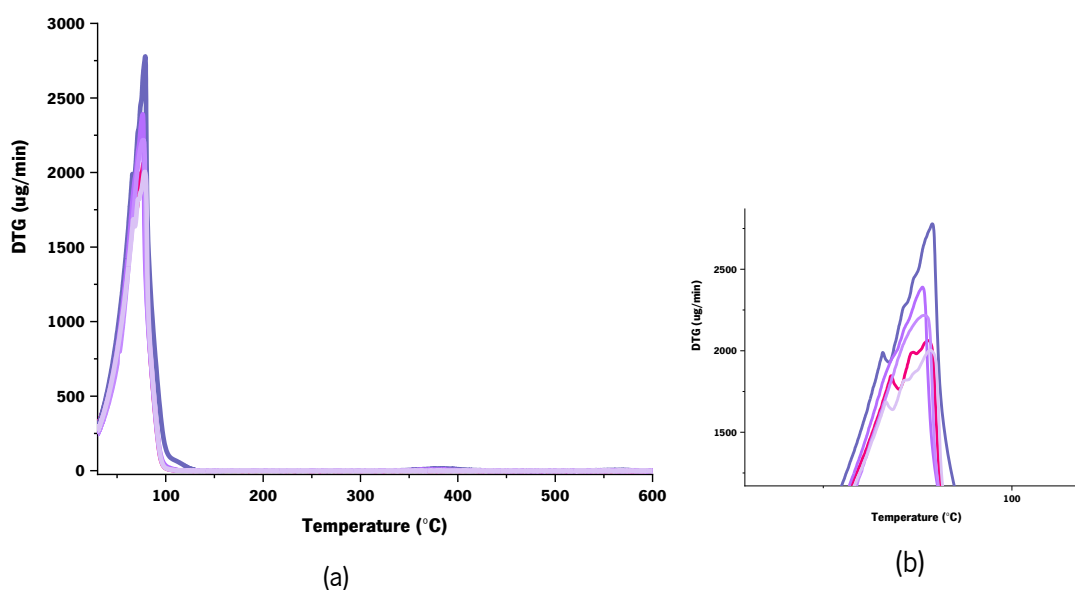




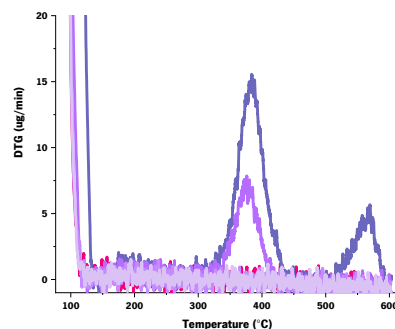
TiO<sub>2</sub>-O<sub>3</sub>-PMMA-MCs-UF irradiated with Xe lamp for 30h.

**Figure 65.** TXRF spectra from TiO<sub>2</sub>-PMMA-MCs-UF in aqueous solution unirradiated and irradiated with Xenon lamp for 30h.

Since the TGA only evaluates the degradation temperature, a 150 ppb solution was also analyzed to be compared with the remaining tested samples, characterized by a low UF concentration. This solution was made because for lower concentrations the TGA can displace the ramps, so it will be easier to identify the degradation steps from the samples collected after the degradation. Additionally, the 150 ppb solution was also made to find out if the released sample has a similar concentration to this control solution. The results revealed that thermograms from the 150 ppb solution have the same profile as for the sample stored in the dark for 30h (**Figure 66**).



■ 150 ppb of UF aqueous solution  
**TiO<sub>2</sub>-O<sub>3</sub>-PMMA-MCs-UF (400 + 400 cycles):**  
■ Precipitate, unirradiated  
■ Precipitate, irradiated  
■ Supernatant, irradiated  
■ Supernatant, irradiated



(c)

**Figure 66.** (a) DTG of a 150 ppb UF solution, aliquots of TiO<sub>2</sub>-O<sub>3</sub>-PMMA-MCs-UF pre-treated with 400 ozone ALD cycles and coated with 400 ALD cycles of TiO<sub>2</sub> placed in the dark (unirradiated) and exposed to Xe lamp (irradiated). From the TiO<sub>2</sub>-O<sub>3</sub>-PMMA-MCs-UF aliquots was extracted the supernatant part and the precipitate containing the water and the TiO<sub>2</sub>-O<sub>3</sub>-PMMA-MCs-UF. (b) and (c) are the DTG amplified in the zones of interest to observe the presence of TiO<sub>2</sub>-O<sub>3</sub>-PMMA-MCs and the agrochemical.

The TGA has three plateaus for the precipitated aliquots. The mass loss associated with the precipitated sample portion analyzed in the dark has 2.62 % of the undegraded mass, the higher value. The precipitated aliquot of the irradiated sample had an undegraded mass, which is equal to the 150 ppb solution (0.05 %). So, the TGA discarded the degradation percentage, and it was focused on the plateaus. The aliquots collected as supernatant have 0.230% and 0.195% of mass per °C for the unirradiated and irradiated sample, respectively.

In the DTG, below 100 °C, there is the typical water curve, but in the unirradiated sample and the UF solution, there are three maxima in the same curve. These results suggest that the peaks exclusively belong to the UF and water. In the DTG from the irradiated sample, the maxima mentioned above vanished and have a peak arises near 50 °C. However, it is not informative or clear that if it is from photocatalysis by-products or if belongs to the solvent (boiling point temperature equals 61.2 °C). Moreover, an aliquot of the solution was collected with the TiO<sub>2</sub>-O<sub>3</sub>-PMMA-MCs-UF to identify the UF and PMMA-MCs parts. **Figure 66** (b) and (c) show that at 100 °C, the precipitated aliquots had a similar amount of UF and present two peaks coincident with the PMMA degradation at higher temperatures.

Besides the TiO<sub>2</sub>-O<sub>3</sub>-PMMA-MCs standard deposition, the other samples with TiO<sub>2</sub>, plus a new one with 400 cycles of oxidation followed by 50 cycles of TiO<sub>2</sub> and the thinner ZnO-O<sub>3</sub>-PMMA-MCs, were tested by using the same conditions (**Figure 67**). The characterization only involved

the TGA technique; the solutions were collected to flasks to compare the color with a 30 ppm UF aqueous solution, also exposed to the dark and Xe lamp, for the same period of time. The controlled release was observed in the samples placed in the dark, and the PMMA-MCs; the control sample released more agrochemical than the other coated samples. Visually, the sample with 600 oxidation cycles has less UF released because it is the one that presents a slighter tone of red. It is evident that the Xe lamp changes the 30 ppm agrochemical solution composition due to oxidation. The irradiated samples are not easy to select the one with higher UF release.

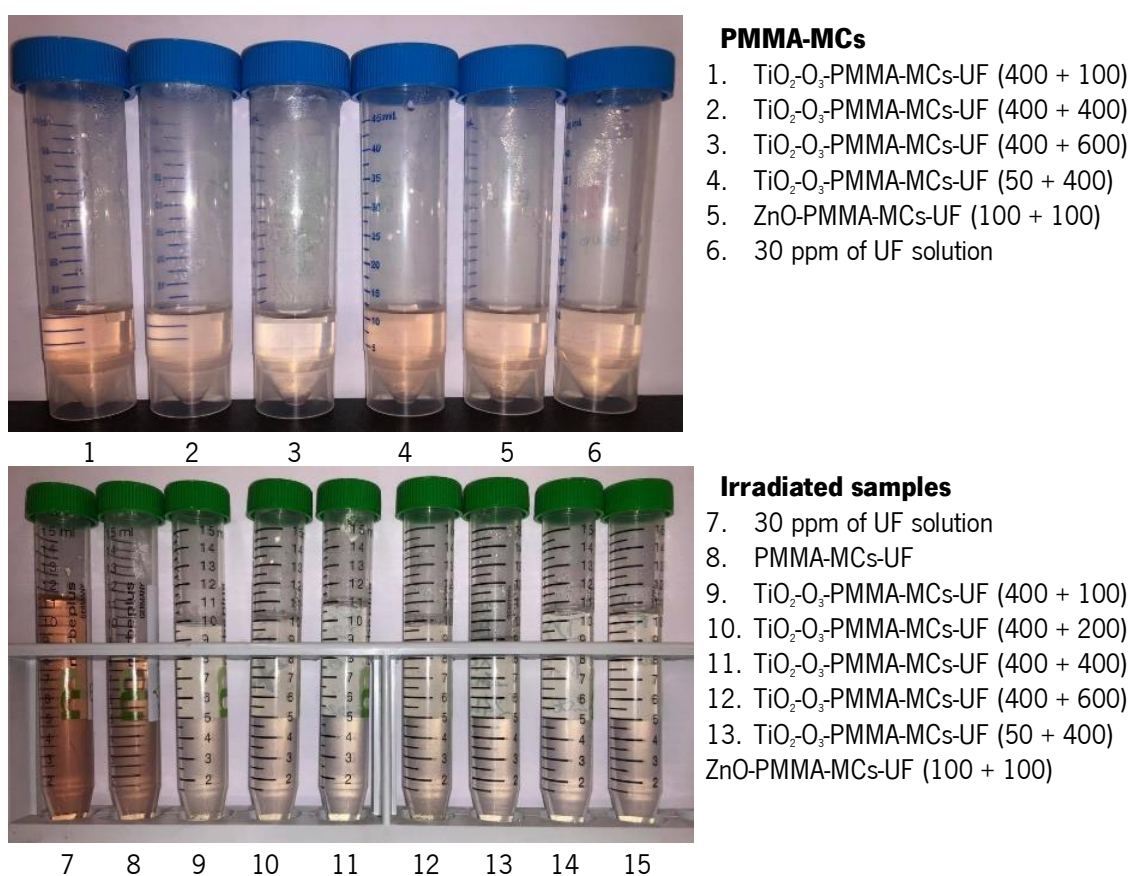
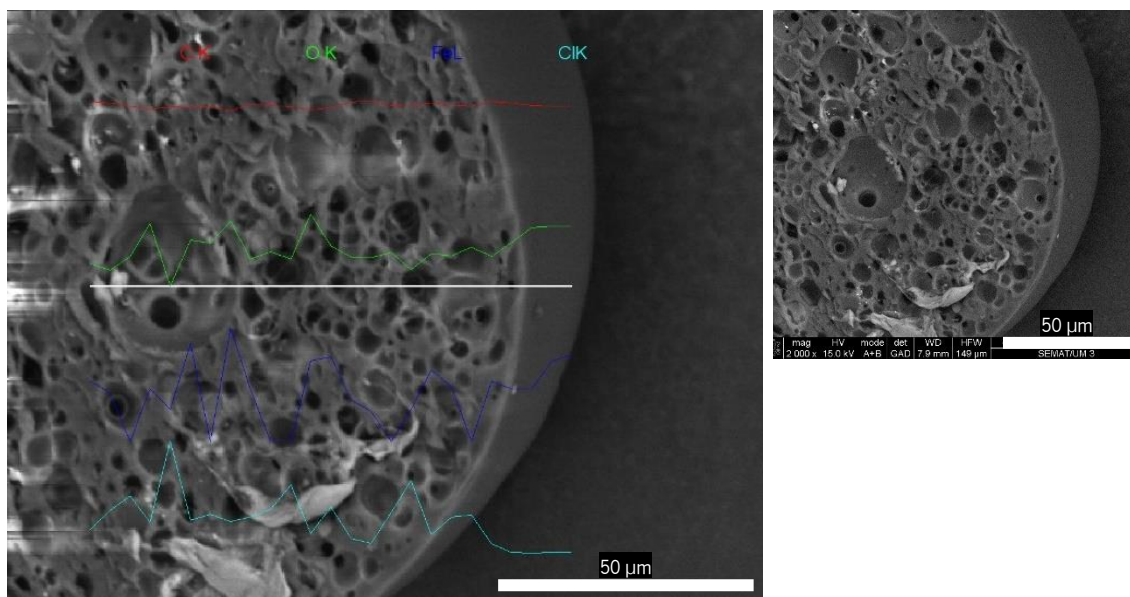


**Figure 67.** Aqueous solutions of agrochemical, uncoated PMMA-MCs, and PMMA-MCs coated with  $\text{TiO}_2$  or ZnO using an *in situ* pre-treatment with ozone. The images were taken in order to observe the controlled release from the variation in the agrochemical color.

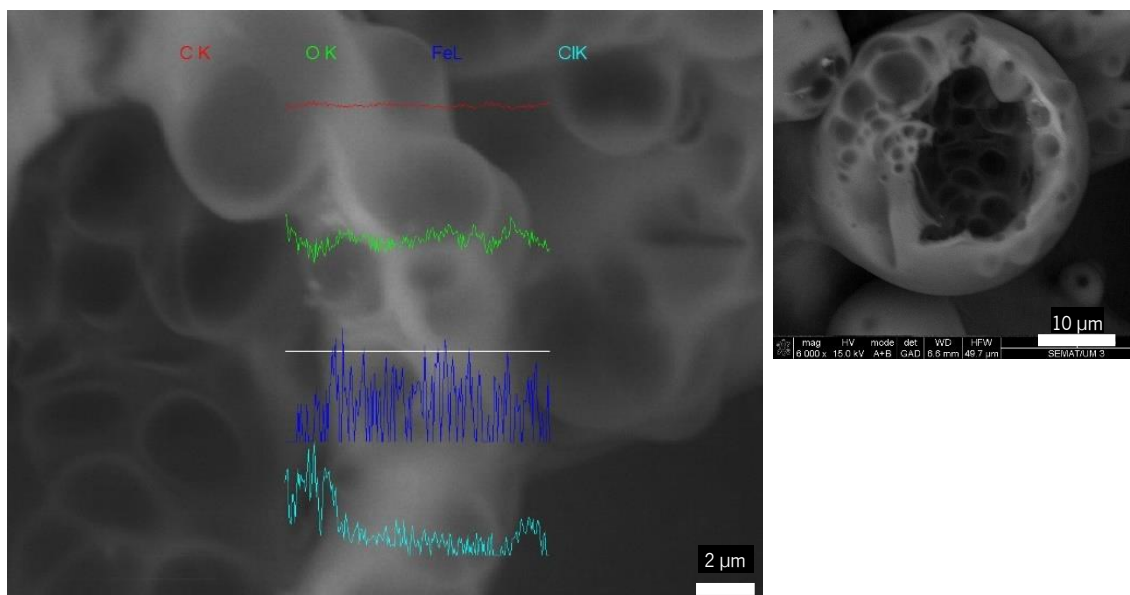
When the UF is released, the UV-vis peaks are from the UF oxidated, making it questionable where the agrochemical is introduced. The PMMA-MCs-UF were cut and visualized by SEM. The UF is present in the MCs core and wall; plus, what was previously established as a core-shell system is predominantly a heteroaggregated type, with multiple voids inside. Also, the EDX



spectrums from this MCs type have an EDX peak associated with Cl, perhaps from the chloroform that is entrapped in the holes. The EDX line scan in **Figure 68** reveals the presence of iron inside the PMMA-MCs-UF. However, the TXRF results from the respective coated MCs detected Ti in the aqueous media, believing that bleaching occurred (**Figure 65**). The PMMA-MCs-UF have a lower value of specific surface area ( $0.513 \text{ m}^2/\text{g}$ ) which can be associated to the denser structure visualized in SEM-EDX analysis.



Heteroaggregated PMMA-MCs-UF



Core-shell PMMA-MCs-UF

**Figure 68.** SEM micrographs and line EDX of cut PMMA-MCs-UF. The elements considered for the EDX line profile were oxygen, iron, carbon and chlorine. The samples were coated with Au/Pd before the SEM-EDX analysis.



From this point, there are several challenges to overcome. (1) The PMMA-MCs changed the volume and consequently difficult the release because it is necessary to degrade a sphere instead of a shell. (2) It is essential to guarantee that the samples do not obstruct the light emission and ensure that all of them are in contact with the radiation source. (3) The MCs should stay in the solution during the illumination because they tend to float and not collect for the absorbance read. (4) The coating must degrade the PMMA-MCs and not the agrochemical. This seems less probable because the UF is dispersed in the polymeric matrix. (5) Water adsorption by PMMA must be minimized to ensure that the UF is not encapsulated, following by degradation. (6) Working with low UF amounts is very risky because some analysis, like UV-vis spectrophotometry, can be under the limit of detection. Yet, it can be overcome increasing the UF concentration.

The TXRF and TGA results makes imperceptible to know if the  $\text{TiO}_2$  was bleached or reacted with the polymer by photocatalysis. Also, it does not inform about the Fe state, that can identify if there was deferration as an effect of the UV exposition (**Figure 65**). This process can be employed in the PMMA-MCs, however the substrate configuration it is not the most efficient to evaluate the system. Based on the previous results and the group knowledge in produce the photocatalytic activity in microcapsules [421,422], this technology has a huge potential to work just by replacing the PMMA-MCs type to a core-shell structure.

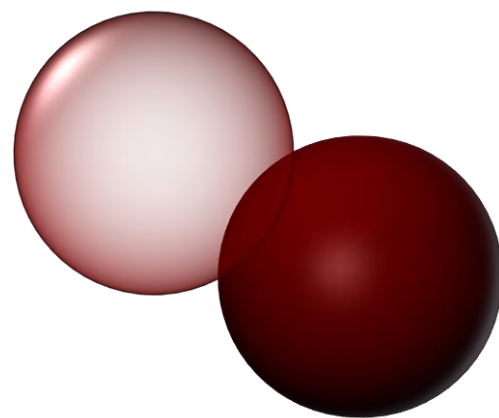
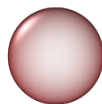
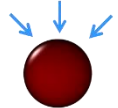
# Chapter 4

## Microspheres

### Results and discussion

**Controlled release**

Hydration



#### 4.1. Gelatin-based MSs from strategy 4

In parallel with strategy 3, microspheres (MSs) were developed to retain the agrochemical. Initially, the polymeric matrix consisted in UF, water and gelatin. Then, PVA was added at different concentrations to improve the MSs shape and prevent the MSs aggregation. These aqueous matrices were dissolved, poured with the aid of a syringe and dispersed into different continuous phases, at different temperatures (**Table 18**). All procedures were made without stirring.

**Table 18.** MSs synthesis parameters, products, and the respective stability overnight.

Matrix	Continuous phase		Gelification temperature	Product formation	Stability overnight
	composition	temperature			
<b>H<sub>2</sub>O</b> gelatin + UF	Olive oil	Room	Room	Paste	
		5°C	Room	MSs	
		5°C	5°C	Paste	
	Sunflower oil	Room	Room	paste	x
		5°C	Room	MSs	
		5°C	5°C	MSs	
Paraffin	Room	Room	Paste		
	5°C	Room	paste		
<b>PVA 0.025%</b> gelatin + UF	Olive oil	Room	Room	Paste	x
		5°C	Room	MSs	✓
		5°C	5°C	Paste	x
	Sunflower oil	Room	Room	paste	x
		Fridge	Room	MSs	✓
		Fridge	Fridge	MSs	✓
	Paraffin	Room	Room	paste	x
5°C		Room	Both	✓	
Paraffin + 10% Span®80	Room	Room	MSs	✓	
<b>PVA 1%</b> gelatin + UF	Olive oil	Room	Room	Paste	
		5°C	Room	MSs	x
		5°C	5°C	Paste	
	Sunflower oil	Room	Room	Paste	
		5°C	Room	MSs	✓
		5°C	5°C	MSs	
Paraffin	Room	Room	Paste	x	
	5°C	Room	MSs	✓	

From all variables presented, the PVA and gelatin concentration show to be necessary to preserve the MSs morphology and prevent the agglomeration. Also, the sunflower oil and the temperature contrasts were crucial to obtain the final product, but the MSs stability was not reached after washing and drying. So, the PVA concentration was increased to 3%, as well as the gelatin concentration. Different water:PVA 3% ratios (100/0, 70/30, 50/50, 35/65, 20/80, 10/90, 5/95, 0/100) were tested, maintaining the gelatin content. The ratio 10:90 was selected because it was

easier to aspirate and compress from the syringe. Also, the samples dried over the days, without filtration, decrease drastically in size. Still, they lose the sphericity when handled, and all of them aggregate during the dehydration. Due to the matrix's lack of concentration, the agglomeration effect is visible during drying (**Figure 69**).

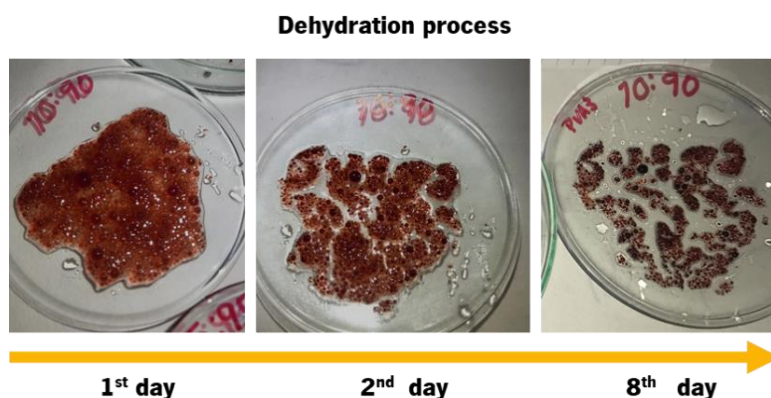


**Figure 69.** Dehydration process in water:PVA 3% 10:90 MSs, with 1 g of gelatin and UF, during 8 days.

To prevent the agglomeration, some additives were added, such as urea, SDS glycerin, and PEG (**Figure 70**). Taking the information from Rahman *et al.* [149], they used urea as a gelatin cross-linker for thin films in biomedical applications, which can have the potential for agroindustry applications and are compatible for MSs. Therefore, it was made a test with 35:2, 35:4, 35:7.75 and 35:12.2 gelatin:urea ratio. The urea was helpful to improve the sphericity of the MSs, decreasing the average size and as well the stiffness. However, the MSs still agglomerate.

SDS is an anionic surfactant that reacts with the gelatin, thus, by changing the solubility it could prevent the MSs agglomeration. The negative charge present in the surfactant will attract to the positively charged amino acids present in the gelatin (lysine, arginine, and histidine) and repel the negatively charged groups from aspartame and glutamate. This effect will create a kind of cross-link and control the micelle [423]. 50 mg of SDS were added into the 35:2 and 3:35 gelatin:urea ratio, a much smaller amount than the article refers to. The produced foam makes it difficult to pipetting of the solution and as result the MSs have heterogeneous sizes. After drying them, they collapse and lose the form. When they are crushed, the MSs fall apart as a crumble, indicating a lack of mechanical resistance.

Glycerin and PEG were added to the UF, gelatin, and urea formulation to control the agglomeration effect. The glycerin is a direct inhibitor, protects the gelatin from dissolution and

PEG is a plasticizer and preservative [424]. The use of this polymer in the formulation results in MSs with larger diameters than glycerin, and, with less capacity to deagglomerate, possibly takes more time to precipitate. Glycerin confers more rigidity, shining and smaller MSs sizes. There are significant differences when dissolved urea and these two compounds, like a synergetic effect, because there is a formation of MSs without agglomerates and without residues. At this stage, the matrix composition is constituted by 471 mg of gelatin, 17.9 mg of urea, and 142.7  $\mu$ L of glycerin or PEG, dissolved into 90:10 PVA 3%:water. The UF mass was varied from 9.4 mg to 23.4 mg, and the MSs maintaining the spherical form, enabling the retention of the UF.

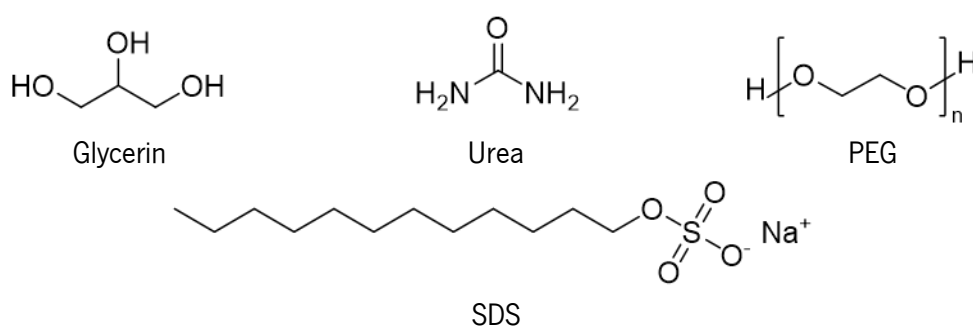


**Figure 70.** Chemical structures of the additives implemented in the gelatin:PVA MSs.

When the two matrices were introduced into the sunflower oil, the droplets coalesced. So, the temperature was lowered from 5 to -5 °C, using for PEG or glycerin into the composition. The MSs from PEG coalesces at  $\geq 1.5$  °C, and the glycerin ones coalesces at  $\geq 0$  °C. The best temperature to produce MSs was stipulated at -1.5 °C, since it provided, spherical MSs. Glycerin was selected as the plasticizer since it can form smaller MSs in all temperatures.

PVA concentration was increased to 10%, the gelatin to 1g, and was tried to pipette the solution with a 21G or 30G needle. The reason was based on improving the diffusion process over time, prolonging the release. It is very difficult to use the 30G needle as the highly dense matrix viscosity, so this variable was discarded. The most suitable ratios that provide hard MSs and are simpler to emulsify are represented in **Figure 71**. This procedure has 100% of PVA 5% as solvent. Nevertheless, there are several PVA percentages from PVA 3% to PVA 7%, for 80:20 and 90:10 PVA:water ratio that result in MSs. The dried MSs are very robust and when they are introduced into the water the diffusion of UF is not instantaneous.

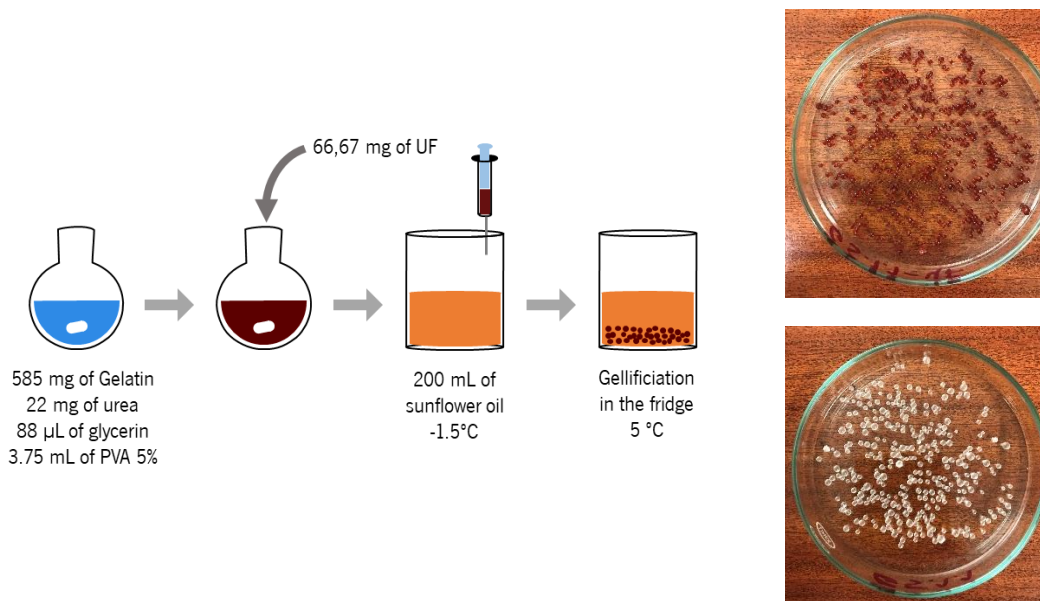


**Figure 71.** Microspherification synthesis parameters and the dried MSs with (top) and without UF (bottom).

The thermal stability was evaluated by thermogravimetric analysis (TGA) and the correspondent derivate (DTGA). To identify TGA steps or DTGA peaks it was necessary to create the following gels' compositions:

1. water and gelatin
2. gelatin and PVA 5%
3. gelatin, PVA 5% and urea
4. gelatin, PVA 5%, urea and glycerin.

One by one, they were placed into the oily phase, at -1.5 °C and reserved overnight. After the gels setting, they were washed and dried, mimicking the MSs procedure. Finally, they were cut with the proper weight to do the thermal characterization following the mentioned order.

**Figure 72** displays the gel's TGAs. The difference between gel 1 and 2 is notable. The thermograms indicate that by changing the solvent from water to PVA results in a different shape of the thermogram. For gel 1 there is something more similar to a curve than to a "plateau", that ends at 183.4 °C, with a mass loss of 12.75%. The PVA decreases all the parameters, and the curve is more similar to a "plateau" with a mass loss of 6.45%, at 158 °C. For the same temperature, the matrix 1 has a mass loss of 10.3%, indicating that PVA can transform the gel. Gel 2 and 3 have a similar "plateau". However, urea reduces the thermal range, meaning that at  $\approx$  140 °C starts to decrease the mass loss abruptly. The more complex gel has also a shorter

“plateau” with a mass loss of 3.13%, at 124 °C. Despite the temperature range window being shorter, glycerin provides more stability, which is not observed for the other gels.

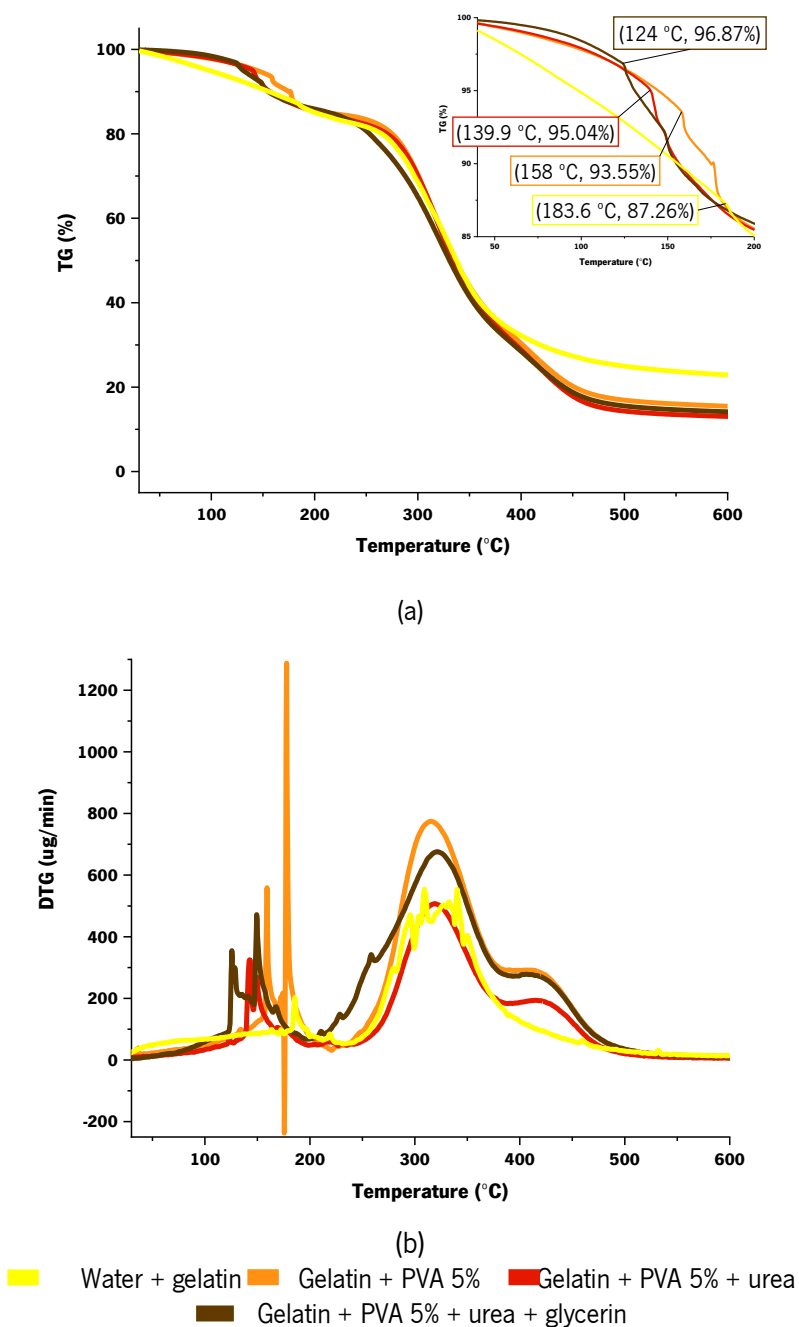


**Figure 72.** Percentual TG (a) and DTG (b) from the different gels to produce MSs: gel 1 (water and gelatin), gel 2 (gelatin and a PVA 5% aqueous solution), gel 3 (gelatin, PVA 5% aqueous solution and urea) and gel 4 (gelatin, PVA 5% aqueous solution, urea and glycerin). Gel 4 corresponds to the MSs formulation.

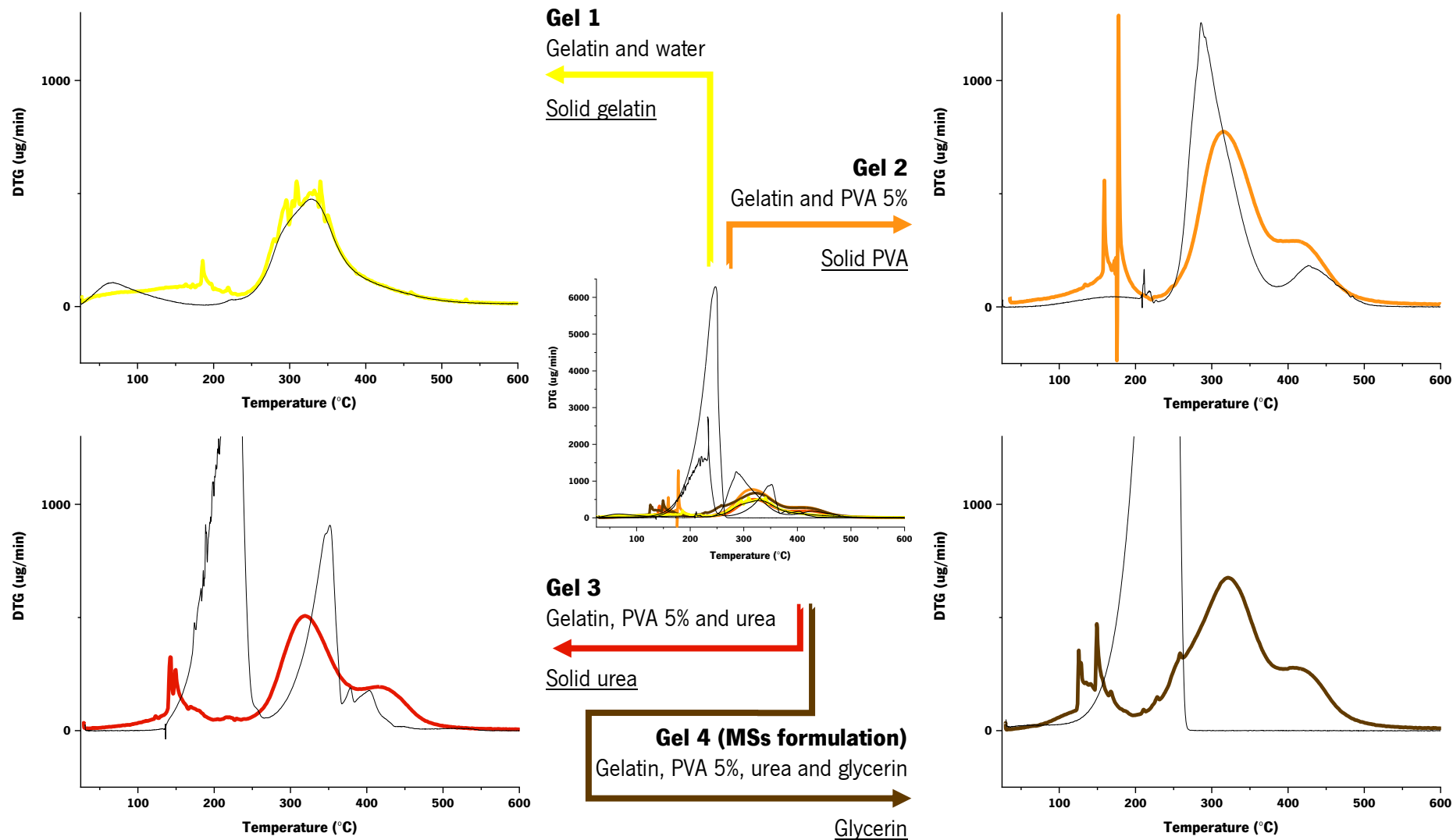


**Figure 73.** DTG from gel 1 to 4 (color line in each graph) and the DTG of each compound added as purchase to form the gel (black thinner line).



The DTG results show that each compound interferes in the gel distinctively (**Figure 73**). Gelatin has two peaks approximately at 186 °C and 219 °C (yellow line), suggesting that the degradation belongs to the susceptible covalent bonds. Then, the final peak corresponds to the C=N bond-breaking decomposition from the main chain complex protein structure. Since gelatin has various proteins, this peak is constituted by an overlap of various peaks.

Adding PVA into the gelatin solution gives the matrix more stability in the first 100 °C, and the number of peaks increases; however, it is not so similar to the solid PVA DTG. The only similarity is in shape. The peaks are intensified and displaced to lower temperatures (160 to 180 °C). Also, the matrix acquires two peaks at higher temperatures (315 °C), related to gelatin and PVA degradation, and the last peak at 430 °C ascribed to the PVA total degradation. These two last peaks are always present in the matrix, oscillating  $\pm 5$  °C.

The third matrix (orange line in the third graph) also shifts the peaks to lower temperatures (140 to 150°C), plus the negative peak from PVA disappears. So, there is no peak associated with urea, but this compound's introduction transforms the MSs thermal stability. Glycerin provides improved thermal stability below 90 °C. The number of peaks increases, and between 125 to 150 °C the two constant peaks are vanished. The presence of glycerin and urea is coincident with the degradation peaks from the compound's degradation as purchased.

In summary, increasing the matrix composition complexity enhanced the thermal stability at lower temperatures. Above 125 °C, the MSs are less thermally stable than the set gelatin in water. So, the crosslinking seems unclear, but all the compounds added into the matrix are essential in the synthesis method.

## 4.2. Gelatin-based MSs in controlled release systems

The diffusion mechanism was observed by UV-VIS spectrophotometry **Figure 74**. 10 mg of MSs or MSs-UF were introduced into a quartz cell with 11.5 mL of deionized water, at room conditions and without stirring. These experiments were performed in the dark for 495 minutes. The first step was measuring the control sample and then the MSs with UF in the composition. Over time, the samples (MSs and MSs-UF) release their matrix, giving multiple overlapped peaks in this plot, that correspond to the matrix dissolution; consequently, the baseline increases due to the dissolution in the aqueous media.

**Figure 74** (b) presents the UF release; two peaks are associated with the agrochemical, one with maximum absorbance between 277 and 280 nm, and the other peak had a maximum

absorbance from 474 to 486 nm. The maximum absorbance correlated with the time describes a non-linear behavior. The process is divided into three stages (1) a constant part that can be possibly related to the matrix swelling; (2) a burst that is associated with the UF diffusion, that is more evident at lower wavelength; (3) a constant part that can indicate the beginning of a saturation. The last phase seems to be more evident in the bigger band. Nonetheless, if the saturation is not beginning, the solution will saturate because the MCs will dissolve entirely in the continuous phase, and the concentration of UF in the solution will be the same as the UF concentration present in the MSs-UF.

These results are auspicious because it was possible to obtain the agrochemical diffusion without radiation. Thus, releasing the UF with a simple process. From the experimental knowledge, the MSs are robust due to the PVA concentration.

Hence, by changing the PVA percentage release is obtained. This is extremely important for a different velocity of UF liberation and stability during the previous processes, like storage and transport, which was the principal concern. Increasing the PVA percentage results in more plasticized MSs. Consequently, the release will more prolonged; for lower percentages of PVA, the release will be faster. From an industrial point of view, having a similar formulation is also an advantage because the UF is employed in different crops and various forms.

Since the MSs preserve the agrochemical, they avoid the UF powder transformation into a paste or solution. This can happen when exposed to certain humidity conditions from packaging or even for the user that opens the flask multiple times. To summarize, the MSs can be the most suitable controlled release system for UF. However, it is necessary to emphasize that there are strong probabilities to release the AC only by exposed to certain humidity or temperature conditions. Also, the polymeric matrix is not inert, mostly because of the gelatin. So, at the first time, this controlled release mechanism can work, however, the combination of gelatin and UF could change the ACs properties. But, there is no certainty about this because the crosslinking effect has not been fully understood.

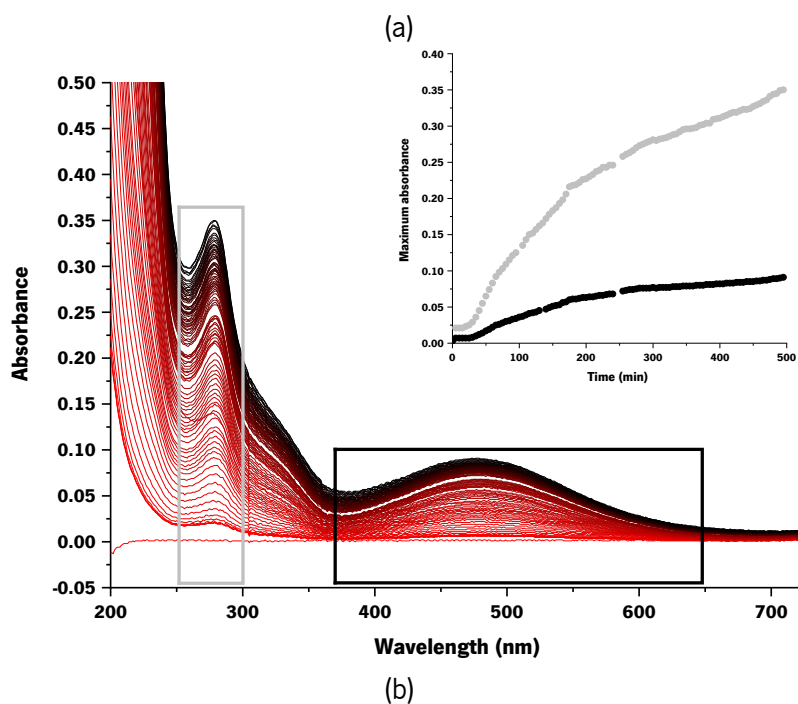
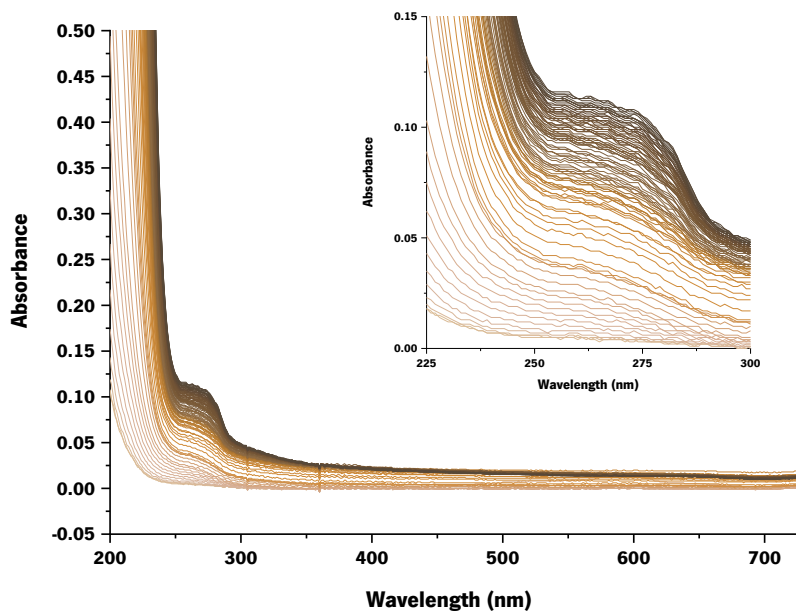
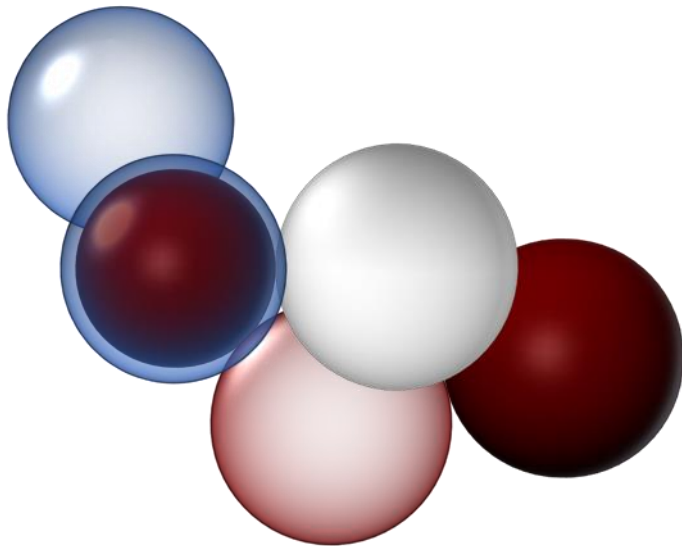


**Figure 74.** spectra of (a) MEs and (b) MEs-UF in aqueous solution, in order to evaluate the cumulative controlled release. The gradient from lighter to darker correspond to the MSs (a) or MSs-UF (b) release overtime, meaning that the brown (a) and black (b) are the spectra at 495 min. Also, in (a) there is the same spectra amplified to visualize the band shape, and in (b) is present the absorbance intensity overtime, at 278 nm (grey curve) and at 480 nm (black curve).

# **Chapter 5**

## **Conclusions and future work**



## 5.1. Conclusions and overview

This work was very challenging in all the tasks, and the success can be measured in different ways. Based on the thesis title, there were three main tasks: i) microencapsulation; ii) ALD coating of MCs; iii) controlled release of ACs.

The initial study was to encapsulate aqueous agrochemicals into a hydrophobic polymeric microcapsule; it seemed feasible, but there was a constant problem involving osmosis. The final products were heteroaggregated-type microcapsules, instead of core-shell. However, the encapsulation works for other compounds soluble in oil. So, with just one method, there are two types of encapsulated cores, which can result in core-shell microcapsules (for empty and oily encapsulated compounds) or heteroaggregated morphology (hydrosoluble compounds). In the end, there were two valid synthesis routes for microencapsulation.

The ALD onto the microcapsules was very difficult to develop and fully understand. Available information on ALD on polymers (not only PMMA) was scarce, with limited literature on the subject. Comparing with ALD on a silicon wafer, the thermal stability and the surface of ALD coated microcapsules are very different. Usually, there are treatments to functionalize the surface and to enable the growth on a silicon wafer. But, the polymeric substrates are susceptible to organic solvents, acids, or bases, so the growth per cycle depends on their chemical structure. Hence, if there are no available groups to create the chemical bonds, the coating does not develop.

This work found a way to improve the ALD technique by pre-treatment of PMMA-MCs prior to deposition: the ozonation was the solution. The TTIP and DEZ demonstrated that no matter the precursor's reactivity, the PMMA needs ozonation to promote the deposition in most of the experiments. With the TiO<sub>2</sub> coating, it was proved that by keeping the TTIP ALD number of cycles, the film can grow if the number of ozonation cycles is increased. Due to the thermal sensibility, the GPC was not calculated because the samples were not stable for SEM analysis.

Thermal stability was another critical parameter that had not been much explored so far in the ALD domain. Comparing again with the silicon wafer, it is possible to perform ALD deposition at higher temperatures; however, in polymers, the ALD temperature window is limited by the T<sub>g</sub> value. So, the crystallinity phases of the coating are dependent on the temperature and the seed layer.

The ZnO layer has been shown to protect PMMA-MCs from TiO<sub>2</sub>, subsequently deposited at temperatures above the T<sub>g</sub> value. SEM images show the spherical structure intact, indicating that the ZnO seed layer approach works efficiently.

In conclusion, the sample pre-treatment and the transition temperature were the highlights of this work. ALD proves to be efficient on several substrates, but in particular, it has been shown to be an excellent technique to provide extra functionality in polymeric materials. The additional functionalities can mean new applications or improvements of specific properties in all kinds of technologies. Thus, ALD in polymers can be an excellent direction to transform consumable materials and give a unique opportunity to develop add-value products.

The heterostructured material characterization was tricky, the same way as the controlled release. When a nanomaterial coats a micrometric material, the techniques to characterize the film are not appropriate to characterize the substrate. Here, the nature of each substrate was different (metallic and a resin), plus the substrate was spherical, and the size heterogeneity was more significant than the mean diameter size. So, the used techniques were very conditioned by the all sample.

The controlled release and degradation studies were the most affected processes because the defects conditioned the other steps. The acorn-shape microcapsules are denser than the core-shell, so the release takes longer, or the photocatalytic activity from the coating needs to be greater. Due to the thermal sensibility, the nature of ALD coatings was amorphous  $\text{TiO}_2$  and wurtzite-type  $\text{ZnO}$ . Unlike the massive photocatalytic activity from the thicker  $\text{ZnO}$  coating,  $\text{TiO}_2$  does not demonstrate a relevant photocatalytic performance, due to the lack of crystallinity.

The controlled release qualification and quantification were difficult to determine because the amount of encapsulated agrochemical was very small. Hence, the standard technique for evaluating the UV-VIS process was discarded. It is necessary to do more studies to understand the mechanism and why there is only released in the dark. Alternatively, if releasing takes place in both situations, the agrochemical degrades during the radiation exposition.

The parallel studies with the MSs resulted in a degradable system that can protect the agrochemical from the external media. The release can be by water dissolution, over more than eight hours, which can provide enough release velocity for specific applications. Besides, the MSs are very customizable because the release is associated with gelatin and PVA percentages. However, it is vital to study toxicology as well the soil dynamics when this compound is applied.

Overall, the thesis' goals were accomplished with success. The coated polymeric microcapsules are not the most suitable controlled release system for aqueous agrochemicals. However, the coated PMMA demonstrated excellent photocatalytic activity for methylene blue degradation, suggesting that it can be employed as 2D (film) or 3D substrate (MCs) for other

purposes (e.g., oily ACs, self-cleaning windows, anti-bacterial agents, etc.). Indeed, there was no information about photocatalytic PMMA-MCs with ZnO or TiO<sub>2</sub> (from TTIP precursor); plus, the *in-situ* ozonation as pre-treatment is also a novelty.

The most crucial goal of this thesis was to create a delivery system for ASCENZA® industrialization, and so far, the studies are preliminary and promising.

## 5.2. Limitations and suggestions for future work

A set of possible strategies is here proposed to overcome, in the future, the limitations found in this work.

The **MCs size** is exceptionally dependent on the environmental conditions that affect the viscosity of the PMMA solution. So, to control the conditions, it was necessary to work in a controlled environment. As a suggestion, there are some procedures using an injection pumping system. Another idea is to use and adapt the Schlenk flat bottom flask to recreate controlled evaporation and agitation flow. The **encapsulation yield** is very difficult to calculate because the diameters are very different in an aliquot of MCs, influencing the encapsulation yield. Also, the agrochemical dissolves in the polymeric matrix. A portion of the UF degrades from the TGA results, so this thermal technique is not the first choice to determine the encapsulation rate. A technique like chromatography or UV-vis could quantify the core's agrochemical presence, discarding the part dissolved in the shell.

In the **ALD** there was a specific factor that drastically slowed the process: the reactor type. The depositions were made in a tubular reactor, so the mass introduced in the furnace was very limited, even though the MCs were protected by the stainless-steel web inside the ceramic boat. Almost a month was necessary to do the minimum mass required for the XRD analysis. So, by changing the reactor for a fluidized bed or a flow-through configuration, the mass loss will be reduced, and the mass per deposition can be higher.

The **degradation and controlled release** are very hard to understand because there is no correlation with the cycles. Also, since the MCs were very unstable to the SEM-EDX analysis, it was impossible to measure the coating dimensions, like films or particles, to elucidate the explanations in the diffusion, degradation, and controlled release processes. As a recommendation, the samples should be placed into an epoxy resin and polished for subsequent SEM-EDX analysis. The goal is to quantify the coatings' metal content (Ti or Zn) and the Fe, so that they can be combine.

Another aspect that needs improvement is the encapsulation of a massive amount of UF to provide a quantified UF signal in laboratory daily techniques, such as UV-VIS. Then, a calibration curve should be made, and the amount of AC release can be quantified instead of qualified.

In the **MSs** section it is vital to study the PVA degradation in soils to evaluate the UF controlled release, because the soil is complex and biological dynamics and cycles can degrade gelatin.



## References

1. Rose, M.T.; Cavagnaro, T.R.; Scanlan, C.A.; Rose, T.J.; Vancov, T.; Kimber, S.; Kennedy, I.R.; Kookana, R.S.; Zwieten, L. Van Impact of Herbicides on Soil Biology and Function. In *Advances in Agronomy*; Sparks, D.L., Ed.; Advances in Agronomy; Academic Press, 2016; Vol. 136, pp. 133–220 ISBN 9780128046814.
2. Gupta, S.M.; Tripathi, M. A review of TiO<sub>2</sub> nanoparticles. *Chinese Sci. Bull.* **2011**, *56*, 1639–1657, doi:10.1007/s11434-011-4476-1.
3. Majumder, S.; Chatterjee, S.; Basnet, P.; Mukherjee, J. ZnO based nanomaterials for photocatalytic degradation of aqueous pharmaceutical waste solutions – A contemporary review. *Environ. Nanotechnology, Monit. Manag.* **2020**, *14*, 100386, doi:10.1016/j.enmm.2020.100386.
4. George, S.M. Atomic Layer Deposition: An Overview. *Chem. Rev.* **2010**, *110*, 111–131, doi:10.1021/cr900056b.
5. Ahmadi, F.; Shahsavari, A.A.; Rahimi-Nasrabadi, M. Automated extraction and preconcentration of multiresidue of pesticides on a micro-solid-phase extraction system based on polypyrrole as sorbent and off-line monitoring by gas chromatography–flame ionization detection. *J. Chromatogr. A* **2008**, *1193*, 26–31, doi:10.1016/j.chroma.2008.04.025.
6. Lavy, T.L. *Safety and Health in the Use of Agrochemicals: A Guide*; International Labour Office: Geneva, 1991; ISBN 9221072819.
7. Neamtu, C.; Popescu, M.; Dima, Ş.-O. Leaching and in vitro agrochemical screening for new slow release fertilizers containing N, P, Ca, and Mg. *Acad. Res. J. Agric. Sci. Res.* **2015**, *3*, 45–53, doi:10.14662/ARJASR2015.003.
8. Newman, L. Pesticide Residues in Coastal Tropical Ecosystems: Distribution, Fate and Effects. *Int. J. Toxicol.* **2004**, *23*, 145–146, doi:10.1080/10915810490436360.
9. Shaw, I. *Is it Safe to Eat? Enjoy Eating and Minimize Food Risks*; 1st ed.; Springer Berlin Heidelberg New York, 2005; ISBN 3-540-21286-8.
10. Kenawy, E.-R.; Sakran, M.A. Controlled release formulations of agrochemicals from calcium alginate. *Ind. Eng. Chem. Res.* **1996**, *35*, 3726–3729, doi:10.1021/ie950448m.
11. Kenawy, E.R.; Sherrington, D.C.; Akelah, A. Controlled release of agrochemical molecules chemically bound to polymers. *Eur. Polym. J.* **1992**, *28*, 841–862, doi:10.1016/0014-3057(92)90310-X.
12. Banin, A.; Kafkafi, U. *Agrochemicals in Soils*; Pergamon Press [for the] Israel Society of Soil Science [and] International Irrigation Information Center, 1980; ISBN 0-08-02-5914-6.
13. Auerswald, K.; Litz, N.; Mayer, R.; Stoy, A.; Alef, K.; Kerndorff, H. Soil, 2. Damage and Soil Pollution. *Ullmann's Encycl. Ind. Chem.* 2011, 421–481.
14. Campos, E.V.R.; de Oliveira, J.L.; Fraceto, L.F. Applications of Controlled Release Systems for Fungicides, Herbicides, Acaricides, Nutrients, and Plant Growth Hormones: A Review. *Adv. Sci. Eng. Med.* **2014**, *6*, 373–387, doi:10.1166/ asem.2014.1538.
15. Campos, E.V.R.; de Oliveira, J.L.; Fraceto, L.F.; Singh, B. Polysaccharides as safer release systems for agrochemicals. *Agron. Sustain. Dev.* **2014**, *35*, 47–66, doi:10.1007/s13593-014-0263-0.
16. Peakall, D.B. DDE-induced eggshell thinning: an environmental detective story. *Environ. Rev.* **1993**, *1*, 13–20, doi:10.1139/a93-002.
17. Moraru, C.; P. Panchapakesan, C.; Huang, Q.; Takhistov, P.; Liu, S.; Kokini, J. *Food technology Magazine*. December 1, 2003, pp. 24–29.
18. Liang, T.T.; Lichtenstein, E.P. Synergism of Insecticides by Herbicides: Effect of

- Environmental Factors. *Science (80- )*. **1974**, *186*, 1128–1130, doi:10.1126/science.186.4169.1128.
19. Ahmad, R.; Kookana, R.S.; Megharaj, M.; Alston, A.M. Aging reduces the bioavailability of even a weakly sorbed pesticide (carbaryl) in soil. *Environ. Toxicol. Chem.* **2004**, *23*, 2084–2089, doi:10.1897/03-569.
  20. Moros, J.; Armenta, S.; Garrigues, S.; de la Guardia, M. Comparison of two vibrational procedures for the direct determination of mancozeb in agrochemicals. *Talanta* **2007**, *72*, 72–79, doi:10.1016/j.talanta.2006.09.027.
  21. Pretty, J.N.; Morison, J.I.L.; Hine, R.E. Reducing food poverty by increasing agricultural sustainability in developing countries. *Agric. Ecosyst. Environ.* **2003**, *95*, 217–234, doi:10.1016/S0167-8809(02)00087-7.
  22. Carvalho, F.P. Pesticides, environment, and food safety. *Food Energy Secur.* **2017**, *6*, 48–60, doi:10.1002/fes3.108.
  23. Carvalho, F.P.; Gonzalez-Farias, F.; Villeneuve, J.-P.; Cattini, C.; Hernandez-Garza, M.; Mee, L.D.; Fowler, S.W. Distribution, Fate and Effects of Pesticide Residues in Tropical Coastal Lagoons of Northwestern Mexico. *Environ. Technol.* **2002**, *23*, 1257–1270, doi:10.1080/09593332308618321.
  24. Carvalho, F.P.; Villeneuve, J.-P.; Cattini, C.; Tolosa, I.; Montenegro-Guillen, S.; Lacayo, M.; Cruz, A. Ecological risk assessment of pesticide residues in coastal lagoons of Nicaragua. *J. Environ. Monit.* **2002**, *4*, 778–787, doi:10.1039/B203728A.
  25. Carvalho, F.P.; Montenegro-Guillén, S.; Villeneuve, J.P.; Cattini, C.; Tolosa, I.; Bartocci, J.; Lacayo-Romero, M.; Cruz-Granja, A. Toxaphene residues from cotton fields in soils and in the coastal environment of Nicaragua. *Chemosphere* **2003**, *53*, 627–636, doi:10.1016/S0045-6535(03)00451-X.
  26. Andreu, V.; Picó, Y. Determination of pesticides and their degradation products in soil: Critical review and comparison of methods. *TrAC - Trends Anal. Chem.* **2004**, *23*, 772–789, doi:10.1016/j.trac.2004.07.008.
  27. Perlatti, B.; Souza Bergo, P.L. de; Fernandes da Silva, M.F. das G.; Batista, J.; Rossi, M.; Bergo, P.D.S.; Fernandes, J.; Forim, M. Polymeric Nanoparticle-Based Insecticides: A Controlled Release Purpose for Agrochemicals. In *Insecticides - Development of Safer and More Effective Technologies*; Trdan, S., Ed.; In Tech, 2013; pp. 523–550 ISBN 978-953-51-0958-7.
  28. Liang, T.T.; Lichtenstein, E.P. Synergism of insecticides by herbicides: Effect of environmental factors. *Science (80- )*. **1974**, *186*, 1128–1130, doi:10.1126/science.186.4169.1128.
  29. Bajpai, A.K.; Giri, A. Swelling dynamics of a macromolecular hydrophilic network and evaluation of its potential for controlled release of agrochemicals. *React. Funct. Polym.* **2002**, *53*, 125–141, doi:10.1016/S1381-5148(02)00168-2.
  30. Ali, D.; Nagpure, N.S.; Kumar, S.; Kumar, R.; Kushwaha, B.; Lakra, W.S. Assessment of genotoxic and mutagenic effects of chlorpyrifos in freshwater fish *Channa punctatus* (Bloch) using micronucleus assay and alkaline single-cell gel electrophoresis. *Food Chem. Toxicol.* **2009**, *47*, 650–656, doi:10.1016/j.fct.2008.12.021.
  31. Villeneuve, J.P.; Carvalho, F.P.; Fowler, S.W.; Cattini, C. Levels and trends of PCBs, chlorinated pesticides and petroleum hydrocarbons in mussels from the NW Mediterranean coast: comparison of concentrations in 1973/1974 and 1988/1989. *Sci. Total Environ.* **1999**, *237–238*, 57–65, doi:10.1016/S0048-9697(99)00124-2.
  32. The Council of the European Communities Council Directive 80/779/EEC. *Off. J. Eur. Communities* 1980, 30–48.

33. Holden, W.T.C. Future formulation trends-the likely impact of regulatory and legislative pressures. In Proceedings of the Brighton Crop Protection Conference Pests and Diseases; 1992; Vol. 1, p. 313.
34. Tsuji, Y. Discrete Element Modeling of Clusters in Gas-Solid Flows. *ASME-PUBLICATIONS-FED* **1996**, *236*, 3–4.
35. Tsuji, K. Microencapsulation of pesticides and their improved handling safety. *J. Microencapsul.* **2001**, *18*, 137–147, doi:10.1080/026520401750063856.
36. Ahmed Akelah *Functionalized polymeric materials in agriculture and the food industry*, 1st ed.; Springer US: Tanta, 2013; ISBN 9781461470601.
37. Becher, P. Surfactants in Agrochemicals, Th. F. Tadros (Surfactant Science Series 54), Marcel Dekker, Inc., 1995, ppx+264. \$115, (ISBN 0-8247-9100-2). *J. Dispers. Sci. Technol.* **1996**, *17*, 97, doi:10.1080/01932699608943491.
38. Foy, L.C. *Adjuvants for Agrichemicals*; 1 st.; CRC Press: Boca Raton, 1992; ISBN 9781351069502.
39. Gam-Derouich, S.; Ngoc Nguyen, M.; Madani, A.; Maouche, N.; Lang, P.; Perruchot, C.; Chehimi, M.M. Aryl diazonium salt surface chemistry and ATRP for the preparation of molecularly imprinted polymer grafts on gold substrates. *Surf. Interface Anal.* **2010**, *42*, 1050–1056, doi:10.1002/sia.3210.
40. Scher, H.B. Human welfare and the environment. In Proceedings of the 15th International Congress of Pesticide Chemistry; Pergamon Press, Oxford: Kyoto, 1983; pp. 295–300.
41. Abraham, J. *Controlled Release Fertilizer Formulations Based on Polymers*, Mahatma Gandhi University, 1997.
42. British Standards Institute Staff. Slow-release fertilizers. Determination of the release of the nutrients. Method for coated fertilizers 2002, 16.
43. Capes, C.E.; Williams, J.C. *Handbook of Powder Technology.: Particle Size Enlargement*, 1st ed.; Elsevier Science B.V., 1980; ISBN 9781483256665.
44. Takai, C.; Hotta, T.; Shiozaki, S.; Matsumoto, S.; Fukui, T. Key techniques to control porous microsphere morphology in S/O/W emulsion system. *Colloids Surfaces A Physicochem. Eng. Asp.* **2011**, *373*, 152–157, doi:10.1016/j.colsurfa.2010.10.049.
45. Milani, P.; França, D.; Balieiro, A.G.; Faez, R. Polymers and its applications in agriculture. *Polímeros* **2017**, *27*, 6–8, doi:10.1590/0104-1428.09316.
46. Sopeña, F.; Maqueda, C.; Morillo, E. Controlled release formulations of herbicides based on micro-encapsulation. *Ciência e Investig. Agrar.* **2009**, *36* (1), 27–42, doi:10.4067/S0718-16202009000100002.
47. Kharine, A.; Manohar, S.; Seeton, R.; G M Kolkman, R.; A Bolt, R.; Steenbergen, W.; de Mul, F. Poly(vinyl alcohol) gels for use as tissue phantoms in photoacoustic mammography. *Phys. Med. Biol.* **2003**, *48*, 357–370, doi:10.1088/0031-9155/48/3/306.
48. Peppas, N.A.; Leobandung, W. Stimuli-sensitive hydrogels: ideal carriers for chronobiology and chronotherapy. *J. Biomater. Sci. Polym. Ed.* **2004**, *15*, 125–144, doi:10.1163/156856204322793539.
49. Kenawy, E.-R.; Sakran, M.A. Controlled release of polymer conjugated agrochemicals. System based on poly(methyl vinyl ether-alt-maleic anhydride). *J. Appl. Polym. Sci.* **2001**, *80*, 415–421, doi:10.1002/1097-4628(20010418)80:3<415::AID-APP1114>3.0.CO;2-K.
50. Davies, M.J. Good news for lab animals. *Trends Biotechnol.* **2001**, *19*, 489, doi:10.1016/S0167-7799(01)01890-X.
51. Tashima, S.; Shimada, S.; Ando, I.; Matsumoto, K.; Takeda, R.; Shiraiishi, T. Effect of Vehicle on Drug Release Profiles of Time-Controlled Release Granule Containing Metominostrobin.

- J. Pestic. Sci.* **2000**, *25*, 128–132, doi:10.1584/jpestics.25.128.
52. Liu, J.; Lin, S.; Li, L.; Liu, E. Release of theophylline from polymer blend hydrogels. *Int. J. Pharm.* **2005**, *298*, 117–125, doi:10.1016/j.ijpharm.2005.04.006.
  53. Vidal, M.M.; Filipe, O.M.S.; Costa, M.C.C. Reducing the Use of Agrochemicals: A Simple Experiment. *J. Chem. Educ.* **2006**, *83*, 245, doi:10.1021/ed083p245.
  54. Li, Z. Use of surfactant-modified zeolite as fertilizer carriers to control nitrate release. *Microporous Mesoporous Mater.* **2003**, *61*, 181–188, doi:10.1016/S1387-1811(03)00366-4.
  55. Hekmat, A.; Barati, A.; Frahani, E.V.; Afraz, A. Synthesis and Analysis of Swelling and Controlled Release Behaviour of Anionic sIPN Acrylamide based Hydrogels. *World Acad. Sci. Eng. Technol.* **2009**, *56*, 96–100.
  56. Roy, A.; Singh, S.K.; Bajpai, J.; Bajpai, A.K. Controlled pesticide release from biodegradable polymers. *Cent. Eur. J. Chem.* **2014**, *12*, 453–469, doi:10.2478/s11532-013-0405-2.
  57. Wu, Z.; Zhao, Y.; Kaleem, I.; Li, C. Preparation of calcium-alginate microcapsuled microbial fertilizer coating *Klebsiella oxytoca* Rs-5 and its performance under salinity stress. *Eur. J. Soil Biol.* **2011**, *47*, 152–159, doi:10.1016/j.ejsobi.2010.11.008.
  58. Bhattacharyya, P.N.; Jha, D.K. Plant growth-promoting rhizobacteria (PGPR): emergence in agriculture. *World J. Microbiol. Biotechnol.* **2012**, *28*, 1327–1350, doi:10.1007/s11274-011-0979-9.
  59. Celis, R.; Hermosín, M.C.; Carrizosa, M.J.; Cornejo, J. Inorganic and Organic Clays as Carriers for Controlled Release of the Herbicide Hexazinone. *J. Agric. Food Chem.* **2002**, *50*, 2324–2330, doi:10.1021/jf011360o.
  60. Solomon, R.D.J.; Satheja, S. Controlled-Release Formulations of Butachlor and Oxadiazon-An Evaluation of Sorption/Desorption. *J. Agron.* **2007**, *6*, 370–373, doi:10.3923/ja.2007.370.373.
  61. Roy, A.; Bajpai, J.; Bajpai, A.K. Development of calcium alginate-gelatin based microspheres for controlled release of endosulfan as a model pesticide. *Indian J. Chem. Technol.* **2009**, *16*, 388–395.
  62. Azeem, B.; KuShaari, K.; Man, Z.B.; Basit, A.; Thanh, T.H. Review on materials & methods to produce controlled release coated urea fertilizer. *J. Control. Release* **2014**, *181*, 11–21, doi:10.1016/j.jconrel.2014.02.020.
  63. Davidson, D.; Gu, F.X. Materials for Sustained and Controlled Release of Nutrients and Molecules To Support Plant Growth. *J. Agric. Food Chem.* **2012**, *60*, 870–876, doi:10.1021/jf204092h.
  64. Melaj, M.A.; Daraio, M.E. HPMC layered tablets modified with chitosan and xanthan as matrices for controlled-release fertilizers. *J. Appl. Polym. Sci.* **2014**, *131*, 40839 1–7, doi:10.1002/app.40839.
  65. Tadros, T.F. Colloids and Interface Science. In *Colloids in Agrochemicals*; Wiley-VCH Verlag GmbH & Co. KGaA: Weinheim, 2009; Vol. 5, pp. 1–276 ISBN 9783527314652.
  66. Karsa, D.R.; Stephenson, R.A.; Royal Society of Chemistry (Great Britain) Industrial Division; North West Region Group, B.A. for C.S.; Water Soluble Polymers Sector *Encapsulation and Controlled Release*; Royal Society of Chemistry: Special publication; 1st ed.; Royal Society of Chemistry: Cambridge, 1993; ISBN 9780851866154.
  67. Chien, Y.W.; Cabana, B.E.; Mares, S.E. *Novel Drug Delivery Systems: Fundamentals, Developmental Concepts, Biomedical Assessments*; M. Dekker: New York, 1982; ISBN 9780824718312.
  68. Chemtob, C.; Chaumeil, J.C.; N'Dongo, M. Tablets of metronidazole microcapsules: release characteristics. *Int. J. Pharm.* **1986**, *29*, 83–92, doi:10.1016/0378-5173(86)90202-4.

69. Ghosh, S.K. Functional Coatings: By Polymer Microencapsulation. In Proceedings of the Functional Coatings: By Polymer Microencapsulation; WILEY-VCH Verlag GmbH & Co. KGaA: Weinheim, 2006; pp. 1–357.
70. Arshady, R. *Microspheres, Microcapsules and liposomes: general concepts and criteria, MML Series, Volume 1*; Citus Books: London, 1999; ISBN 978-0953218769.
71. Arshady, R. In the name of particle formation. *Colloids Surfaces A Physicochem. Eng. Asp.* **1999**, *153*, 325–333, doi:10.1016/S0927-7757(98)00454-3.
72. Berkland, C.; Kipper, M.J.; Narasimhan, B.; Kim, K. (Kevin); Pack, D.W. Microsphere size, precipitation kinetics and drug distribution control drug release from biodegradable polyanhydride microspheres. *J. Control. Release* **2004**, *94*, 129–141, doi:10.1016/j.jconrel.2003.09.011.
73. Brazel, C.S.; Peppas, N.A. Modeling of drug release from Swellable polymers. *Eur. J. Pharm. Biopharm.* **2000**, *49*, 47–58, doi:10.1016/S0939-6411(99)00058-2.
74. Mura, P.; Maestrelli, F.; González-Rodríguez, M.L.; Michelacci, I.; Ghelardini, C.; Rabasco, A.M. Development, characterization and in vivo evaluation of benzocaine-loaded liposomes. *Eur. J. Pharm. Biopharm.* **2007**, *67*, 86–95, doi:https://doi.org/10.1016/j.ejpb.2007.01.020.
75. González-Rodríguez, M.L.; Barros, L.B.; Palma, J.; González-Rodríguez, P.L.; Rabasco, A.M. Application of statistical experimental design to study the formulation variables influencing the coating process of lidocaine liposomes. *Int. J. Pharm.* **2007**, *337*, 336–345, doi:10.1016/j.ijpharm.2007.01.024.
76. Lamprecht, A.; Bodmeier, R. Microencapsulation. *Ullmann's Encycl. Ind. Chem.* 2000, 157–172.
77. Nack, H. Microencapsulation Techniques Applications and Problem. *J. Soc. Cosmet. Chem.* **1970**, *21*, 85–98.
78. Mishra, M. *Overview of Encapsulation and Controlled Release*; Munmaya Mishra, Ed.; 1st ed.; CRC Press: Boca Raton, 2015; ISBN 1482232340.
79. Costa, P.; Lobo, J.M.S. Modeling and comparison of dissolution profiles. *Eur. J. Pharm. Sci.* **2001**, *13*, 123–133, doi:https://doi.org/10.1016/S0928-0987(01)00095-1.
80. Feczko, T.; Kardos, A.F.; Németh, B.; Trif, L.; Gyenis, J. Microencapsulation of n-hexadecane phase change material by ethyl cellulose polymer. *Polym. Bull.* **2014**, *71*, 3289–3304, doi:10.1007/s00289-014-1250-y.
81. Loxley, A.; Vincent, B. Preparation of Poly(methylmethacrylate) Microcapsules with Liquid Cores. *J. Colloid Interface Sci.* **1998**, *208*, 49–62, doi:10.1006/jcis.1998.5698.
82. Zhang, Z.; Feng, S.-S. The drug encapsulation efficiency, in vitro drug release, cellular uptake and cytotoxicity of paclitaxel-loaded poly(lactide)–tocopheryl polyethylene glycol succinate nanoparticles. *Biomaterials* **2006**, *27*, 4025–4033, doi:10.1016/j.biomaterials.2006.03.006.
83. M. Dittrich J. Hampl, F.S. Branched oligoester microspheres fabricated by a rapid emulsion solvent extraction method. *J. Microencapsul.* **2000**, *17*, 587–598, doi:10.1080/026520400417649.
84. Pisani, E.; Fattal, E.; Paris, J.; Ringard, C.; Rosilio, V.; Tsapis, N. Surfactant dependent morphology of polymeric capsules of perfluorooctyl bromide: Influence of polymer adsorption at the dichloromethane–water interface. *J. Colloid Interface Sci.* **2008**, *326*, 66–71, doi:10.1016/j.jcis.2008.07.013.
85. Trojer, M.A.; Mohamed, A.; Eastoe, J. A highly hydrophobic anionic surfactant at oil–water, water–polymer and oil–polymer interfaces: Implications for spreading coefficients, polymer interactions and microencapsulation via internal phase separation. *Colloids Surfaces A*

- Physicochem. Eng. Asp.* **2013**, *436*, 1048–1059, doi:10.1016/j.colsurfa.2013.08.005.
86. Trongsatitkul, T.; Budhlall, B.M. Multicore–Shell PNIPAm-co-PEGMa Microcapsules for Cell Encapsulation. *Langmuir* **2011**, *27*, 13468–13480, doi:10.1021/la203030j.
  87. Torza, S.; Mason, S.G. Three-phase interactions in shear and electrical fields. *J. Colloid Interface Sci.* **1970**, *33*, 67–83, doi:10.1016/0021-9797(70)90073-1.
  88. Whelehan, M.; Marison, I.W. Microencapsulation using vibrating technology. *J. Microencapsul.* **2011**, *28*, 669–688, doi:10.3109/02652048.2011.586068.
  89. Singh, A.; Dhiman, N.; Kar, A.K.; Singh, D.; Purohit, M.P.; Ghosh, D.; Patnaik, S. Advances in controlled release pesticide formulations: Prospects to safer integrated pest management and sustainable agriculture. *J. Hazard. Mater.* **2020**, *385*, 121525 1–20, doi:10.1016/j.jhazmat.2019.121525.
  90. Oertli, J.J.; Lunt, O.R. Controlled Release of Fertilizer Minerals by Incapsulating Membranes: I. Factors Influencing the Rate of Release1. *Soil Sci. Soc. Am. J.* **1962**, *26*, 579–583, doi:10.2136/sssaj1962.03615995002600060019x.
  91. Allan, G.G.; Chopra, C.S.; Neogi, A.N.; Wilkins, R.M. Design and Synthesis of Controlled Release Pesticide-Polymer Combinations. *Nature* **1971**, *234*, 349–351, doi:10.1038/234349a0.
  92. Otey, F.H.; Trimnell, D.; Westhoff, R.P.; Shasha, B.S. Starch matrix for controlled release of urea fertilizer. *J. Agric. Food Chem.* **1984**, *32*, 1095–1098, doi:10.1021/jf00125a041.
  93. Knowles, A. *New Developments in Crop Protection Product Formulation*; T&F Informa UK Ltd: London, 2005;
  94. Knowles, A. Recent developments of safer formulations of agrochemicals. *Environmentalist* **2008**, *28*, 35–44, doi:10.1007/s10669-007-9045-4.
  95. McWhorter, C.G. Controlled Delivery of Crop-Protection Agents. *Weed Technol.* **1993**, *7*, 271, doi:10.1017/S0890037X0003726X.
  96. Kim, H.; Fassihi, R. A Ternary Polymeric Matrix System for Controlled Drug Delivery of Highly Soluble Drug with High Drug Loading Diltiazem Hydrochloride. *J. Kor. Pharm Sci.* **2001**, *31*, 19–25.
  97. Maitra, J.; Shukla, V.K. Cross-linking in Hydrogels - A Review. *Am. J. Polym. Sci.* **2014**, *4*, 25–31, doi:10.5923/j.ajps.20140402.01.
  98. Kashyap, P.L.; Xiang, X.; Heiden, P. Chitosan nanoparticle based delivery systems for sustainable agriculture. *Int. J. Biol. Macromol.* **2015**, *77*, 36–51, doi:10.1016/j.ijbiomac.2015.02.039.
  99. Jurić, S.; Šegota, S.; Vinceković, M. Influence of surface morphology and structure of alginate microparticles on the bioactive agents release behavior. *Carbohydr. Polym.* **2019**, *218*, 234–242, doi:10.1016/j.carbpol.2019.04.096.
  100. Hayashi, T.; Kanbe, H.; Okada, M.; Suzuki, M.; Ikeda, Y.; Onuki, Y.; Kaneko, T.; Sonobe, T. Formulation study and drug release mechanism of a new theophylline sustained-release preparation. *Int. J. Pharm.* **2005**, *304*, 91–101, doi:10.1016/j.ijpharm.2005.07.022.
  101. Wilkins, R.M. Controlled Release Technology, Agricultural. *Kirk-Othmer Encycl. Chem. Technol.* 2000.
  102. Shahidi, F.; Han, X. Encapsulation of food ingredients. *Crit. Rev. Food Sci. Nutr.* **1993**, *33*, 501–547, doi:10.1080/10408399309527645.
  103. Hickey, A.J.; Tian, Y.; Parasrampur, D.; Kanke, M. Biliary elimination of bromsulphthalein, phenolphthalein, and doxorubicin released from microspheres following intravenous administration. *Biopharm. Drug Dispos.* **1993**, *14*, 181–186, doi:10.1002/bdd.2510140209.
  104. Beck, L.R.; Cowsar, D.R.; Lewis, D.H.; Cosgrove, R.J.; Riddle, C.T.; Lowry, S.L.; Epperly, T.

- A New Long-Acting Injectable Microcapsule System for the Administration of Progesterone. *Fertil. Steril.* **1979**, *31*, 545–551, doi:10.1016/S0015-0282(16)44002-1.
105. Viswanathan, N.B.; Thomas, P.A.; Pandit, J.K.; Kulkarni, M.G.; Mashelkar, R.A. Preparation of non-porous microspheres with high entrapment efficiency of proteins by a (water-in-oil)-in-oil emulsion technique. *J. Control. Release* **1999**, *58*, 9–20, doi:10.1016/S0168-3659(98)00140-0.
  106. Sturesson, C.; Carlfors, J.; Edsman, K.; Andersson, M. Preparation of biodegradable poly(lactic-co-glycolic) acid microspheres and their in vitro release of timolol maleate. *Int. J. Pharm.* **1993**, *89*, 235–244, doi:10.1016/0378-5173(93)90249-F.
  107. Wang, H.T.; Schmitt, E.; Flanagan, D.R.; Linhardt, R.J. Influence of formulation methods on the in vitro controlled release of protein from poly (ester) microspheres. *J. Control. Release* **1991**, *17*, 23–31, doi:10.1016/0168-3659(91)90127-Y.
  108. Ito, F.; Fujimori, H.; Honnami, H.; Kawakami, H.; Kanamura, K.; Makino, K. Control of drug loading efficiency and drug release behavior in preparation of hydrophilic-drug-containing monodisperse PLGA microspheres. *J. Mater. Sci. Mater. Med.* **2010**, *21*, 1563–1571, doi:10.1007/s10856-010-3995-7.
  109. Lassalle, V.; Ferreira, M.L. PLA Nano- and Microparticles for Drug Delivery: An Overview of the Methods of Preparation. *Macromol. Biosci.* **2007**, *7*, 767–783, doi:10.1002/mabi.200700022.
  110. Kim, B.K.; Hwang, S.J.; Park, J.B.; Park, H.J. Preparation and characterization of drug-loaded polymethacrylate microspheres by an emulsion solvent evaporation method. *J. Microencapsul.* **2002**, *19*, 811–822, doi:10.1080/0265204021000022770.
  111. Li, M.; Rouaud, O.; Poncelet, D. Microencapsulation by solvent evaporation: State of the art for process engineering approaches. *Int. J. Pharm.* **2008**, *363*, 26–39, doi:10.1016/j.ijpharm.2008.07.018.
  112. Yang, Y.-Y.; Chung, T.-S.; Ng, N.P. Morphology, drug distribution, and in vitro release profiles of biodegradable polymeric microspheres containing protein fabricated by double-emulsion solvent extraction/evaporation method. *Biomaterials* **2001**, *22*, 231–241, doi:10.1016/S0142-9612(00)00178-2.
  113. Sansdrap, P.; Moës, A.J. Influence of manufacturing parameters on the size characteristics and the release profiles of nifedipine from poly(DL-lactide-co-glycolide) microspheres. *Int. J. Pharm.* **1993**, *98*, 157–164, doi:10.1016/0378-5173(93)90052-H.
  114. Gabor, F. Ketoprofen-poly(D,L-lactic-co-glycolic acid) microspheres: influence of manufacturing parameters and type of polymer on the release characteristics. *J. Microencapsul.* **1999**, *16*, 1–12, doi:10.1080/026520499289266.
  115. Mateovic, T.; Kriznar, B.; Bogataj, M.; Mrhar, A. The influence of stirring rate on biopharmaceutical properties of Eudragit RS microspheres. *J. Microencapsul.* **2002**, *19*, 29–36, doi:10.1080/02652040010055289.
  116. Gibson, J.W.; Holl, R.J.; Tipton, A.J. Emulsion-based processes for making microparticles 2002.
  117. Arshady, R. Preparation of biodegradable microspheres and microcapsules: 2. Polyactides and related polyesters. *J. Control. Release* **1991**, *17*, 1–21, doi:10.1016/0168-3659(91)90126-X.
  118. Suzuki, K.; Price, J.C. Microencapsulation and Dissolution Properties of a Neuroleptic in a Biodegradable Polymer, Poly(d,l-lactide). *J. Pharm. Sci.* **1985**, *74*, 21–24, doi:10.1002/jps.2600740106.
  119. Jalil, R.-U. Biodegradable Poly(Lactic Acid) and Poly (Lactide-Co-Glycolide) Polymers in Sustained Drug Delivery. *Drug Dev. Ind. Pharm.* **1990**, *16*, 2353–2367,

- doi:10.3109/03639049009058535.
120. Jelvehgari, M.; Barar, J.; Valizadeh, H.; Heidari, N. Preparation and Evaluation of Poly ( $\epsilon$ -caprolactone) Nanoparticles-in- Microparticles by W/O/W Emulsion Method. *Iran. J. Basic Med. Sci. Iran J Basic Med Sci Iran J Basic Med Sci* **2010**, *13*, 85–96.
  121. Nihant, N.; Schugens, C.; Grandfils, C.; Jérôme, R.; Teyssié, P. Polylactide Microparticles Prepared by Double Emulsion/Evaporation Technique. I. Effect of Primary Emulsion Stability. *Pharm. Res.* **1994**, *11*, 1479–1484, doi:10.1023/A:1018912426983.
  122. Ito, F.; Fujimori, H.; Honnami, H.; Kawakami, H.; Kanamura, K.; Makino, K. Study of types and mixture ratio of organic solvent used to dissolve polymers for preparation of drug-containing PLGA microspheres. *Eur. Polym. J.* **2009**, *45*, 658–667, doi:https://doi.org/10.1016/j.eurpolymj.2008.12.037.
  123. Jyothi, N.V.N.; Prasanna, P.M.; Sakarkar, S.N.; Prabha, K.S.; Ramaiah, P.S.; Srawan, G.Y. Microencapsulation techniques, factors influencing encapsulation efficiency. *J. Microencapsul.* **2010**, *27*, 187–197, doi:10.3109/02652040903131301.
  124. Orsolini, P.; Vuaridel, E. One-step dispersion method for the microencapsulation of water soluble substances 2000.
  125. Rickey, M.E.; Ramstack, J.M.; Lewis, D.H. Preparation of biodegradable, biocompatible microparticles containing a biologically active agent 2002.
  126. Chaisri, W.; Hennink, W.E.; Ampasavate, C.; Okonogi, S. Cephalexin Microspheres for Dairy Mastitis: Effect of Preparation Method and Surfactant Type on Physicochemical Properties of the Microspheres. *AAPS PharmSciTech* **2010**, *11*, 945–951, doi:10.1208/s12249-010-9453-5.
  127. Passerini, N.; Craig, D.Q.M. An investigation into the effects of residual water on the glass transition temperature of polylactide microspheres using modulated temperature DSC. *J. Control. Release* **2001**, *73*, 111–115, doi:10.1016/S0168-3659(01)00245-0.
  128. Wischke, C.; Schwendeman, S.P. Principles of encapsulating hydrophobic drugs in PLA/PLGA microparticles. *Int. J. Pharm.* **2008**, *364*, 298–327, doi:10.1016/j.ijpharm.2008.04.042.
  129. Iwata, M.; McGinity, J.W. Preparation of multi-phase microspheres of poly(D,L-lactic acid) and poly(D,L-lactic-co-glycolic acid) containing a W/O emulsion by a multiple emulsion solvent evaporation technique. *J. Microencapsul.* **1991**, *9*, 201–214, doi:10.3109/02652049109021237.
  130. Thakur, V.K.; Thakur, M.K. Recent Advances in Graft Copolymerization and Applications of Chitosan: A Review. *ACS Sustain. Chem. Eng.* **2014**, *2*, 2637–2652, doi:10.1021/sc500634p.
  131. Fernández-Pérez, M.; Garrido-Herrera, F.J.; González-Pradas, E.; Masuda, M.; Johanningsmeier, J.S.; Formulation, P.; Gouge, T.; Development, F.; Bash, E. Chapter 4 Pesticide Formulation. *PhD Propos.* **2011**, *190*, 85–108, doi:10.1017/CBO9781107415324.004.
  132. Rashidzadeh, A.; Olad, A. Slow-released NPK fertilizer encapsulated by NaAlg-g-poly(AA-co-AAm)/MMT superabsorbent nanocomposite. *Carbohydr. Polym.* **2014**, *114*, 269–278, doi:10.1016/j.carbpol.2014.08.010.
  133. Roy, A.; Bajpai, J.; Bajpai, A.K. Dynamics of controlled release of chlorpyrifos from swelling and eroding biopolymeric microspheres of calcium alginate and starch. *Carbohydr. Polym.* **2009**, *76*, 222–231, doi:10.1016/j.carbpol.2008.10.013.
  134. Singh, B.; Sharma, D.K.; Negi, S.; Dhiman, A. Synthesis and characterization of agar-starch based hydrogels for slow herbicide delivery applications. *Int. J. Plast. Technol.* **2015**, *19*, 263–274, doi:10.1007/s12588-015-9126-z.



135. Mujtaba, M.; Khawar, K.M.; Camara, M.C.; Carvalho, L.B.; Fraceto, L.F.; Morsi, R.E.; Elsabee, M.Z.; Kaya, M.; Labidi, J.; Ullah, H.; et al. Chitosan-based delivery systems for plants: A brief overview of recent advances and future directions. *Int. J. Biol. Macromol.* **2020**, *154*, 683–697, doi:10.1016/j.ijbiomac.2020.03.128.
136. Hussain, M.R.; Devi, R.R.; Maji, T.K. Controlled release of urea from chitosan microspheres prepared by emulsification and cross-linking method. *Iran. Polym. J.* **2012**, *21*, 473–479, doi:10.1007/s13726-012-0051-0.
137. Thakur, V.K.; Thakur, M.K. Recent trends in hydrogels based on psyllium polysaccharide: a review. *J. Clean. Prod.* **2014**, *82*, 1–15, doi:10.1016/j.jclepro.2014.06.066.
138. Thakur, V.K.; Thakur, M.K. Recent advances in green hydrogels from lignin: a review. *Int. J. Biol. Macromol.* **2015**, *72*, 834–847, doi:10.1016/j.ijbiomac.2014.09.044.
139. Saravanan, M.; Rao, K.P. Pectin–gelatin and alginate–gelatin complex coacervation for controlled drug delivery: Influence of anionic polysaccharides and drugs being encapsulated on physicochemical properties of microcapsules. *Carbohydr. Polym.* **2010**, *80*, 808–816, doi:10.1016/j.carbpol.2009.12.036.
140. Holland, T.A.; Tabata, Y.; Mikos, A.G. Dual growth factor delivery from degradable oligo(poly(ethylene glycol) fumarate) hydrogel scaffolds for cartilage tissue engineering. *J. Control. Release* **2005**, *101*, 111–125, doi:10.1016/j.jconrel.2004.07.004.
141. Chang, C.-P.; Leung, T.-K.; Lin, S.-M.; Hsu, C.-C. Release properties on gelatin-gum arabic microcapsules containing camphor oil with added polystyrene. *Colloids Surfaces B Biointerfaces* **2006**, *50*, 136–140, doi:10.1016/j.colsurfb.2006.04.008.
142. Way, D.V.; Nele, M.; Pinto, J.C. Preparation of gelatin beads treated with glucose and glycerol. *Polimeros* **2018**, *28*, 468–476, doi:10.1590/0104-1428.04317.
143. Miao, T.; Miller, E.J.; McKenzie, C.; Oldinski, R.A. Physically crosslinked polyvinyl alcohol and gelatin interpenetrating polymer network theta-gels for cartilage regeneration. *J. Mater. Chem. B* **2015**, *3*, 9242–9249, doi:10.1039/c5tb00989h.
144. Alves, P.M.A.; Carvalho, R.A.; Moraes, I.C.F.; Luciano, C.G.; Bittante, A.M.Q.B.; Sobral, P.J.A. Development of films based on blends of gelatin and poly(vinyl alcohol) cross linked with glutaraldehyde. *Food Hydrocoll.* **2011**, *25*, 1751–1757, doi:10.1016/j.foodhyd.2011.03.018.
145. Zhu, X.; Zhang, Y.; Deng, J.; Luo, X. Effect of Glycerol on the Properties of the Cross-Linked Polyvinyl Alcohol Hydrogel Beads. *ChemistrySelect* **2018**, *3*, 467–470, doi:10.1002/slct.201701975.
146. He, F.; Zhou, Q.; Wang, L.; Yu, G.; Li, J.; Feng, Y. Fabrication of a sustained release delivery system for pesticides using interpenetrating polyacrylamide/alginate/montmorillonite nanocomposite hydrogels. *Appl. Clay Sci.* **2019**, *183*, 1–10, doi:10.1016/j.clay.2019.105347.
147. Borges, D.F.; Lopes, E.A.; Fialho Moraes, A.R.; Soares, M.S.; Visôto, L.E.; Oliveira, C.R.; Moreira Valente, V.M. Formulation of botanicals for the control of plant-pathogens: A review. *Crop Prot.* **2018**, *110*, 135–140, doi:10.1016/j.cropro.2018.04.003.
148. Ferreira, F.; Cividanes, L.; Gouveia, R.F.; Lona, L. An overview on properties and applications of poly(butylene adipate-co-terephthalate)–PBAT based composites. *Polym. Eng. Sci.* **2019**, *58*, E7–E15, doi:10.1002/pen.24770.
149. Fizur Rahman, M.; Islam, J.M.M.; Hassan, M.M.; Ahsan Habib, S.M.; Pervez, M.S.; Khan, M.A. Development of urea crosslinked thin film for biomedical application. *Int. J. Polym. Mater. Polym. Biomater.* **2013**, *62*, 695–699, doi:10.1080/00914037.2013.769228.
150. Chang, C.; Duan, B.; Cai, J.; Zhang, L. Superabsorbent hydrogels based on cellulose for smart swelling and controllable delivery. *Eur. Polym. J.* **2010**, *46*, 92–100,

- doi:<https://doi.org/10.1016/j.eurpolymj.2009.04.033>.
151. Lee, J.; Cuddihy, M.J.; Kotov, N.A. Three-Dimensional Cell Culture Matrices: State of the Art. *Tissue Eng. Part B Rev.* **2008**, *14*, 61–86, doi:10.1089/teb.2007.0150.
  152. Nguyen, K.T.; West, J.L. Photopolymerizable hydrogels for tissue engineering applications. *Biomaterials* **2002**, *23*, 4307–4314, doi:[https://doi.org/10.1016/S0142-9612\(02\)00175-8](https://doi.org/10.1016/S0142-9612(02)00175-8).
  153. Aly, A.S. Self-dissolving chitosan, I. Preparation, characterization and evaluation for drug delivery system. *Die Angew. Makromol. Chemie* **1998**, *259*, 13–18, doi:doi:10.1002/(SICI)1522-9505(19981001)259:1<13::AID-APMC13>3.0.CO;2-T.
  154. Connell, J.J. The role of formaldehyde as a protein crosslinking agent acting during the frozen storage of cod. *J. Sci. Food Agric.* **1975**, *26*, 1925–1929, doi:doi:10.1002/jsfa.2740261216.
  155. Weiner, A.A.; Moore, M.C.; Walker, A.H.; Shastri, V.P. Modulation of protein release from photocrosslinked networks by gelatin microparticles. *Int. J. Pharm.* **2008**, *360*, 107–114, doi:10.1016/j.ijpharm.2008.04.037.
  156. He, S.; Zhang, W.; Li, D.; Li, P.; Zhu, Y.; Ao, M.; Li, J.; Cao, Y. Preparation and characterization of double-shelled avermectin microcapsules based on copolymer matrix of silica–glutaraldehyde–chitosan. *J. Mater. Chem. B* **2013**, *1*, 1270, doi:10.1039/c2tb00234e.
  157. Miyazaki, T.; Takeda, Y.; Akane, S.; Itou, T.; Hoshiko, A.; En, K. Role of boric acid for a poly (vinyl alcohol) film as a cross-linking agent: Melting behaviors of the films with boric acid. *Polymer (Guildf)*. **2010**, *51*, 5539–5549, doi:10.1016/j.polymer.2010.09.048.
  158. Xu, X.; Weng, Y.; Xu, L.; Chen, H. Sustained release of avastin® from polysaccharides cross-linked hydrogels for ocular drug delivery. *Int. J. Biol. Macromol.* **2013**, *60*, 272–276, doi:10.1016/j.ijbiomac.2013.05.034.
  159. Raut, N.S.; Deshmukh, P.R.; Umekar, M.J.; Kotagale, N.R. Zinc cross-linked hydroxamated alginates for pulsed drug release. *Int. J. Pharm. Investig.* **2013**, *3*, 194–202, doi:10.4103/2230-973X.121292.
  160. Coviello, T.; Grassi, M.; Lapasin, R.; Marino, A.; Alhaique, F. Scleroglucan/borax: characterization of a novel hydrogel system suitable for drug delivery. *Biomaterials* **2003**, *24*, 2789–2798, doi:[https://doi.org/10.1016/S0142-9612\(03\)00087-5](https://doi.org/10.1016/S0142-9612(03)00087-5).
  161. Gómez-Mascaraque, L.G.; Méndez, J.A.; Fernández-Gutiérrez, M.; Vázquez, B.; Román, J. [San Oxidized dextrans as alternative crosslinking agents for polysaccharides: Application to hydrogels of agarose–chitosan. *Acta Biomater.* **2014**, *10*, 798–811, doi:10.1016/j.actbio.2013.10.003.
  162. Maestrelli, F.; Zerrouk, N.; Cirri, M.; Mennini, N.; Mura, P. Microspheres for colonic delivery of ketoprofen-hydroxypropyl- $\beta$ -cyclodextrin complex. *Eur. J. Pharm. Sci.* **2008**, *34*, 1–11, doi:10.1016/j.ejps.2008.02.001.
  163. Emeline, A. V.; Kuznetsov, V.N.; Ryabchuk, V.K.; Serpone, N. Heterogeneous Photocatalysis: Basic Approaches and Terminology. In *New and Future Developments in Catalysis: Solar Photocatalysis*; Elsevier B.V., 2013; pp. 1–47 ISBN 9780444538727.
  164. Nowotny, J. *Oxide semiconductors for solar energy conversion: titanium dioxide*; 2012; Vol. 37; ISBN 9781439848395.
  165. Cargnello, M.; Fornasiero, P. Photocatalysis by Nanostructured TiO<sub>2</sub>-based Semiconductors. In *Cargnello*; Perosa, A., Selva, M., Eds.; Wiley-VCH Verlag GmbH & Co. KGaA, 2012; Vol. 8, pp. 89–136.
  166. Peter, L.M.; Jalinous, R. Photoelectrochemistry: From Basic Principles to Photocatalysis. In *Photocatalysis: Fundamentals and Perspectives*; The Royal Society of Chemistry, 2016; pp.

- 1–28 ISBN 978-1-78262-041-9.
167. Wang, C.; Ao, Y.; Wang, P.; Hou, J.; Qian, J. A facile method for the preparation of titania-coated magnetic porous silica and its photocatalytic activity under UV or visible light. *Colloids Surfaces A Physicochem. Eng. Asp.* **2010**, *360*, 184–189, doi:https://doi.org/10.1016/j.colsurfa.2010.02.030.
  168. Herrmann, J.-M. *Photocatalysis*; John Wiley & Sons, Inc., 2017; ISBN 0471238961.
  169. Decroly, A.; Krumpmann, A.; Debliquy, M.; Lahem, D. Nanostructured TiO<sub>2</sub> Layers for Photovoltaic and Gas Sensing Applications. In *Green Nanotechnology - Overview and Further Prospects*; Larramendy, M.L., Soloneski, S.B.T.-G.N.-O. and F.P., Eds.; InTech: Rijeka, 2016; pp. 117–146.
  170. Fujishima, A.; Zhang, X.; Tryk, D.A. TiO<sub>2</sub> photocatalysis and related surface phenomena. *Surf. Sci. Rep.* **2008**, *63*, 515–582, doi:10.1016/j.surfrep.2008.10.001.
  171. Fujishima, A.; Rao, T.N.; Tryk, D.A. Titanium dioxide photocatalysis. *J. Photochem. Photobiol. C Photochem. Rev.* **2000**, *1*, 1–21, doi:10.1016/S1389-5567(00)00002-2.
  172. Ikeda, K.; Sakai, H.; Baba, R.; Hashimoto, K.; Fujishima, A. Photocatalytic Reactions Involving Radical Chain Reactions Using Microelectrodes. *J. Phys. Chem. B* **1997**, *101*, 2617–2620, doi:10.1021/jp9627281.
  173. Sakai, H.; Baba, R.; Hashimoto, K.; Fujishima, A.; Heller, A. Local Detection of Photoelectrochemically Produced H<sub>2</sub>O<sub>2</sub> with a “Wired” Horseradish Peroxidase Microsensor. *J. Phys. Chem.* **1995**, *99*, 11896–11900, doi:10.1021/j100031a017.
  174. Wang, R.; Hashimoto, K.; Fujishima, A.; Chikuni, M.; Kojima, E.; Kitamura, A.; Shimohigoshi, M.; Watanabe, T. Light-induced amphiphilic surfaces. *Nature* **1997**, *388*, 431.
  175. Wang, W.; Xiong, Y.; Du, F.-Y.; Huang, W.-H.; Wu, W.-Z.; Wang, Z.-L.; Cheng, J.-K.; Yang, Y.-F. Imaging and detection of morphological changes of single cells before and after secretion using scanning electrochemical microscopy. *Analyst* **2007**, *132*, 515–518.
  176. Pookmanee, P.; Phanichphant, S. Titanium dioxide powder prepared by a sol-gel method. *J. Ceram. Process. Res.* **2009**, *10*, 167–170, doi:10.36410/jcpr.2009.10.2.167.
  177. Sclafani, A.; Palmisano, L.; Schiavello, M. Influence of the preparation methods of titanium dioxide on the photocatalytic degradation of phenol in aqueous dispersion. *J. Phys. Chem.* **1990**, *94*, 829–832, doi:10.1021/j100365a058.
  178. Penn, R.L.; Banfield, J.F. Morphology development and crystal growth in nanocrystalline aggregates under hydrothermal conditions: Insights from titania. *Geochim. Cosmochim. Acta* **1999**, *63*, 1549–1557, doi:10.1016/S0016-7037(99)00037-X.
  179. Zaban, A.; Aruna, S.T.; Tirosh, S.; Gregg, B.A.; Mastai, Y. The Effect of the Preparation Condition of TiO<sub>2</sub> Colloids on Their Surface Structures. *J. Phys. Chem. B* **2000**, *104*, 4130–4133, doi:10.1021/jp993198m.
  180. Oskam, G.; Nellore, A.; Penn, R.L.; Searson, P.C. The Growth Kinetics of TiO<sub>2</sub> Nanoparticles from Titanium(IV) Alkoxide at High Water/Titanium Ratio. *J. Phys. Chem. B* **2003**, *107*, 1734–1738, doi:10.1021/jp021237f.
  181. Carp, O.; Huisman, C.L.; Reller, A. Photoinduced reactivity of titanium dioxide. *Prog. Solid State Chem.* **2004**, *32*, 33–177, doi:https://doi.org/10.1016/j.progsolidstchem.2004.08.001.
  182. Zhang, Z.; Wang, C.-C.; Zakaria, R.; Ying, J.Y. Role of Particle Size in Nanocrystalline TiO<sub>2</sub>-Based Photocatalysts. *J. Phys. Chem. B* **1998**, *102*, 10871–10878, doi:10.1021/jp982948+.
  183. Vase, K.H.; Holm, A.H.; Norrman, K.; Pedersen, S.U.; Daasbjerg, K. No Title. *Langmuir* **2008**, *24*, 182.

184. Zhang, H.; Banfield, J. Thermodynamic analysis of phase stability of nanocrystalline titania. *J. Mater. Chem.* **1998**, *8*, 2073–2076, doi:10.1039/A802619J.
185. Zhang, H.; Banfield, J.F. Understanding Polymorphic Phase Transformation Behavior during Growth of Nanocrystalline Aggregates: Insights from TiO<sub>2</sub>. *J. Phys. Chem. B* **2000**, *104*, 3481–3487, doi:10.1021/jp000499j.
186. Anderson, M.A.; Gieselmann, M.J.; Xu, Q. Titania and alumina ceramic membranes. *J. Memb. Sci.* **1988**, *39*, 243–258, doi:10.1016/S0376-7388(00)80932-1.
187. Navrotsky, A. Energetics of nanoparticle oxides: interplay between surface energy and polymorphism. *Geochem. Trans.* **2003**, *4*, 34, doi:10.1186/1467-4866-4-34.
188. Naicker, P.K.; Cummings, P.T.; Zhang, H.; Banfield, J.F. Characterization of Titanium Dioxide Nanoparticles Using Molecular Dynamics Simulations. *J. Phys. Chem. B* **2005**, *109*, 15243–15249, doi:10.1021/jp050963q.
189. Dambournet, D.; Belharouak, I.; Amine, K. Tailored Preparation Methods of TiO<sub>2</sub> Anatase, Rutile, Brookite: Mechanism of Formation and Electrochemical Properties. *Chem. Mater.* **2010**, *22*, 1173–1179, doi:10.1021/cm902613h.
190. Ocaña, M.; Garcia-Ramos, J. V; Serna, C.J. Low-Temperature Nucleation of Rutile Observed by Raman Spectroscopy during Crystallization of TiO<sub>2</sub>. *J. Am. Ceram. Soc.* **1992**, *75*, 2010–2012, doi:10.1111/j.1151-2916.1992.tb07237.x.
191. Bakardjieva, S.; Stengl, V.; Szatmary, L.; Subrt, J.; Lukac, J.; Murafa, N.; Niznansky, D.; Cizek, K.; Jirkovsky, J.; Petrova, N. Transformation of brookite-type TiO<sub>2</sub> nanocrystals to rutile: correlation between microstructure and photoactivity. *J. Mater. Chem.* **2006**, *16*, 1709–1716, doi:10.1039/B514632A.
192. Li, G.; Li, L.; Boerio-Goates, J.; Woodfield, B.F. High Purity Anatase TiO<sub>2</sub> Nanocrystals: Near Room-Temperature Synthesis, Grain Growth Kinetics, and Surface Hydration Chemistry. *J. Am. Chem. Soc.* **2005**, *127*, 8659–8666, doi:10.1021/ja050517g.
193. Mahouche, S.; Mekni, N.; Abbassi, L.; Lang, P.; Perruchot, C.; Jouini, M.; Mammeri, F.; Turmine, M.; Romdhane, H. Ben; Chehimi, M.M. Tandem diazonium salt electroreduction and click chemistry as a novel, efficient route for grafting macromolecules to gold surface. *Surf. Sci.* **2009**, *603*, 3205–3211, doi:10.1016/j.susc.2009.09.004.
194. Baur, W.H. Atomabstände und Bindungswinkel im Brookit, TiO<sub>2</sub>. *Acta Crystallogr.* **1961**, *14*, 214–216, doi:10.1107/S0365110X61000747.
195. Mo, S.-D.; Ching, W.Y. Electronic and optical properties of three phases of titanium dioxide: Rutile, anatase, and brookite. *Phys. Rev. B* **1995**, *51*, 13023–13032, doi:10.1103/PhysRevB.51.13023.
196. Thompson, T.L.; Yates, J.T. Surface Science Studies of the Photoactivation of TiO<sub>2</sub>New Photochemical Processes. *Chem. Rev.* **2006**, *106*, 4428–4453, doi:10.1021/cr050172k.
197. Banerjee, S.; Gopal, J.; Muraleedharan, P.; Tyagi, A.K.; Raj, B. Physics and chemistry of photocatalytic titanium dioxide: Visualization of bactericidal activity using atomic force microscopy. *Curr. Sci.* **2006**, *90*, 1378–1383.
198. Linsebigler, A.L.; Lu, G.; Yates, J.T. Photocatalysis on TiO<sub>2</sub> Surfaces: Principles, Mechanisms, and Selected Results. *Chem. Rev.* **1995**, *95*, 735–758, doi:10.1021/cr00035a013.
199. Diebold, U. Structure and properties of TiO<sub>2</sub> surfaces: A brief review. *Appl. Phys. A Mater. Sci. Process.* **2003**, *76*, 681–687, doi:10.1007/s00339-002-2004-5.
200. Nozik, A.J.; Memming, R. Physical Chemistry of Semiconductor–Liquid Interfaces. *J. Phys. Chem.* **1996**, *100*, 13061–13078, doi:10.1021/jp953720e.

201. Rahimi, N.; Pax, R.A.; Gray, E.M.A. Review of functional titanium oxides. I: TiO<sub>2</sub> and its modifications. *Prog. Solid State Chem.* **2016**, *44*, 86–105, doi:10.1016/j.progsolidstchem.2016.07.002.
202. Herrmann, J.-M.; Disdier, J.; Pichat, P. Effect of chromium doping on the electrical and catalytic properties of powder titania under UV and visible illumination. *Chem. Phys. Lett.* **1984**, *108*, 618–622, doi:10.1016/0009-2614(84)85067-8.
203. Khataee, A.; Mansoori, G.A. *Nanostructured Titanium Dioxide Materials Properties, Preparation and Applications*; World Scientific Publishing Co. Pte. Ltd.: Singapore, 2012; Vol. 297; ISBN 9789814374729.
204. Choi, W.; Termin, A.; Hoffmann, M.R. Effects of Metal-Ion Dopants on the Photocatalytic Reactivity of Quantum-Sized TiO<sub>2</sub> Particles. *Angew. Chemie Int. Ed. English* **1994**, *33*, 1091–1092, doi:10.1002/anie.199410911.
205. Choi, W.; Termin, A.; Hoffmann, M.R. The Role of Metal Ion Dopants in Quantum-Sized TiO<sub>2</sub>: Correlation between Photoreactivity and Charge Carrier Recombination Dynamics. *J. Phys. Chem.* **1994**, *98*, 13669–13679, doi:10.1021/j100102a038.
206. He, H. Metal oxide semiconductors and conductors. In *Solution Processed Metal Oxide Thin Films for Electronic Applications*; Cui, Z., Korotcenkov, G., Eds.; Elsevier Inc.: Amsterdam, 2020; pp. 7–30 ISBN 9780128149300.
207. Özgür, Ü.D.; Avrutin, V.; Morkoç, H. Zinc oxide materials and devices grown by MBE. In *Molecular Beam Epitaxy*; Henini, M., Ed.; Elsevier Inc.: Waltham, 2013; pp. 369–416 ISBN 9780123878397.
208. Sharma, D.K.; Shukla, S.; Sharma, K.K.; Kumar, V. A review on ZnO: Fundamental properties and applications. In *Proceedings of the Materials Today: Proceedings*; Elsevier Ltd., 2020.
209. Morkoç, H.; Özgür, Ü. General properties of ZnO. In *Zinc Oxide: Fundamentals, Materials and Device Technology*; WILEY-VCH Verlag GmbH & Co. KGaA: Weinheim, 2009; pp. 1–76 ISBN 9783527408139.
210. Klingshirn, C.F.; Meyer, B.F.; Waag, A.; Hoffmann, A.; Geurts, J. *Zinc Oxide From Fundamental Properties Towards Novel Applications*; Springer, Berlin, Heidelberg, 2010; ISBN 0898520479.
211. Ashrafi, A.; Jagadish, C. Review of zincblende ZnO: Stability of metastable ZnO phases. *J. Appl. Phys.* **2007**, *102*, 0711011-1–12, doi:10.1063/1.2787957.
212. Song, J.; Wang, X.; Liu, J.; Liu, H.; Li, Y.; Wang, Z.L. Piezoelectric Potential Output from ZnO Nanowire Functionalized with p-Type Oligomer. *Nano Lett.* **2008**, *8*, 203–207, doi:10.1021/nl072440v.
213. Kogure, T.; Bando, Y. Formation of ZnO nanocrystallites on ZnS surfaces by electron beam irradiation. *J. Electron Microsc. (Tokyo)*. **1998**, *47*, 135–141, doi:10.1093/oxfordjournals.jmicro.a023570.
214. Zhang, M.; Liu, K.; Xiang, L.; Lin, Y.; Su, L.; Mao, L. Carbon Nanotube-Modified Carbon Fiber Microelectrodes for In Vivo Voltammetric Measurement of Ascorbic Acid in Rat Brain. *Anal. Chem.* **2007**, *79*, 6559–6565, doi:doi.org/10.1021/ac0705871.
215. Lee, G.H.; Kawazoe, T.; Ohtsu, M. Room temperature near-field photoluminescence of zinc-blend and wurtzite ZnO structures. *Appl. Surf. Sci.* **2005**, *239*, 394–397, doi:10.1016/j.apsusc.2004.06.004.
216. Jaffe, J.E.; Hess, A.C. Hartree-Fock study of phase changes in ZnO at high pressure. *Phys. Rev. B* **1993**, *48*, 7903–7909, doi:10.1103/physrevb.48.7903.
217. Recio, J.; Blanco, M.; Luaña, V.; Pandey, R. Compressibility of the high-pressure rocksalt phase of ZnO. *Phys. Rev. B - Condens. Matter Mater. Phys.* **1998**, *58*, 8949–8954,

- doi:10.1103/PhysRevB.58.8949.
218. Boon, C.; Yong, L.; Wahab, A. A review of ZnO nanoparticles as solar photocatalysts : Synthesis , mechanisms and applications. *Renew. Sustain. Energy Rev.* **2018**, *81*, 536–551, doi:10.1016/j.rser.2017.08.020.
  219. Oshikiri, M.; Aryasetiawan, F. Band gaps and quasiparticle energy calculations on ZnO, ZnS, and ZnSe in the zinc-blende structure by the GW approximation. *Phys. Rev. B* **1999**, *60*, 10754–10757, doi:10.1103/PhysRevB.60.10754.
  220. Tryk, D.A.; Fujishima, A.; Honda, K. Recent topics in photoelectrochemistry: achievements and future prospects. *Electrochim. Acta* **2000**, *45*, 2363–2376, doi:10.1016/S0013-4686(00)00337-6.
  221. Hagfeldt, A.; Graetzel, M. Light-Induced Redox Reactions in Nanocrystalline Systems. *Chem. Rev.* **1995**, *95*, 49–68, doi:10.1021/cr00033a003.
  222. Fox, M.A.; Dulay, M.T. Heterogeneous photocatalysis. *Chem. Rev.* **1993**, *93*, 341–357, doi:10.1021/cr00017a016.
  223. Hoffmann, M.R.; Martin, S.T.; Choi, W.; Bahnemann, D.W. Environmental Applications of Semiconductor Photocatalysis. *Chem. Rev.* **1995**, *95*, 69–96, doi:10.1021/cr00033a004.
  224. Lan, Y.; Lu, Y.; Ren, Z. Mini review on photocatalysis of titanium dioxide nanoparticles and their solar applications. *Nano Energy* **2013**, *2*, 1031–1045, doi:10.1016/j.nanoen.2013.04.002.
  225. Tavares, C.J.; Vieira, J.; Rebouta, L.; Hungerford, G.; Coutinho, P.; Teixeira, V.; Carneiro, J.O.; Fernandes, A.J. Reactive sputtering deposition of photocatalytic TiO<sub>2</sub> thin films on glass substrates. *Mater. Sci. Eng. B Solid-State Mater. Adv. Technol.* **2007**, *138*, 139–143, doi:10.1016/j.mseb.2005.11.043.
  226. Tavares, C.J.; Marques, S.M.; Viseu, T.; Teixeira, V.; Carneiro, J.O.; Alves, E.; Barradas, N.P.; Munnik, F.; Girardeau, T.; Rivire, J.P. Enhancement in the photocatalytic nature of nitrogen-doped PVD-grown titanium dioxide thin films. *J. Appl. Phys.* **2009**, *106*, 113535 1–8, doi:10.1063/1.3269702.
  227. Ng, S.M.; Wong, D.S.N.; Phung, J.H.C.; Chua, H.S. Integrated miniature fluorescent probe to leverage the sensing potential of ZnO quantum dots for the detection of copper (II) ions. *Talanta* **2013**, *116*, 514–519, doi:10.1016/j.talanta.2013.07.031.
  228. Dai, Y.; Zhang, Y.; Li, Q.; Nan, C. Synthesis and optical properties of tetrapod-like zinc oxide nanorods. *Chem. Phys. Lett.* **2002**, *358*, 83–86, doi:10.1016/S0009-2614(02)00582-1.
  229. Yang, Y.; Jin, Y.; He, H.; Wang, Q.; Tu, Y.; Lu, H.; Ye, Z. Dopant-Induced Shape Evolution of Colloidal Nanocrystals: The Case of Zinc Oxide. *J. Am. Chem. Soc.* **2010**, *132*, 13381–13394, doi:10.1021/ja103956p.
  230. Rosenberg, R.A.; Shenoy, G.K.; Chisholm, M.F.; Tien, L.; Norton, D.; Pearton, S. Getting to the Core of the Problem: Origin of the Luminescence from (Mg,Zn)O Heterostructured Nanowires. *Nano Lett.* **2007**, *7*, 1521–1525, doi:10.1021/nl0702923.
  231. Hou, D.; Ma, Y.; Gao, C.; Chaudhuri, J.; Lee, R.G.; Yang, H. Compression of a crystalline ZnO nanotube: An experimental exploration of the B4 to B1 transition mechanism. *J. Appl. Phys. (Melville, NY, U.S.)* **2009**, *105*, 104317 1–4, doi:10.1063/1.3132095.
  232. Kong, X.Y.; Wang, Z.L. Spontaneous Polarization-Induced Nanohelices, Nanosprings, and Nanorings of Piezoelectric Nanobelts. *Nano Lett.* **2003**, *3*, 1625–1631, doi:10.1021/nl034463p.
  233. Djurišić, A.B.; Leung, Y.H. Optical Properties of ZnO Nanostructures. *Small* **2006**, *2*, 944–961.
  234. Zhang, Q.; Dandeneau, C.S.; Zhou, X.; Cao, G. ZnO Nanostructures for Dye-Sensitized Solar

- Cells. *Adv. Mater.* **2009**, *21*, 4087–4108, doi:10.1002/adma.200803827.
235. Wan, Q.; Li, Q.H.; Chen, Y.J.; Wang, T.H.; He, X.L.; Li, J.P.; Lin, C.L. Fabrication and ethanol sensing characteristics of ZnO nanowire gas sensors. *Appl. Phys. Lett.* **2004**, *84*, 3654–3656, doi:10.1063/1.1738932.
  236. Özgür, U.; Alivov, Y.I.; Liu, C.; Teke, A.; Reshchikov, M.A.; Doan, S.; Avrutin, V.; Cho, S.-J.; Morko, H. A comprehensive review of ZnO materials and devices. *J. Appl. Phys. (Melville, NY, U.S.)* **2005**, *98*, 41301 1–103, doi:10.1063/1.1992666.
  237. Hamad, S.; Azeez, H. Structure , Synthesis and Applications of ZnO Nanoparticles : *Jordan J. Phys.* **2020**, *13*, 123–135.
  238. Sabir, S.; Arshad, M.; Chaudhari, S.K. Zinc oxide nanoparticles for revolutionizing agriculture: Synthesis and applications. *Sci. World J.* **2014**, 1–8, doi:10.1155/2014/925494.
  239. Auer, G.; Woditsch, P.; Westerhaus, A.; Kischkewitz, J.; Griebler, W.-D.; Rohe, M.; Liedekerke, M. Pigments, Inorganic, 2. White Pigments. In *Ullmann's Encyclopedia of Industrial Chemistry*, Wiley-VCH Verlag GmbH & Co. KGaA: Weinheim, 2017; pp. 1–36.
  240. Abebe, B.; Zereffa, E.A.; Tadesse, A.; Murthy, H.C.A. A Review on Enhancing the Antibacterial Activity of ZnO: Mechanisms and Microscopic Investigation. *Nanoscale Res. Lett.* **2020**, *15*, 1–19.
  241. Liu, L.; Chen, X. Titanium Dioxide Nanomaterials: Self-Structural Modifications. *Chem. Rev.* **2014**, *114*, 9890–9918, doi:10.1021/cr400624r.
  242. Kusior, A.; Banas, J.; Trenczek-Zajac, A.; Zubrzycka, P.; Micek-Ilnicka, A.; Radecka, M. Structural properties of TiO<sub>2</sub> nanomaterials. *J. Mol. Struct.* **2018**, *1157*, 327–336, doi:10.1016/j.molstruc.2017.12.064.
  243. Wang, C.; Ao, Y.; Wang, P.; Hou, J.; Qian, J. Photocatalytic performance of Gd ion modified titania porous hollow spheres under visible light. *Mater. Lett.* **2010**, *64*, 1003–1006, doi:10.1016/j.matlet.2010.02.013.
  244. Yu, J.C.; Zhang, L.; Zheng, Z.; Zhao, J. Synthesis and Characterization of Phosphated Mesoporous Titanium Dioxide with High Photocatalytic Activity. *Chem. Mater.* **2003**, *15*, 2280–2286, doi:10.1021/cm0340781.
  245. Shanmugam, S.; Gabashvili, A.; Jacob, D.S.; Yu, J.C.; Gedanken, A. Synthesis and Characterization of TiO<sub>2</sub>@C Core–Shell Composite Nanoparticles and Evaluation of Their Photocatalytic Activities. *Chem. Mater.* **2006**, *18*, 2275–2282, doi:10.1021/cm052790n.
  246. Ma, Y.; Xu, Q.; Zong, X.; Wang, D.; Wu, G.; Wang, X.; Li, C. Photocatalytic H<sub>2</sub> production on Pt/TiO<sub>2</sub>-SO<sub>4</sub><sup>2-</sup> with tuned surface-phase structures: enhancing activity and reducing CO formation. *Energy Environ. Sci.* **2012**, *5*, 6345–6351, doi:10.1039/C1EE02053F.
  247. Wang, X.; Yu, J.C.; Chen, Y.; Wu, L.; Fu, X. ZrO<sub>2</sub>-Modified Mesoporous Nanocrystalline TiO<sub>2</sub>-xN<sub>x</sub> as Efficient Visible Light Photocatalysts. *Environ. Sci. Technol.* **2006**, *40*, 2369–2374, doi:10.1021/es052000a.
  248. Tanaka, K.; Capule, M.F. V; Hisanaga, T. Effect of crystallinity of TiO<sub>2</sub> on its photocatalytic action. *Chem. Phys. Lett.* **1991**, *187*, 73–76, doi:10.1016/0009-2614(91)90486-S.
  249. Irie, H.; Ping, T.S.; Shibata, T.; Hashimoto, K. Reversible Control of Wettability of a TiO<sub>2</sub> Surface by Introducing Surface Roughness. *Electrochem. Solid-State Lett.* **2005**, *8*, D23–D25, doi:10.1149/1.1979455.
  250. Vinodgopal, K.; Bedja, I.; Hotchandani, S.; Kamat, P. V A Photocatalytic Approach for the Reductive Decolorization of Textile Azo Dyes in Colloidal Semiconductor Suspensions. *Langmuir* **1994**, *10*, 1767–1771, doi:10.1021/la00018a024.
  251. Vinodgopal, K.; Kamat, P. V Photochemistry of textile azo dyes. Spectral characterization of excited state, reduced and oxidized forms of Acid Orange 7. *J. Photochem. Photobiol. A*

- Chem.* **1994**, *83*, 141–146, doi:https://doi.org/10.1016/1010-6030(94)03810-4.
252. Zhang, J.; Zhou, P.; Liu, J.; Yu, J. New understanding of the difference of photocatalytic activity among anatase, rutile and brookite TiO<sub>2</sub>. *Phys. Chem. Chem. Phys.* **2014**, *16*, 20382–20386, doi:10.1039/c4cp02201g.
  253. Chen, X.; Mao, S.S. Titanium dioxide nanomaterials: Synthesis, Properties, Modifications and Applications. *Chem. Rev.* 2007, *107*, 2891–2959.
  254. Su, C.; Hong, B.-Y.; Tseng, C.-M. Sol–gel preparation and photocatalysis of titanium dioxide. *Catal. Today* **2004**, *96*, 119–126, doi:10.1016/j.cattod.2004.06.132.
  255. Castro, M. V.; Cerqueira, M.F.; Rebouta, L.; Alpuim, P.; Garcia, C.B.; Júnior, G.L.; Tavares, C.J. Influence of hydrogen plasma thermal treatment on the properties of ZnO:Al thin films prepared by dc magnetron sputtering. *Vacuum* **2014**, *107*, 145–154, doi:https://doi.org/10.1016/j.vacuum.2014.04.022.
  256. Ribeiro, J.M.; Correia, F.C.; Salvador, P.B.; Rebouta, L.; Alves, L.C.; Alves, E.; Barradas, N.P.; Mendes, A.; Tavares, C.J. Compositional analysis by RBS, XPS and EDX of ZnO:Al,Bi and ZnO:Ga,Bi thin films deposited by d.c. magnetron sputtering. *Vacuum* **2019**, *161*, 268–275, doi:https://doi.org/10.1016/j.vacuum.2018.12.038.
  257. Castro, M. V.; Tavares, C.J. Dependence of Ga-doped ZnO thin film properties on different sputtering process parameters: Substrate temperature, sputtering pressure and bias voltage. *Thin Solid Films* **2015**, *586*, 13–21, doi:https://doi.org/10.1016/j.tsf.2015.04.036.
  258. Correia, F.C.; Bundaleski, N.; Teodoro, O.M.N.D.; Correia, M.R.; Rebouta, L.; Mendes, A.; Tavares, C.J. XPS analysis of ZnO:Ga films deposited by magnetron sputtering: Substrate bias effect. *Appl. Surf. Sci.* **2018**, *458*, 1043–1049, doi:https://doi.org/10.1016/j.apsusc.2018.07.135.
  259. Correia, F.C.; Salvador, P.B.; Ribeiro, J.M.; Mendes, A.; Tavares, C.J. Effect on the electrical and morphological properties of Bi incorporation into ZnO:Ga and ZnO:Al thin films deposited by confocal magnetron sputtering. *Vacuum* **2018**, *152*, 252–260, doi:https://doi.org/10.1016/j.vacuum.2018.03.033.
  260. Aleskovskii, V.B.; Koltsov, S.I. Some characteristics of molecular layering reactions. In Proceedings of the Abstract of Scientific and Technical Conference of the Leningrad Technological Institute by Lensovet; Goskhimizdat, Leningrad, 26-29th Nov., 1965; p. 67.
  261. Sveshnikova, G. V.; Koltsov, S.I.; Aleskovskii, V.B. Interaction of titanium tetrachloride with hydroxylated silicon surfaces. *J. Appl. Chem. USSR* **1970**, *43*, 432–434.
  262. Sveshnikova, G. V.; Koltsov, S.I.; Aleskovskii, A.B. Measuring thicknesses of ultra-thin silicon oxide films deposited by molecular layering on the surface of single crystal silicon using polarization method. In Proceedings of the in Abstract of Scientific and Technical Conference of the Leningrad Technological Institute by Lensovet; Goskhimizdat, Leningrad, 1969; pp. 18–19.
  263. Suntola, T. Atomic layer epitaxy. *Mater. Sci. Reports* **1989**, *4*, 261–312, doi:10.1016/S0920-2307(89)80006-4.
  264. Ahvenniemi, E.; Akbashev, A.R.; Ali, S.; Bechelany, M.; Berdova, M.; Boyadjiev, S.; Cameron, D.C.; Chen, R.; Chubarov, M.; Cremers, V.; et al. Recommended reading list of early publications on atomic layer deposition—Outcome of the “Virtual Project on the History of ALD.” *J. Vac. Sci. Technol. A Vacuum, Surfaces, Film.* **2017**, *35*, 10801 1–13, doi:10.1116/1.4971389.
  265. Puurunen, R.L. Surface chemistry of atomic layer deposition: A case study for the trimethylaluminum/water process. *J. Appl. Phys.* **2005**, *97*, 121301 1–52, doi:10.1063/1.1940727.



266. Suntola, T.; Antson, J.; Suntola, Tuomo Antson, J. Method for producing compound thin films. *US Pat. 4,058,430*, 15th Nov. 1977, 1–9.
267. Niinistö, J.; Leskelä, M.; Ritala, M. *Exhibition by the Finnish Centre of Excellence in Atomic Layer Deposition*. Espoo, Finland 2014, pp. 1–31.
268. Motsenyat, B.Z.; Ezhovskii, Y.K.; Levankova, L.M.; Mikhailova, N. V Formation and reactions of hydroxyl-groups on polyimide surface with titanium tetrachloride. *J. Appl. Chem. USSR* **1984**, *57*, 153–155.
269. Parsons, G.N.; Elam, J.W.; George, S.M.; Haukka, S.; Jeon, H.; (Erwin) Kessels, W.M.M.; Leskelä, M.; Poodt, P.; Ritala, M.; Rossnagel, S.M. History of atomic layer deposition and its relationship with the American Vacuum Society. *J. Vac. Sci. Technol. A Vacuum, Surfaces, Film*. **2013**, *31*, 050818 1–11, doi:10.1116/1.4816548.
270. Parsons, G.N.; George, S.M.; Knez, M. Progress and future directions for atomic layer deposition and ALD-based chemistry. *MRS Bull.* **2011**, *36*, 865–871, doi:10.1557/mrs.2011.238.
271. Heil, S.B.S.S.; Van Hemmen, J.L.; van de Sanden, M.C.M.M.; Kessels, W.M.M.M. Reaction mechanisms during plasma-assisted atomic layer deposition of metal oxides: A case study for Al<sub>2</sub>O<sub>3</sub>. *J. Appl. Phys.* **2008**, *103*, 103302 1–14, doi:10.1063/1.2924406.
272. Oviroh, P.O.; Akbarzadeh, R.; Pan, D.; Coetzee, R.A.M.; Jen, T.C. New development of atomic layer deposition: processes, methods and applications. *Sci. Technol. Adv. Mater.* **2019**, *20*, 465–496, doi:10.1080/14686996.2019.1599694.
273. Knoop, H.C.M.; Potts, S.E.; Bol, A.A.; Kessels, W.M.M. Atomic Layer Deposition. In *Handbook of Crystal Growth: Thin Films and Epitaxy: Second Edition*; Kuech, T.F., Ed.; Elsevier B.V.: North-Holland, 2015; Vol. 3, pp. 1101–1134 ISBN 9780444633057.
274. Pan, D.; Ma, L.; Xie, Y.; Jen, T.C.; Yuan, C. On the physical and chemical details of alumina atomic layer deposition: A combined experimental and numerical approach. *J. Vac. Sci. Technol. A* **2015**, *33*, 21511 1–11, doi:10.1116/1.4905726.
275. Wilson, C.A.; Grubbs, R.K.; George, S.M. Nucleation and growth during Al<sub>2</sub>O<sub>3</sub> atomic layer deposition on polymers. *Chem. Mater.* **2005**, *17*, 5625–5634, doi:10.1021/cm050704d.
276. Miikkulainen, V.; Leskelä, M.; Ritala, M.; Puurunen, R.L. Crystallinity of inorganic films grown by atomic layer deposition: Overview and general trends. *J. Appl. Phys.* **2013**, *113*, 021301 1–101, doi:10.1063/1.4757907.
277. Losego, M.D.; Peng, Q. Atomic Layer Deposition and Vapor Phase Infiltration. In *Surface Modification of Polymers: Methods and Applications*; Pinson, J., Thiry, D., Eds.; Wiley-VCH Verlag GmbH & Co. KGaA: Weinheim, 2019; pp. 135–159.
278. Ali, U.; Karim, K.J.B.A.; Buang, N.A. A Review of the Properties and Applications of Poly (Methyl Methacrylate) (PMMA). *Polym. Rev.* **2015**, *55*, 678–705, doi:10.1080/15583724.2015.1031377.
279. Goseki, R.; Ishizone, T. Poly(methyl methacrylate) (PMMA). *Encycl. Polym. Nanomater.* **2014**, 1–11, doi:10.1007/978-3-642-36199-9.
280. Duval-Terrié, C.; Lebrun, L. Polymerization and characterization of PMMA: Polymer chemistry laboratory experiments for undergraduate students. *J. Chem. Educ.* **2006**, *83*, 443–446, doi:10.1021/ed083p443.
281. Chang, L.; Woo, E.M. Tacticity effects on glass transition and phase behavior in binary blends of poly(methyl methacrylate)s of three different configurations. *Polym. Chem.* **2010**, *1*, 198–202, doi:10.1039/b9py00237e.
282. Shin, S.; Park, J. Effect of self-assembled monolayer and aluminum oxide ALD film on a PMMA substrate. *J. Ceram. Process. Res.* **2018**, *19*, 525–529.
283. Ylivaara, O.M.E.; Liu, X.; Kilpi, L.; Lyytinen, J.; Schneider, D.; Laitinen, M.; Julin, J.; Ali, S.;

- Sintonen, S.; Berdova, M.; et al. Aluminum oxide from trimethylaluminum and water by atomic layer deposition: The temperature dependence of residual stress, elastic modulus, hardness and adhesion. *Thin Solid Films* **2014**, *552*, 124–135, doi:10.1016/j.tsf.2013.11.112.
284. Groner, M.D.; Fabreguette, F.H.; Elam, J.W.; George, S.M. Low-Temperature Al<sub>2</sub>O<sub>3</sub> Atomic Layer Deposition. *Chem. Mater.* **2004**, *16*, 639–645, doi:10.1021/cm0304546.
285. Darwish, G.; Huang, S.; Knoernschild, K.; Sukotjo, C.; Campbell, S.; Bishal, A.K.; Barão, V.A.; Wu, C.D.; Taukodis, C.G.; Yang, B. Improving Polymethyl Methacrylate Resin Using a Novel Titanium Dioxide Coating. *J. Prosthodont.* **2019**, *28*, 1011–1017, doi:10.1111/jopr.13032.
286. Paul, P.; Pfeiffer, K.; Szeghalmi, A.; Deposition, A.L. Antireflection coating on PMMA substrates by atomic layer deposition. *Coatings* **2020**, *10*, 1–13, doi:10.3390/coatings10010064.
287. Coll, M.; Palau, A.; Gonzalez-Rosillo, J.C.; Gazquez, J.; Obradors, X.; Puig, T. Integration of atomic layer deposition CeO<sub>2</sub> thin films with functional complex oxides and 3D patterns. *Thin Solid Films* **2014**, *553*, 7–12, doi:10.1016/j.tsf.2013.08.131.
288. Haider, A.; Yilmaz, M.; Deminskyi, P.; Eren, H.; Biyikli, N. Nanoscale selective area atomic layer deposition of TiO<sub>2</sub> using e-beam patterned polymers. *RSC Adv.* **2016**, *6*, 106109–106119, doi:10.1039/c6ra23923d.
289. Pinna, N.; Knez, M. *Atomic Layer Deposition of Nanostructured Materials*; Pinna, N., Mato Knez, Eds.; First Edit.; Wiley-VCH Verlag & Co. KGaA: Weinheim, 2011; ISBN 9780470109526.
290. Gong, B.; Parsons, G.N. Quantitative in situ infrared analysis of reactions between trimethylaluminum and polymers during Al<sub>2</sub>O<sub>3</sub> atomic layer deposition. *J. Mater. Chem.* **2012**, *22*, 15672–15682, doi:10.1039/c2jm32343e.
291. Kääriäinen, T.O.; Kelly, P.J.; Cameron, D.C.; Beake, B.; Li, H.; Barker, P.M.; Struller, C.F. Nanoscratch testing of atomic layer deposition and magnetron sputtered TiO<sub>2</sub> and Al<sub>2</sub>O<sub>3</sub> coatings on polymeric substrates. *J. Vac. Sci. Technol. A Vacuum, Surfaces, Film.* **2012**, *30*, 01A132 1-9, doi:10.1116/1.3665418.
292. Chen, Y.; Ginga, N.J.; LePage, W.S.; Kazyak, E.; Gayle, A.J.; Wang, J.; Rodríguez, R.E.; Thouless, M.D.; Dasgupta, N.P. Enhanced Interfacial Toughness of Thermoplastic-Epoxy Interfaces Using ALD Surface Treatments. *ACS Appl. Mater. Interfaces* **2019**, *11*, 43573–43580, doi:10.1021/acsami.9b15193.
293. Shahmohammadi, M.; Pensa, E.; Bhatia, H.; Yang, B.; Jursich, G.; Takoudis, C.G. Enhancing the surface properties and functionalization of polymethyl methacrylate with atomic layer-deposited titanium(IV) oxide. *J. Mater. Sci.* **2020**, *55*, 17151–17169, doi:10.1007/s10853-020-05274-2.
294. Hofmann, C.L.M.L.M.; Fischer, S.; Reitz, C.; Richards, B.S.; Goldschmidt, J.C. Comprehensive analysis of photonic effects on upconversion of β-NaYF<sub>4</sub>:Er<sup>3+</sup> nanoparticles in an organic-inorganic hybrid 1D photonic crystal. In Proceedings of the Photonic Crystal Materials and Devices XII; SPIE Photonics Europe, Brussels, Belgium, 18th Ap., 2016; Vol. 9885.
295. Hofmann, C.L.M.; Fischer, S.; Eriksen, E.H.; Bläsi, B.; Reitz, C.; Yazicioglu, D.; Howard, I.A.; Richards, B.S.; Goldschmidt, J.C. Experimental validation of a modeling framework for upconversion enhancement in 1D-photonic crystals. *Nat. Commun.* **2021**, *12*, 1–10, doi:10.1038/s41467-020-20305-x.
296. Singh, A.; Mathur, A.; Pal, D.; Sengupta, A.; Singh, R.; Chattopadhyay, S. Near room temperature atomic layer deposition of ZnO thin films on poly (methyl methacrylate)

- (PMMA) templates: A study of structure, morphology and photoluminescence of ZnO as an effect of template confinement. *Vacuum* **2019**, *161*, 398–403, doi:10.1016/j.vacuum.2019.01.006.
297. Kéri, O.; Kócs, L.; Hórvölgyi, Z.; Baji, Z.; László, K.; Takáts, V.; Erdélyi, Z.; Szilágyi, I.M. Photocatalytically active amorphous and crystalline TiO<sub>2</sub> prepared by atomic layer deposition. *Period. Polytech. Chem. Eng.* **2019**, *63*, 378–387, doi:10.3311/PPch.13873.
  298. Di Mauro, A.; Farrugia, C.; Abela, S.; Refalo, P.; Grech, M.; Falqui, L.; Privitera, V.; Impellizzeri, G. Synthesis of ZnO/PMMA nanocomposite by low-temperature atomic layer deposition for possible photocatalysis applications. *Mater. Sci. Semicond. Process.* **2020**, *118*, 105214 1–6, doi:10.1016/j.mssp.2020.105214.
  299. Di Mauro, A.; Farrugia, C.; Abela, S.; Refalo, P.; Grech, M.; Falqui, L.; Nicotra, G.; Sfuncia, G.; Mio, A.; Buccheri, M.A.; et al. Ag/ZnO/PMMA nanocomposites for efficient water reuse. *ACS Appl. Bio Mater.* **2020**, *3*, 4417–4426, doi:10.1021/acsabm.0c00409.
  300. Di Mauro, A.; Cantarella, M.; Nicotra, G.; Pellegrino, G.; Gulino, A.; Brundo, M.V.; Privitera, V.; Impellizzeri, G. Novel synthesis of ZnO/PMMA nanocomposites for photocatalytic applications. *Sci. Rep.* **2017**, *7*, 1–12, doi:10.1038/srep40895.
  301. Shahmohammadi, M.; Yang, B.; Takoudis, C.G. Applications of Titania Atomic Layer Deposition in the Biomedical Field and Recent Updates. *Am. J. Biomed. Sci. Res.* **2020**, *8*, 465–468, doi:10.34297/ajbsr.2020.08.001321.
  302. Wilson, C.A.; McCormick, J.A.; Cavanagh, A.S.; Goldstein, D.N.; Weimer, A.W.; George, S.M. Tungsten atomic layer deposition on polymers. *Thin Solid Films* **2008**, *516*, 6175–6185, doi:10.1016/j.tsf.2007.11.086.
  303. Minton, T.K.; Wu, B.; Zhang, J.; Lindholm, N.F.; Abdulagatov, A.I.; O’Patchen, J.; George, S.M.; Groner, M.D. Protecting polymers in space with atomic layer deposition coatings. *ACS Appl. Mater. Interfaces* **2010**, *2*, 2515–2520, doi:10.1021/am100217m.
  304. Kemell, M.; Färm, E.; Ritala, M.; Leskelä, M.; Färm, E.; Ritala, M.; Leskelä, M. Surface modification of thermoplastics by atomic layer deposition of Al<sub>2</sub>O<sub>3</sub> and TiO<sub>2</sub> thin films. *Eur. Polym. J.* **2008**, *44*, 3564–3570, doi:10.1016/j.eurpolymj.2008.09.005.
  305. Napari, M.; Malm, J.; Lehto, R.; Julin, J.; Arstila, K.; Sajavaara, T.; Lahtinen, M. Nucleation and growth of ZnO on PMMA by low-temperature atomic layer deposition. *J. Vac. Sci. Technol. A Vacuum, Surfaces, Film.* **2015**, *33*, 01A128 1-7, doi:10.1116/1.4902326.
  306. Profijt, H.B.; Potts, S.E.; van de Sanden, M.C.M.; Kessels, W.M.M. Plasma-Assisted Atomic Layer Deposition: Basics, Opportunities, and Challenges. *J. Vac. Sci. Technol. A Vacuum, Surfaces, Film.* **2011**, *29*, 050801 1–26, doi:10.1116/1.3609974.
  307. Potts, S.E.; Kessels, W.M.M. Energy-enhanced atomic layer deposition for more process and precursor versatility. *Coord. Chem. Rev.* **2013**, *257*, 3254–3270, doi:https://doi.org/10.1016/j.ccr.2013.06.015.
  308. Kääriäinen, T.O.; Lehti, S.; Kääriäinen, M.L.; Cameron, D.C. Surface modification of polymers by plasma-assisted atomic layer deposition. *Surf. Coatings Technol.* **2011**, *205*, S475–S479, doi:10.1016/j.surfcoat.2011.03.094.
  309. Lehnert, W.; Ruhl, G.; Gschwandtner, A. Plasma enhanced atomic layer batch processing of aluminum doped titanium dioxide. *J. Vac. Sci. Technol. A* **2011**, *30*, 01A152 1-6, doi:10.1116/1.3670876.
  310. Kääriäinen, T.; Cameron, D.; Kääriäinen, M.L.; Sherman, A. *Atomic Layer Deposition: Principles, Characteristics, and Nanotechnology Applications*, Scrivener, M., Carmical, P., Eds.; 2 nd.; John Wiley & Sons, Inc: Hoboken, 2013; ISBN 9781118062777.
  311. Levy, D.H.; Nelson, S.F. Thin-film electronics by atomic layer deposition. *J. Vac. Sci. Technol. A Vacuum, Surfaces, Film.* **2012**, *30*, 018501 1–9, doi:10.1116/1.3670748.

312. Huebner, U.; Weber, K.; Cialla, D.; Haehle, R.; Schneidewind, H.; Zeisberger, M.; Mattheis, R.; Meyer, H.G.; Popp, J. Microfabricated polymer-substrates for SERS. *Microelectron. Eng.* **2012**, *98*, 444–447, doi:10.1016/j.mee.2012.05.036.
313. Hosseini, S.; Ibrahim, F.; Djordjevic, I.; Koole, L.H. Recent advances in surface functionalization techniques on polymethacrylate materials for optical biosensor applications. *Analyst* **2014**, *139*, 2933–2943, doi:10.1039/c3an01789c.
314. Goddard, J.M.; Hotchkiss, J.H. Polymer surface modification for the attachment of bioactive compounds. *Prog. Polym. Sci.* **2007**, *32*, 698–725, doi:10.1016/j.progpolymsci.2007.04.002.
315. Hetemi, D.; Pinson, J. Surface functionalisation of polymers. *Chem. Soc. Rev.* **2017**, *46*, 5701–5713, doi:10.1039/c7cs00150a.
316. Andreozzi, A.; Lamagna, L.; Seguíni, G.; Fanciulli, M.; Schamm-Chardon, S.; Castro, C.; Perego, M. The fabrication of tunable nanoporous oxide surfaces by block copolymer lithography and atomic layer deposition. *Nanotechnology* **2011**, *22*, 335303 1–8, doi:10.1088/0957-4484/22/33/335303.
317. Sinha, A.; Hess, D.W.; Henderson, C.L. Area-Selective ALD of Titanium Dioxide Using Lithographically Defined Poly(methyl methacrylate) Films. *J. Electrochem. Soc.* **2006**, *153*, G465–G469, doi:10.1149/1.2184068.
318. Chen, W.; Luo, J.; Meng, L.; Li, J.; Xiang, J.; Li, J.; Wang, W.; Chen, D.; Ye, T.; Zhao, C. Atomic layer deposition assisted pattern transfer technology for ultra-thin block copolymer films. *Thin Solid Films* **2016**, *613*, 32–37, doi:10.1016/j.tsf.2015.10.032.
319. Färm, E.; Kemell, M.; Ritala, M.; Leskelä, M. Selective-Area Atomic Layer Deposition Using Poly(methyl methacrylate) Films as Mask Layers. *J. Phys. Chem. C* **2008**, *112*, 972–975, doi:10.1016/j.tsf.2008.08.191.
320. Cho, T.H.; Farjam, N.; Allemang, C.R.; Pannier, C.P.; Kazyak, E.; Huber, C.; Rose, M.; Trejo, O.; Peterson, R.L.; Barton, K.; et al. Area-Selective Atomic Layer Deposition Patterned by Electrohydrodynamic Jet Printing for Additive Manufacturing of Functional Materials and Devices. *ACS Nano* **2020**, *14*, 17262–17272, doi:10.1021/acsnano.0c07297.
321. Wei, X.; Kumagai, S.; Sasaki, M.; Watanabe, S.; Takeya, J. Stabilizing solution-processed metal oxide thin-film transistors via trilayer organic-inorganic hybrid passivation. *AIP Adv.* **2021**, *11*, 035027 1–5, doi:10.1063/5.0038128.
322. Tamm, A.; Kozlova, J.; Aarik, L.; Aidla, A.; Lu, J.; Kiisler, A.A.; Kasikov, A.; Ritslaid, P.; Mändar, H.; Hultman, L.; et al. Atomic layer deposition of ZrO<sub>2</sub> for graphene-based multilayer structures: In situ and ex situ characterization of growth process. *Phys. Status Solidi Appl. Mater. Sci.* **2014**, *211*, 397–402, doi:10.1002/pssa.201330106.
323. Nelson-Fitzpatrick, N.; Guthy, C.; Poshtiban, S.; Finley, E.; Harris, K.D.; Worfolk, B.J.; Evoy, S. Atomic layer deposition of TiN for the fabrication of nanomechanical resonators. *J. Vac. Sci. Technol. A Vacuum, Surfaces, Film.* **2013**, *31*, 021503 1–7, doi:10.1116/1.4790132.
324. Vervuurt, R.H.J.; Karasulu, B.; Thissen, N.F.W.; Jiao, Y.; Weber, J.W.; Kessels, W. (Erwin) M.M.; Bol, A.A. Pt–Graphene Contacts Fabricated by Plasma Functionalization and Atomic Layer Deposition. *Adv. Mater. Interfaces* **2018**, *5*, 1–15, doi:10.1002/admi.201800268.
325. Woo, J.Y.; Jo, S.; Oh, J.H.; Kim, J.T.; Han, C.S. Facile and precise fabrication of 10-nm nanostructures on soft and hard substrates. *Appl. Surf. Sci.* **2019**, *484*, 317–325, doi:10.1016/j.apsusc.2019.04.035.
326. Li, N.; Wei, Z.; Zhao, J.; Wang, Q.; Shen, C.; Wang, S.; Tang, J.; Yang, R.; Shi, D.; Zhang, G. Atomic Layer Deposition of Al<sub>2</sub>O<sub>3</sub> Directly on 2D Materials for High-Performance Electronics. *Adv. Mater. Interfaces* **2019**, *6*, 1802055 1–7,

- doi:10.1002/admi.201802055.
327. Klement, P.; Anders, D.; Gümbel, L.; Bastianello, M.; Michel, F.; Schörmann, J.; Elm, M.T.; Heiliger, C.; Chatterjee, S. Surface Diffusion Control Enables Tailored Aspect Ratio Nanostructures in Area-Selective Atomic Layer Deposition Available online: <https://arxiv.org/ftp/arxiv/papers/2012/2012.04465.pdf>.
  328. Schilirò, E.; Lo Nigro, R.; Roccaforte, F.; Deretzis, I.; La Magna, A.; Armano, A.; Agnello, S.; Pecz, B.; Ivanov, I.G.; Yakimova, R.; et al. Seed-Layer-Free Atomic Layer Deposition of Highly Uniform Al<sub>2</sub>O<sub>3</sub> Thin Films onto Monolayer Epitaxial Graphene on Silicon Carbide. *Adv. Mater. Interfaces* **2019**, *6*, 1–11, doi:10.1002/admi.201900097.
  329. Sinha, A.; Henderson, C.; Hess, D.W. Area Selective Atomic Layer Deposition of Titanium Dioxide. *ECS Trans.* **2019**, *3*, 233–241, doi:10.1149/1.2721492.
  330. Niinistö, L.; Nieminen, M.; Päiväsääri, J.; Niinistö, J.; Putkonen, M.; Nieminen, M. Advanced electronic and optoelectronic materials by Atomic Layer Deposition: An overview with special emphasis on recent progress in processing of high-k dielectrics and other oxide materials. *Phys. status solidi* **2004**, *201*, 1443–1452, doi:10.1002/pssa.200406798.
  331. Tan, L.K.; Chong, M.A.S.S.; Gao, H. Free-Standing Porous Anodic Alumina Templates for Atomic Layer Deposition of Highly Ordered TiO<sub>2</sub> Nanotube Arrays on Various Substrates. *J. Phys. Chem. C* **2008**, *112*, 69–73, doi:<https://doi.org/10.1021/jp076949q>.
  332. Vervuurt, R.H.J.; Sharma, A.; Jiao, Y.; Kessels, W.M.M.; Bol, A.A. Area-selective atomic layer deposition of platinum using photosensitive polyimide. *Nanotechnology* **2016**, *27*, 405302 1–6, doi:10.1088/0957-4484/27/40/405302.
  333. Färm, E.; Kemell, M.; Santala, E.; Ritala, M.; Leskelä, M. Selective-Area Atomic Layer Deposition Using Poly(vinyl pyrrolidone) as a Passivation Layer. *J. Electrochem. Soc.* **2010**, *157*, K10-k14, doi:10.1149/1.3250936.
  334. Hua, Y.; King, W.P.; Henderson, C.L. Nanopatterning materials using area selective atomic layer deposition in conjunction with thermochemical surface modification via heated AFM cantilever probe lithography. *Microelectron. Eng.* **2008**, *85*, 934–936, doi:10.1016/j.mee.2008.01.105.
  335. Sinha, A.; Hess, D.W.; Henderson, C.L. Area selective atomic layer deposition of titanium dioxide: Effect of precursor chemistry. *J. Vac. Sci. Technol. B Microelectron. Nanom. Struct.* **2006**, *24*, 2523–2532, doi:10.1116/1.2359728.
  336. Levy, D.H.; Nelson, S.F.; Freeman, D. Oxide Electronics by Spatial Atomic Layer Deposition. *J. Disp. Technol.* **2009**, *5*, 484–494, doi:10.1109/JDT.2009.2022770.
  337. Tang, X.; Francis, L.A.; Simonis, P.; Haslinger, M.; Delamare, R.; Deschaume, O.; Flandre, D.; Defrance, P.; Jonas, A.M.; Vigneron, J.P.; et al. Room temperature atomic layer deposition of Al<sub>2</sub>O<sub>3</sub> and replication of butterfly wings for photovoltaic application. *J. Vac. Sci. Technol. A Vacuum, Surfaces, Film.* **2012**, *30*, 01A146-01A146-5, doi:10.1116/1.3669521.
  338. Biercuk, M.J.; Monsma, D.J.; Marcus, C.M.; Backer, J.S.; Gordon, R.G.; Becker, J.S.; Gordon, R.G. A Low-temperature atomic-layer-deposition lift-off method for microelectronic and nanoelectronic applications. *Appl. Phys. Lett.* **2003**, *83*, 2405–2407, doi:10.1063/1.1612904.
  339. Färm, E.; Kemell, M.; Ritala, M.; Leskelä, M. Selective-area atomic layer deposition with microcontact printed self-assembled octadecyltrichlorosilane monolayers as mask layers. *Thin Solid Films* **2008**, *517*, 972–975, doi:10.1021/jp803872s.
  340. Sharma, A.; Mahlouji, R.; Wu, L.; Verheijen, M.A.; Vandalon, V.; Balasubramanyam, S.; Hofmann, J.P.; Erwin Kessels, W.M.M.; Bol, A.A. Large area, patterned growth of 2D MoS<sub>2</sub> and lateral MoS<sub>2</sub>-WS<sub>2</sub> heterostructures for nano-and opto-electronic applications.

- Nanotechnology* **2020**, *31*, 255603 1–12, doi:10.1088/1361-6528/ab7593.
341. Dhuey, S.; Peroz, C.; Olynick, D.; Calafiore, G.; Cabrini, S. Obtaining nanoimprint template gratings with 10 nm half-pitch by atomic layer deposition enabled spacer double patterning. *Nanotechnology* **2013**, *24*, 105303-105303–5, doi:10.1088/0957-4484/24/10/105303.
  342. Suresh, V.; Huang, M.S.; Srinivasan, M.P.; Guan, C.; Fan, H.J.; Krishnamoorthy, S. Robust, high-density zinc oxide nanoarrays by nanoimprint lithography-assisted area-selective atomic layer deposition. *J. Phys. Chem. C* **2012**, *116*, 23729–23734, doi:10.1021/jp307152s.
  343. Zhang, Z.; Dwyer, T.; Sirard, S.M.; Ekerdt, J.G. Area-selective atomic layer deposition of cobalt oxide to generate patterned cobalt films. *J. Vac. Sci. Technol. A* **2019**, *37*, 020905 1–9, doi:10.1116/1.5066437.
  344. Peng, Q.; Tseng, Y.C.; Darling, S.B.; Elam, J.W. Nanoscopic patterned materials with tunable dimensions via atomic layer deposition on block copolymers. *Adv. Mater.* **2010**, *22*, 5129–5133, doi:10.1002/adma.201002465.
  345. Gay, G.; Baron, T.; Agraffeil, C.; Salhi, B.; Chevolleau, T.; Cunge, G.; Grampeix, H.; Tortai, J.H.; Martin, F.; Jalaguier, E.; et al. CMOS compatible strategy based on selective atomic layer deposition of a hard mask for transferring block copolymer lithography patterns. *Nanotechnology* **2010**, *21*, 435301 1–7, doi:10.1088/0957-4484/21/43/435301.
  346. Jeong, S.J.; Xia, G.; Kim, B.H.; Shin, D.O.; Kwon, S.H.; Kang, S.W.; Kim, S.O. Universal block copolymer lithography for metals, semiconductors, ceramics, and polymers. *Adv. Mater.* **2008**, *20*, 1898–1904, doi:10.1002/adma.200702930.
  347. Singh, A.; Mathur, A.; Pal, D.; Sengupta, A.; Singh, R.; Chattopadhyay, S. Structure and morphology of atomic layer deposition grown ZnO thin film/nanostructure on polymeric template. *Mater. Today Proc.* **2019**, *18*, 1517–1523, doi:10.1016/j.matpr.2019.06.621.
  348. Sinha, A.; Hess, D.W.; Henderson, C.L. Transport behavior of atomic layer deposition precursors through polymer masking layers: Influence on area selective atomic layer deposition. *J. Vac. Sci. Technol. B Microelectron. Nanom. Struct.* **2007**, *25*, 1721–1728, doi:10.1116/1.2782546.
  349. FITOALGAS GREEN - Ficha de Dados de Segurança.
  350. ULTRAFERRO - Ficha de Dados de Segurança.
  351. Folivex Crescimento - Ficha de Dados de Segurança.
  352. Teeka, P.; Chaiyasat, A.; Chaiyasat, P. Preparation of poly (methyl methacrylate) microcapsule with encapsulated jasmine oil. *Energy Procedia* **2014**, *56*, 181–186, doi:10.1016/j.egypro.2014.07.147.
  353. Jelvehgari, M.; Montazam, S.H. Comparison of microencapsulation by emulsion-solvent extraction/ evaporation technique using derivatives cellulose and acrylate-methacrylate copolymer as carriers. *Jundishapur J. Nat. Pharm. Prod.* **2012**, *7*, 144–152, doi:10.5812/jjnpp.3986.
  354. Zydowicz, N.; Nzimba-Ganyanad, E.; Zydowicz, N. PMMA microcapsules containing water-soluble dyes obtained by double emulsion/solvent evaporation technique. *Polym. Bull.* **2002**, *47*, 457–463, doi:10.1007/s002890200009.
  355. Mestiri, M.; Puisieux, F.; Benoit, J.P. Preparation and characterization of cisplatin-loaded polymethyl methacrylate microspheres. *Int. J. Pharm.* **1993**, *89*, 229–234, doi:10.1016/0378-5173(93)90248-E.
  356. Mohanty, A.K.; Misra, M.; Hinrichsen, G. Biofibres, biodegradable polymers and biocomposites: An overview. *Macromol. Mater. Eng.* **2000**, *276-277*, 1–24, doi:10.1002/(SICI)1439-2054(20000301)276:1<1::AID-MAME1>3.0.CO;2-W.

357. Puls, J.; Wilson, S.A.; Hölter, D. Degradation of Cellulose Acetate-Based Materials: A Review. *J. Polym. Environ.* **2011**, *19*, 152–165, doi:10.1007/s10924-010-0258-0.
358. Pitol-Filho, L.; Kokol, V.; Voncina, B. Synthesis and characterization of ethyl cellulose microcapsules containing model active ingredients. *Macromol. Symp.* **2013**, *328*, 45–55, doi:10.1002/masy.201350605.
359. Wang, X.; Yin, H.; Chen, Z.; Xia, L. Epoxy resin/ethyl cellulose microcapsules prepared by solvent evaporation for repairing microcracks: Particle properties and slow-release performance. *Mater. Today Commun.* **2020**, *22*, 100854 1–9, doi:10.1016/j.mtcomm.2019.100854.
360. Prasertmanakit, S.; Praphairaksit, N.; Chiangthong, W.; Muangsin, N. Ethyl cellulose microcapsules for protecting and controlled release of folic acid. *AAPS PharmSciTech* **2009**, *10*, 1104–1112, doi:10.1208/s12249-009-9305-3.
361. Jangde, R.; Daharwal, S.; Singh, D.; Sahu, R.K. Development and characterization of ethyl cellulose coated microcapsules for controlled release of ampicillin. *Biosci. Biotechnol. Res. Asia* **2011**, *8*, 747–752, doi:10.13005/bbra/929.
362. Badulescu, R.; Vivod, V.; Jausovec, D.; Voncina, B. *Treatment of Cotton Fabrics with Ethyl Cellulose Microcapsules*; Woodhead Publishing Limited, 2010; ISBN 9781845692247.
363. Brlek, I.; Ludaš, A.; Sutlovi, A. Synthesis and Spectrophotometric Analysis of Microcapsules Containing Immortelle Essential Oil. *molecules* **2021**, *26*, 1–9, doi:https://www.mdpi.com/1420-3049/26/8/2390.
364. Patil, D.K.; Agrawal, D.S.; Mahire, R.R.; More, D.H. Synthesis, characterization and controlled release studies of ethyl cellulose microcapsules incorporating essential oil using an emulsion solvent evaporation method. *Am. J. Essent. Oils Nat. Prod.* **2016**, *23*, 23–31.
365. Sharma, S.; Choudhary, V. Parametric study for epoxy loaded PMMA microcapsules using Taguchi and ANOVA methods. *Express Polym. Lett.* **2017**, *11*, 1023–1036, doi:10.3144/expresspolymlett.2017.96.
366. Forte, M.A.; Silva, R.M.; Tavares, C.J.; Silva, R.F. e Is Poly(methyl methacrylate) (PMMA) a Suitable Substrate for ALD?: A Review. *Polymers (Basel)*. **2021**, *13*, doi:10.3390/polym13081346.
367. Marques, J.; Gomes, T.D.; Forte, M.A.; Silva, R.F.; Tavares, C.J. A new route for the synthesis of highly-active N-doped TiO<sub>2</sub> nanoparticles for visible light photocatalysis using urea as nitrogen precursor. *Catal. Today* **2019**, *326*, 36–45, doi:https://doi.org/10.1016/j.cattod.2018.09.002.
368. Duconseille, A.; Astruc, T.; Quintana, N.; Meersman, F.; Sante-Lhoutellier, V. Gelatin structure and composition linked to hard capsule dissolution: A review. *Food Hydrocoll.* **2015**, *43*, 360–376, doi:10.1016/j.foodhyd.2014.06.006.
369. Pandey, S.P.; Shukla, T.; Dhote, V.K.; K. Mishra, D.; Maheshwari, R.; Tekade, R.K. Chapter 4 - Use of Polymers in Controlled Release of Active Agents. In *Advances in Pharmaceutical Product Development and Research*; Tekade, R.K.B.T.-B.F. of D.D., Ed.; Academic Press, 2019; pp. 113–172 ISBN 978-0-12-817909-3.
370. Kawai, F.; Hu, X. Biochemistry of microbial polyvinyl alcohol degradation. *Appl. Microbiol. Biotechnol.* **2009**, *84*, 227–237, doi:10.1007/s00253-009-2113-6.
371. Corti, A.; Cinelli, P.; D'Antone, S.; Kenawy, E.R.; Solaro, R. Biodegradation of poly(vinyl alcohol) in soil environment: Influence of natural organic fillers and structural parameters. *Macromol. Chem. Phys.* **2002**, *203*, 1526–1531, doi:10.1002/1521-3935(200207)203:10/11<1526::AID-MACP1526>3.0.CO;2-R.
372. *A Beginners' Guide to Scanning Electron Microscopy*, Ul-Hamid, A., Ed.; 1st ed.; Springer

- Nature Switzerland AG: Cham, 2018; ISBN 978-3-319-98482-7.
373. Guo, Q. *Polymer Morphology - Principles, Characterization and Processing*, John Wiley & Sons, Inc. All: Hoboken, 2016; ISBN 9781118452158.
  374. Canevarolo Jr., S.V. *Técnicas de Caracterização de Polímeros*, 1st ed.; Artliber Editora Ltda.: São Paulo, 2004; ISBN 8588098199.
  375. *Polymer Characterisation*; Hunt, B.J., James, M.I., Eds.; 1 st.; Springer-Science+Business Media, B.V.: Dordrecht, 1993; ISBN 9789401049566.
  376. Ng, H.M.; Saidi, N.M.; Omar, F.S.; Ramesh, K.; Ramesh, S.; Bashir, S. Thermogravimetric Analysis of Polymers. *Encycl. Polym. Sci. Technol.* 2018, 1–29.
  377. Pielichowski, Krzysztof; Njuguna, J. *Thermal Degradation of Polymeric Materials*; 1st ed.; Rapra Technology Limited All: Shawbury, 2005; ISBN 185957498X.
  378. Kashiwagi, T.; Brown, J.E.; Inaba, A.; Hatada, K.; Kitayama, T.; Masuda, E. Effects of Weak Linkages on the Thermal and Oxidative Degradation of Poly(methyl methacrylates). *Macromolecules* **1986**, *19*, 2160–2168, doi:10.1021/ma00162a010.
  379. Shobhana, E. X-Ray Diffraction and UV-Visible Studies of PMMA Thin Films. *Int. J. Mod. Eng. Res.* **2012**, *2*, 1092–1095.
  380. Keeler, J. *Understanding NMR spectroscopy*, 1st ed.; Wiley, 2006; ISBN 978-0-470-74608-0.
  381. Nahim-Granados, S.; Oller, I.; Malato, S.; Sánchez Pérez, J.A.; Polo-Lopez, M.I. Commercial fertilizer as effective iron chelate (Fe<sup>3+</sup>-EDDHA) for wastewater disinfection under natural sunlight for reusing in irrigation. *Appl. Catal. B Environ.* **2019**, *253*, 286–292, doi:10.1016/j.apcatb.2019.04.041.
  382. Acquafredda, P. XRF technique. *Phys. Sci. Rev.* **2019**, *4*, 1–20, doi:10.1515/psr-2018-0171.
  383. Nakano, A.; Minoura, Y. Effects of solvent and concentration on scission of polymers with high-speed stirring. *J. Appl. Polym. Sci.* **1975**, *19*, 2119–2130, doi:10.1002/app.1975.070190806.
  384. Murov, S. Properties of Solvents Used in Organic Chemistry Available online: <http://murov.info/orgsolvents.htm>.
  385. Ellis, B.; Smith, R. P-381 Poly(methyl methacrylate), General. In *Polymers, A property database*; CRC Press, Taylor & Francis Group: Boca Raton, 2009; pp. 726–735 ISBN 9781420005707.
  386. Abedel-Fattah, E. Surface Activation of Poly(Methyl Methacrylate) with Atmospheric Pressure Ar + H<sub>2</sub>O Plasma. *Coatings* **2019**, *9*, 1–12, doi:10.3390/coatings9040228.
  387. Liu, F.; Cai, M.; Zhang, B.; Fang, Z.; Jiang, C.; Ostrikov, K. (Ken) Hydrophobic surface modification of polymethyl methacrylate by two-dimensional plasma jet array at atmospheric pressure. *J. Vac. Sci. Technol. A* **2018**, *36*, 061302 1–10, doi:10.1116/1.5030718.
  388. Thakur, V.K.; Vennerberg, D.; Madbouly, S.A.; Kessler, M.R. Bio-inspired green surface functionalization of PMMA for multifunctional capacitors. *RSC Adv.* **2014**, *4*, 6677–6684, doi:10.1039/c3ra46592f.
  389. Vesel, A.; Mozetic, M. Surface modification and ageing of PMMA polymer by oxygen plasma treatment. *Vacuum* **2012**, *86*, 634–637, doi:10.1016/j.vacuum.2011.07.005.
  390. Liu, C.; Cui, N.Y.; Osbeck, S.; Liang, H. Air plasma processing of poly(methyl methacrylate) micro-beads: Surface characterisations. *Appl. Surf. Sci.* **2012**, *259*, 840–846, doi:10.1016/j.apsusc.2012.07.140.
  391. Riau, A.K.; Mondal, D.; Yam, G.H.F.; Setiawan, M.; Liedberg, B.; Venkatraman, S.S.; Mehta, J.S. Surface Modification of PMMA to Improve Adhesion to Corneal Substitutes in a



- Synthetic Core-Skirt Keratoprosthesis. *ACS Appl. Mater. Interfaces* **2015**, *7*, 21690–21702, doi:10.1021/acsami.5b07621.
392. Brown, L.; Koerner, T.; Horton, J.H.; Oleschuk, R.D. Fabrication and characterization of poly(methylmethacrylate) microfluidic devices bonded using surface modifications and solvents. *Lab Chip* **2006**, *6*, 66–73, doi:10.1039/b512179e.
  393. Ortiz, R.; Chen, J.L.; Stuckey, D.C.; Steele, T.W.J. Poly(methyl methacrylate) Surface Modification for Surfactant-Free Real-Time Toxicity Assay on Droplet Microfluidic Platform. *ACS Appl. Mater. Interfaces* **2017**, *9*, 13801–13811, doi:10.1021/acsami.7b02682.
  394. Tanahashi, M.; Yao, T.; Kokubo, T.; Minoda, M.; Miyamoto, T.; Nakamura, T.; Yamamuro, T. Apatite coated on organic polymers by biomimetic process: Improvement in its adhesion to substrate by NaOH treatment. *J. Appl. Biomater.* **1994**, *5*, 339–347, doi:10.1002/jab.770050409.
  395. Cheng, J.Y.; Wei, C.W.; Hsu, K.H.; Young, T.H. Direct-write laser micromachining and universal surface modification of PMMA for device development. *Sensors Actuators, B Chem.* **2004**, *99*, 186–196, doi:10.1016/j.snb.2003.10.022.
  396. Shah, J.J.; Geist, J.; Locascio, L.E.; Gaitan, M.; Rao, M. V.; Vreeland, W.N. Surface modification of poly(methyl methacrylate) for improved adsorption of wall coating polymers for microchip electrophoresis. *Electrophoresis* **2006**, *27*, 3788–3796, doi:10.1002/elps.200600118.
  397. Patel, S.; Thakar, R.G.; Wong, J.; McLeod, S.D.; Li, S. Control of cell adhesion on poly(methyl methacrylate). *Biomaterials* **2006**, *27*, 2890–2897, doi:10.1016/j.biomaterials.2005.12.009.
  398. Situma, C.; Wang, Y.; Hupert, M.; Barany, F.; McCarley, R.L.; Soper, S.A. Fabrication of DNA microarrays onto poly(methyl methacrylate) with ultraviolet patterning and microfluidics for the detection of low-abundant point mutations. *Anal. Biochem.* **2005**, *340*, 123–135, doi:10.1016/j.ab.2005.01.044.
  399. Di Mauro, A.; Cantarella, M.; Nicotra, G.; Privitera, V.; Impellizzeri, G. Low temperature atomic layer deposition of ZnO: Applications in photocatalysis. *Appl. Catal. B Environ.* **2016**, *196*, 68–76.
  400. Silva, R.M.; Ferro, M.C.; Araujo, J.R.; Achete, C.A.; Clavel, G.; Silva, R.F.; Pinna, N. Nucleation, Growth Mechanism, and Controlled Coating of ZnO ALD onto Vertically Aligned N-Doped CNTs. *Langmuir* **2016**, *32*, 7038–7044, doi:10.1021/acs.langmuir.6b00869.
  401. Manring, L.E. Thermal Degradation of Poly(methyl methacrylate). 4. Random Side-Group Scission. *Macromolecules* **1991**, *24*, 3304–3309.
  402. SpectraBase Compound ID=Jk7oLgP89yO SpectraBase Spectrum ID=Gj4rylrJWCf Available online: <https://spectrabase.com/spectrum/Gj4rylrJWCf>.
  403. Nagai, H. Infrared spectra of stereoregular polymethyl methacrylate. *J. Appl. Polym. Sci.* **1963**, *7*, 1697–1714, doi:10.1002/app.1963.070070512.
  404. Nagaraju, G.; Udayabhanu; Shivaraj; Prashanth, S.A.; Shastri, M.; Yathish, K. V.; Anupama, C.; Rangappa, D. Electrochemical heavy metal detection, photocatalytic, photoluminescence, biodiesel production and antibacterial activities of Ag–ZnO nanomaterial. *Mater. Res. Bull.* **2017**, *94*, 54–63, doi:10.1016/j.materresbull.2017.05.043.
  405. Handore, K.; Bhavsar, S.; Horne, A.; Chhattise, P.; Mohite, K.; Ambekar, J.; Pande, N.; Chabukswar, V. Novel green route of synthesis of ZnO nanoparticles by using natural biodegradable polymer and its application as a catalyst for oxidation of aldehydes. *J. Macromol. Sci. Part A Pure Appl. Chem.* **2014**, *51*, 941–947, doi:10.1080/10601325.2014.967078.

406. Patra, N.; Barone, A.C.; Salerno, M. Solvent Effects on the Thermal and Mechanical Properties of Poly(methyl methacrylate) Casted from Concentrated Solutions. *Adv. Polym. Technol.* **2012**, *30*, 1–20, doi:10.1002/adv.20203.
407. Stuart, B.H. Infrared Spectroscopy: Fundamentals and Applications. In *Analytical Techniques in the Sciences*; Ando, D.J., Stuart, B.H., Eds.; John Wiley & Sons, Ltd, 2005; pp. 1–224 ISBN 9780470011140.
408. Dhaiveegan, P.; Manivannan, M.; Rajendran, N. Fabrication of ordered porous bioceramic coating via evaporation induced self assembly on 316L stainless steel for biomedical applications. *Trends Biomater. Artif. Organs* **2015**, *29*, 327–338.
409. Tang, E.; Cheng, G.; Ma, X. Preparation of nano-ZnO/PMMA composite particles via grafting of the copolymer onto the surface of zinc oxide nanoparticles. *Powder Technol.* **2006**, *161*, 209–214, doi:10.1016/j.powtec.2005.10.007.
410. Abasi, C.Y.; Wankasi, D.; Dikio, E.D. Adsorption study of lead(II) ions on poly(methyl methacrylate) waste material. *Asian J. Chem.* **2018**, *30*, 859–867, doi:10.14233/ajchem.2018.21112.
411. Abdelrazek, E.M.; Hezma, A.M.; El-khodary, A.; Elzayat, A.M. Spectroscopic studies and thermal properties of PCL/PMMA biopolymer blend. *Egypt. J. Basic Appl. Sci.* **2016**, *3*, 10–15, doi:10.1016/j.ejbas.2015.06.001.
412. Khairy, M.; Amin, N.H.; Kamal, R. Optical and kinetics of thermal decomposition of PMMA/ZnO nanocomposites. *J. Therm. Anal. Calorim.* **2017**, *128*, 1811–1824, doi:10.1007/s10973-016-6062-x.
413. Mishra, S.; Sen, G. Microwave initiated synthesis of polymethylmethacrylate grafted guar (GG-g-PMMA), characterizations and applications. *Int. J. Biol. Macromol.* **2011**, *48*, 688–694, doi:10.1016/j.ijbiomac.2011.02.013.
414. Christofferson, A.J.; Yiapanis, G.; Ren, J.M.; Qiao, G.G.; Satoh, K.; Kamigaito, M.; Yarovsky, I. Molecular mapping of poly(methyl methacrylate) super-helix stereocomplexes. *Chem. Sci.* **2015**, *6*, 1370–1378, doi:10.1039/c4sc02971b.
415. Jalali, E.; Maghsoudi, S.; Noroozian, E. A novel method for biosynthesis of different polymorphs of TiO<sub>2</sub> nanoparticles as a protector for *Bacillus thuringiensis* from Ultra Violet. *Sci. Rep.* **2020**, *10*, 1–9, doi:10.1038/s41598-019-57407-6.
416. Soria, J.; Sanz, J.; Sobrados, I.; Coronado, J.M.; Maira, A.J.; Hernández-Alonso, M.D.; Fresno, F. FTIR and NMR study of the adsorbed water on nanocrystalline anatase. *J. Phys. Chem. C* **2007**, *111*, 10590–10596, doi:10.1021/jp071440g.
417. Sanz, J.; Soria, J.; Sobrados, I.; Yurdakal, S.; Augugliaro, V. Influence of amorphous TiO<sub>2-x</sub> on titania nanoparticle growth and anatase-to-rutile transformation. *J. Phys. Chem. C* **2012**, *116*, 5110–5115, doi:10.1021/jp2112044.
418. M, C.; Rhm, H.; Ae, W.; M, M.; Ca, E.; Am, H. H-1 Nmr Spectroscopy Of Titania - Chemical Shift Assignments For Hydroxy Groups In Crystalline and Amorphous Forms Of TiO<sub>2</sub>. *J. Chem. Soc. Trans.* **1996**, *92*, 2791–2798.
419. Kawamura, T.; Toshima, N.; Matsuzaki, K. Assignment of finely resolved <sup>13</sup>C NMR spectra of poly(methyl methacrylate). *Macromol. Rapid Commun.* **1994**, *15*, 385–385, doi:10.1002/marc.1994.030150413.
420. Brar, A.S.; Singh, G.; Shankar, R. Structural investigations of poly(methyl methacrylate) by two-dimensional NMR. *J. Mol. Struct.* **2004**, *703*, 69–81, doi:10.1016/j.molstruc.2004.05.030.
421. Ribeiro, A.D.; Marques, J.; Forte, M.; Correia, F.C.; Parpot, P.; Oliveira, C.; Pereira, A.I.; Andrade, L.; Azenha, C.; Mendes, A.; et al. Microencapsulation of citronella oil for solar-activated controlled release as an insect repellent. *Appl. Mater. Today* **2016**, *5*, 90–97,

- doi:10.1016/j.apmt.2016.09.003.
422. Tavres, C.; Marques, J. Micro - or nanocapsules having photocatalytic properties for controlled release of diffusing agents and respective method of production 2018, 1–15.
  423. Miller, D.D.; Lenhart, W.; Antalek, B.J.; Williams, A.J.; Hewitt, J.M. The Use of NMR To Study Sodium Dodecyl Sulfate-Gelatin Interactions. *Langmuir* **1994**, *10*, 68–71, doi:10.1021/la00013a010.
  424. Singh, S.; Rao, K.V.R.; Venugopal, K.; Manikandan, R. Alteration in Dissolution Characteristics of Gelatin-Containing Formulations A Review of the Problem , Test Methods , and Solutions. *Pharm. Technol.* **2002**, *26*, 36–58.
  425. CHEMMUNIQUE *The HLB SYSTEM a time-saving guide to emulsifier selection*; ICI Americas Inc: Wilmington, Delaware 19897, 1980; ISBN 0376-7388.
  426. Gaonkar, A.G.; Vasisht, N.; Khare, A.R.; Sobel, R. *Microencapsulation in the Food industry A Practical Implementation Guide*; Academic Press: USA, 2014; ISBN 9788578110796.

## Appendix 1

### PMMA-MCs from strategy 1

This strategy was developed with the double emulsion technique, using UF in the solid-state and dissolved UF (**Figure i.1**). The procedure was based on the Zydowicz *et al.* method [354]. The AC was introduced in this native form (S/O/W) or was previously dissolved and then added into the PMMA solution ( $W_1/O/W_2$ ). Both were emulsified by magnetic stirring, where the S/O emulsion took 5 minutes to emulsify and the  $W_1/O$  24h. The resultant microcapsules were vacuum filtrated and washed with water to remove the excess PVA from the surface. The UF rich redness color from the iron present in the UF indicates this agrochemicals retention because the core and the PMMA-MCs-UF wall acquired the same color. Additionally, during the double emulsion step, the osmosis effect from the  $W_1$  or S to  $W_2$  was instantaneous because the agrochemical migrates and colors the  $W_2$  solution. In this stage, the procedure was improved to minimize osmosis and to obtain a better encapsulation yield.

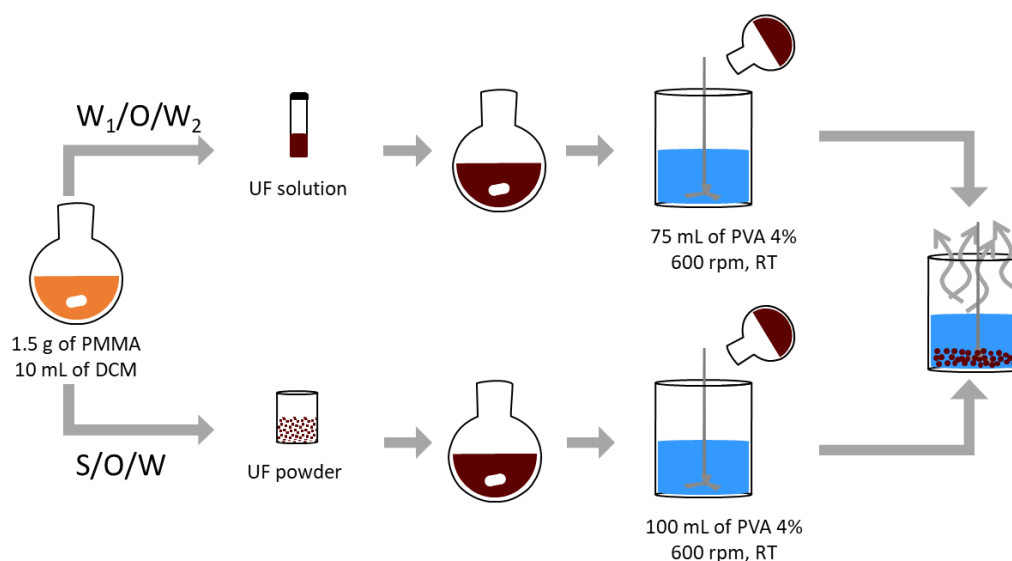


**Figure i.1.** Experimental procedures for S/O/W and  $W_1/O/W_2$  double emulsions in the solvent (DCM) evaporation method, using a 4-blade helix as impeller.

Besides the time to emulsify, the other difference was the 4% PVA volume, which, for this experiment, was not a determinant variable for the results visualized in **Figure i.2**. The PMMA-MCs from S/O/W emulsion are very heterogenous in terms of encapsulation yield (**Figure i.2** a and c). Conversely, the PMMA-MCs from  $W_1/O/W_2$  emulsion had a homogenous tone, suggesting a consistent encapsulation. Overall, there are microcapsules totally or partially formed and

polymeric residues wired shaped residues. The presence of a solid core provides a smooth surface, but most of them are open. Since it is the same solvent (DCM), it could be due to the UF grains that inhibit the solvent evaporation and the walls do not close. The UF solution transformed the PMMA wall into a structure with micro pores.

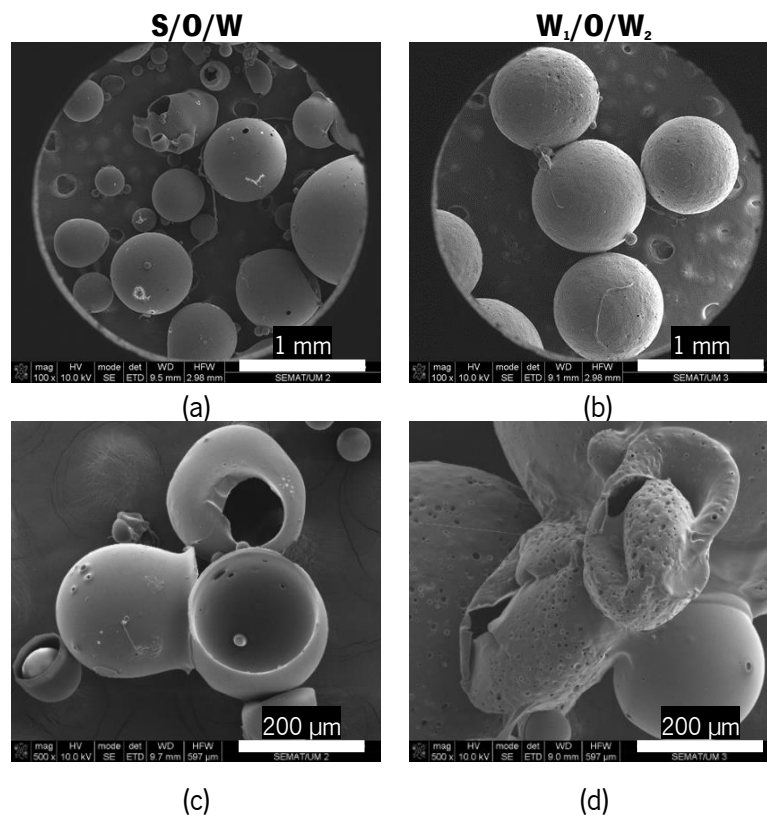


**Figure i.2.** SEM micrographs of PMMA-MCs with UF, made from (a and c) S/O/W and (b and d)  $W_1/O/W_2$ , using 4% of PVA. The samples were coated with Au before SEM analysis.

Additionally, these PMMA-MCs had more homogenous in terms of size and sphericity. In **Figure i.2** (d), the microcapsules are aggregated, and one of them has a smooth surface, which could indicate that this one in specific does not contain UF and forms a similar morphology to the PMMA-MCs-UF from the S/O/W emulsion. Hence the results were satisfactory; it was necessary to reformulate the synthesis, and there were two options. It would be more straightforward to control the porosity or close the MCs? At an early stage, it was challenging to make a clever choice; therefore, the two procedures were studied independently.

From this moment on, the work was dedicated to avoiding the UF migration, control the porosity in the  $W_1/O/W_2$  and/ or close the MCs from the other experimental detail. DCM was changed to the solvents from **Table 11**; the PMMA mass was varied; the 4-blade helix was

changed to Cowles, 3-blade naval and magnetic stirring. The rotation speed was changed to 500 and 1000 rpm to understand the efficiency of the process. Additionally, the emulsification system was changed using Span® emulsifiers in the oily phase, and Arabic gum or Tween® emulsifiers as the PVA substitutes. Some reactions were interrupted at 15 or 30 min to see if the stirring and time influenced the PMMA-MCs morphology.

In the S/O/W method, toluene, acetone, n-hexane, cyclohexane and chloroform substituted DCM to dissolve PMMA. The synthesis occurs at room conditions in order to obtain PMMA-MCs by solvent extraction technique. Because of similarities in the processes, some solvents were also tested in  $W_1/O/W_2$ . Since toluene and chlorobenzene have a high boiling point, they were tested with ramp temperatures to evaporate the solvent. The emulsion was poured into the continuous phase at 40 °C for 15 minutes, followed by a temperature increase to 60 °C for 15 minutes and from 60 to 80 °C for the same time (**Figure i.3**).

Regardless of the amount of UF introduced in the S/O/W emulsion, osmosis will always occur. So, for a higher UF mass, the respective diffusion will be more considerable. It is worthy to notice that the amount of UF does not interfere with the PMMA-MCs size, but produces an overall tone uniformity. The other alternatives to retain this agrochemical was to modify the PMMA mass or the stirring velocity. However, again, it resulted in the formation of residues with less or higher mass, heterogenous PMMA-MCs-UF sizes, making it challenging to make conclusions. Nevertheless, it maintained the characteristics of the procedures mentioned in **Figure i.1**.

A few experiments with Span®80 and Span®85 emulsifiers mixed into the DCM solution (individually) were attempted to create a more stable emulsion to overcome this obstacle (**Table i.1**) [425]. When employing the Span®85 and Tween®20 emulsifiers, the solvents from the oily phase to toluene and chloroform. The same was repeated for PVA instead of Tween®20. The results are very distinct for each solvent. From the results in **Figure i.4**, there are some theories: DCM seems to be the most suitable solvent when combined with emulsifiers like Span®85 and PVA or Span®85 and Tween®20. All synthesis was made at 50°C; this temperature is over the methylene chloride boiling point, ensuring solvent evaporation. The vapor pressure value is significantly elevated, and the viscosity is lower; both chemical properties help in the microencapsulation procedure. Contrarily, toluene is the solvent with lower vapor pressure and higher boiling point, so it will be challenging to obtain PMMA-MCs at this temperature (the other procedures with this solvent were at higher temperatures) (**Table 11**). When chloroform was used as a solvent the result was the less efficient. One possible explanation is based on the high density that inhibits the

shear.

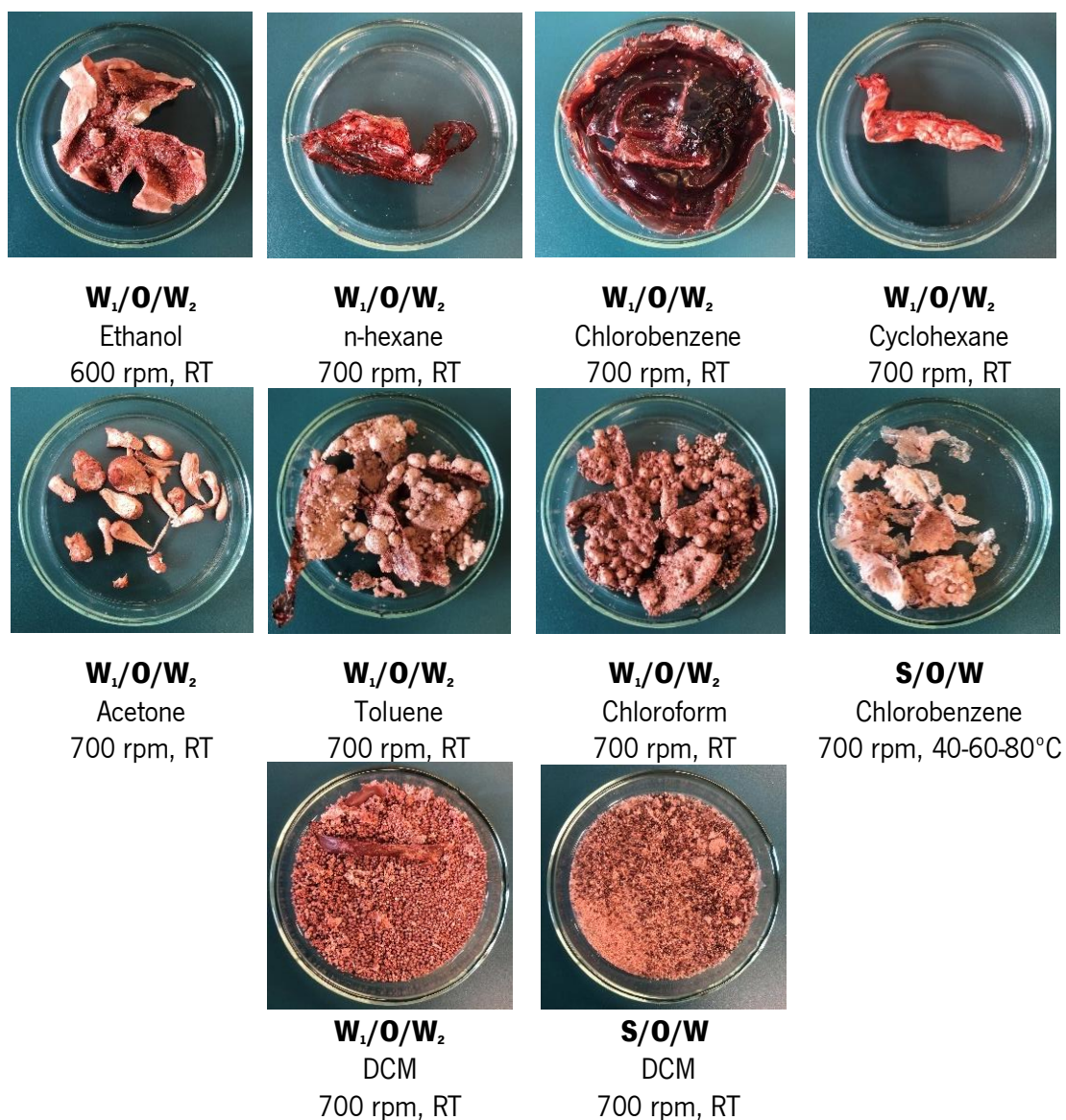


**Figure i.3.** Photographs of products from the double emulsions made by solvent evaporation technique with different solvents and maintaining the reaction temperature.

**Table i.1.** Surfactants and hydrophilic-lipophilic balance values.

Hydrophobic					Hydrophilic				
0	2	4	6	8	10	12	14	16	18
		1.83 Span <sup>®</sup> 85						15 Tween <sup>®</sup> 20	
			4.3 Span <sup>®</sup> 80					15.6 Tween <sup>®</sup> 40	
			4.7 Span <sup>®</sup> 60					16.7 Tween <sup>®</sup> 80	

Span<sup>®</sup>85 and PVA produced similar PMMA-MCs-UF. The 4% PVA solution is more viscous than the Tween<sup>®</sup>20. So, during the agitation in the Tween<sup>®</sup>20 aqueous solution, PMMA will not



stabilize the droplets, creating more agglomerates. Another important aspect is the PMMA affinity to the solvents that influence all the parameters presented before, especially the solution viscosity. Span®85 and Tween®20 were eliminated from the synthesis, and the  $W_2$  was again a PVA aqueous solution.

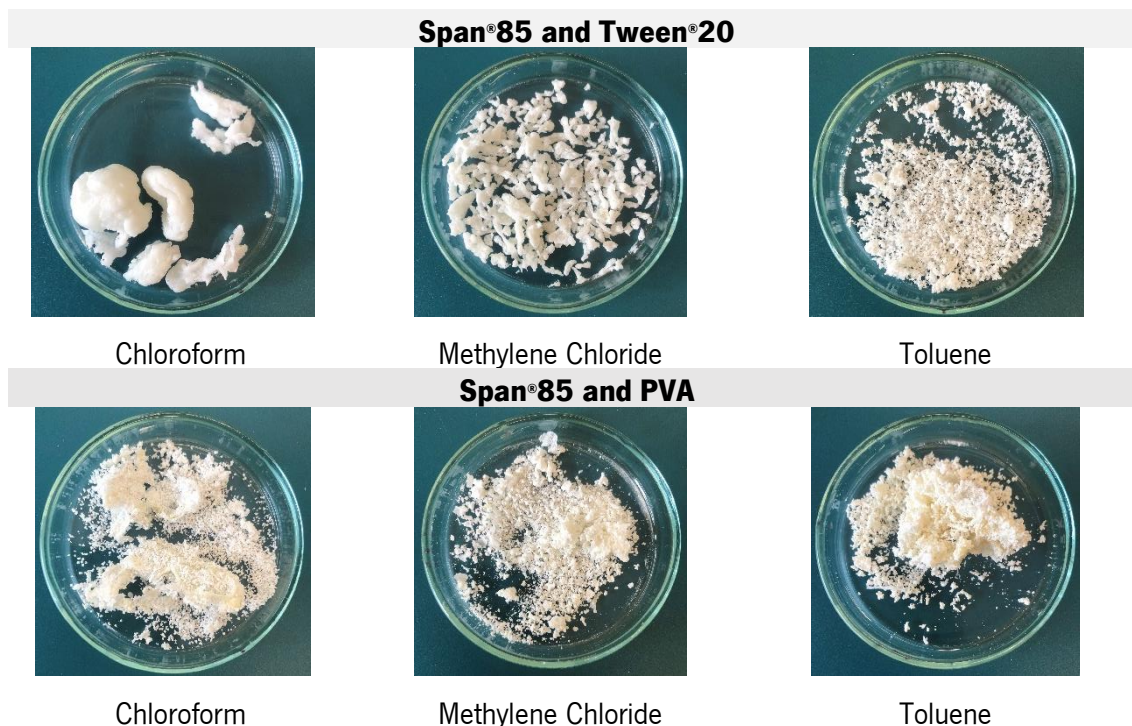


**Figure i.4.** Photographs of products from solvent evaporation, using Span®85 in the oily phase and PVA or Tween®20 aqueous solution as continuous phase.

The PVA percentage was studied from 1 to 4%, being the most concentrated PVA solution previously presented in **Figure i.2** (a), and the MCs from lower PVA percentages in **Figure i.5**. The PVA percentage is crucial for the method. The PVA volume seems to influence the MCs formation, which is plausible because there is more volume to stir for an equal speed. As a consequence, the shear is reduced, and the resulting PMMA-MCs-UF have larger sizes. After a closer inspection, the PMMA-MCs-UF walls are not well formed, and a part of them are aggregated, sharing the polymeric wall. All MCs present porous walls, and the amount of the residue is more or less the same.

The SEM images from the PVA concentration variation have similar effects from lower and higher concentrations suggesting a gaussian-like effect in the encapsulation. For PVA 1%, the droplets cannot reach an equilibrium in the continuous phase because they do not have sufficient



viscosity. The instability compromises the MCs, producing heterogeneous diameters and faster solvent evaporation, meaning significant holes in the structure. For 4% (**Figure i.2**) and 3% of PVA, there is the formation of more uniform MCs, the spots from the solvent are eliminated, however the porosity was maintained. Additionally, the residue amount is higher, possibly due to the longer solvent evaporation from the PVA's high viscosity. Therefore, the more balanced choice was the MCs from the 3% PVA, and the subsequent experiments were with this continuous phase concentration. The only expectations were the MCs from the Arabic gum as surfactant.

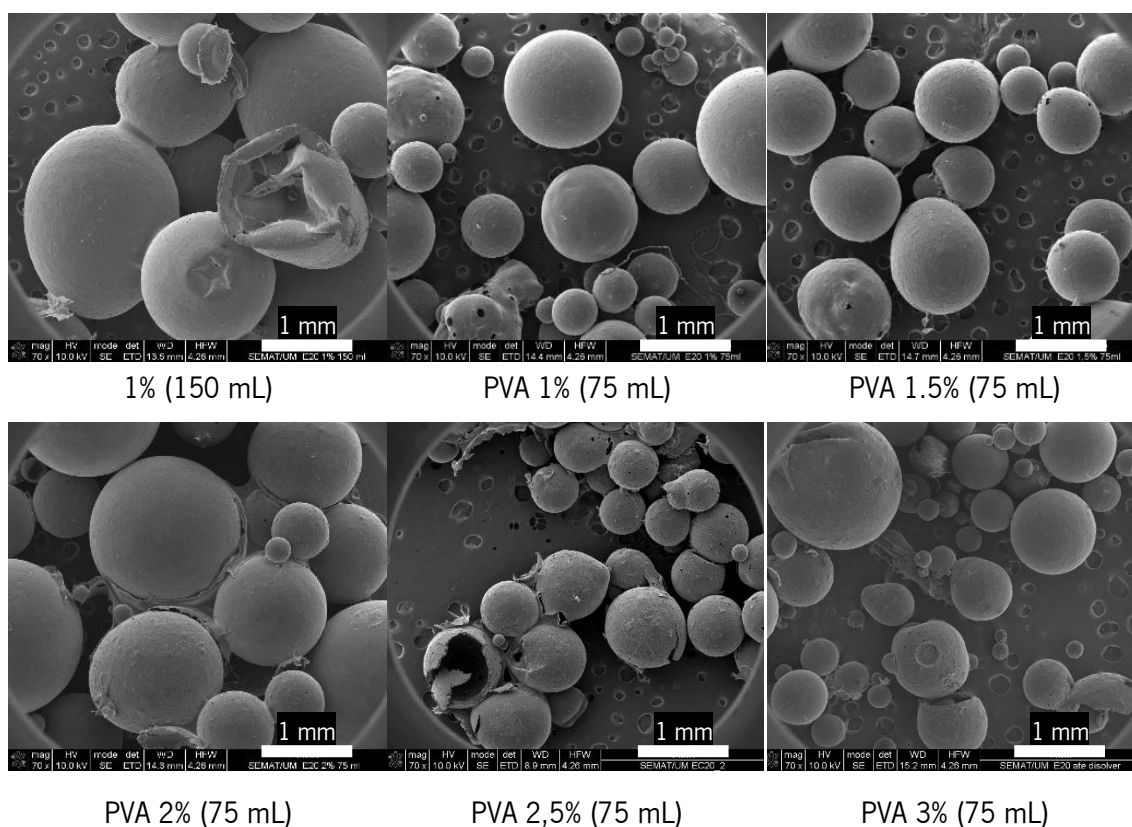


**Figure i.5.** SEM micrographs of PMMA-MCs with UF from the S/O/W emulsion with varying PVA percentage. The samples were coated with Au before SEM analysis.

The Arabic gum or Acacia gum is a complex hydrophilic surfactant rich in polysaccharides, glycoproteins, and arabinogalactan oligosaccharides. This natural surfactant is provided from the *Acacia* species, and the different parts of the gum have other functions. For this work, the most relevant is the protein content responsible for the emulsification, and the amino acids are the emulsion stabilizers. This negative charge surfactant employs repulsive forces to avoid coalescence [78,426].

Following the standard procedure for double emulsion with the UF dissolved in water, some procedures were terminated when agitation lasted for 15 or 100 minutes, using PVA or Arabic gum. During the 100 minutes of agitation the PVA formed a foam and the pores in the walls of the microcapsules were considered to arise from the foam. Therefore, the alternatives under consideration were to reduce the stirring time and change the surfactant to one that did not foam, such as Arabic gum.

A 10% (w/w) Arabic gum solution was made by shaking for 15 and 100 minutes as before in PVA. The gum has less viscosity, and this was reflected in the final PMMA-MCs as it has more homogeneous diameters than PMMA-MCs using PVA. Interestingly, the Arabic gum does not affect the pores in the microcapsule walls. Stirring time proved to be essential for the two surfactants as it ensures solvent evaporation and the foam it is not related with the stirring time.

For this specific study - and possibly due to the PMMA molecular weight as well concentration in the oily phase - the rotation speed and the choice of and the impellers do not favor the PMMA-MCs morphology. Using a 4-blade helix impeller and duplicating the speed decrease the MCs size, although there is polymer waste, and some MCs are not completely formed. The MCs produced with 500 rpm larger sizes; the sphericity is also compromised because the speed is not sufficient to create spheres. The transition to magnetic stirring produces MCs with narrow diameters and coalesced. The Cowles impeller produced better MCs than 700 rpm with a 4-blade helix impeller, but the amount of polymeric waste does not encourage to change the procedure. The naval impeller enables better results than the other stirring methods and uniformizes the PMMA-MCs size **Figure i.6**.

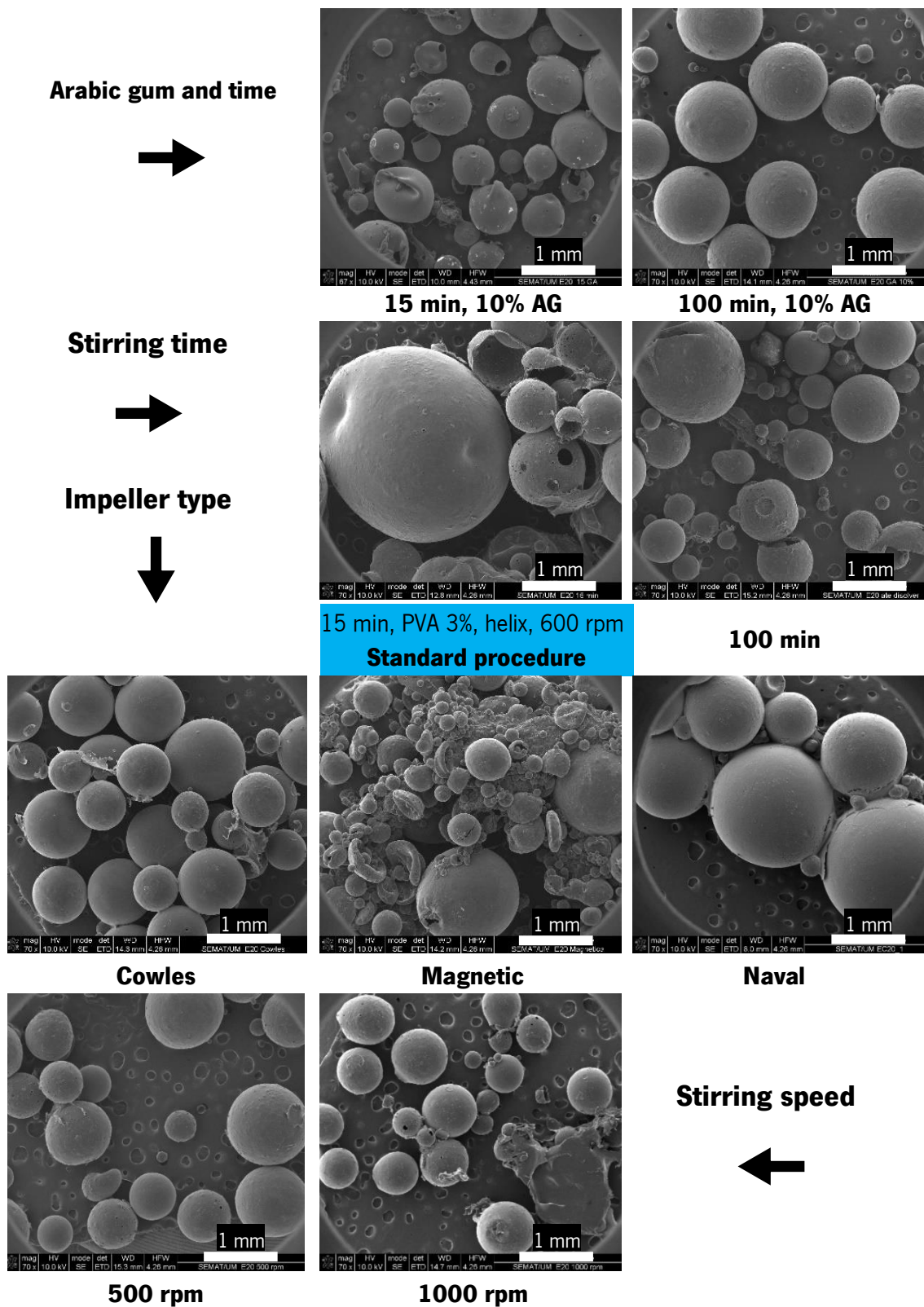


**Figure i.6.** SEM micrographs of PMMA-MCs with UF from the following variables in the synthesis: surfactant and stirring time, impeller and stirring speed. The samples were coated with Au before SEM analysis.

**Figure i.7** shows SEM micrographs of catted the PMMA-MCs-UF. Some of them have pores inside but not outside of the structure, and the rotation confirms this. The holes in the MCs seem to be filled with UF. Also, the walls are very thick and not equal in all the perimeter. **Figure i.7 (c)** confirms that the AC is inside of some PMMA-MCs-UF as powder, and the wall thickness is  $\approx 35 \mu\text{m}$ . Overall, the core is not distributed homogenously inside of all PMMA-MCs-UF and, despite the massive heterogeneity, increasing the amount of UF to 0.5 g creates MCs with some grains inside.

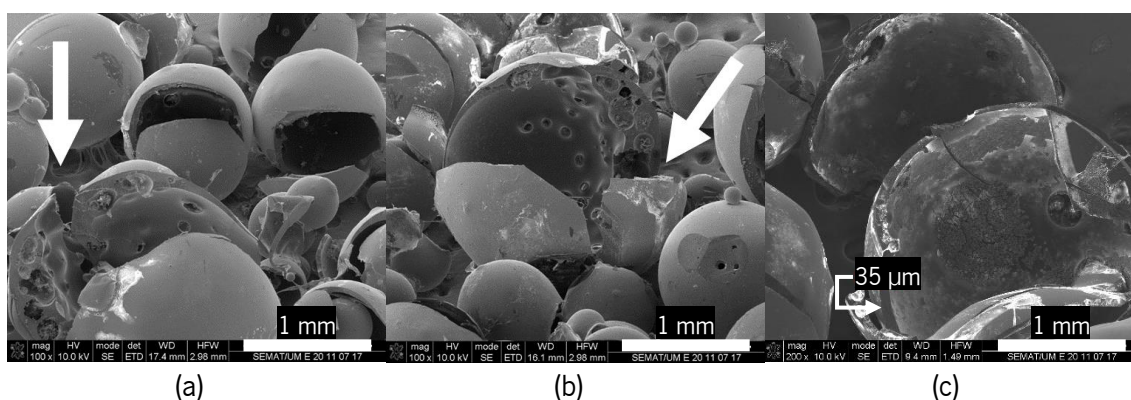


**Figure i.7.** SEM micrographs of (a) cut MCs from the S/O/W solvent evaporation technique, (b) the same MCs with a rotation of  $180^\circ$ , (c) amplified MC with UF inside. The samples were coated with Au before SEM analysis.

It is noteworthy that in all configurations, the osmosis or the MCs porosity were not controlled or attenuated. This strategy failed, unfortunately, with no experimental procedures to be applied in the ALD phase. The knowledge acquired was that the most critical parameters are the PMMA mass, the solvent, and the impeller.

## PMMA-MCs from strategy 2

In theory, the easiest way to end the UF migration is to eliminate one aqueous phase since it is impossible to eradicate the UF phase, as solid or in solutions. Phase  $W_2$  was the selected phase to be changed by an oily phase. The following experiments were inspired in the Jelvehgari [353], Viswanathan [105] works, with the  $W/O_1/O_2$  emulsions to produce MCs. Despite the polymer differences, the solvent and the method employed were the same, as well the chosen surfactants.

The cellulose acetate solubility was tested in some organic solvents like chloroform and

ethyl acetate, that were the solvents with important role in the first strategy. Some emulsifiers and stirring systems were analyzed, essentially using the naval impeller and magnetic stirring. After obtaining some MCs, the principal concern was to create a suitable washing procedure. When the continuous phase is PVA or Arabic gum, the washing system is a vacuum filtration with water. This type of emulsion is necessary to remove the oils, but the water is an incompatible phase. Therefore, the washing procedure was under vacuum to optimize the washing and minimize the volume of the solvent per washing.

A significant percentage of the experiments showed that the PMMA in W/O<sub>1</sub>/O<sub>2</sub> emulsions cannot form microcapsules. In this case, it was PMMA-MCs-UF formation, because there is a polymeric wall and a core inside. Again, an empty shell or filled with continuous phase. These results were kind of expected, because the continuous phase was always more viscous than the PMMA phase.

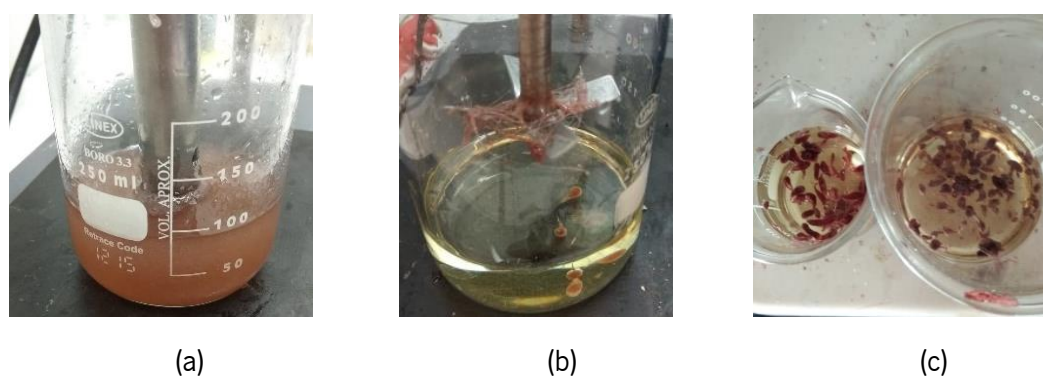


**Figure i.8.** Products from the encapsulation W/O<sub>1</sub>/O<sub>2</sub> synthesis using different impellers (Ultra-Turrax®, 4-blade helix and magnetic stirring), where the W is a UF solution, O<sub>1</sub> is the PMMA solution and O<sub>2</sub> is sunflower oil.

In a certain way, the method to obtain MCs in this strategy was achieved by reducing the parameters associated with the emulsification. The Ultra-Turrax® formed a stable emulsion with all phases. The polymer cannot be agitated mechanically because the W/O<sub>1</sub> emulsion agglomerates around the impeller. Also, utilizing the magnetic agitation was verified giving the equivalent products. Therefore, the only way to obtain PMMA-MCs-UF was to remove the stirring by pouring the first emulsion in the continuous phase (**Figure i.8**). However, increased polymer concentration was needed because the lower concentrations do not have enough volume to sink in the oil. Subsequently, during the pouring, the solution droplets produced repellency. This phenomenon



incapacitates the PMMA-MCs-UF formation and the solvent evaporation; also, there was coalescence. The resultant capsules (not micrometric) were very wrinkled and, indeed, because the solvent evaporation was too slow. A few had an aspect like a droplet, with a tailored termination due to the mass increment. In opposition, decreasing  $O_1$  viscosity does not sink in the  $O_2$  phase, impeding the MCs formation. At this point, the polymeric wall was more uniform, even with relief.

PMMA was replaced by cellulose acetate to enhance MCs. This polymer was dissolved in ethyl acetate and poured into sunflower oil. Apart from the similar behavior with PMMA, the viscosity and the solvent evaporation are more defined. Since the droplets were not closing, it was necessary to add stirring in these experiments. Therefore, the magnetic stirring was added for cellulose acetate concentrations, and each one was tested in paraffin and sunflower oil. Further, the continuous phase was replaced by mineral oil, isopropanol mixed with Span®80, and the combination of paraffin with Span®80 or toluene to decrease the medium viscosity.

The best cellulose acetate capsules with 5% concentration in the same solvent were poured into paraffin or sunflower oil, stirred with a 3-blade naval impeller (**Figure i.9**). After crushing the capsules, it was visible that the core was filled with UF solution and  $O_2$  phase. Another limiting factor from this strategy was finding a suitable washing system. The solvents employed were water, Tween®20, 40 and 80 dissolved in water, n-hexane, toluene, cyclohexane. The utilization of organic solvents damaged the capsules, by collapsing or agglomerating. Furthermore, changing the ethyl acetate to chloroform was not an improvement because the solution was not homogenized.



**Figure i.9.** (a) Amplified image of cellulose acetate capsules with UF as core (5%). (b) Photos of crushed cellulose acetate capsules with UF, synthesized with paraffin or sunflower oil as surfactants. The UF stained the filter and the capsules with sunflower oil also release the surfactant.

Reuniting all these limitations, the new polymeric wall was not enough to encapsulate the UF. To take advantage of the two materials, study blending both was endured. The  $O_1$  phase with

4% cellulose acetate and 1% of PMMA had satisfactory results in paragon and sunflower oil as surfactants. As expected, the higher cellulose acetate concentration determined the capsule's shape and mechanical resistance. The ratio was modified to a 50:50 and 75:25 PMMA and cellulose acetate. This approach resulted in no capsules formation.

To summarize, this strategy is more accessible to produce capsules with cellulose acetate as W/O<sub>i</sub>/O<sub>2</sub> than PMMA. In all cases, the agrochemical stayed in the supposed phase or migrated to the polymers. The optimization parameters are not straight-forward e to substitute the polymer and create MCs in a reproducible way.

## Appendix 2

### NMR spectra

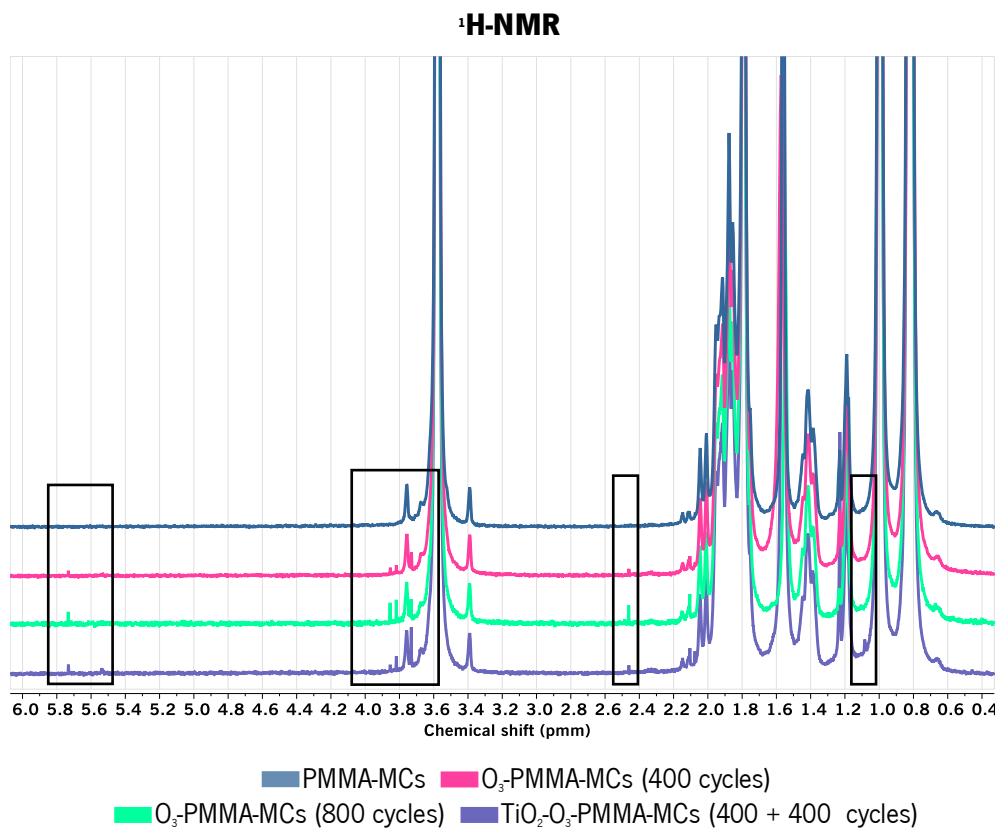


**Figure ii.1.** Amplified <sup>1</sup>H-NMR spectra of PMMA-MCs, PMMA-MCs pre-treated microcapsules (O<sub>3</sub>-PMMA-MCs) with 400 and 800 cycles of ozone by ALD treatment, and coated microcapsules (TiO<sub>2</sub>-O<sub>3</sub>-PMMA-MCs) previously pre-treated with 400 cycles of ozone and further coated with 400 cycles of TiO<sub>2</sub> deposited by ALD. All samples were dissolved into CDCl<sub>3</sub>.



## HBQC spectra

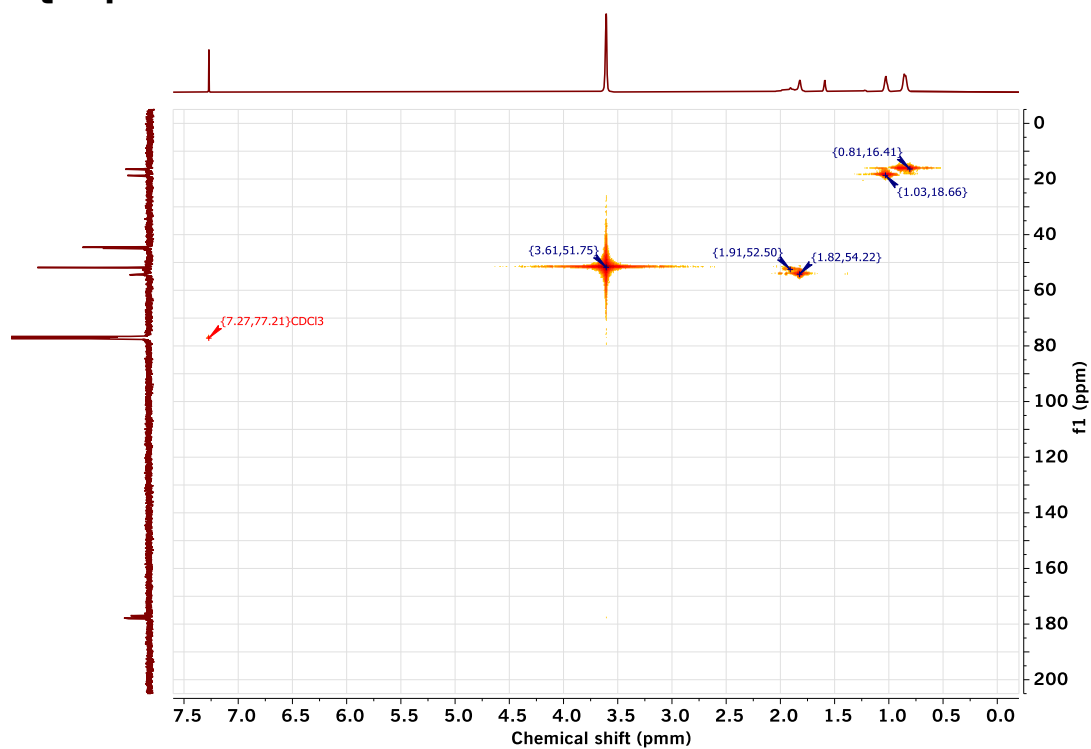


**Figure ii.2.** HMQC spectrum of PMMA-MCs.

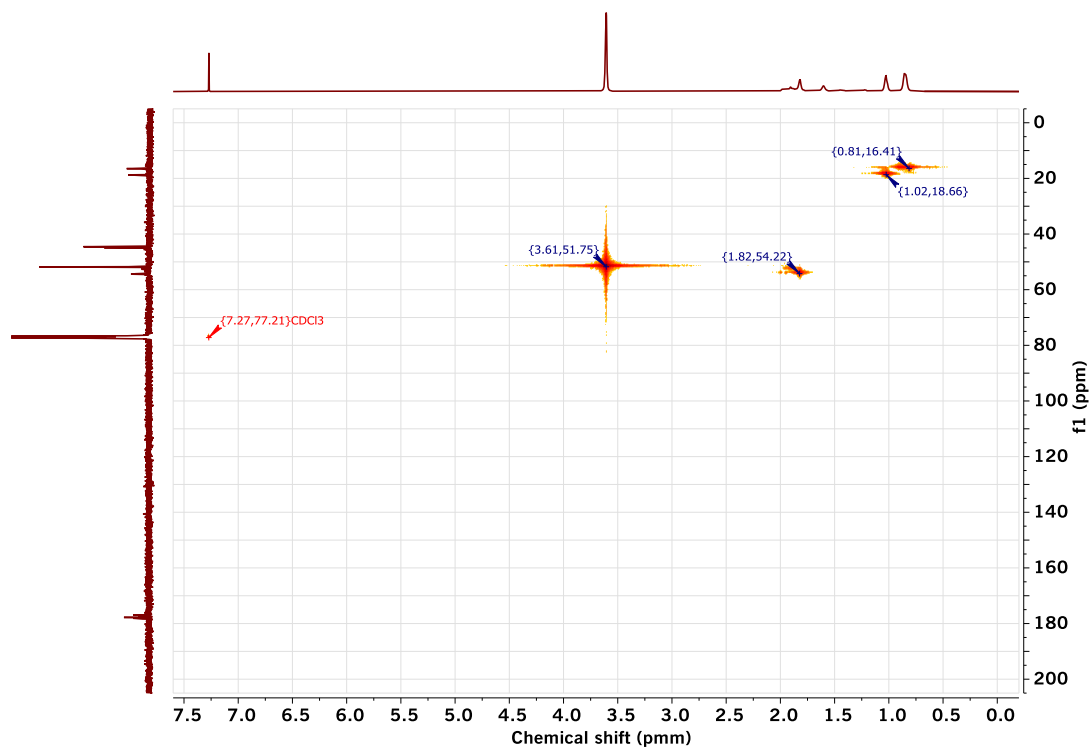


**Figure ii.3.** HMQC of O<sub>3</sub>-PMMA-MCs pre-treated with 400 cycles of ozone by ALD.

## HMBC spectra and signal table

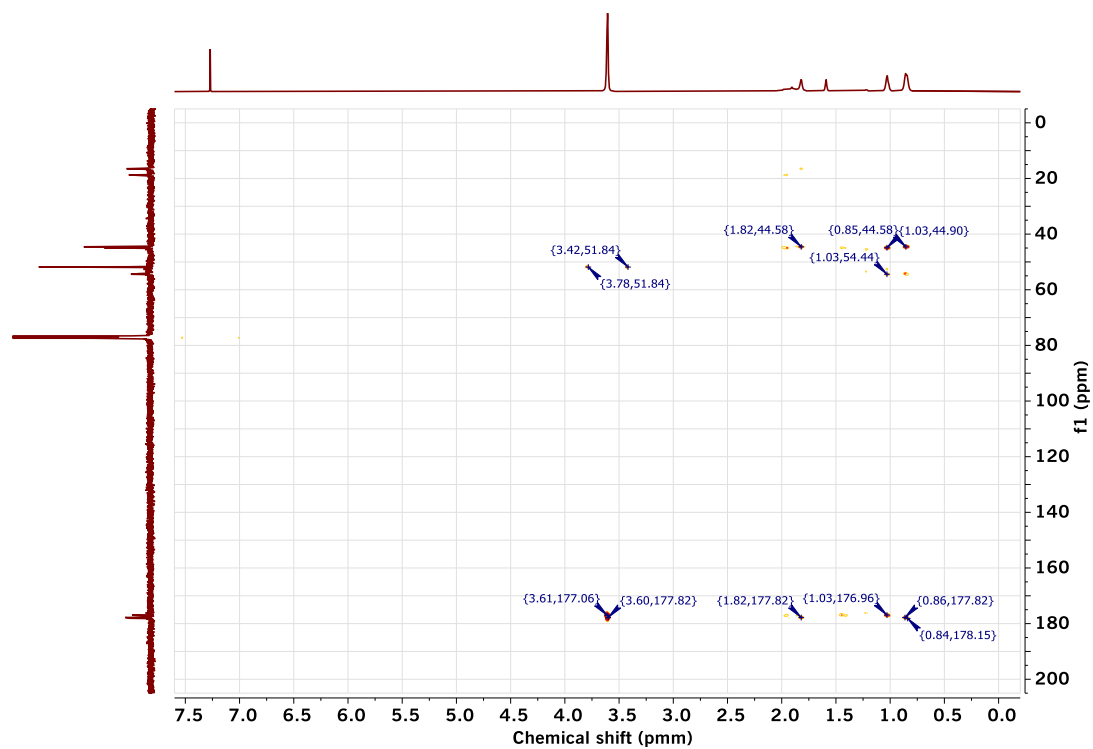


**Figure ii.4.** HMBC spectrum of PMMA-MCs.

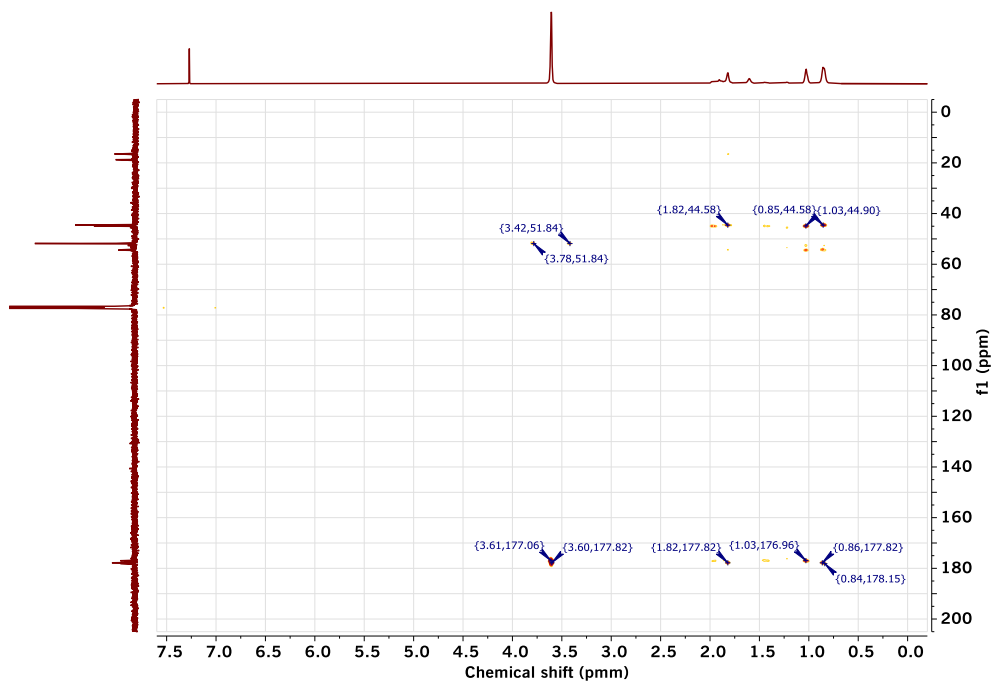


**Figure ii.5.** HMBC of  $\text{O}_3$ -PMMA-MCs pre-treated with 400 cycles of ozone by ALD

**Table ii.1.** HMBC signals for the PMMA-MCs and the O<sub>3</sub>-PMMA-MCs and the respective chemical groups identification. The grey zones are unknown peaks.

PMMA-MCs				O <sub>3</sub> -PMMA-MCs			
δ (ppm)		Signal identification		δ (ppm)		Signal identification	
<sup>13</sup> C-NMR	<sup>1</sup> H-NMR	<sup>13</sup> C	<sup>1</sup> H	<sup>13</sup> C-NMR	<sup>1</sup> H-NMR	<sup>13</sup> C	<sup>1</sup> H
15.08	0.85		-CH <sub>3</sub> (syndiotactic)				
16.50	1.81	-CH <sub>3</sub> , rr (syndiotactic)	-CH <sub>2</sub> , rrr, (syndiotactic)	16.50	1.81	-CH <sub>3</sub> , rr (syndiotactic)	-CH <sub>2</sub> , rrr, (syndiotactic)
18.73	2.74	-CH <sub>3</sub> , rmrr+mmrr and mrrm+rmmr (atactic)					
18.76	1.94	-CH <sub>3</sub> , rmrr+mmrr and mrrm+rmmr (atactic)	-CH <sub>2</sub> , rmr	18.76	1.94	-CH <sub>3</sub> , rmrr+mmrr and mrrm+rmmr (atactic)	-CH <sub>2</sub> , rmr
18.98	1.43	-CH <sub>3</sub> , rr (syndiotactic)	-CH <sub>2</sub> , rmr	18.98	1.94	-CH <sub>3</sub> , rmrr+mmrr and mrrm+rmmr (atactic)	-CH <sub>2</sub> , rmr
44.14	0.85		-CH <sub>3</sub> (syndiotactic)	44.14	0.85		-CH <sub>3</sub> (syndiotactic)
44.14	1.81		-CH <sub>2</sub> , rrr (syndiotactic)	44.14	1.81		-CH <sub>2</sub> , rrr (syndiotactic)
44.14	0.84		-CH <sub>3</sub> (syndiotactic)				
44.55	1.43	-αC, rr (syndiotactic)	-CH <sub>2</sub> , rmr				
44.55	1.94	-αC, rr (syndiotactic)	-CH <sub>2</sub> , rmr				
44.55	1.02	-αC, rr (syndiotactic)	-CH <sub>3</sub> (atactic)				
44.55	0.85	-αC, rr (syndiotactic)	-CH <sub>3</sub> (syndiotactic)				
44.57	1.81	-αC, rr (syndiotactic)	-CH <sub>2</sub> , rrr (syndiotactic)	44.57	1.81	-αC, rr (syndiotactic)	-CH <sub>2</sub> , rrr (syndiotactic)
				44.57	1.02	-αC, mr+rm (atactic)	-CH <sub>3</sub> (atactic)
				44.57	0.84	-αC, mr+rm (atactic)	-CH <sub>3</sub> (syndiotactic)
44.88	1.43	-αC, mr+rm (atactic)	-CH <sub>2</sub> , rmr				
44.88	0.84	-αC, mr+rm (atactic)	-CH <sub>3</sub> (syndiotactic)	44.88	0.84	-αC, mr+rm (atactic)	-CH <sub>3</sub> (syndiotactic)
44.89	1.02	-αC, mr+rm (atactic)	-CH <sub>3</sub> (atactic)	44.89	1.02	-αC, mr+rm (atactic)	-CH <sub>3</sub> (atactic)
				44.88	1.39	-αC, mr+rm (atactic)	-CH <sub>2</sub> , rmr

44.89	1.94	- $\alpha$ C, mr+rm (atactic)	-CH <sub>2</sub> , rmr				
44.89	1.81	- $\alpha$ C, mr+rm (atactic)	-CH <sub>2</sub> , rrr (syndiotactic)	44.89	1.81	- $\alpha$ C, mr+rm (atactic)	-CH <sub>2</sub> , rrr (syndiotactic)
45.05	1.43		-CH <sub>2</sub> , rmr				
45.05	1.22		-CH <sub>3</sub> (isotactic)				
45.05	0.84		-CH <sub>3</sub> (syndiotactic)				
45.05	1.02		-CH <sub>3</sub> (atactic)				
45.05	1.20		-CH <sub>3</sub> (isotactic)				
				45.05	1.94		-CH <sub>2</sub> , rmr
45.23	1.01		-CH <sub>3</sub> (atactic)	45.23	1.02		-CH <sub>3</sub> (atactic)
45.23	1.94		-CH <sub>2</sub> , rmr	45.23	1.94		-CH <sub>2</sub> , rmr
45.41	1.43	$\alpha$ C, mm (isotactic)	-CH <sub>2</sub> , rmr				
45.41	1.22	$\alpha$ C, mm (isotactic)	-CH <sub>3</sub> (isotactic)	45.41	1.20	$\alpha$ C, mm (isotactic)	-CH <sub>3</sub> (isotactic)
45.41	1.01	$\alpha$ C, mm (isotactic)	-CH <sub>3</sub> (atactic)				
45.52	1.22	$\alpha$ C, mm (isotactic)	-CH <sub>3</sub> (isotactic)	45.52	1.20	$\alpha$ C, mm (isotactic)	-CH <sub>3</sub> (isotactic)
45.89	1.22		-CH <sub>3</sub> (isotactic)				
51.83	3.41	-OCH <sub>3</sub>	-OCH <sub>3</sub>	51.83	3.41	-OCH <sub>3</sub>	-OCH <sub>3</sub>
51.83	3.77	-OCH <sub>3</sub>	-OCH <sub>3</sub>	51.83	3.77	-OCH <sub>3</sub>	-OCH <sub>3</sub>
52.49	1.02	-CH <sub>2</sub> , mrr and mmm (isotactic)	-CH <sub>3</sub> (atactic)	52.49	1.02	-CH <sub>2</sub> , mrr and mmm (isotactic)	-CH <sub>3</sub> (atactic)
53.42	1.22	-CH <sub>2</sub> , mmr	-CH <sub>3</sub> (isotactic)	53.42	1.22	-CH <sub>2</sub> , mmr	-CH <sub>3</sub> (isotactic)
54.12	1.81	-CH <sub>2</sub> , rrr (syndiotactic) and rmr	-CH <sub>2</sub> , rrr (syndiotactic)	54.12	1.81	-CH <sub>2</sub> , rrr (syndiotactic) and rmr	-CH <sub>2</sub> , rrr (syndiotactic)
				54.12	1.19	-CH <sub>2</sub> , rrr (syndiotactic) and rmr	-CH <sub>3</sub> (isotactic)
54.20	0.84	-CH <sub>2</sub> , rrr (syndiotactic) and rmr	-CH <sub>3</sub> (syndiotactic)				
				54.20	1.02	-CH <sub>2</sub> , rrr (syndiotactic) and rmr	-CH <sub>3</sub> (atactic)

54.21	1.02	-CH <sub>2</sub> , rrr (syndiotactic) and rmr	-CH <sub>3</sub> (atactic)	54.21	0.85	-CH <sub>2</sub> , rrr (syndiotactic) and rmr	-CH <sub>3</sub> (syndiotactic)
54.43	1.02	-CH <sub>2</sub> , rrr (syndiotactic) and rmr	-CH <sub>3</sub> (atactic)	54.43	1.02	-CH <sub>2</sub> , rrr (syndiotactic) and rmr	-CH <sub>3</sub> (atactic)
				54.43	1.81	-CH <sub>2</sub> , rrr (syndiotactic) and rmr	-CH <sub>2</sub> , rrr (syndiotactic)
54.44	0.84	-CH <sub>2</sub> , rrr (syndiotactic) and rmr	-CH <sub>3</sub> (syndiotactic)	54.44	0.85	-CH <sub>2</sub> , rrr (syndiotactic) and rmr	-CH <sub>3</sub> (syndiotactic)
176.95	1.02	-C=O, mmrr and rmrr	-CH <sub>3</sub> (atactic)	176.95	1.02	-C=O, mmrr and rmrr	-CH <sub>3</sub> (atactic)
176.96	1.42	-C=O, mmrr and rmrr	-CH <sub>2</sub> , rmr	176.96	1.43	-C=O, mmrr and rmrr	-CH <sub>2</sub> , rmr
176.96	1.94	-C=O, mmrr and rmrr	-CH <sub>2</sub> , rmr	176.96	1.94	-C=O, mmrr and rmrr	-CH <sub>2</sub> , rmr
176.96	1.85	-C=O, mmrr and rmrr	-CH <sub>2</sub> , rrr (syndiotactic)				
176.96	3.60	-C=O, mmrr and rmrr	-OCH <sub>3</sub>	176.96	3.60	-C=O, mmrr and rmrr	-OCH <sub>3</sub>
177.13	3.60	-C=O, mmrm and rrmr	-OCH <sub>3</sub>	177.13	3.60	-C=O, mmrm and rrmr	-OCH <sub>3</sub>
				177.13	1.02	-C=O, mmrm and rrmr	-CH <sub>3</sub> (atactic)
				177.13	1.43	-C=O, mmrm and rrmr	-CH <sub>2</sub> , rmr
177.13	1.85	-C=O, mmrm and rrmr	-CH <sub>2</sub> , rmr				
177.13	1.94	-C=O, mmrm and rrmr	-CH <sub>2</sub> , rmr				
				177.81	1.94	C=O, rrr (syndiotactic)	-CH <sub>2</sub> , rmr
177.81	1.81	-C=O, rrr (syndiotactic)	-CH <sub>2</sub> , rrr (syndiotactic)	177.81	1.81	-C=O, rrr (syndiotactic)	-CH <sub>2</sub> , rrr (syndiotactic)
177.81	3.59	-C=O, rrr (syndiotactic)	-OCH <sub>3</sub>	177.81	3.60	C=O, rrr (syndiotactic)	-OCH <sub>3</sub>
177.81	0.85	-C=O, rrr (syndiotactic)	-CH <sub>3</sub> (syndiotactic)	177.81	0.85	C=O, rrr (syndiotactic)	-CH <sub>3</sub> (syndiotactic)
178.09	3.59	-C=O, mrrr and rrrm	-OCH <sub>3</sub>	178.09	3.60	C=O, mrrr and rrrm	-OCH <sub>3</sub>
				178.09	1.90	C=O, mrrr and rrrm	-CH <sub>2</sub> , rmr
				178.09	1.81	C=O, mrrr and rrrm	-CH <sub>2</sub> , rrr (syndiotactic)
				178.09	0.85	C=O, mrrr and rrrm	-CH <sub>3</sub> (syndiotactic)